LABORATORY MEASUREMENTS OF DEEP WATER BREAKING WAVES

Vol. 1

by

Ronald James Rapp

B.S.M.E. The Pennsylvania State University
(1977)

SUBMITTED TO THE DEPARTMENT OF OCEAN ENGINEERING
IN PARTIAL FULFILLMENT OF THE REQUIREMENTS
FOR THE DEGREE OF

DOCTOR OF PHILOSOPHY

at the

MASSACHUSETTS INSTITUTE OF TECHNOLOGY

January 1986

Signature of Author _____
Department of Ocean Engineering
January 1986

Certified by _____
Associate Professor Wallace K. Melville
Thesis Supervisor

Accepted by _____
Professor A. D. Carmichael
Chairman, Department Committee on Graduate Students

LABORATORY MEASUREMENTS OF DEEP WATER BREAKING WAVES

by

RONALD J. RAPP

Submitted to the Massachusetts Institute of Technology
in partial fulfillment for the requirements for
the Degree of Doctor of Philosophy

ABSTRACT

Breaking surface waves in deep water are studied for their role in dissipating wave energy, in mixing, and in transferring horizontal momentum from waves to currents. These topics are investigated in a program of experimental research where a single breaking wave group is generated in a laboratory channel. A frequency modulated wave packet evolves to breaking by the superposition of frequency components.

The loss of excess momentum flux and energy flux from the carrier waves are determined as functions of the wave packet parameters. Losses of 10 to 25% of the initial carrier wave momentum flux were measured as the result of breaking, ranging from moderate spilling to violent plunging.

Mixing due to breaking is studied by photographing the spatial evolution of dye, as it is mixed into the water column. The maximum dyed depth and dyed area were found to follow power laws in time of $t^{1/4}$ and $t^{1/2}$ respectively over a range of breaking wave intensities and scales. The dyed region reaches depths of 2 - 3 waveheights and 0.8 to 1.0 wavelengths in horizontal extent within 5 wave periods from breaking.

A detailed survey of the velocity field was made by ensemble averaging the measurements of repetitions of the breaking wave in this nonstationary flow. Mean surface currents were generated by breaking of 0.02 - 0.03 C, where C is the wave phase speed. These were very long lived, decaying to 0.005 C after 60 wave periods. A deeper return flow was also set up, apparently due to the loss of negative going momentum from the forced wave traveling with the wave group. Together these flows formed a large circulation cell in the breaking region. Turbulence rms velocities of 0.02 C were measured near the surface. Significant turbulence reached depths of 3 - 4 wave heights. Ninety Seven percent of the total kinetic energy lost from the waves is dissipated within four wave periods, while 60 - 90% of the horizontal momentum lost from the carrier waves is accounted for in the surface current and decays slowly. At later times the total kinetic energy decays in time as t^{-1}. The application of these results to ocean breaking is discussed.

Thesis Supervisor: Professor W. K. Melville
Title: Associate Professor of Civil Engineering

To Mary

Acknowledgments

The research presented in this thesis came about only through the assistance, contributions, and support of many people.

My thesis advisor, Professor W. K. Melville, provided the direction which was followed in this research. His excitment over experimental research was contagious. I also thank Professor J. N. Newman for his advice and support in my first year at MIT spent working on wave power devices. Professor O. S. Madsen is thanked for his insightful comments on the final draft and for his 1976 Toyota. Special thanks to Professors Milgram and Mei. June Harner's late nights at the word processor, typing this work is greatly appreciated.

The assistance of then fellow graduate student Eng-Soon Chan was immeasurable.

Special thanks to Karl Helfrich, Edmund Lo, Liz Macomb for helpful discussion, and Donghuo Zhou for his great help in data taking. Jack Crocker, Roy Milley and Ysabel "Midge" Megia were extremely helpful in building hardware. Photographic advice came from Charlie Miller, "Doc" Edgerton, and my father, Gene Rapp. Thanks to all in the Ocean Engineering Department and in the Parsons Laboratory, especially Patty Leblanc-Gedney and Pat Dixon.

The greatest thanks goes to my wife Mary for putting up with the long hours of graduate school and for her care of our daughter, Laurel. Mary, you were always there for that needed emotional support. Laurel, your always smiling face put all problems in their proper perspective. Thanks to my mother, father and brothers for their support.

This research was supported by the National Science Foundation.

TABLE OF CONTENTS

Page

LIST OF FIGURES

Page

Page

LIST OF TABLES

Chapter 1

INTRODUCTION

1.0 Purpose

The breaking of surface waves in deep water represents an important fluid dynamical process that has yet to be fully understood. Theoretical and numerical treatments of the problem fail at the point in the breaking process when the flow becomes turbulent. Models of the later stages of breaking can only be developed from extensive measurements of the unsteady breaking flow field throughout breaking. Field measurements alone can not fill this need due to the difficulty of identifying and following breaking waves in the field. Well controlled laboratory measurements can go far in adding to the understanding of many aspects of wave breaking.

In this thesis, an experimental program of laboratory research is presented that investigates the role of unsteady breaking on energy dissipation from the wave field, on turbulent mixing, and on the transfer of horizontal momentum flux from waves to currents.

1.1 Importance of Wave Breaking, Previous Research

Waves break over a wide range of scales and intensities, ranging from very gentle spilling waves only a few centimeters long with no air entrainment, to violent plunging over several hundred meters. The resultant turbulence and mean motions generated by breaking also cover a wide range of length and time scales. Breaking is very widespread and is seen to occur at all times except under the lightest winds. Wave breaking is considered to be the most important mechanism in the dissipation of wave

energy, which in turn, limits the heights of ocean waves (Phillips, 1977). It is believed to be a principal mechanism whereby momentum from the wind is transferred to surface currents (Longuet-Higgins, 1969). The turbulence generated by breaking is responsible for mixing in the surface layer, to depths speculated to be greater than the wave height (Peregrine, 1979). This includes mixing of gases through the dispersion of bubbles (Thorpe and Humphries, 1980), of heat and mixing of particulate matter and fluids such as oil spills (Naess, 1980; Milgram, 1978). The resultant small scale motions induced by breaking show up in the signals from remote sensing satellites (Banner, 1985). From an engineering perspective, breaking waves impose large loads on structures, and have been responsible for ship capsizings (Kjeldsen, 1981; Kjeldsen and Myrhaug, 1979; Vinje and Brevig, 1981). Also, the energy lost by the quasi-steady breaking bow waves generated by ships, represents drag, not accounted for in the Kelvin wave system downstream (Baba, 1969, 1976).

Other than ship waves, deep water wave breaking in the ocean is generally a random, intermittent and unsteady process. Steep and breaking waves may be caused directly by wind blowing over the water surface resulting in small scale breaking (Banner and Phillips, 1974) or by linear and nonlinear wave-wave interactions or wave-current interactions which can result in a high concentration of wave energy. Wave-wave interactions are responsible for the large scale breaking under storm conditions. Breaking has also been shown to result from the inherent modulational instability of uniform waves (Melville, 1981).

Hasselmann (1974) identified two aspects of the problem: 1) the fluid mechanical process of an individual white cap or breaking event and

2) the influence of breaking on the balance of energy in a wave spectrum. Theoretically, the two can be related through the breaking wave statistics. Research efforts have been made in all three of these areas, with no full understanding in any one. Longuet-Higgins (1969) has made an estimate of the energy loss from a breaking wave field; however, the crude assumption that inherently unsteady waves break when they reach the Stokes steady limit (Stokes, 1847) was made. Hasselmann (1974) has proposed a form for the dissipation source term in the spectral energy balance equation without entering into the local details of breaking. Some experimental confirmation was provided by Plant (1980), and Wu et al. (1979). A model of the breaking wave statistics has been proposed by Nath and Ramsey (1976) but again a steady breaking criteria was used.

The experimental research presented in this thesis addresses the first aspect of the problem; individual unsteady breaking waves and wave groups are investigated.

The evolution of an individual breaking wave can be broken into two stages: the early or prebreaking stage, characterized by steepening of the wave, where potential theory is still valid, and the later or post-breaking stage, characterized by a breakup of the organized fluid motion, turbulence, energy dissipation, and, in many cases, air entrainment (whitecaps). Numerous results have appeared giving a limiting wave height, but where a steady wave is assumed (Stokes, 1847; Michell, 1893; Schwartz, 1974; Cokelet, 1977; Longuet-Higgins, 1963, 1973a; Banner and Phillips, 1974; Longuet-Higgins and Fox, 1977, 1978; Byatt-Smith and Longuet-Higgins, 1976), to name a few. Melville and Rapp (1983) showed through velocity measurements that waves break over a wide range of

amplitudes well below these steady limits, making these steady breaking theories less useful in practice. To date, no complete analytical solution for the unsteady breaking case has been found, but work is progressing in this area (Longuet-Higgins, 1980, 1981a, 1981b; Greenhow, 1983). The numerical techniques of Longuet-Higgins and Cokelet (1976) and Vinje and Brevig (1981) give results that compare well with observation of surface displacement and fluid velocity at depths greater than one wave amplitude, but tend to underpredict velocities in the crest when compared to experiments (Kjeldsen, et al., 1980). Recent comparisons between results of the numerical scheme of Vinje and Brevig applied to a wavemaker (Lin et al., 1984) show good agreement with measurements of waves generated with the same initial forcing (Chan, 1985). These methods utilize potential theory and fail when the free surface overturns on itself; beyond this point other models must be developed to describe the flow.

Several models of the later stages of breaking have been proposed. These include a model of a turbulent wedge originating from a point of flow separation at the leading edge of the whitecap (Longuet-Higgins, 1973b). A second proposed model is one of a turbulent gravity current riding down the forward slope of the wave. Work is done on the wave by the whitecap at a rate equal to the downslope weight of the whitecap multiplied by the downslope phase speed; therefore energy is lost to the wave at this rate (Longuet-Higgins and Turner, 1974). The estimate of the energy dissipation in one wave period is $E_{diss} = 0.12E_o$ for their model where E_o is the energy in the base wave. To support this steady model, Longuet-Higgins (1974) reported on films of spilling breakers made

by Kjeldsen and Olsen (1971). Although these films show an intermitancy in the length of the whitecap, which the model does not predict; he claims that at least during part of the breaking evolution, this model may apply.

Peregrine and Svendsen (1978) proposed the model of a turbulent mixing layer for the leading edge of a white cap.

Laboratory investigations of these steady models have been carried out by Longuet-Higgins (1974) where a spilling bow wave was generated by a ship model, traveling at constant speed. Turbulent velocities of 4% of the wave phase speed were measured in this steady spilling wave. Measurements were made by Duncan (1981), and Battjes and Sakai (1981), where a steady breaking wave was produced by the relative motion of fluid over a submerged hydrofoil. Measurements of dissipation roughly agree with that predicted by the model of Longuet-Higgins and Turner (1974). Both show downstream turbulence to decay like that of a wake in contrast to Peregrine and Svendsen's (1978) model of a mixing layer.

Research on the later stages of the more realistic unsteady breaking has been rather limited. Van Dorn and Pazan (1975) measured dissipation in unsteady breaking waves produced by converging channel walls. They show that energy is conserved up to a point they define as the breaking point. The energy dissipation rate during the transition to breaking was found to depend upon the wave initial steepness and the wave growth rate. A small initial steepness and high growth rate produced a plunging wave with a fractional dissipation rate of 57%, while high initial steepness and low growth rate produced a light spilling wave with 19% fractional dissipation rate. The fractional dissipation rate equals the dissipation rate divided by the energy flux in the base wave.

In some preliminary experiments by Donelan (1978) an unsteady spilling wave was produced by the linear superposition of a group of short waves followed by steep long waves. Here the mixing of dye placed on the surface was photographed which showed a wedged shape patch of diffuse dye depth of the order of the wave height. The rate of mixing was not reported in these preliminary results. He also measured the turbulent velocities under wind generated waves which showed the $f^{-5/3}$ power law in the frequency spectrum above the wave frequencies. He concludes that turbulence is produced at low frequencies through the wind shear current instability, and at high frequency above the wave peak, due to white-capping. Further, he claims that the vertical flux of horizontal momentum is entirely due to the low frequency fluctuations, i.e., the shear current instability.

Experiments by Milgram et al., 1977, on the dispersion of oil slicks by breaking waves showed oil droplets going to depths of two wave heights in about two wave periods. Subsequently, turbulent diffusion was observed to carry the oil deeper. Their preliminary measurements of turbulence showed the largest rms velocity to be 10% of the underlying wave motion. These breaking waves were produced by converging walls.

From this review it is evident that additional measurements on unsteady breaking waves are warranted. We have not found any work where the fluxes of momentum or energy have been measured in breaking waves generated by wave-wave interactions, in what may be regarded as a natural mechanism of breaking generation. Also, there are no measurements to show the extent to which wave breaking is responsible for the transfer of horizontal momentum from waves to currents.

1.2 Introduction to the experiments

The intent of these experiments is to generate a single breaking wave group in the laboratory, modeling a process that normally occurs at random times and locations in the ocean. Of interest is the loss of momentum flux, and energy flux from the wave group under various levels of breaking intensity. This loss is then related to the growth of the turbulent mixed region under the breaking wave and to mean surface currents generated due to the breaking. Most importantly, these losses are determined as functions of the wave group amplitude, bandwidth and breaking location. Of the several mechanisms that cause or influence breaking, one of the most important is due to the random superposition of wave components in time and space. This is what we model by generating a unidirectional frequency modulated wave packet so that wave energy is focussed at a predetermined time and location. The breaking generates currents and turbulence in an isolated region while the wave packet continues to propagate downstream. The wave motions and the induced motions are effectively separated in space so that each can be measured separately (figure 1.2.1). Waves of other frequencies may be expected to be radiated both upstream and downstream from the breaking region and can also be measured. The effects of wind are not considered in these experiments, although it is known to influence wave breaking and also generate wind shear currents at the surface layer. The vertical velocities due to breaking waves are speculated to act on the windshear resulting in a vertical flux of horizontal momentum (Donelan, 1978). In these experiments, we will determine the extent to which breaking alone is responsible for generating surface currents and Reynolds stresses. Measurements of this type must be

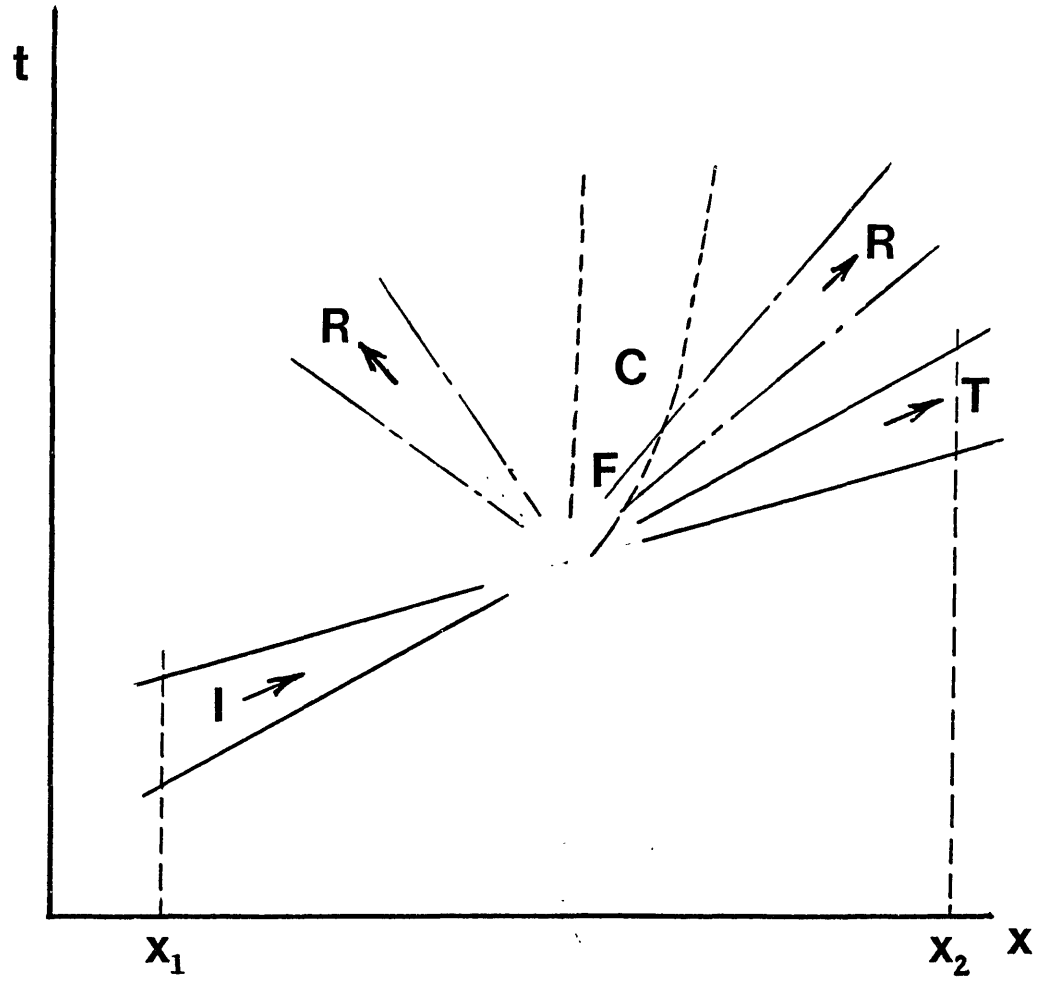

Figure 1.2.1 Schematic of separation of motion as a wave packet goes through breaking. Incident waves, I; Transmitted waves, T; Radiated waves, R; Turbulence, F; Currents, C.

performed on a single wave packet where measurements can be made on the packet before and after breaking to determine the losses from the waves. Also, since the turbulent flow field generated at breaking is nonstationary, turbulent statistics can only be determined by ensemble averages of many repeats of the experiment under identical initial and boundary conditions. These types of measurements are practically impossible to obtain in the field and so are done in a well controlled laboratory wave channel. Also, the long lived, slowly decaying fluid motions generated by the breaking can be measured without the influence of the motions generated by another breaking wave nearby or at the same location as in the field.

Modeling breaking in the laboratory also allows accurate control over the input wave parameters, and allows use of instrumentation not suited to the field. Since the wave is very repeatable, the measurement point can be varied to obtain the entire turbulent flow field under identical wave conditions. The inherent disadvantage of laboratory simulations in a finite length channel is the problem of scaling the results to full scale. This problem is addressed by performing measurement at three scales. Wave groups are generated with center frequencies over the range f_c = 0.88 Hz to 1.28 Hz, which correspond to wavelengths of 2m to 1m. A comparison over this range will give some confidence as to scaling the results to field conditions. The problem of reflections is minimized by installing an efficient dissipating beach. Since a finite length packet is generated in these transient experiments, measurement can be made on the transmitted packet before reflections travel back to the measurement point.

In the course of these measurements, we have found it advantageous to consider the momentum flux and energy flux loss from the wave packet as opposed to considering individual waves. The packet envelope may be considered as the important feature since the carrier waves propagate through the packet and disappear at the front. Any loss of momentum flux results in a decrease of the envelope amplitude. Also, the wave energy travels with the group. In some cases several wave breaking events were observed to occur in the packet at intervals of twice the carrier wave period. The sum of these losses is determined by measuring the entire packet downstream of breaking. Finally it is anticipated that breaking wave statistics can be related to wave group statistics of which a body of work is being developed (Longuet-Higgins, 1984).

Critical to the understanding of the losses from the waves and the momentum entering the mean flow and energy going into turbulence, is the ability to identify and separate these motions. With field measurements, the assumption is usually made that under stationary wave conditions, the turbulence is also stationary; the contributions from many overlapping breaking waves are added together. The wave motions and turbulent motions are separated using linear filtration methods. (Thorton 1979, Benilov 1978, Kitaigorodski et. al., 1983). The assumption that the wave velocity, considered to be a linear function of the surface displacement, is not correlated with the turbulence must be made in this filtration method. This may not be completely true, as will be shown. The turbulence under an isolated breaking wave cannot be assumed to be stationary, however. In these experiments, the ensemble averaging effectively separates these two contributions without assuming that the waves and

turbulence are uncorrelated. Also, the turbulence and mean motion can be separated in time from the wave packet since the wave packet propagates away from the breaking region (figure 1.2.1).

The experiments are divided into three sections, addressing 1) the losses of momentum flux and energy flux from the waves, 2) the rate and extent of mixing, 3) the velocity field in the breaking region. The losses from the waves, as a function of the wave packet parameters, are based on surface displacement measurements upstream and downstream of breaking. The momentum flux and energy flux due to the carrier waves is estimated to second order in wave slope using weakly nonlinear wave theory and shown to be proportional to the surface displacement variance, $\overline{\eta}^2$ (section 2.3). These results are presented in Chapter 3. Then the distribution of momentum and energy lost from the wave field is investigated. This is done by first establishing the spatial limits of the region of the water column affected by breaking. Breaking causes dye, initially floating on the surface, to be mixed down. The dye boundary is recorded photographically and is used as an estimate of the mixed region. These results were found to be of importance in their own right and are presented in Chapter 4. Measurements of horizontal and vertical velocities are made at grid points in the breaking region, defined by the dye boundary. Ten repeats at each point are ensemble averaged to determine the mean flow pattern and extent and levels of turbulent velocities. These are all determined as functions of space and time. Using the measured velocities, the total momentum and energy remaining in the breaking region is compared to that lost from the waves. The time rate of decay of the kinetic energy is also presented in Chapter 5. Experimental methods are discussed and estimates of the wave fluxes are derived, in Chapter 2.

Chapter 2

THE EXPERIMENTS

2.1. The Experimental Facility and Instrumentation

2.1.1 The Wave Channel

The experiments were performed at the Ralph M. Parsons Laboratory of the Massachusetts Institute of Technology in a glass walled channel 25 m long, 0.7 m wide, and filled to a depth of 0.6 mwith fresh water (figure 2.1.1). A wooden beach of slope 1:10 covered with 2 inch thick fibrous mats dissipated the waves at the far end of the tank with reflections of less than 0.16 % of the incident energy or 4% of the incident wave amplitude. The beach slope begins at 19.5 m from the wave paddle and extends to 25 m at the waterline. In these transient experiments, measurements were completed on the incident packet before the most energetic wave frequencies were reflected back to the measurement point, further reducing the influence of reflections.

The channel is equipped with a servo-controlled, hydraulically driven wave maker allowing pre-programmed wave packets to be generated. The wave group analog voltage signal (in the range ±10 V) is input to a MOOG model 82-300 dc servocontroller, which controls the hydraulic servovalve. The servoamplifier is operated in a closed loop with feedback from a paddle displacement transducer. The hydraulic unit has a variable flowrate and constant pressure pump capable of 15 GPM at 1800 psi. The pressure in the system was set at 1000 psi by adjusting a bypass valve in the flow system. The hydraulic cylinder drives a rigid vertical bulkhead in a horizontal motion so the velocity at the paddle is uniform with depth. The paddle is supported from above by a carriage riding on rails fitted

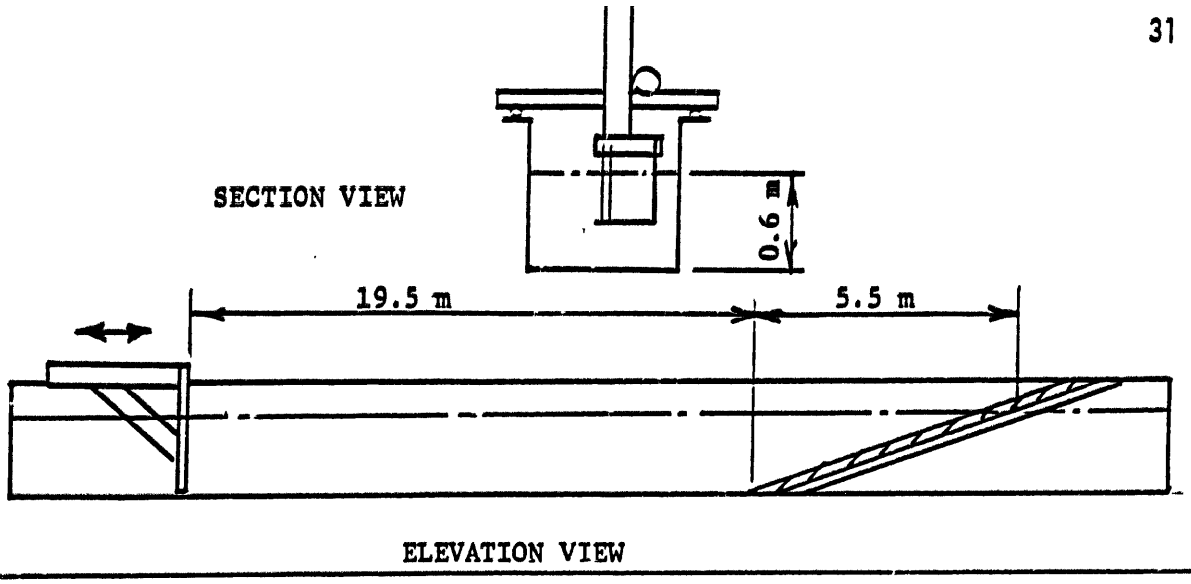

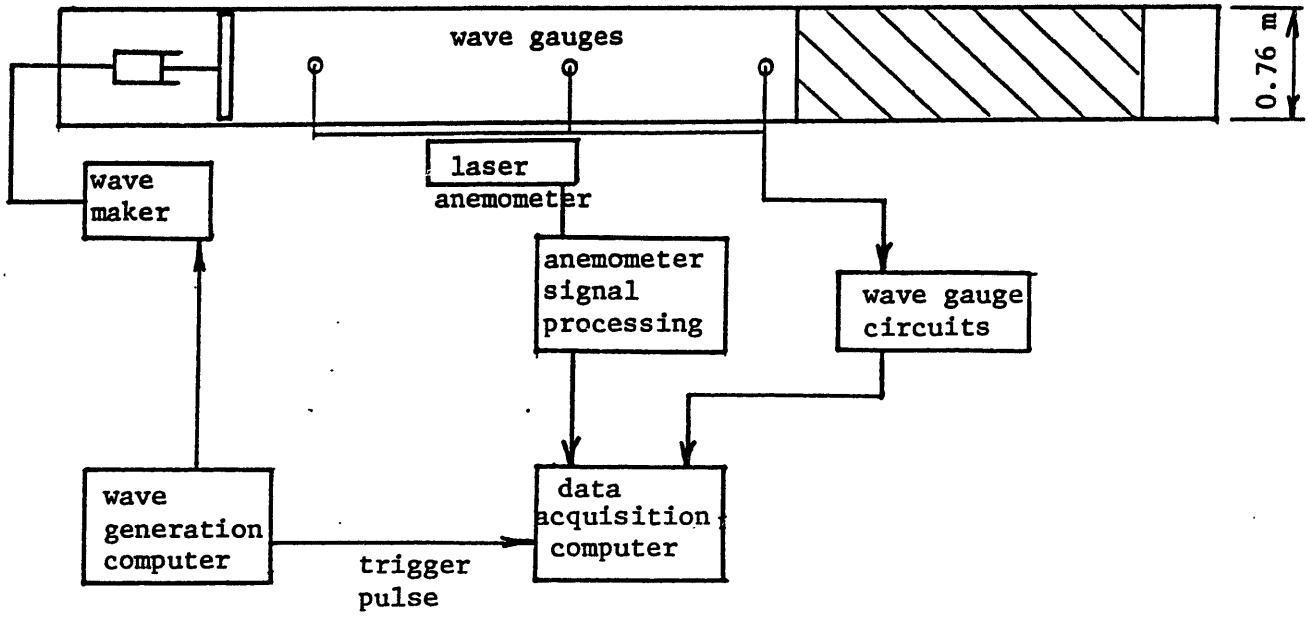

Figure 2.1.1 Wave Channel and Instrumentation

with linear ball bearings (manufactured by Thompson). The paddle is equipped with rubber wiper seals along the sides and bottom to reduce leakage and thus undesirable harmonic generation (Madsen, 1970). The wavemaker system transfer function was carefully measured as will be described in section 2.2. Figure 2.2.4 shows negligible change in the transfer function over the course of one year. Very small variations in the paddle transfer function were detected due to hydraulic oil temperature variation in wave input pressure measurements (Chan, 1985). These small variations could not be distinguished from the stochastic process of breaking itself as far as the parameters measured in these experiments are concerned (surface displacement and fluid velocity).

2.1.2 Wave Gauges

The fluid surface displacement was measured with a set of six surface piercing resistance wire wave gauges (constructed at MIT) and resistance measuring circuitry purchased from the Danish Hydraulic Institute (Model 80-74G). (After a thorough search for wave probes, this model was found to give excellent performance at a reasonable cost). The principle is to measure the total conductivity in the fluid between two wires, which is a function of depth of submergence. The MIT gauge is comprised of two 0.127 mm diameter Nichrome wires (20% chromium, 80% nickel) (supplied by C.O. Jelliff Corp., Southport, CT; also known as Chrommel A, by Hoskins Mfg., Detroit, MI) spaced 4 mm apart, and stretched on a 45 cm by 15 cm frame made of 0.25 inch diameter stainless steel tubing (figure 2.1.2). The thin profile of the support, 15 cm away from the wires, gave no detectable flow disturbance on the surface displacement measurements or on the

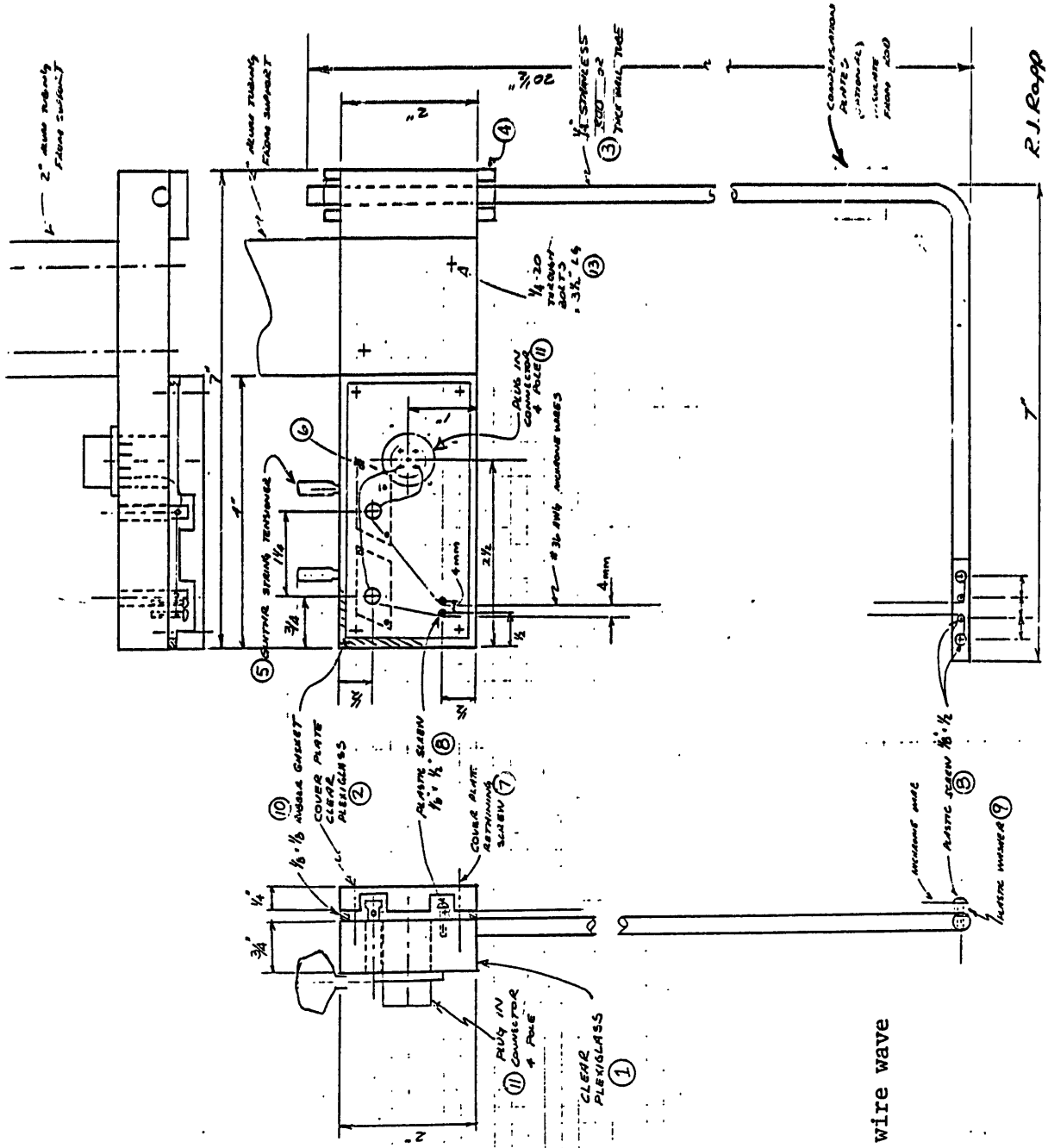

Figure 2.1.2 Resistance wire wave gauge

velocity measurements made near the probe. The Nichrome wires do not form an oxide film as stainless steel does which appreciably affects calibration.

The gauge frame was mounted from above to a vertical 2 in. square tube with a rack and pinion to allow accurate vertical positioning. This was mounted to a carriage riding on rails along the tank.

The circuitry provides an AC excitation voltage to the wires. The return signal is amplified, demodulated, and filtered to provide a DC voltage proportional to the wave amplitude. The excitation signal and return signals are isolated by transformers in the circuits to eliminate interference between closely spaced gauges. The circuits also have a provision for water temperature compensation, but this was not used since small submerged plates are required on the gauge which may have disturbed the flow. Also, the temperature effect was very small without them. The output gain and zero offset could be easily adjusted; no balancing was required.

To calibrate, the wires were wiped clean of any contaminants and the output voltage set to zero. The complete system, including A/D sampling board, was calibrated by positioning the gauge at 2 cm increments from +16 cm to -10cm and sampling the static water level for 5 sec. A second or third order polynomial was fit to the average voltage at each elevation. The fit standard error for linear, 2nd, 3rd, 4th order polynomials was typically 0.13, 0.09, 0.01, 0.01 cm respectively. This error is interpreted as the gauge resolution. The variation of the linear term was less than 1% over 8 hours. A "zero" record of the still water level was recorded for 40 seconds before each run and subtracted from the measured data

to remove any zero drift. It was found to be less than 0.5 cm over 8 hours. (See program WGCAL3 in Appendix 3 for gauge calibration software.)

2.1.3 Laser Doppler Anemometer

Simultaneous horizontal and vertical fluid velocity measurements were made with a laser doppler anemometer (LDA) operated in the dual beam back-scatter mode with counter data processors.

The laser is a Lexcel Model 95-2, 2 watt argon ion laser which outputs wavelengths in the range 514.5 - 457.9 mm; the strongest wavelengths being 488.0 nm and 514.5 nm. These lines were used for measuring the horizontal and vertical velocities respectively. The laser was equipped with an etalon filter to obtain the required beam coherence length. The laser and optics (TSI Incorp., essentially their model 9100-7 system) were mounted on a 2-inch thick rigid bench which in turn was mounted to a cantelevered carriage riding on rails above the channel. The carriage allowed vertical, transverse, and longitudinal motion so the measurement point could be positioned anywhere in the channel (see figure 2.1.3).

The laser output beam was directed through a collimator, polarizer and into a dispersion prism color separator. The green and blue beams were each split into two beams 50 mm apart. One beam of each color passed through individual Bragg cells to shift their frequencies. This causes a zero velocity offset in the output to resolve flow direction. All four beams were turned 90° with a 3-inch diameter mirror (Newport Corp., Pyrex with dielectric multilayer coating DM.1) and directed into a lens that focused all four beams to a common crossing point. The usual procedures

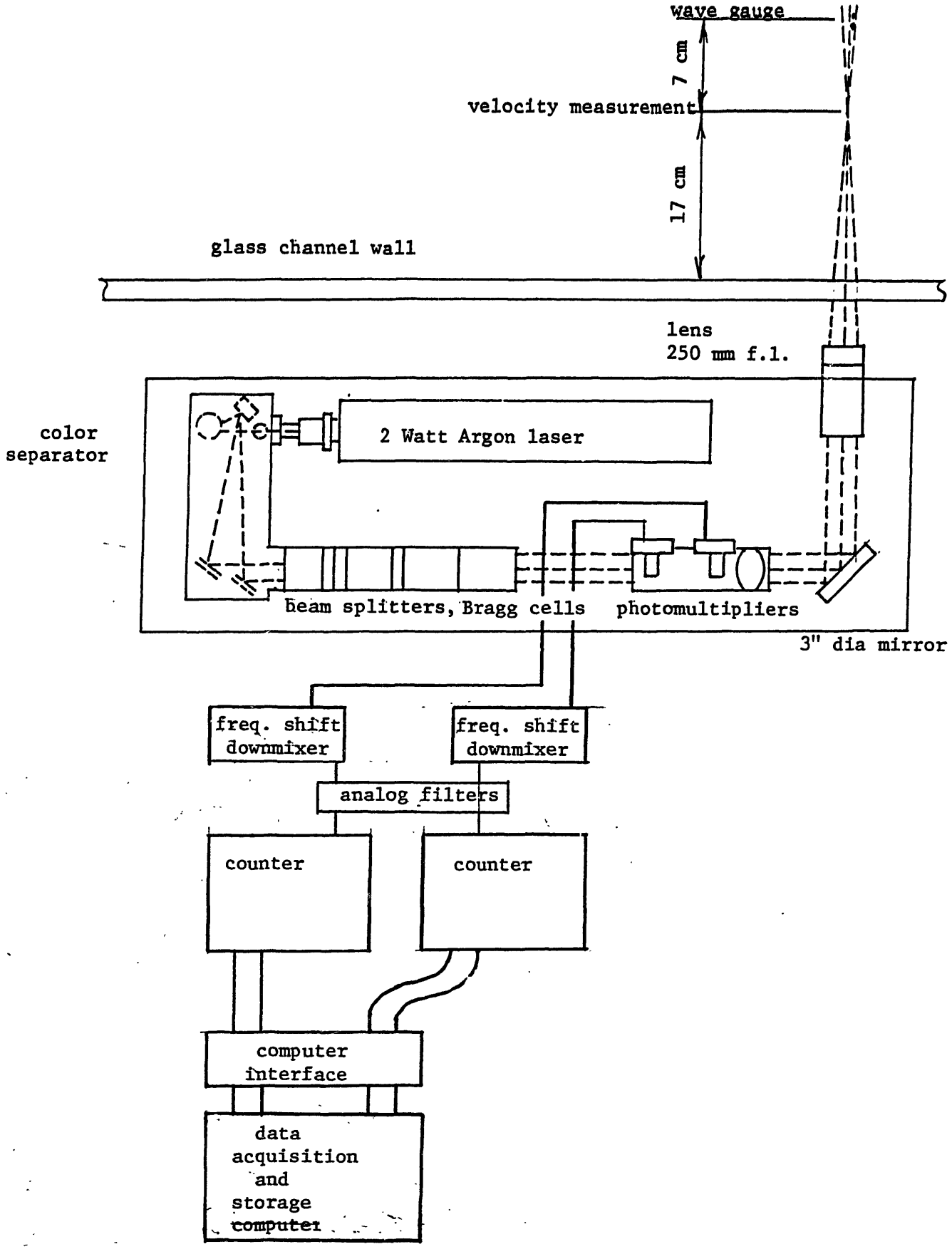

Figure 2.1.3 Laser Doppler Anemometer layout with sampling instrumentation

for alignment and insuring a coincident beam crossing were carefully followed (TSI, system 9100-7 Instruction Manual 1984). The focusing lens was placed close to the glass so that the required focal length could be minimized (250 mm) since the amplitude of the backscattered signal is proportional to the inverse of the focal length squared, $1/(f.l.)^2$. It is also important that the measurement point be close to the channel center, away from the glass boundary layer estimated to be $\sim \delta = (2\nu/\omega)^{1/2} \sim 0.06$ cm thick. (ν is viscosity, ω is the wave radian frequency.) The beam crossing was typically 17 cm away from the channel wall.

Backscattered light from particles in the measurement volume, travels back through the transmitting lens, the 3" diameter mirror and into the receiving optics. Here the colors are separated using mirrors and filters and focused onto separate photomultiplier tubes.

The simple model of the dual beam mode of operation is as follows. An interference, fringe pattern is set up at the beam crossing made up of bands of bright light, the spacing of which is a function of the laser wavelength λ, and the intersection half-angle κ given by $d_f = \lambda/(2 \sin \kappa)$. The frequency of the backscattered light is then proportional to the particle velocity component u, given by $f_d = 2(\sin \kappa)u/\lambda$. If frequency shifting is used, the fringes may be thought of as moving so

$$u = (f_m - f_{shift}) \frac{\lambda}{2 \sin\kappa} \tag{2.1}$$

where f_m is the measured frequency.

An alternative model is the doppler model. When a particle crosses a beam, a doppler shifted signal (due to the beam angle and moving particle) is picked up on the photomultiplier. This frequency is very high and on the order of the laser frequency which is too high to be accurately measured with good resolution. The second beam, angled in the other direction, also produces a high frequency doppler signal but shifted in the opposite direction. If the particle crosses both beams simultaneously (as can happen only at the crossing), the two signals are heterodyned and the resulting difference frequency is low enough to be accurately measured and is used to estimate the velocity according to equation 2.1.

When frequency shifting is used, the Bragg cell shifts one beam by 40 MHz. The signal at the photomultiplier is also shifted by this amount; however, this signal can be further downmixed with the frequency shifting equipment to any desired effective total shift in order to optimize the signal. The effective shift is selected via pushbuttons on the shifting equipment and is what will be referred to as the frequency shift.

This signal from the photomultiplier/downmixer circuit is input to a Krohn Hite Model 3202 low pass analog filter (used in the RC mode) which allows a continuous selection of cutoff frequencies. (The filters on the TSI counters are fixed at discrete values). The signal was also highpass filtered by the TSI counter (3 KHz lower limit). The counters (TSI Models 1990 and 1980) have 1 ns and 2 ns of resolution respectively. They were operated in the continuous cycle mode, counting N = 16 cycles for each measurement, then counting again as long as at least 16 cycles remain in the burst produced by the particle crossing. Here N is the number of interference fringes crossed by a particle.

In this mode it is possible to count one particle more than once, especially if frequency shifting is used. This is in contrast to the single burst mode where only one data point per burst, or particle crossing, is output. The continuous mode obviously tends to give higher data rates making the signal appear more continuous, although no new information is obtained since the particle velocity is rather constant as it crosses the measurement volume.

One source of noise in the LDA systems is due to phase jumps when a second particle enters the measurement volume, while one is being counted. This error is reduced by a validation circuit which compares the time of crossing the first 10 fringes, with the total 16. If this ratio differs from 5/8 by more than 1% (adjustable) then the measurement is ignored. With this setting, the resolution of the measured frequency is $0.01f_m$. From this and equation 2.1 it can be seen that a large frequency shift or offset has the undesirable effect of degrading the resolution of the measurement. The frequency offset, however, must be large enough to resolve negative velocities but not so large as to swamp out the unshifted doppler frequency.Before leaving the subject of frequency shifting there is one other point to consider, the fringe or directional bias. If the particle crosses the fringe pattern at a steep angle, it may not cross the minimum number of fringes, N, to output a measurement. This problem can be essentially averted if the frequency shift is made so that

$$f_s = 2f_d \qquad \text{for} \qquad \frac{N}{N_{FR}} = \frac{1}{2}$$

where f_d is the unshifted frequency of the highest expected frequency. N_{FR} is the number of fringes across the probe volume. In our geometry $N/N_{FR} = 16/52 = 0.31$ so this criterion was relaxed slightly to obtain better resolution and less noise.

The selection of N, the number of cycles counted per measurement, was made on the basis of reducing output noise (increasing accuracy of the measurement) but yet maintaining a high data rate. Intuitively, one may think of doubling N as equivalent to averaging two output measurements, as a low pass filter. However because of the validation circuitry just described, doubling N input reduces the output noise to lower levels than just filtering the output signal.

Table 2.1.1 lists the important parameters and their optimum values for the measurements in these experiments. Considerable effort was made to optimize these parameters to obtain a clean signal with an adequate dynamic range and negligible directional biases. These tests included varying the beam spacing, adding beam expansion, using different focal length lenses, and attempting to dynamically vary the frequency shift to follow the measured signal. Decreasing the beam spacing to 22 mm neither increased the data rate nor reduced the noise levels, nor was any advantage found using the 2.27 beams expansion. Reducing the transmitting lens focal length from 600 mm to 250 mm greatly improved the signal quality and data rates; this change was ultimately responsible for the high quality data. Reducing the frequency shifting is also important in obtaining accurate low noise data. However, doing this dynamically with the present equipment was not possible due to the large (1/2 sec.) time

Table 2.1.1

Laser Doppler Anemometer Configuration

	Horizontal Velocity	Vertical Velocity
Laser Wavelength	488.0nm (blue)	514.5 nm (green)
De^{-2} beam diameter	2.3 mm	2.3 mm
Power	(800-1000 mw all lines)	
Lens focal length (f.l.)	250.4	250.4
Beam Separation	50 mm	50 mm
Beam interaction half angle (κ)	5.538°	5.538°
Beam expansion B.E.	1	1
Fringe spacing	2.67 μm	2.67 μm
Probe volume (width)	0.137 mm	0.137 mm
(length)	0.408 mm	0.408 mm
No. of fringes N_{FR}	52	52
Frequency shift (direction) Zero velocity offset	200 kHz(-x) (50.512 cm/s)	200 kHz (down)(-z) (53.33 cm/s)
Signal processer-TSI Counters	Model 1980B 2 ns resolution	1990 1 ns resolution
Cycles N	16	16
Exponent	auto	auto
Transfer function	3.96 kHz = 1 cm/s	3.75 kHz=1 cm/s
Doppler signal filters	3 kHz - 1 MHz	3 kHz - 1 MHz
Velocity range	(-49.8 → 202 cm/s)	(-52.5 → 213cm/s)
Digital Sampling board (16 bit)	DT-2768I	DT-2768I
Channel	0	1
Seeding	Silicon carbide 1.5 μm mean diameter	
Typical LDV data rates	1000-3000	1000-3000

lag to lock onto a new frequency shift. A typical raw velocity time history is shown in figure 5.2.1 measured with the LDA configured as listed in table 2.1.1. The rms noise levels for this signal are 0.34 cm/s and 0.2 cm/s for u,w velocities, respectively. See section 5.2 for details. This noise is broadband so cannot be removed by frequency filtering.

As a practical point, the photo multiplier current and counter input gain should be increased just to the point where large spikes begin appearing in the analog output of the velocity (monitor output) and then reduced slightly to eliminate them.

The particle seeding used was the TSI Model 10081 silicon carbide of 1.5 μm mean diameter and density 3.2 g/cm^3. This monodispersive seeding gave the best signals when mixed into clean tap water. Essentially a 1/4 teaspoon premixed in a bucket of water, was added up and down stream of the measurement point and mixed with a paddle by hand. Reseeding was necessary every four hours. Silver coated glass spheres were also used (Potter Industries, N.Y.) with good results but they tended to settle out within one hour and were not as monodispersive in size as the silicon carbide.

The LDV signal was sampled via the digital output, 37 pin D connector. This port outputs 16 bits of data (12 mantissa, 4 exponent) representing the clock counts of the time for the particle to cross N fringes. The bit pattern changes every time a new data point is validated unless the data hold pin is shorted. A special flip-flop circuit was built to interface with the Data Translation DT digital I/O board and SMS 11/23 computer. The interface is shown in figure 2.1.4. Since the LDV

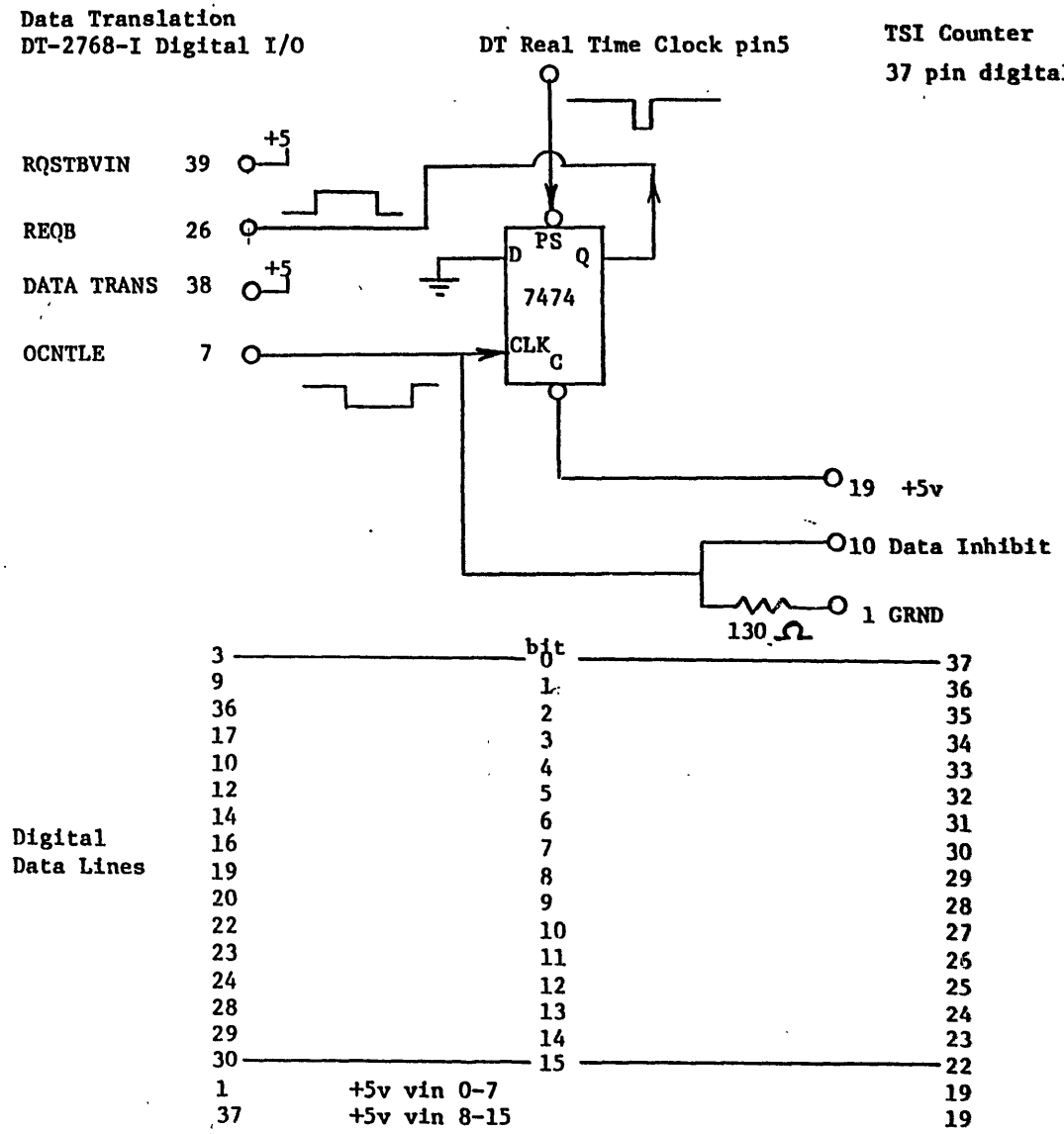

OPERATION

1. **A pulse from real time clock sets Q to logical 1(+5v)**
2. **DT board sees REQB go high and send logical 1 to register. OCNTLE then goes low while data linesare read. Data Inhibit goes low to hold Data on TSI lines.**
3. **The trailing edge of OCNTLE triggers 7474 flip-flop resetting Q to 0.**

Timing Diagram

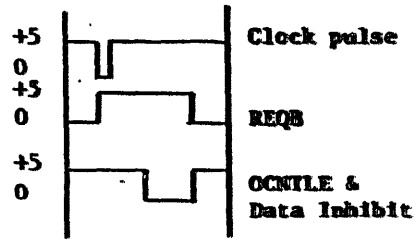

Figure 2.1.4 Laser Doppler Anemometer- Computer Interface

data rates were relatively high (1000-3000 Hz) compared to the sampling frequencies (50-200 Hz), the signal on the LDV was assumed to be continuous and sampled at equal increments in time rather than reading every data point. In this mode it is not necessary to record the time of the data point since they are equally spaced in time.

2.1.4 Data Acquisition

The data acquisition system was based on an SMS (Scientific Micro systems) LSI 11/23 computer with a 30 Megabyte Winchester hard disk and an 8"floppy drive. A magnetic tape drive was also installed for bulk data storage.Installed in the Q-bus was a DT 2769 (Data Translation) Real Time clock, DT 2781 analog/digital I/O board, used to sample the wave gauges, two optically isolated digital I/O boards DT-2768-I, sampling the two digital LDA channels. A high speed A/D convertor (DT 3382) was also installed to sample directly to hard disk and used to sample the line scan photodiode array camera when used. The wave signal was input to the wave-maker from a separate Charles River Data Systems (CRDS) computer via a DT 2781 D/A channel. A BATCH run master program ADDAT3.BAT (Appendix 3) was used to control the sampling, convert the raw data to physical units, using gauge calibration files and LDA parameters, and compute means, variances or do filtering and plotting. This was all performed while the motions in the channel decayed out for the next run. The data sampling was initiated by a trigger step signal from the CRDS computer that marked the start of the wavepacket signal. The step signal triggered the real time clock in the SMS computer. A minimum of 6 to 10 minutes lapsed between runs of the experiment. Data translation subroutines were

incorporated into FORTRAN program to sample the two digital boards and scan the channels on the analog input board. A double buffering configuration and a completion routine allowed continuous sampling and writing to disk for an almost unlimited time (limited by disk space). Also, when sampling the two digital channels and four analog channels a sampling rate limitation of about 500 Hz was observed. When ensemble averaging many repeats of the experiment, a slow timing loop was set up with the program RJAOUT to send trigger pulses and the wave signal at 8 minute intervals. Data was automatically sampled and analyzed between each repeat and no operators intervention was required. The signal means and variance were printed for each run to insure the integrity of data.

2.1.5 Photography

The single point measurements of the surface displacement and velocity produced time series of these quantities; however, in this unsteady flow, the conversions to spatial dependence is not easy (if at all possible). Still photographs and cine films were made to record the spatial profile of the free surface with time and also of dye being mixed from the surface.

The still photographs were taken with a 2-1/4 inch × 2-1/4 inch format Hasselblad 500 EL/M camera with motor drive and with a 35 mm Olympus OM 10 camera . The procedures were not novel but did require varying the lighting and exposure in tests for optimum results. Two lighting techniques were employed.

A series of 35 mm color slides was taken with the Olympus camera and 35 mm focal length lens, by backlighting a long translucent white cloth

stretched behind the channel. This acted as an inexpensive diffusion screen. Two 1000-watt quartz lights (Lowe Tota) were placed near the floor and aimed up from behind the channel (figure 2.1.5a.) A 600 watt quartz light and various 100-watt floods were placed directly under the tank glass bottom to light up the miniscus along the front glass at the free surface. A front light was also used to light up the scale markings. A light meter was used to give an initial guess on the exposure.

A shutter speed of 1/500 th sec and f/2.8 were used for this continuous lighting setup with Ektachrome tungsten film of ASA 160. A polarizing filter was also used to reduce glare from the glass and particles in the water. Dye mixing slides were exposed at f/2.8 and 1/250 sec.

The 2-1/4" × 2-1/4" black and white photographs of figures 3.1.5 and 3.1.6 were taken with the Hasselblad camera and zoom lens set at a focal length of 140 mm or 280 mm, with a similar lighting arrangement, except the continuous lights were replaced with three flash units (Vivitar model 285, Vivitar model 100 and equivalent) to better "freeze" the breaking. See figure 2.1.5b. A flash was placed above the tank to light up the air entrainment at the free surface. The higher power Vivitar model 285 flash was used at 1/4 power to reduce its flash duration to ~ 1/1000 second as the others. An f stop of f/11 with Plus-X film at ASA 120 was used. A polarizing filter was also used. Blue vegetable dye was mixed into the water to add contrast.

Another lighting technique (figure 2.1.5c) produced the dramatic series of photographs in figure 3.1.7. Here a black vinyl coated cloth was placed behind the tank. Two flash units were placed under the tank and one overhead. Only the surface miniscus and the bubbles reflected light

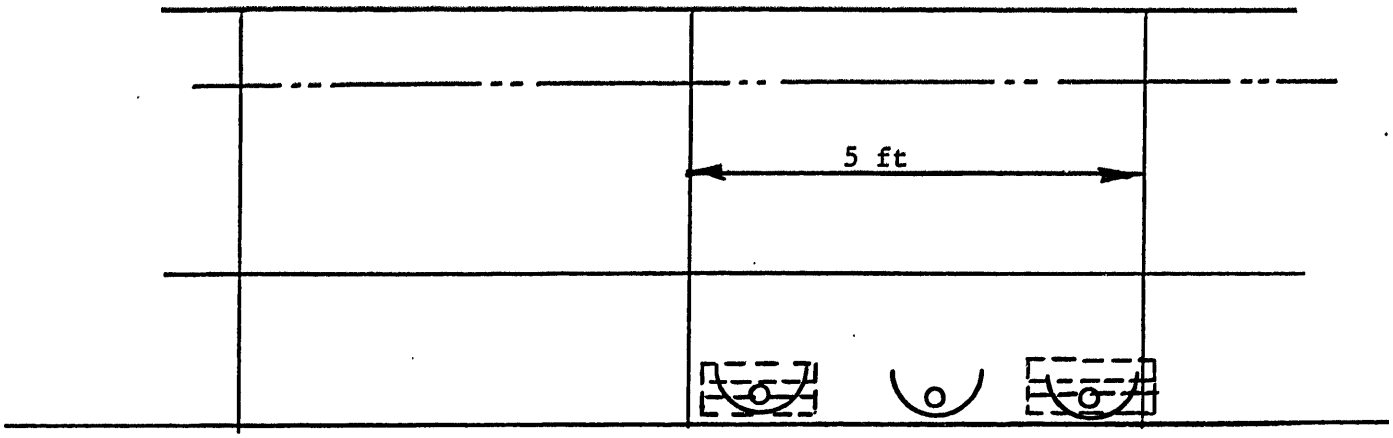

ELEVATION VIEW

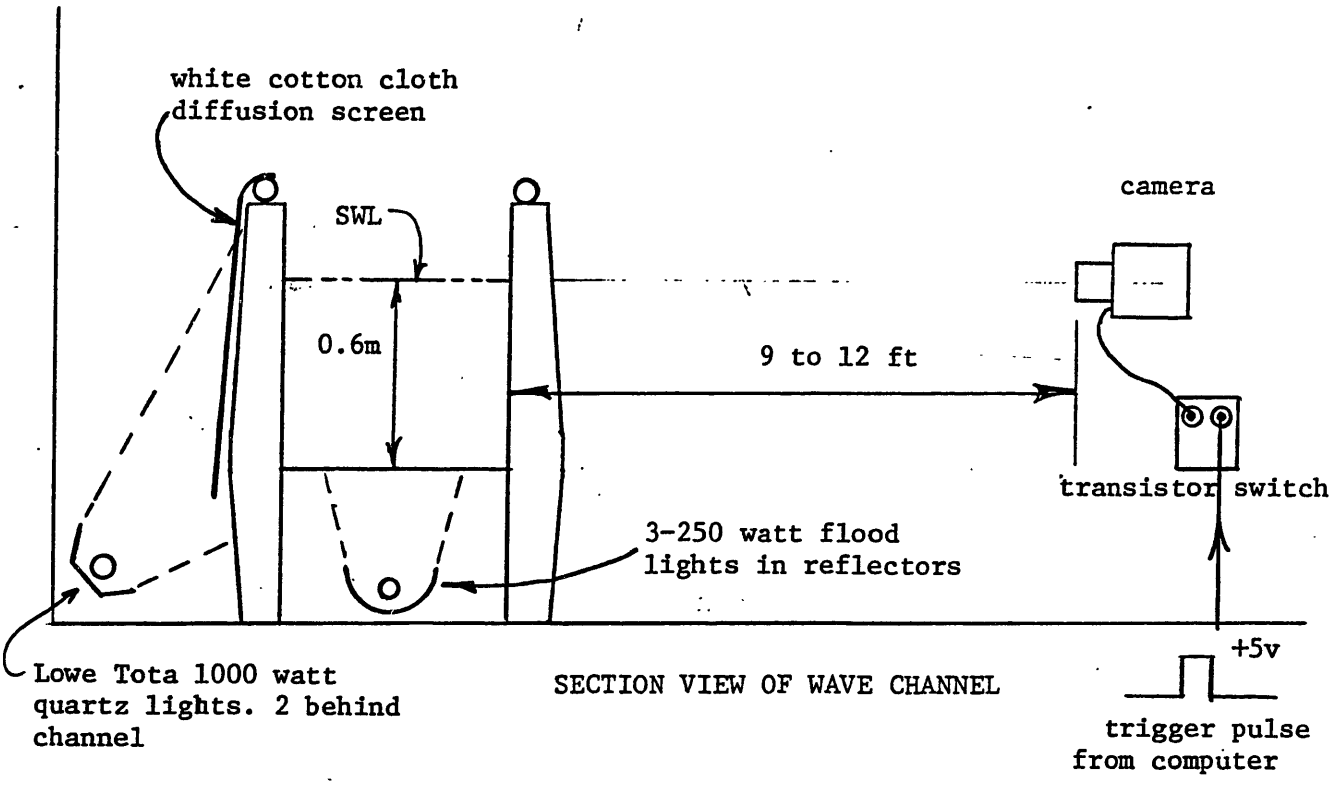

Figure 2.1.5a Photographic lighting arrangement with continuous lighting and white background

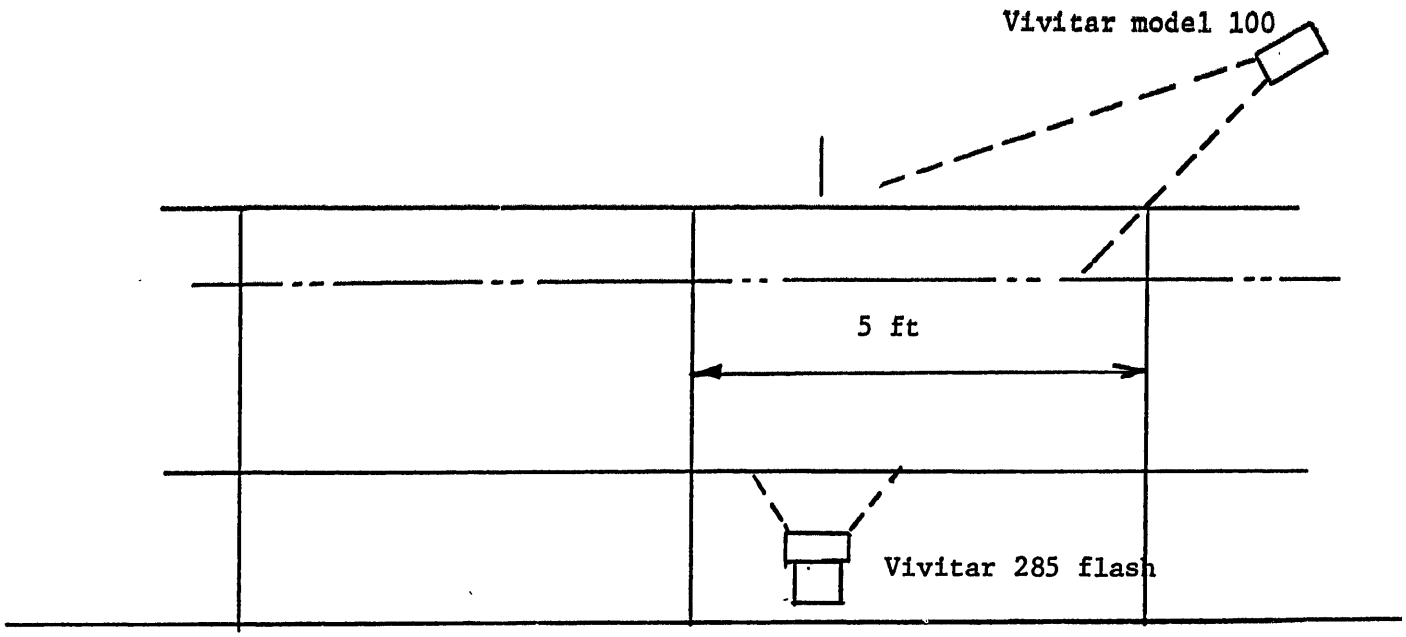

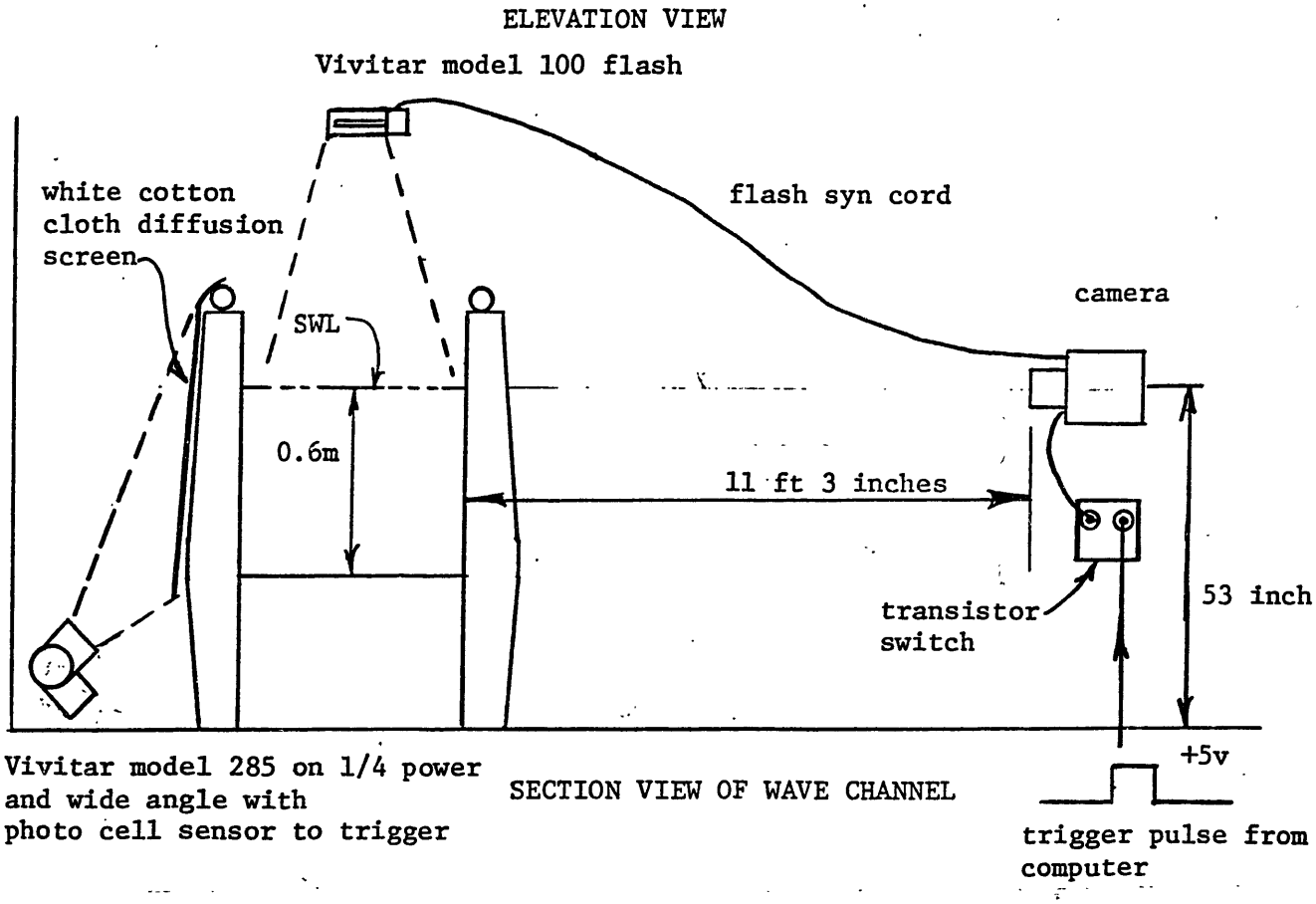

Figure 2.1.5b Photographic lighting arrangement with electronic flash lighting and white background

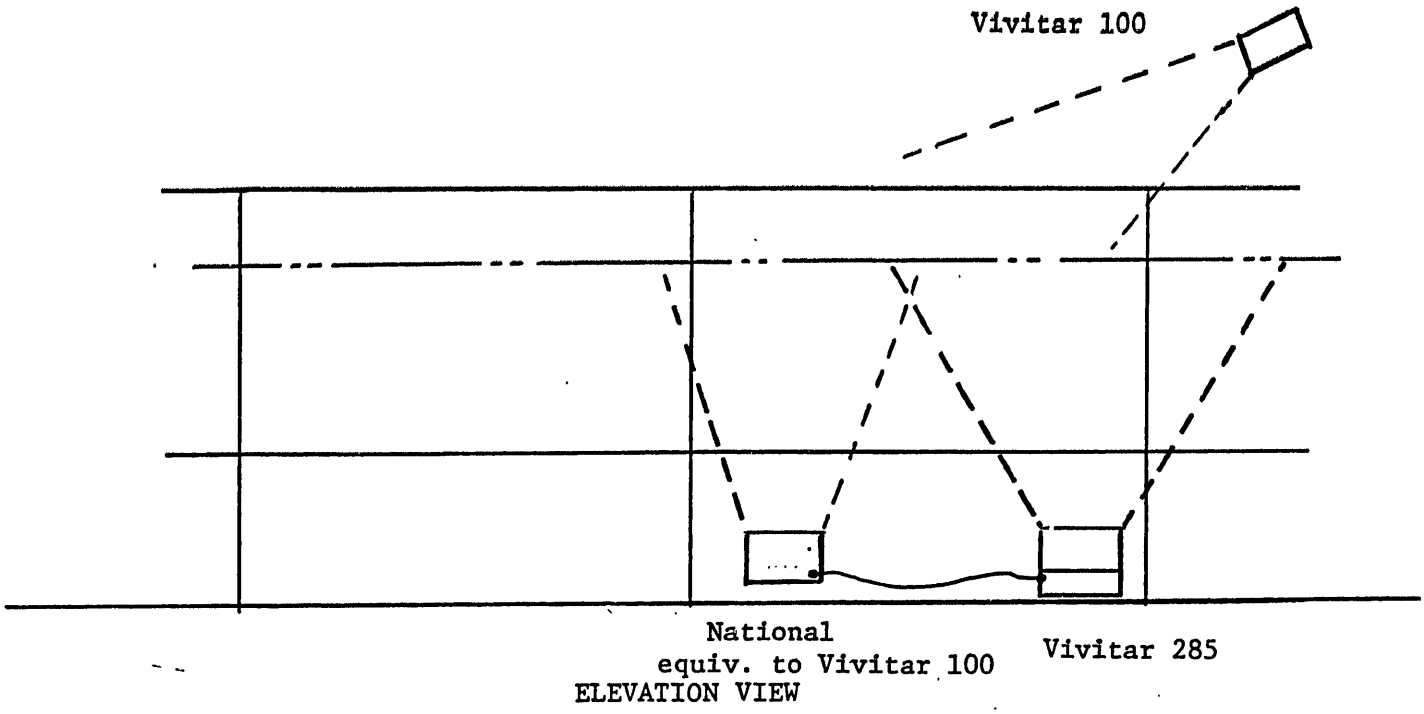

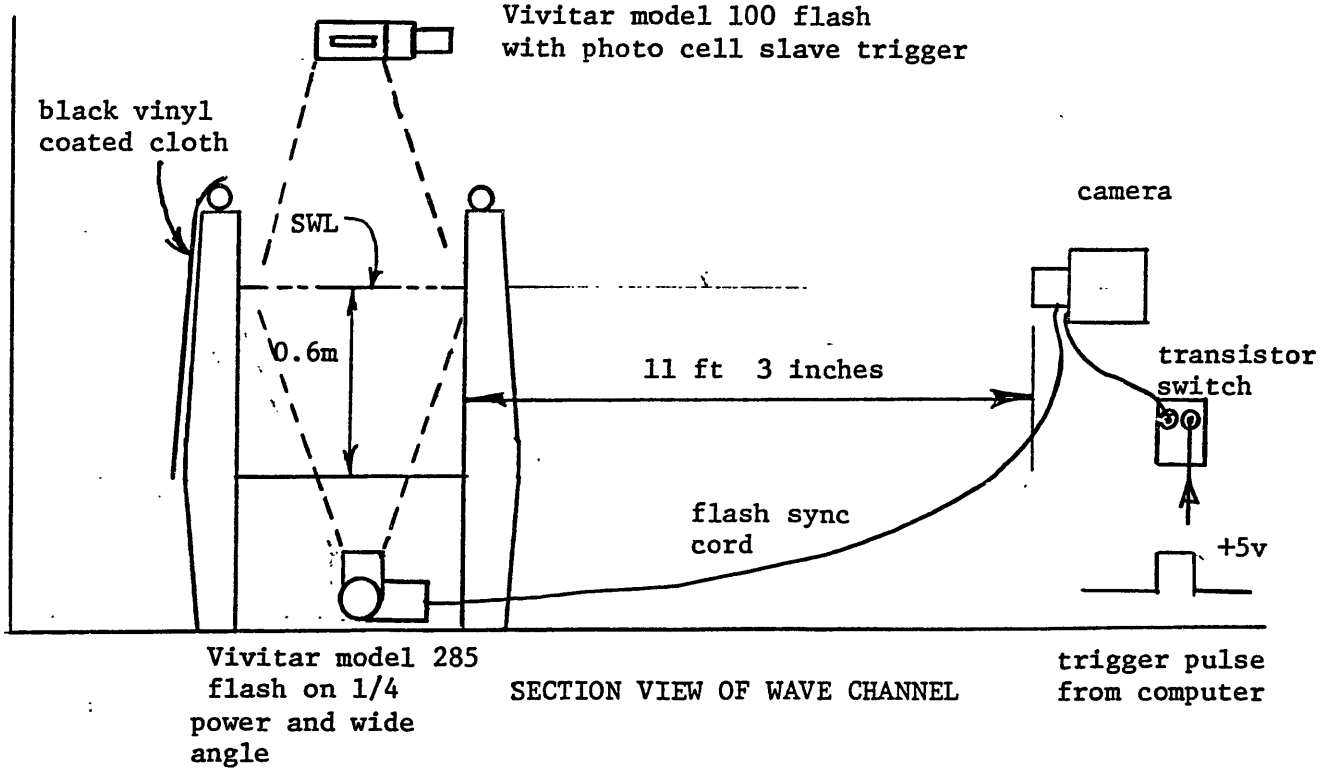

Figure 2.1.5c Photographic lighting arrangement with electronic flash and black background

to the camera. The photographs were taken at night, in complete darkness. The flash speed again was 1/1000 sec and f stop f/4 (camera set at 1/60 sec) with Ektachrome daylight film of ASA 200. To reduce haze effects, the water was filtered and a polarizing filter used on the camera.

In all the still photographs the camera motor drive was triggered with a step from the CRDS computer, and transistor switch circuit, (figure 2.1.6) that was delayed by progressively longer times from the start of the wave signal. Each photograph is a separate run of the wave packet.

Cine films were made under the continuous lighting arrangement and white background as described. A Bolex REX H16 movie camera was run at 64, 48 and 24 frames per second. The variable shutter was set at 1 which gave a shutter speed of 1/400, 1/300, 1/150 for the three frame speeds used. The effective shutter speed for exposure computations was 1/500, 1/375, 1/188.

A series of films was made of the wave packet corresponding to incipient breaking, spilling and plunging for various bandwidth parameters; no dye was used. Another series of films was made of dye mixing for three scales of wave packets corresponding to incipient breaking, spilling and plunging.The exposure data for these runs is listed in table 2.1.2 along with a summary of the still photographs. (Details of the dye mixing experiment will be given in Chapter 4).

2.1.6 Photo Diode Array Camera

An EG & G Reticon Model LC 110 Photodiode array camera was used to image dye concentration along a vertical laser beam. The powdered

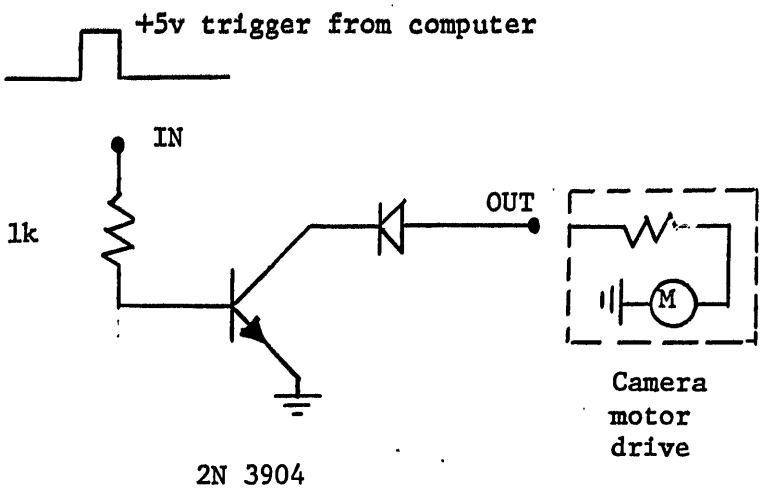

Figure 2.1.6 Transistor switch circuit for camera triggering. Diode reduces inductive loading effects of motor drive.

Table 2.1.2

Photography Summary

CINE — Bolex REX H16 with 25 mm or 10 mm Lens

	No Dye	Dye Mixing	
frame speed	64 f/s	48	24
actual shutter speed	1/400 sec	1/300	1/150
effective shutter speed for exposure	1/500 sec	1/375	1/188
f stop	f/2.8	f/2.8 with 7250 film	f/4 ASA 400
film Kodak Ektachrome	7250 film ASA 400	f/2.0 with 7240 film	4/2.8 ASA 125

Still Photographs

35 mm Olympus, OM 10 35 mm lens w/polarizer
Kodak Ektachrome Tungsten 160 ASA film

f/2.8	1/500 sec	continuous lighting, figure 2.1.5 a, w/o dye white background
	1/250 sec	with dye

2-1/4" × 2-1/4" Hasselblad 500 EL/M, 140 or 280 mm lens w/polarizer
Kodak Ektachrome Daylight ASA 200

f/11	1/500	3-flash units 1/1000 sec white background arrangement lighting figure 2.1.5 b
f/4	1/60	3-flash units 1/1000 sec. black background lighting arrangement figure 2.1.5 c

fluorescein dye (Aldrich #16, 630-8, Milwaukee, Wisconsin) laid on the water surface, was mixed down in the breaking wave. The fluorescein is excited by a laser wavelength ~ 488 mm and emits at a wavelength of ~ 512 nm. The laser beam was directed from below the wave channel aimed vertically upwards. The camera consists of a line array of 1024 photodiodes on 25 μm centers placed at the focal plane behind a camera lens. The camera lens is interchangeable for various magnifications. Housed in the camera is a real time digital clock and array scanning and sampling circuitry. The camera was set to scan the array continuously a rate of (f_{scan} = 103.3 KHz). The analog output of the camera is a voltage between 0 and -1 representing the light intensity on each photo diode. The signal is steplike with time between steps equal to 1/scan rate. The camera was aligned and focused so that the vertical laser beam was aligned with the array. The intensity of light falling on the photo diode is controlled by the lens aperture. Also an effective "shutter speed" was determined by the scan rate. By adjusting these two things, the signal can be kept from saturating at 1 volt. This particular array is <u>not</u> a sample and hold type so to obtain a near "snapshot" of the dye pattern the array was scanned as rapidly as possible (limited by exposure criteria). This analog signal was sampled by the DT 3382 high speed direct memory access board in the SMS computer. The sampling rate of the line was then

$$f_{line} = \frac{f_{scan}}{1024}$$

This rate produced a very large amount of data in a very short time.

In order to hold f_{scan} constant but vary f_{line} a burst gating circuit was designed to interface with the SMS computer. This circuit generated a pulse of length $t = 1024/f_{scan}$ at any specified interval. (See figure 2.1.7). This signal was put into an AND Gate to turn sampling on and off. The length imaged by the array was calibrated by sampling the image of a scale with thick black markings placed at the laser beam location. The scale was front lit with a bright light.

The data sampling program is RJDSK shown in Appendix 3. The sampling frequency f_{line} was typically 50 or 100 Hz, $f_{scan} = 103.3$ kHz. The laser beam power was 1.5 Watts. A Pentax 50 mm lens with f/1.8 aperature setting was mounted to the array camera body.

2.2 Generation of the Breaking Wave Group

Several techniques for generating breaking waves in a laboratory channel have been reported by Kjeldsen et al.(1980) and Longuet-Higgins (1974). Steady spilling breakers have been produced by the relative motion of a submerged hydrofoil and the surrounding fluid (Duncan, 1981; Battjes and Sakai, 1981) and by the steady motion of a surface piercing hull (Longuet-Higgins, 1974). A steady source of energy proportional to the drag times the velocity of the body is required to maintain the breaking. Unsteady breaking waves can be generated by focusing the wave energy in space; this causes a local increase in energy density. For two-dimensional waves (i.e., unidirectional), the energy may be focused by a laterally converging channel wall (Van Dorn and Pazan, 1975; Milgram, 1977) or by a longitudinal focusing caused by the frequency dispersion. (Longuet-Higgins, 1974; Kjeldsen, et al., 1980, Greenhow, et al., 1982).

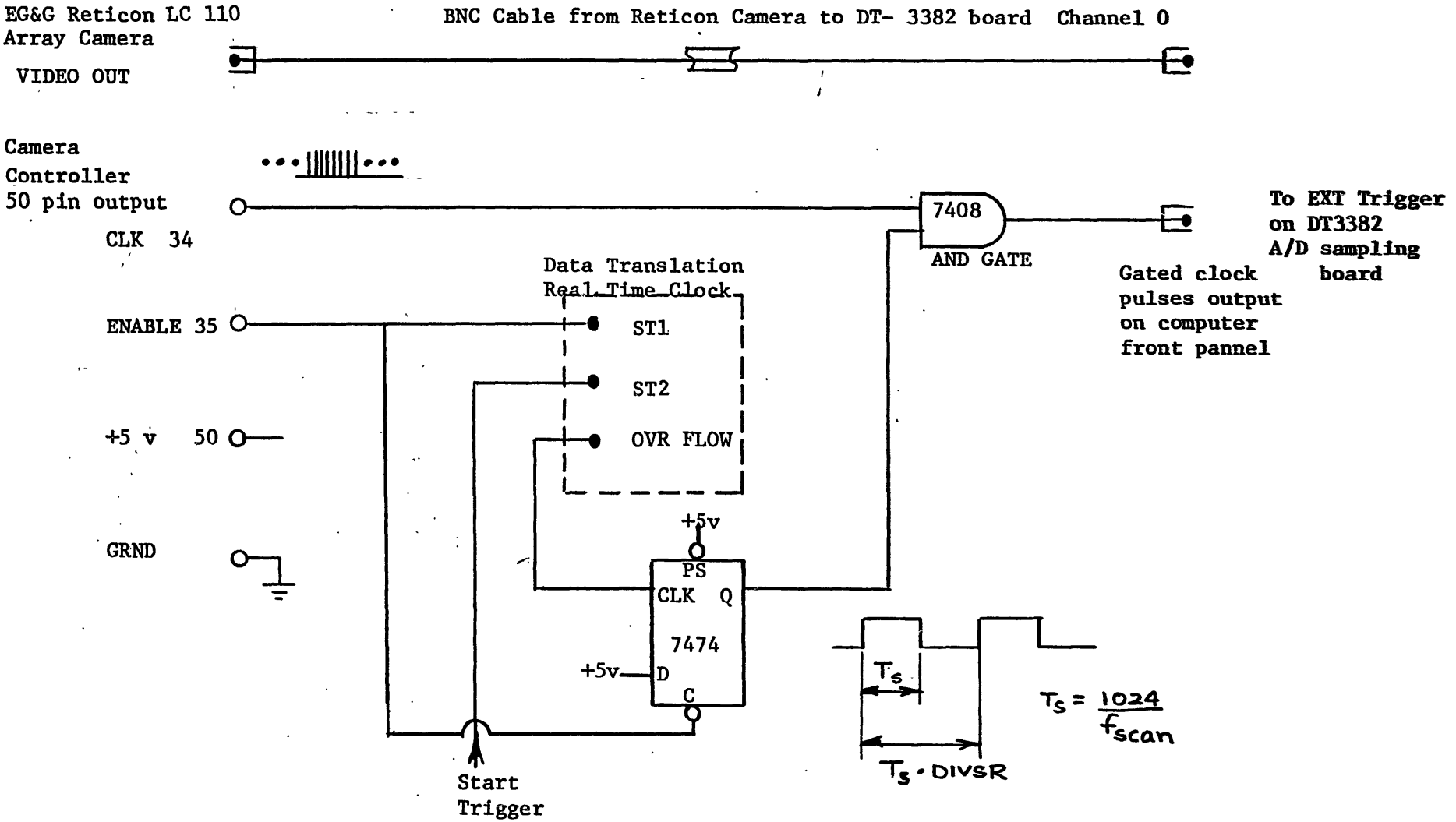

Figure 2.1.7 Reticon photodiode array camera- computer interface

Waves have also been shown to break as they pass through the Fresnel envelope at an advancing wave front produced when the wavemaker is started impulsively (Longuet-Higgins, 1974). Melville (1981) experimentally showed that an initially uniform wave train undergoes the Benjamin-Feir instability which can lead to breaking as the carrier waves pass through the modulated envelope. This breaking is quasi-periodic; however, the breaking location tends to oscillate along the channel length making repeatable measurements difficult.

The technique used in these experiments is, in principle, that described by Longuet-Higgins (1974) where wave energy is focused longitudinally by linearly decreasing the wavemaker frequency and thus increasing the group velocity of the generated waves leading to a focusing of energy. In deepwater this is achieved by varying the paddle radian frequency, ω, by

$$\frac{d\omega}{dt} = \frac{-g}{2x_b}$$

where x_b is the energy focal point, according to linear theory, as measured from the paddle. This signal is well known in the communications field as a "chirp" pulse (Clay and Medwin, p. 131, 1977). To reduce startup transients, the signal must also be smoothly brought to zero at the ends of the pulse. This technique has been shown to produce plunging breakers, however x_b can only be specified to within a wavelength of the wave since no provision is available to specify the individual wave phases. The starting phase of the signal must be empirically determined to fine tune the breaking location (Milgram, 1985).

We use a refinement of this basic focusing principle, that given by Greenhow, et al., (1982), where a quasi-periodic signal is generated by a summation of 32 equal amplitude wave frequency components spaced uniformly in frequency over a specified band. Making use of frequency dispersion given by linear theory, the phase of each component is specified at the paddle to cause all wave crests to arrive simultaneously at a point in space and time resulting in a constructive interference. Since the purpose of these experiments is not only to produce a breaking wave, but also to be able to parameterize the input wave group, this method was considered superior.

The formulation is a most general specification of the wave field in terms of parameters that are easily applied to the field, namely the nondimensional amplitude, the bandwidth, and a phase specification. It is believed that this method models a naturally occurring mechanism of unsteady breaking wave generation in the field. A range of breaker types or intensities from gentle spilling to vigorous plunging can be generated. In this formulation, the resultant signal applied to the wavemaker is already modulated smoothly to zero in amplitude, making any further smoothing windows unnecessary. The method is simple to repeat and follows from basic principles of linear wave theory. The resultant breaking (or nonbreaking packet) was extremely repeatable in time and space (to 1/100 sec over 17 sec and to within ±2 cm in the horizontal direction in the 7 meters of propagation from the paddle). The resultant signal is similar to that of the method given by Longuet-Higgins (1974) in that short waves are generated first, followed by increasingly longer waves. The difference between the methods is in the formulation of the

packet, which allows a specification of the theoretical x_b. Also a separate amplitude smoothing is not required. The details of the method follow.

The free surface displacement, $\eta(x,t)$, can be specified by

$$\eta(x,t) = \sum_{n=1}^{N} a_n \cos(k_n x - 2\pi f_n t - \phi_n) \tag{2.1}$$

where a_n is the amplitude of the nth frequency component, k_n is the wavenumber, $2\pi f_n = \omega_n$ the radian frequency, and ϕ_n the phase. N is the number of components. k_n and f_n are related by the dispersion relation

$$\frac{(2\pi f_n)^2}{g} = k_n \tanh k_n d \tag{2.2}$$

where d is the water depth. The phase of each component is computed by setting

$$\cos(k_n x - 2\pi f_n t - \phi_n) = 1$$

at $x = x_b$ and $t = t_b$, the location and time of focusing.

Then

$$\phi_n = k_n x_b - 2\pi f_n t_b + 2\pi m \qquad m = 0, \pm 1, \pm 2 \ldots$$

The surface displacement specification becomes

$$\eta(x,t) = \sum_{n=1}^{N} a_n \cos[k_n(x - x_b) - 2\pi f_n(t - t_b)] \tag{2.3}$$

We define the mean paddle position to be $x = 0$, and the desired surface displacement at the paddle is

$$\eta(0,t') = \sum_{n=1}^{N} a_n \cos(-k_n x_b - 2\pi f_n t') \qquad (2.4)$$

where $t' = t - t_b$. The effect of changing t_b is to delay or advance the entire signal with no change in form or theoretical focal point, x_b. Note that this formulation is based on linear theory and no nonlinear amplitude dispersion is included.

The variables that completely specify $\eta(x,t)$ in equation (2.3) are

$$N,\ a_n,\ f_n,\ k_n,\ x_b,\ t_b$$

since f_n and k_n are related by equation (2.2), k_n can be eliminated but the depth, d, and gravity, g, are added as independent parameter. To simplify the experiment, we set

$$a_n = a_1 = a_2 \cdots a_N = \text{constant}$$

and define

$$a = a_n N \ . \qquad (2.5)$$

We also specify the discrete frequencies f_n to be uniformly spaced over the band

$$\Delta f = f_N - f_1 \qquad (2.6)$$

and define

$$f_c = \frac{f_N + f_1}{2} \qquad (2.7)$$

the central frequency. The nondimensional wave packet parameters then become

$$ak_c,\ \frac{\Delta f}{f_c},\ x_b k_c,\ k_c d,\ N$$

where

$$\frac{(2\pi f_c)^2}{g} = k_c \tanh k_c d \qquad \text{defines } k_c. \tag{2.8}$$

This is the wavenumber of the wave having the center frequency f_c.

A priori, $k_c d$ was considered to be of minor importance in the wave dynamics since $\tanh(k_c d) = 0.96, 0.99, 1.00 \sim$ constant for the three packet center frequencies used (f_c = 0.88, 1.08, 1.28 Hz). These were effectively deep water waves. To be consistent in this regard, the <u>deep</u> water dispersion relationship was used to compute k_n from f_n in equation (2.4).

N was made relatively large (N = 32) to approximate a continuous spectrum and to eliminate its dependence. Finally, the following functional relationship results from the dimensional analysis:

$$\eta k_c = \eta k_c\left(xk_c,\ tf_c;\ ak_c,\ \frac{\Delta f}{f_c},\ x_b k_c\right) \tag{2.9}$$

Families of wave packets were computed by systematically varying $\Delta f/f_c$ and $x_b k_c$. The amplitude, ak_c, was varied by multiplying the summed packet by a gain factor (see program EW6 in Appendix 3 by E.S. Chan, (1985)). The desired spectrum and signal for a typical set of packet parameters is shown in figure 2.2.1. The signal envelope is periodic with period $T' = 1/\delta f$ where δf is the input spectral resolution $\delta f = \Delta f/N$.

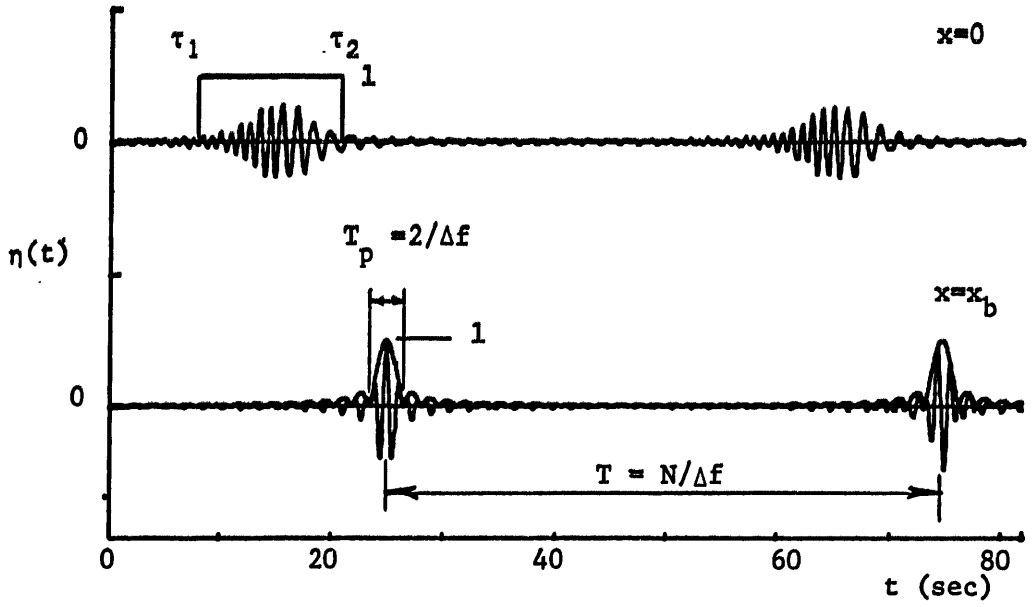

Figure 2.2.1a Ideal packet signal for $a_n = 1/N$ (N = 32), $\Delta f/f_c$ = 0.73, f_c = 1.08 Hz. Also shown are input signal window limits τ_1 and τ_2

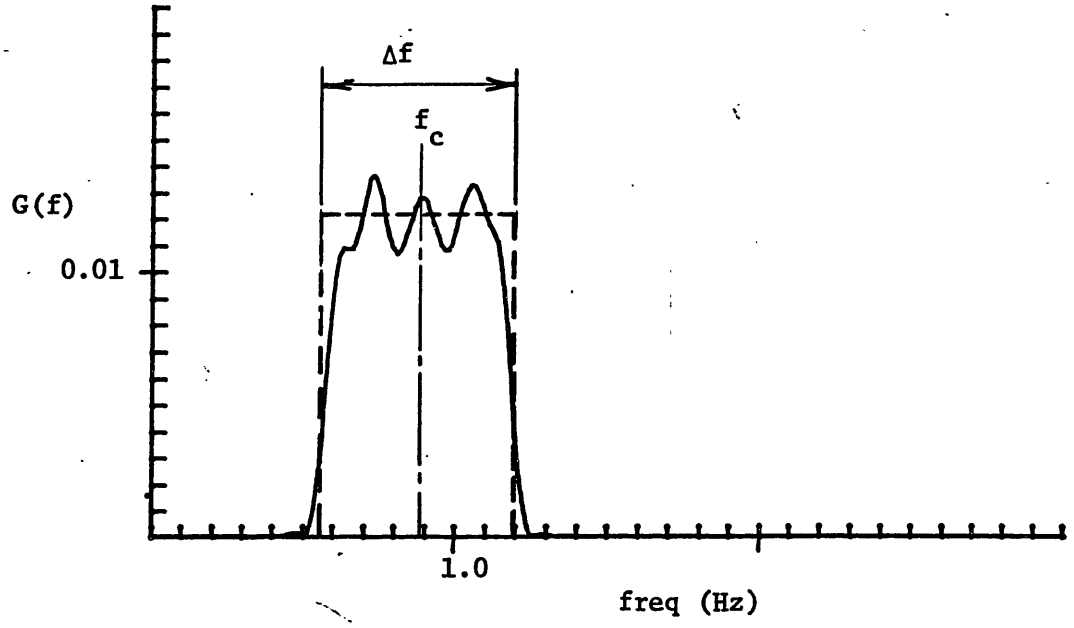

Figure 2.2.1b Frequency spectra of ideal periodic signal in figure 2.2.1a,---- , and spectra of windowed signal,——— .

As the number of components within the band Δf is made large, T' also increases. For practical reasons, the signal was truncated or windowed in time with a box car function w(t), giving a signal at x = 0 of

$$\eta'(0,t) = \eta(0,t) \cdot w(t) \tag{2.10}$$

where $w(t) = 1 \qquad \tau_1 < t < \tau_2$

$= 0$ elsewhere.

The effect of the window on the ideal frequency spectrum is found by taking the Fourier transform of $\eta'(0,t)$, which is the convolution of the original spectrum with the Fourier transform of the window.

Thus $$\Pi'(0,f) = \Pi(0,f) * W(f) \tag{2.11}$$

where $$\Pi(0,f) = \int_{-T'/2}^{T'/2} \eta(0,t) e^{-i2\pi ft}\, dt \tag{2.12}$$

and $$W(f) = \int_{-T'/2}^{T'/2} w(t) e^{-i2\pi ft}\, dt \tag{2.13}$$

are Fourier transforms.

The resultant spectrum is also shown in figure 2.2.1b. The Gibbs' phenomenon is manifested in this spectrum. Various techniques are available to reduce these oscillations to better approximate the ideal spectrum. However, for the purpose of this experiment and to reduce the complexity of the input packet formulation additional optimization was considered unnecessary. The reader is referred to Openheim and Shafer (1975, pp. 239-250) for a more detailed account of these methods.

The window limits were approximated by requiring that a negligible amount of energy be excluded from the window (less than 4% of the energy in the entire signal $0 < t < T'$) and that at least the main lobe of the amplitude envelope was intact at the breaking location or focal point.

However, a computation of the energy in the main lobe of a continuous spectrum ($N \to \infty$) showed that this energy is only $0.9027\ E_0$ where E_0 is the energy in the full period. In the discrete spectrum case, where $N = 32$, this ratio was numerically computed as 0.90396, which is less than the desired value of 0.96. It was then necessary to include the first side lobes in the window to reduce the lost energy to $0.04E_0$.

The specification of τ_1 and τ_2 can be understood by considering the x-t diagram of the packet in figure 2.2.2. The original formulation assumes that all wave components are present at any particular x location. However, in practice the windowed packet is started from rest at the paddle and no waves are present in the channel. During paddle motion, from τ_1 to τ_2 (see figure 2.2.2) all frequencies are generated within the band Δf. A long transient wave is also generated which was measured and found to be very small compared to the carrier waves. Each frequency component propagates at its own group velocity. The cross hatched area represents the region where the required components are present for the summation. Since it is desired that a length of $L = 4\pi/\Delta k$ (Δk is the difference in wave number between f_1 and f_N) be present at breaking to include the packet side lobes, then the appropriate group velocity lines can be followed back to $x = 0$ to determine the required minimum window.

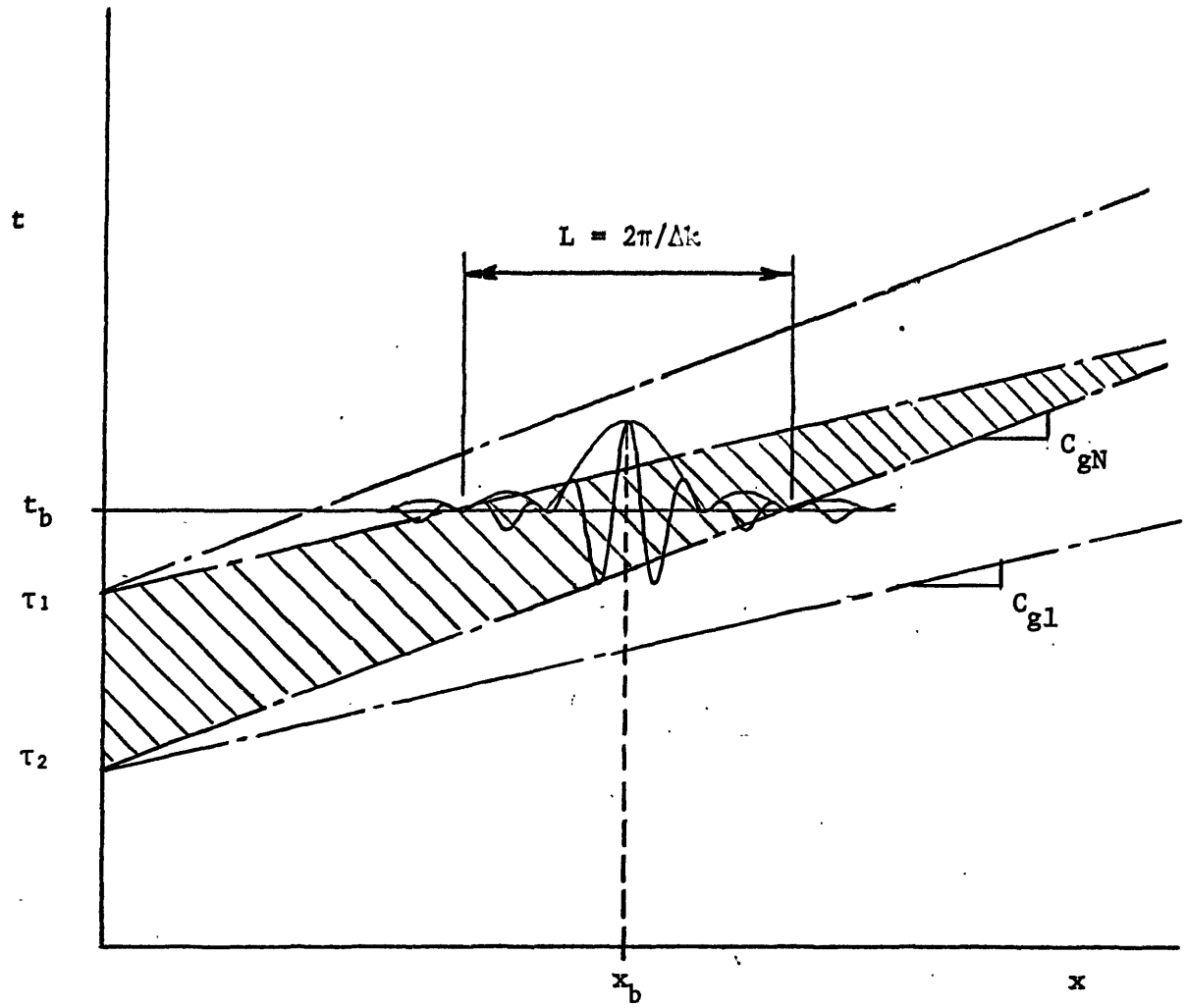

Figure 2.2.2 Schematic of wave packet dispersion down the channel. C_{gN} is the group velocity of the Nth frequency component. τ_1 and τ_2 are the paddle motion window limits.

In practice these limits were made wider to account for nonlinear dispersion effects. Increasing the window length beyond $\tau_1 < t_2 < \tau$ had negligible effect on the measured quantities in this experiment.

The theoretical value, ak_c, specifying the amplitude of the wave packet, is reduced as a result of windowing the input signal. An estimate of this reduction is computed as follows.

The energy density computed from the ideal input spectrum is

$$\bar{E}_o = \rho g \int_{f_1}^{f_N} S(f)\, df \tag{2.14}$$

where the over bar is a time average. In the discrete case this is

$$\bar{E}_o = \frac{1}{2} \rho g \sum_{n=1}^{N} a_n^2 = \frac{1}{2} \rho g\, a_n^2\, N \,. \tag{2.15}$$

$$\text{Since } a = a_n N \,, \qquad E_o = \frac{1}{2} \rho g \frac{a}{N} \,. \tag{2.16}$$

According to Parseval's theorem this is also equal to

$$\bar{E}_o = \rho g \frac{1}{T'} \int_{-T'/2}^{T'/2} \eta^2(x,t)\, dt \tag{2.17}$$

$$\text{where } T' = \frac{1}{\delta f} = \frac{N}{\Delta f} \,. \tag{2.18}$$

The energy in the windowed signal, however, is

$$\bar{E}_w\,(x) = \rho g \frac{1}{T'} \int_{-T'/2}^{T'/2} \eta^2(x,t) \cdot w(t)\, dt \tag{2.19}$$

The requirement that $\frac{\overline{E}_w}{\overline{E}_o} > R = 0.96$

leads to

$$(\overline{E}_w)^{1/2} = (\overline{E}_o R)^{1/2} \quad \text{and}$$

$$a_w = a\, R^{1/2} = 0.98\, a \tag{2.20}$$

resulting in a 2% error by using the ideal input value of a versus that of a windowed signal.

The effect of varying the nondimensional wave amplitude ak_c is simply to vary the wave height and thus the momentum and energy flux in the propagating packet. Thus a is a measure of the theoretical wave amplitude at the focal point and is independent of $\Delta f/f_c$ and xk_c, but depends on N. Increasing $\Delta f/f_c$ results in decreasing the length or period of the packet and thus increasing the packet envelope steepness. For a given wave center frequency, f_c, the number of waves in the packet equals $2f_c/\Delta f$. Also, since N = constant, the frequency spectrum resolution varies as $\delta f = N/\Delta f$ and the power spectrum energy density is $S(f) \propto \frac{a_n^2 \cdot N}{\Delta f}$. According to linear theory, changes in $x_b k$, theoretically, should have no effect on the breaking dynamics, but only change the x reference location. This can be seen from equation (2.3). The phase distribution is a function of $(x_b - x)$ and not x_b alone. (In practice, phase mismatch error between frequency components and nonlinear dispersion effects become greater as x_b is increased. These will be discussed in Section 3).

The desired surface displacement at the paddle position, $\eta'(0,t)$, is realized by applying an input voltage to the wavemaker system that is

corrected in amplitude and phase for the complete servo controller, hydraulic system, and wave paddle transfer function. The wavemaker system is modeled as two cascaded linear systems (figure 2.2.3). The transfer functions $H_1 f$ giving the paddle position and $H_2(f)$ giving the fluid surface displacement were measured by applying a constant frequency sinusoidal signal of uniform amplitude to the system. The paddle position and wave height 2 meters from the paddle were measured for a range of frequencies. The measurement was made with two different input amplitudes to verify the linear system assumption. Measurements of the generated waves were made after the Fresnel wave front oscillations had passed the measurement point. The measured transfer functions are shown in figure 2.2.4. The measured phase of the surface wave at 2m from the paddle was extrapolated back to the paddle position x=0, using the finite depth wave number corresponding to the frequencies measured. Wave height measurements at 2m are far enough from the paddle (>3h) where evanescent modes have decayed to negligible values.

A third order polynomial was fit to the data of $|H(f)|$ and a linear fit to the phase $\psi_{v\eta}(f)$. These waves were then used to compute corrections to the input voltage signal,

$$v(t) = \sum_{n=1}^{32} a_n |H_n| \cos\left(-k_n x_b - 2\pi f_n (t-t_b) - \psi\right] . \qquad (2.21)$$

This overall transfer function also includes a calibration of the D/A output board from the computer.

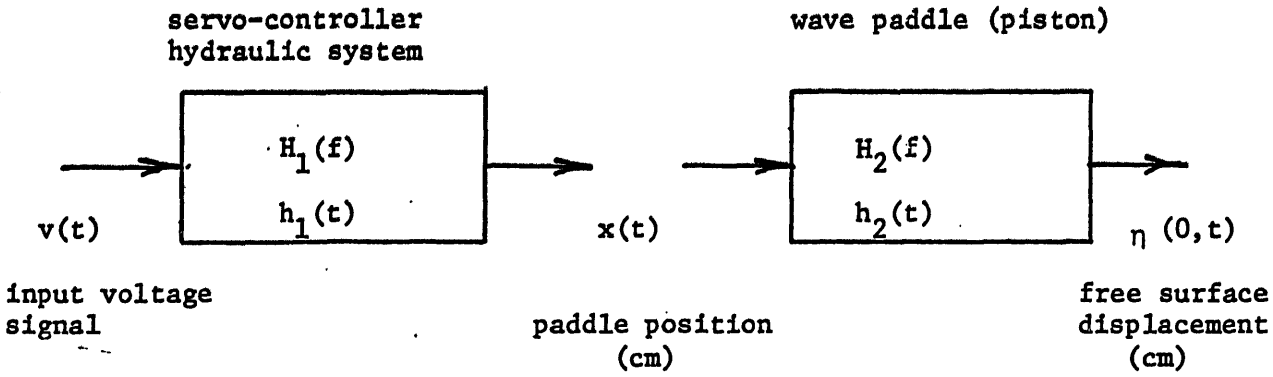

$$H(f) = H_1(f) \cdot H_2(f)$$

$$h(t) = h_1(t) * h_2(t)$$

$$\eta(0,t) = v(t) * h(t)$$

Figure 2.3.3. Definition sketch of wave maker transfer functions
* represents convolution.

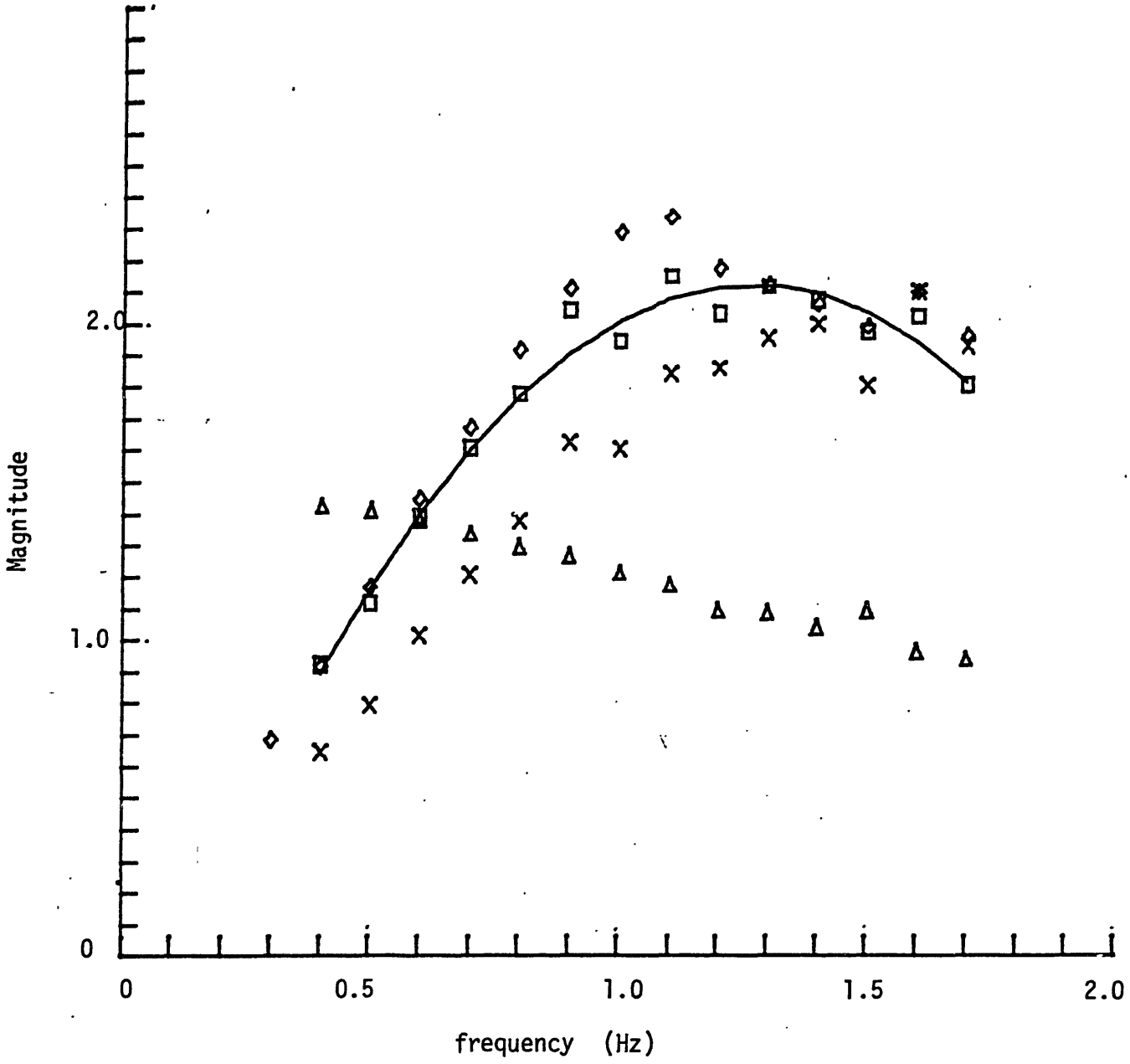

Figure 2.2.4a Wave maker transfer function magnitude. H(f) (□), $H_1(f)$ (△), $H_2(f)$ (×) all measured on date of 6-5-84. Solid line is fit to H(f) data,

$H(f) = -0.0499 + 4.15\ f(Hz) - 1.644\ f^2$;

Measured H(f) on date 4-5-85 is shown by (◇). See figure 2.2.3 for definitions.

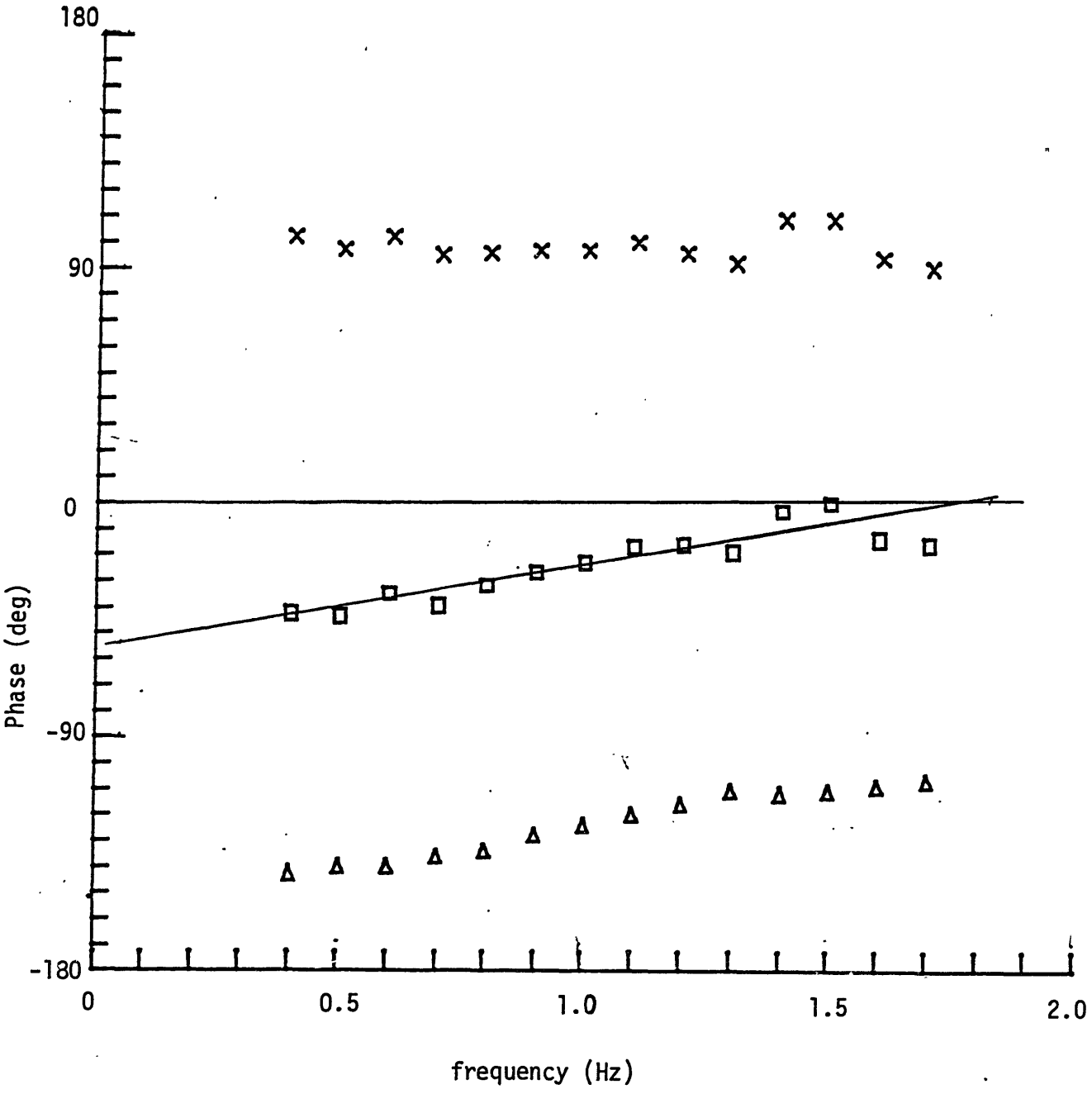

Figure 2.2.4b Wave maker transfer function phase. H(f) (□), $H_1(f)$ (Δ), $H_2(f)$ (×). See figure 2.2.3 for definitions. Solid line is ψ = -56 deg + 31.9 deg/Hz f

2.3 Conservation Equations

2.3.1 Conservation of Mass, Momentum, and Energy

The net loss of total mass flux, horizontal momentum flux, and energy flux from the wave packet as a result of breaking and the net gains to the water column are determined by applying the conservation equations to a control volume bounded from below by the tank bottom, $z = -d$, and above by the free surface, η. Two verticals, far upstream and downstream of breaking at x_1, x_2 (figure 2.3.1), close the volume. The deterministic motion is considered to be two-dimensional so the quantities are expressed per unit width across the tank. The coordinate system is defined in figure 2.3.1 with x, the longitudinal dimension referenced from the paddle, z is vertically upward from the still water line and y is across the channel. The Eulerian velocities in the x,z,y direction are u,w,v respectively.

The incident wave packet enters from upstream (the left) crossing x_1, breaking ensues in the control volume, and waves are transmitted downstream crossing x_2. The fluid motion at x_1 and x_2 is assumed to be completely due to waves; all mean currents and turbulence associated with breaking is contained within the control volume. The change in total mass, momentum and energy in the control volume from the initial state, can then be compared with the difference in the corresponding fluxes crossing x_1 and x_2. This is expressed by the conservation equations given by Whitham (1962) as follows

mass
$$\frac{\partial(\rho\bar{\eta})}{\partial t} + \frac{\partial M}{\partial x} = 0 \qquad (2.22)$$

momentum
$$\frac{\partial M}{\partial t} + \frac{\partial S}{\partial x} = \overline{\tau_x} \qquad (2.23)$$

energy
$$\frac{\partial E}{\partial t} + \frac{\partial F}{\partial x} = \rho \int_{-d}^{\eta} \overline{\varepsilon} \; dz \qquad (2.24)$$

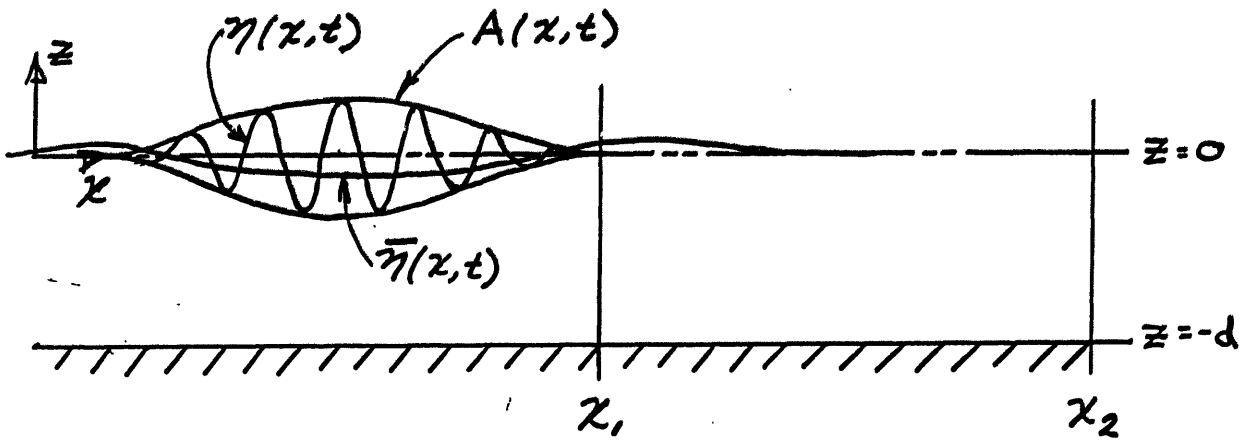

Figure 2.3.1. Defintion sketch of wave packet.

Where $\bar{\eta} = \frac{1}{T}\int_0^T \eta(x,t)dt$ (2.25)

$$M = \overline{\int_{-d}^{\eta} \rho u dz} \tag{2.26}$$

$$S = \overline{\int_{-d}^{\eta} (P + \rho u^2)\, dz} \tag{2.27}$$

$$E = \overline{\int_{-d}^{\eta} (\tfrac{1}{2}\rho \underline{V}^2 + \rho g z)dz}\,, \qquad \underline{V}^2 = u^2 + w^2 + v^2 \tag{2.28, 2.29}$$

$$F = \overline{\int_{-d}^{\eta} (P + \tfrac{1}{2}\rho \underline{V}^2 + \rho g z)udz} \tag{2.30}$$

The overbar is a time average over the carrier wave period T. Here, $\bar{\eta}$ is the setdown of the free surface, ρ is the fluid density. The average horizontal mass flux, horizontal momentum flux, and energy flux crossing the vertical are given by M, S, and F respectively. In equation (2.26) M is also interpreted as the time averaged momentum density, and E is the energy density. The term $\overline{\tau_x}$ is the time averaged horizontal shear stress at the boundaries of the channel and ε is the rate of energy dissipation unit mass.

The above equations are derived by integration of the differential, Eulerian forms of the conservation equations from $-d$ to η and then time averaging over the carrier wave period. Also, use is made of the free surface and bottom boundary conditions. These are rederived in Appendix 1.

Ultimately the <u>total</u> fluxes are found by integrating M, S, F over the entire packet period. The intermediate averages are made so that comparison with the results in the literature can be made and so motion at the packet scale is not filtered out. The <u>total</u> balance is done by

integrating the equations over long time and over the distance between stations x_1 and x_2 where the flux is measured. For example, the total the total momentum balance becomes

$$\int_{t_1}^{t_2}\int_{x_1}^{x_2}\frac{\partial M}{\partial t}\,dxdt + \int_{t_1}^{t_2}\int_{x_1}^{x_2}\frac{\partial S}{\partial x}\,dxdt = \int_{t_1}^{t_2}\int_{x_1}^{x_2}\overline{\tau}_x\,dxdt \tag{2.31}$$

then

$$\int_{x_1}^{x_2} M_{t_2}\,dx - \int_{x_1}^{x_2} M_{t_1} = -\int_{t_1}^{t_2} S_{x_2}\,dt + \int_{t_1}^{t_2} S_{x_1}\,dt + \int_{t_1}^{t_2}\int_{x_1}^{x_2}\overline{\tau}_x\,dxdt \tag{2.32}$$

giving,

$$\underline{\Delta M} = -\overline{\overline{\Delta S}} + \overline{\overline{\underline{\tau_x}}} \tag{2.33}$$

where here the double overbar is a long time integration and the underbar is a space integration. Likewise for mass and energy, the total balance becomes

$$\Delta\,\rho\,\overline{\underline{\eta}} = -\Delta\,\overline{\overline{M}} \tag{2.34}$$

$$\Delta\,\underline{E} = -\Delta\,\overline{\overline{F}} - \rho\,\overline{\overline{\underline{\int_{-d}^{\eta}\varepsilon\,dz}}} \tag{2.35}$$

To experimentally determine the fluxes, it is necessary to measure the velocities $u(x,z,t)$, $w(x,z,t)$, the pressure $P(x,z,t)$, simultaneously, all along the verticals x_1 and x_2 and also measure the instantaneous free surface elevation. Alternatively, one may derive the pressure by the vertical momentum equation. Gradients in x and y are required, which can only be determined with measurements along two closely spaced vertical lines. These measurements are theoretically possible with two scanning

laser doppler anemometers. However, there is a limitation on the sampling rate as well as equipment cost considerations. The approach used in these experiments is to estimate the fluxes by measuring the free surface displacement only. In this way a great number of repeats and packet types can be measured for their losses due to breaking with only two wave gauges. (Note that the momentum and energy density can only be measured by velocitymeasurements at grid points throughout the control volume and will be discussed in Chapter 5.) This flux estimation is possible since at these stations, x_1 and x_2, the fluid motion contains only surface wave components. Also, the carrier wave steepness is $ak=\varepsilon=0.25$ and the steepness of the packet envelope is of order ε^2 so that a weakly nonlinear wave theory can be used to predict the subsurface velocity and pressure field from the measured surface displacement.

The flux terms and densities shown above will generally contain contributions from the carrier waves, and also from the nonlinearly forced wave traveling with the group. The flux terms have been derived to second order in wave slope by Whitham (1962, Section 3) and Longuet-Higgins and Stewart (1961, 1962, 1964) for the case of a slowly varying wave group of steepness $(ak)^2$, Mei (1983) treats the case where the wave amplitude is varying more rapidly in space. At locations far upstream and downstream of breaking the slowly varying assumption is valid and relatively small errors (2%, (see section 3.2)) result from using the second order estimate for the momentum flux and energy flux. Closer to breaking, the higher order terms become appreciable, and it is of interest to determine the form of these corrections. The details of this analysis are shown in Appendix 1 and summarized here.

Following Dysthe (1979) the free surface displacement is represented to second order as:

$$\eta(x,t) = \bar{\eta} + \eta' \tag{2.36}$$

where $$\eta' = A(x_1,t_1)e^{i\theta} + A_2(x_1,t_1)e^{i2\theta} \tag{2.37}$$

$$\theta = k_c x - \omega_c t$$

The velocity potential is represented as

$$\phi = \bar{\phi} + B\,F(Z)\,e^{i\theta} + B_2F_2(Z)\,e^{2i\theta} \tag{2.38}$$

The coefficients A, A_2, B, B_2, and the forced wave variables, $\bar{\eta}$, $\bar{\phi}$ are all assumed to be functions of slow time and space

$$t_1 = \mu t,\ x_1 = \mu x \tag{2.39}$$

where $\mu = \frac{\Delta\omega}{\omega_c}$ gives the envelope steepness of $\mu ak = \mu\varepsilon$ and $\varepsilon = ak$ is the carrier wave steepness. Also, $\bar{\phi}$ is allowed a slow depth dependence $z_1 = \mu z$. The horizontal and vertical velocities are given by

$$u = \frac{\partial\phi}{\partial x}, \qquad w = \frac{\partial\phi}{\partial z} \tag{2.40, 2.41}$$

where

$$\frac{\partial}{\partial x} \to \frac{\partial}{\partial x} + \mu\frac{\partial}{\partial x_1}$$

$$\frac{\partial}{\partial z} \to \frac{\partial}{\partial z} + \mu\frac{\partial}{\partial z_1}$$

The velocities are represented as

$$u = \bar{u} + u^{(1)} + u^{(2)} \tag{2.42}$$

$$w = \bar{w} + w^{(1)} + w^{(2)} \tag{2.43}$$

and are given in Appendix 1.

The wave variables $\bar{\phi}$, $\bar{\eta}$, $\bar{u}$, $\bar{w}$ can be determined for $kd = 0(ka)^{-1}$ as shown by Dysthe (1979) with the following set of equations:

$$\nabla^2\bar{\phi} = 0 \qquad 0 < z < -d \tag{2.44}$$

$$\frac{\partial\bar{\phi}}{\partial t} + g\bar{\eta} = 0 \qquad z = 0 \tag{2.45}$$

$$\bar{w} - \frac{\partial\bar{\eta}}{\partial t} = \frac{\omega}{2}\frac{\partial}{\partial x}|A|^2 \qquad z = 0 \tag{2.46}$$

$$\bar{w} = \frac{\partial\bar{\phi}}{\partial z} = 0 \qquad z = -d \tag{2.47}$$

Assuming a packet of permanent form so that $\frac{\partial}{\partial x} \to \frac{-1}{C_g}\frac{\partial}{\partial t}$, where C_g is the group group velocity, the above set of equations is solved using Fourier transform methods provided $|A|^2$ is known and we can set

$$|A|^2 = 2\overline{\eta^2} \,. \tag{2.48}$$

These forced wave variables were earlier derived by Longuet-Higgins and Stewart (1962) using a perturbation expansion approach and expressed as a sum of Fourier components. Dysthe (1979) showed the two methods to give the same result. The important results of their analysis show that

in the case when the depth is small compared to the group length, the forced wave velocity $\bar{u}$, being constant in depth, can be expressed in terms of the local surface displacement variance by

$$\bar{u} = \frac{-g}{d}\left[\frac{C_g}{2(gd - C_g^2)} + \frac{1}{C}\right]\overline{\eta^2} \tag{2.49}$$

and

$$\bar{w} = 0 \tag{2.50}$$

$$\bar{\eta} = \left[\frac{-g}{2(gd - C_g^2)}\right]\overline{\eta^2}\ . \tag{2.51}$$

In deep water it is not generally possible to express the forced wave variables in terms of the local radiation stress, $\overline{\eta^2}$, since the solution is a summation of Fourier components that decay in depth at different rates. One should refer to Longuet-Higgins and Stewart (1962, equation (3.13)). In the sample case of periodic packets where $|A|^2 = A_o^2[1 + \cos \mu k(x-C_g t)]$, the forced wave variables are given in terms of the local radiation stress as shown in Appendix 1.

2.3.2 Mass flux

Upon substitution of the horizontal velocity due to the carrier waves and forced wave into equation (2.26) for the mass flux the following is obtained

$$M = \rho\,\overline{\eta'^2}\,\omega_c \coth k_c d + \rho \int_{-d}^{\bar{\eta}} \bar{u}\, dz \tag{2.52}$$

The first term on the right represents the mass flux due to the carrier

waves or Stokes drift. The second term is the mass flux in the return flow due to the forced wave. For shallow water, compared to the group length, equation (2.49) is substituted for $\bar{u}$ and the following is obtained

$$M = -\frac{1}{2}\rho g\left[\frac{C_g}{gd - C_g^2}\right]\overline{\eta^2} \tag{2.53}$$

(Longuet-Higgins and Stewart, 1962, equation 3.36).

In this situation the net mass flux is in the opposite direction to the carrier wave propagation. Physically this must be true since by conservation of mass the return flow must not only balance the Stokes drift but also account for the fluid displaced by the forced long wave depression under the group. In the case of very deep water the net mass flux must go to zero.

$$M = 0 \tag{2.54}$$

This states that the Stokes drift in the carrier waves is exactly balanced by the return flow in the forced wave. This fact has been previously noted by Longuet-Higgins and Stewart (1964), and also shown by Iusim and Stiassnie (1982) using Dysthes (1979) equations. This also implies that the total momentum integrated over the packet length and depth is also zero as is pointed out by McIntyre (1981).

2.3.3 Momentum flux

The total time averaged horizontal momentum flux, equation (2.27) can be put in terms of u,w,η by substituting for the pressure. The pressure $P(z)$ is obtained by integrating the vertical momentum equation over depth. Also, use is made of the kinematic free surface boundary condition

(see Appendix 1 for details), which yields:

$$S = \frac{\rho g}{2}\overline{(\eta + d)^2} + \rho \overline{\int_{-d}^{\eta} (u^2 - w^2)\, dz} + \rho \overline{\int_{-d}^{\eta} \frac{\partial}{\partial t} \int_{z}^{\eta} w\, dz\, dz'} +$$

$$+ \rho \overline{\int_{-d}^{\eta} \frac{\partial}{\partial x} \int_{z}^{\eta} uw\, dz\, dz'} \qquad (2.55)$$

This equation is exact for a general flow field. The velocities and surface displacement may contain wave components u', forced waves $\bar{u}$, and turbulence, u_t. In general one may expect interactions between these motions which makes separating S into component parts impossible. However, if the time scales of the motions are sufficiently separated, then the averaging will cancel out these terms, and there is no interaction. At stations far from breaking, turbulent velocities are zero and the wave packet is indeed slowly varying, making $\bar{u}$ slowly varying. A separation of scales is is then possible.

Substituting for the various wave variables and neglecting terms higher than 2nd order the momentum flux becomes

$$S = \rho\, g\, \overline{\eta^2} \left[\frac{2kd}{\sinh 2kd} + \frac{1}{2} \right] - \rho \int_{-d}^{0} \frac{\partial \bar{\phi}}{\partial t}\, dz + O(\varepsilon^3) \qquad (2.56)$$

where the hydrostatic term $1/2\ \rho g d^2$ is neglected.

The first term is due to the carrier waves and the second term is due to the pressure of the forced wave. In shallow water, the forced wave pressure is constant in depth and hydrostatic and given by the free surface boundary condition,

$$\frac{\partial \bar{\phi}}{\partial t} + g\bar{\eta} = 0 \quad . \tag{2.57}$$

The momentum flux in this case is,

$$S = \rho\, g\, \overline{\eta^2}\left[\frac{2kd}{\sinh 2kd} + \frac{1}{2}\right] + \rho\, g\, \bar{\eta}\, d \tag{2.58}$$

and is that given by Longuet-Higgins and Stewart (1962) and Whitham (1962). An alternative form is given by

$$S = \rho\, g\, \overline{\eta^2}\left[\frac{2C_g}{C} - \frac{1}{2}\right] + \rho\, g\, \bar{\eta}\, d \tag{2.59}$$

where C_g is the linear group velocity and C is the linear phase speed.

In deep water the contribution from the carrier waves becomes

$$S_{c.w.} = \frac{\rho\, g\, \overline{\eta^2}}{2} \quad . \tag{2.60}$$

Higher order corrections were obtained in the derivation of the momentum flux for the purpose of estimating the errors in our use of the second order estimate. These are given in Appendix 1. The higher order corrections are a result of the steepness of the envelope in terms containing $\partial |A|^2/\partial x$ and $\partial A/\partial x\, \partial A/\partial x$ which are of $O(\varepsilon^4)$. The steepness of the carrier waves gives terms of $|A|^4$ and $|B_2|^2$, also of $O(\varepsilon^4)$. The The forced long wave velocities $\bar{u}^2$, $\bar{w}^2$ also contribute to the momentum flux but are of order $O(\varepsilon^6)$ in deep water. In water shallow compared to the group length, $\bar{w} = 0$, $\bar{u}^2 = (\varepsilon^4)$. An interaction term of form $\bar{\eta}|A|^2$

was also found. These corrections will be used in Chapter 3 to estimate the order of the errors in the measurements of the momentum flux.

2.3.4 Energy flux

The second order estimate of the energy flux due to waves is given by

$$F = C_g E + O(\varepsilon^3) \qquad \text{where } E = \frac{1}{2} \rho g \overline{\eta^2} \tag{2.61}$$

Whitham (1962), where his mean velocity, U, is considered second order.

Chapter 3

Surface Displacement Measurements of Breaking Wave Groups

3.0 Summary

Measurements of the free surface displacement are used to estimate the momentum and energy fluxes due to waves propagating down the channel. Many wave conditions are quickly measured with only a few instruments. The results presented in this chapter are all based on measurements of surface displacement upstream, at, and downstream of the theoretical energy focal point or breaking location, x_b.

The evolution of the surface displacement is followed down the channel and shows good agreement between scales when the time and length scales are normalized by the packet center frequency and corresponding finite depth wavenumber; the linear group velocity is well followed. The effect of breaking on the shape of the packet downstream is compared with a nonbreaking packet; changes are noted in the high frequency waves. Photographs of the packet at breaking show the local details of breaking for two levels of breaking. Variations in the surface displacement variance, integrated over the packet, $\overline{\eta^2}$, show the momentum flux and energy loss due to breaking. These losses are measured by differencing the upstream and downstream values of these fluxes, where they are nearly constant in x. The losses are determined for variations in ak_c, $\Delta f/f_c$, and $x_b k_c$. The measurements of the local wave amplitude at breaking are compared with the predictions of linear theory for a range of bandwidths; poor correlation is found, with waves breaking over a wide range of amplitudes and steepnesses. The evolution of the spectra through breaking

is presented and shows that most of the loss is from the high frequency end of the band. A preliminary estimate of the frequency and energy in the high frequency waves radiated both upstream and downstream of the breaking disturbance is made. It appears that this energy is concentrated around the second harmonic band (of the incident waves) and is roughly 1% of the incident energy. The energy in the upstream and downstream going waves are comparable.

The measurements were made with the resistance wire gauges and data acquisition system described in section 2.

3.1 General Observations, Time Series and Photographs

The wave packets generated at the paddle were composed of short waves followed by long waves as shown in figure 3.1.1. As the group propagates down the tank, the length and period of the group decrease to a minimum near the predicted focal point, $k_c(x - x_b) = 0$, and disperse downstream. At the focal point, linear theory predicts the packet period to be $T = 2/\Delta f$, and The number of waves in the packet as $Tf_c = 2f_c/\Delta f$. This equals 2.8 waves for the case of $\Delta f/f_c = 0.73$, which is what is observed. For the packet in this particular figure, the conditions are such that a plunging breaker occurs between $k_c(x - x_b) = -5$ and 0, as observed by the sudden drop in the wave amplitude.

A comparison of the surface displacement evolution for three packet center frequencies is shown in figure 3.1.2 where the other nondimensional packet parameters are held constant. The amplitude is such that the packet is near breaking (incipient breaking). Near the wave paddle, the amplitudes and phase show good agreement between scales. The time of breaking t_b in the packet generation (2.3) was scaled using f_c. No phase

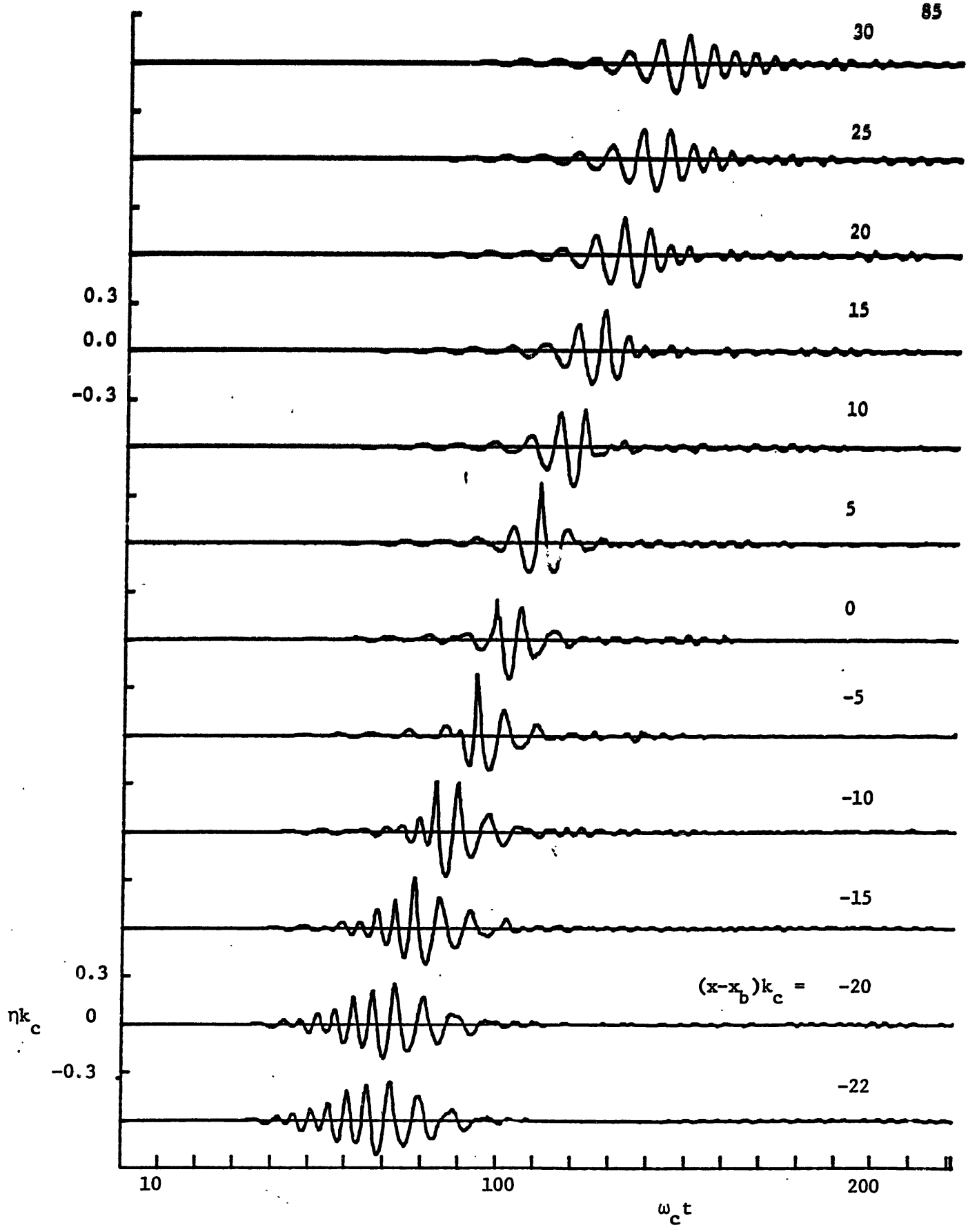

Figure 3.1.1 Time history of surface displacement at various distances from the theoretical energy focal point, x_b. Wave group parameters f_c = 0.88 Hz, ak = 0.352, $\Delta f/f_c$ = 0.73, $x_b k_c$ = 27.4. A single plunging wave was observed between $(x - x_b)k_c$ = -5 and 0.

adjustment was made in the measurements. For these packets the individual phases between frequency components were computed using the deep water dispersion relation, so the phase distribution over the packet frequencies is the same for all three scales. This gives the good agreement in phase, between scales, near the paddle. As the packet propagates down the channel, the largest waves in the packets disperse at the finite depth phase speed which is different between scales. Therefore, downstream, the phase agreement between scales in the low frequency waves, now at the front of the group, is poor. The agreement is still very good in the higher frequency waves at the rear, as can be seen in figure 3.1.2. The group velocity lines are shown based on the large scale center frequency for finite depth, and also for deep water.

For a fixed packet bandwidth $\Delta f/f_c$ and focal point, $x_b k_c$, as ak_c was increased, the resultant group went from nonbreaking to a slight spilling occurring approximately one wavelength downstream of x_b. This critical value at incipient breaking, $ak_c \approx 0.25$, varied little between various packets and scales. As ak_c was increased further, spilling was also triggered upstream near x_b. This breaking became more energetic with increasing ak_c, while spilling at the original location was no longer observed. Presumably energy is dissipated at the upstream breaking so it is below a critical level downstream. At a value of $ak_c \approx 0.3$ only one spilling breaker was produced near x_b. A further increase of ak_c triggered breaking also one wavelength upstream; and at $ak_c \approx 0.39$ only one plunging breaker was observed at this upstream location. At intermediate values of ak_c, two or three breakers were observed spaced roughly one wavelength apart and at a period of twice the carrier wave

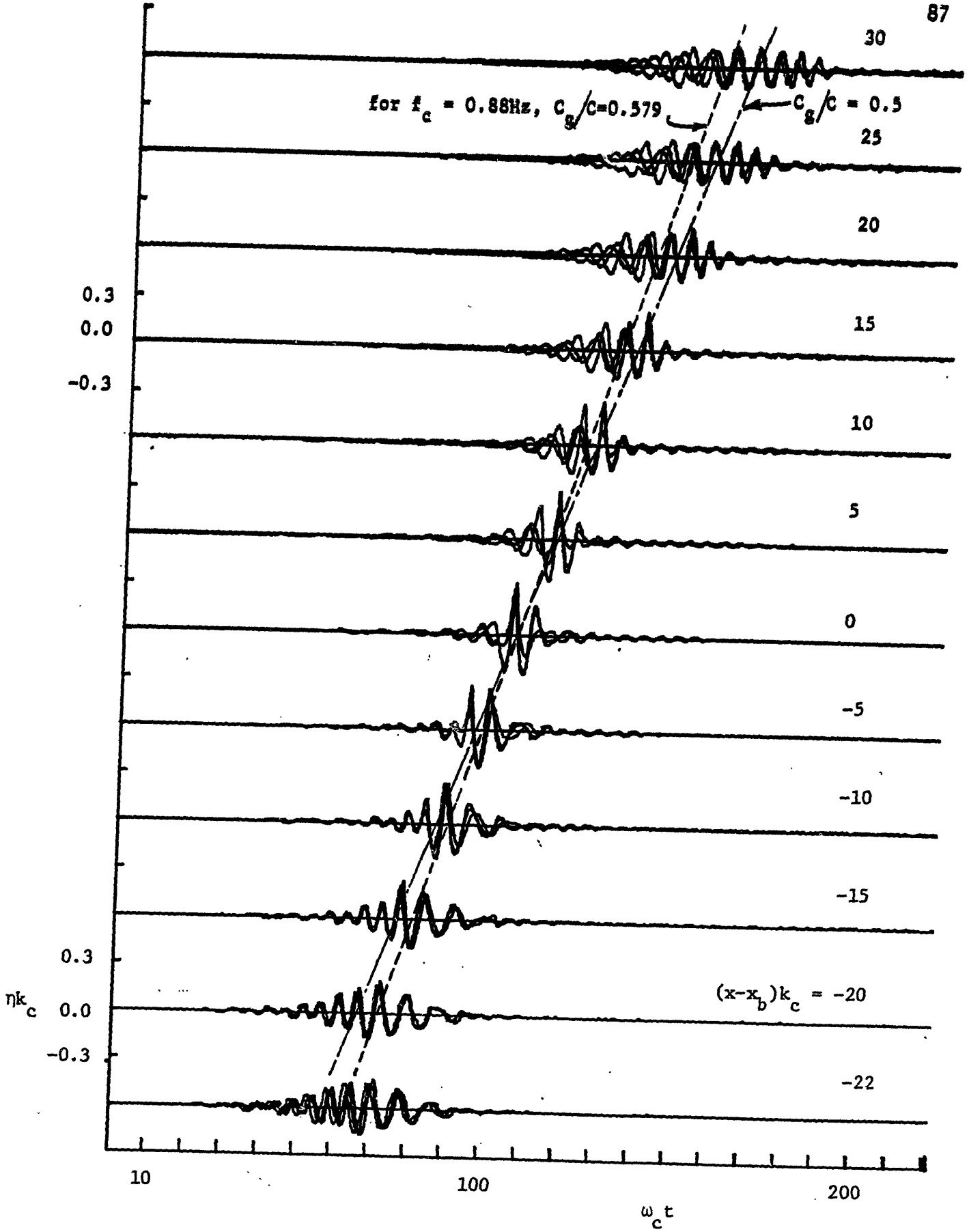

Figure 3.1.2. Comparison of surface displacement time history for three scales of packets, f_c = 0.88 Hz, 1.08, 1.28. All packet amplitudes at incipient breaking ak = (0.25-0.26) $\Delta f/f_c$ = 0.73, $x_b k_c$ = 27.4. Broken lines represent the group velocity.

period. This periodicity has been observed in the field (Donelan, et al., 1977).

The deviation in the breaking location from that predicted by linear theory may be attributed to nonlinear amplitude dispersion which becomes important as the amplitude is increased. This effect can be seen in figure 3.1.3 showing details of the packet at closely spaced locations around breaking. The spilling case shows a relatively symmetric packet envelope with breaking occurring near the peak of the packet. The plunging breaking packet, one wavelength upstream, shows a forward skewed envelope and breaking on the steep front face. The carrier waves cannot sustain the rapid change in amplitude as it propagates through the steep envelope and thus breaking ensues.

Figure 3.1.4 shows a comparison of time histories between a packet that has broken and one that is at incipient breaking. Far downstream the nonbreaking packet is relatively symmetric, while the broken packet is very asymmetric with lower amplitude high frequency waves at the rear of the packet. The phases of the low frequency waves are well matched in contrast to the high frequency waves which are slightly advanced for the breaking packet. The spectra corresponding to these time histories, discussed in section 3.5, also shows this loss in the high frequency waves.

The temporal evolution of breaking in two space coordinates is shown in a series of photographs in figures 3.1.5 - 3.1.7. Each frame represents a separate run of the wave group where the camera and flash unit were triggered at increasingly longer times in 0.05 sec increments. The times are referenced from the paddle startup and can be compared directly

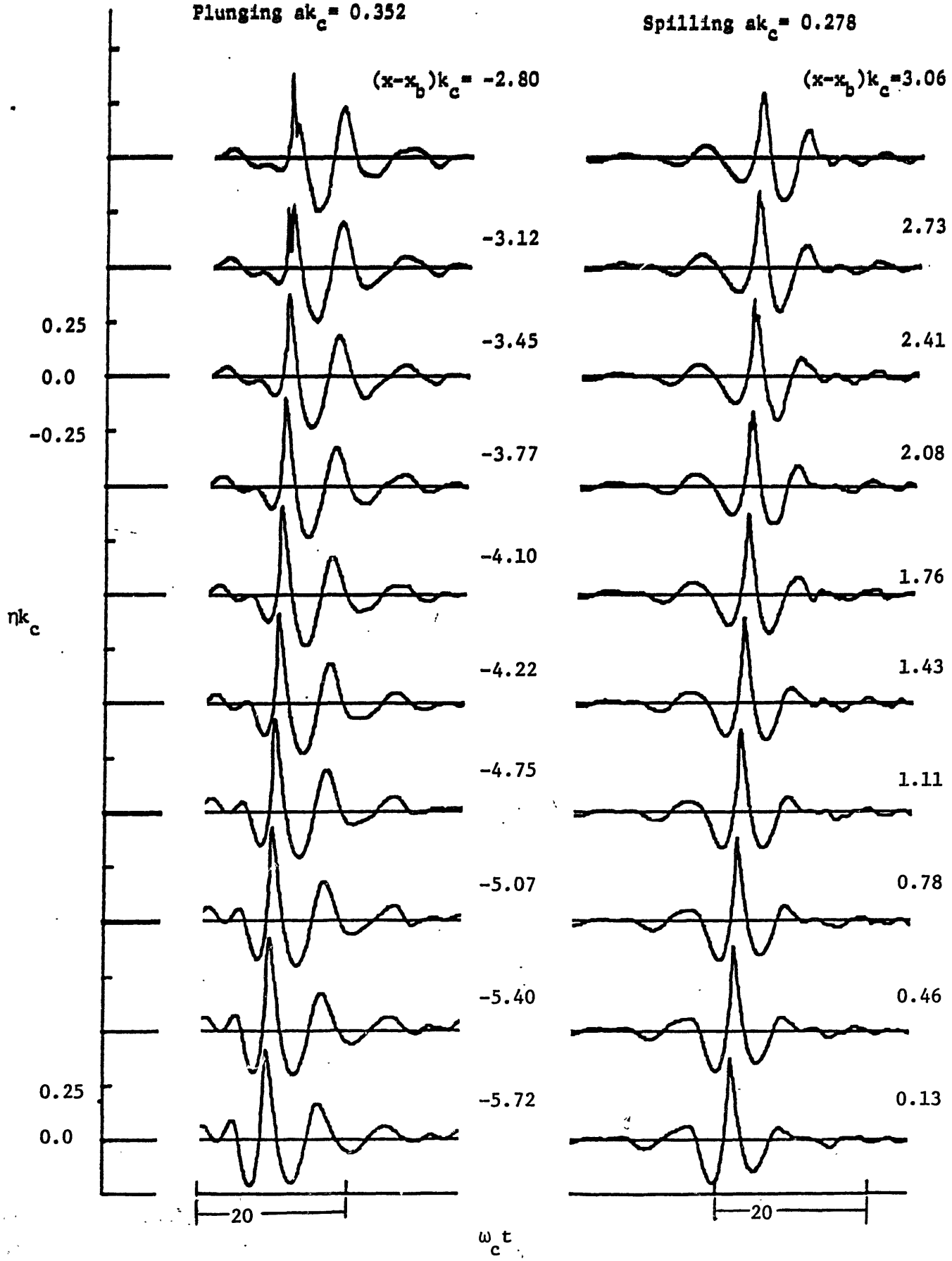

Figure 3.1.3 Detail of surface displacement time history around breaking. f_c = 0.88 Hz, $\Delta f/f_c$ = 0.73, $x_b k_c$ = 27.4.

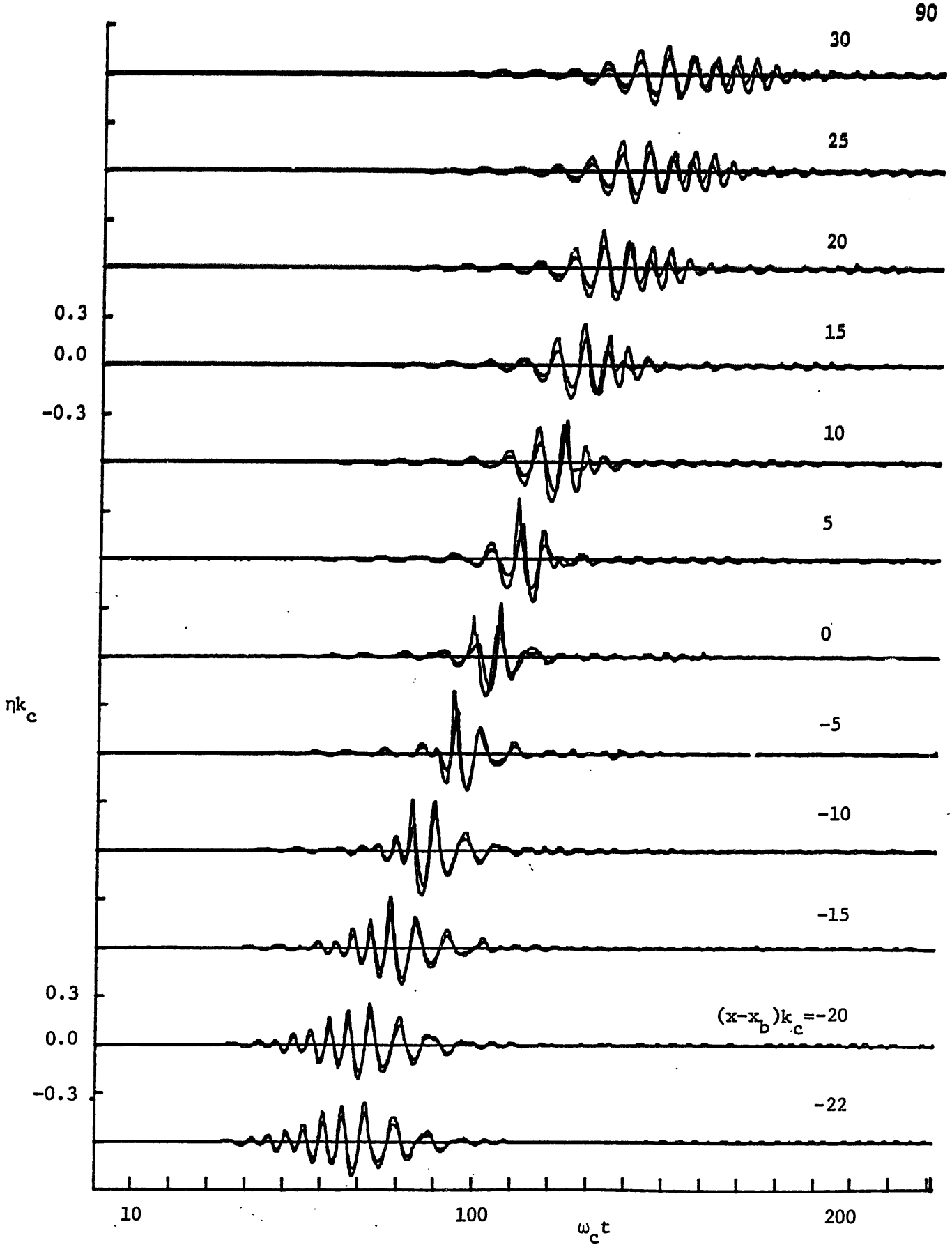

Figure 3.1.4 Evolution of the surface displacement as a function of distance from theoretical focal point. x_b, for an incipient breaking packet $ak_c = 0.250$ and a plunging wave, $ak_c = 0.352$ for $f_c = 0.88$ Hz, $\Delta f/f_c = 0.73$, $x_b k_c = 27.4$. Bold line is incipient breaking.

Figure 3.1.5a. Photographs of a single spilling wave for f_c=0.88Hz ak_c=0.278, $\Delta f/f_c$=0.73, and $x_b k_c$=27.4. Tick marks are at 10 cm intervals and times at right are referenced from paddle start.

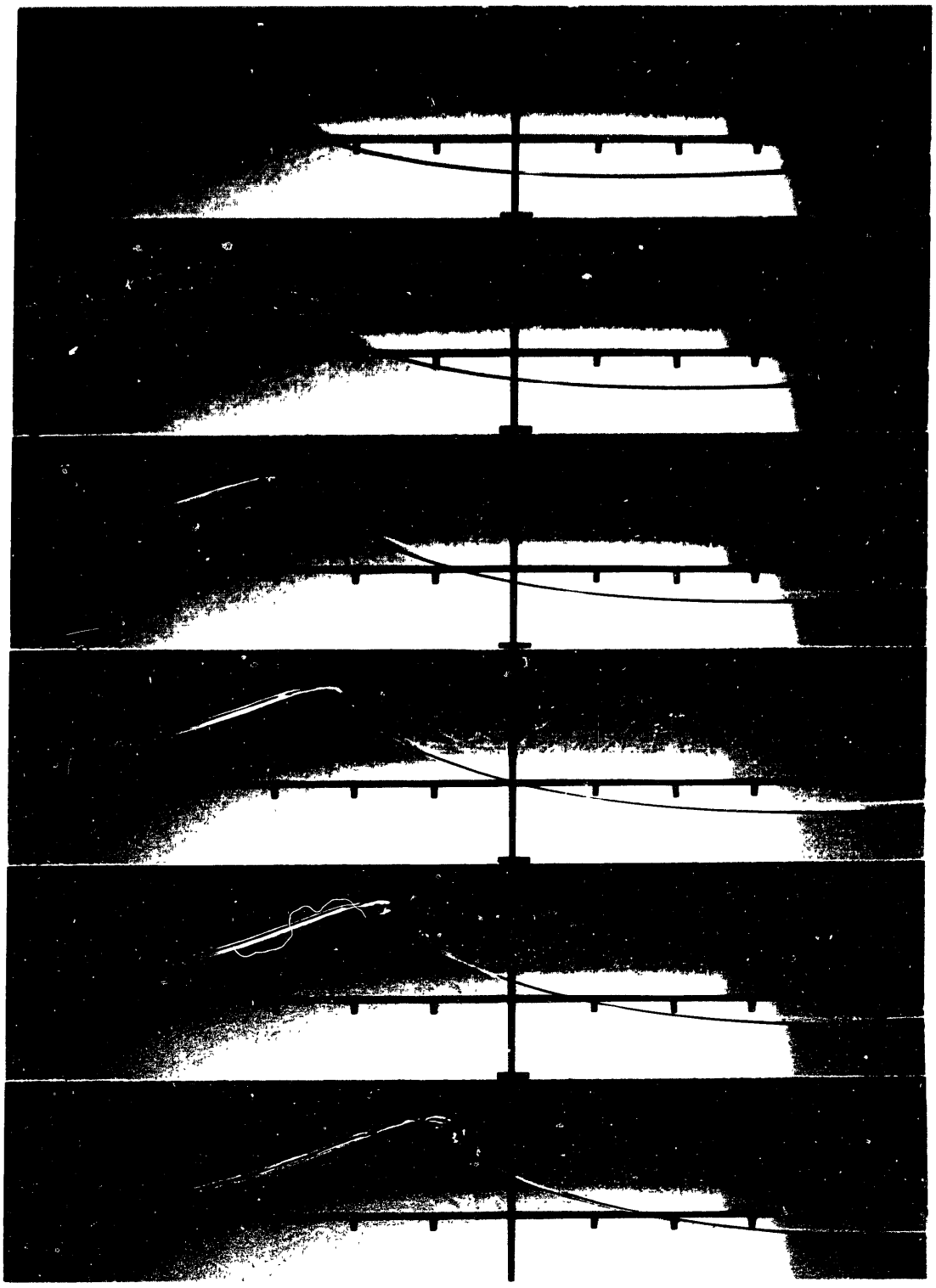
19.00
19.0
19.10
19.1
19.20
19.

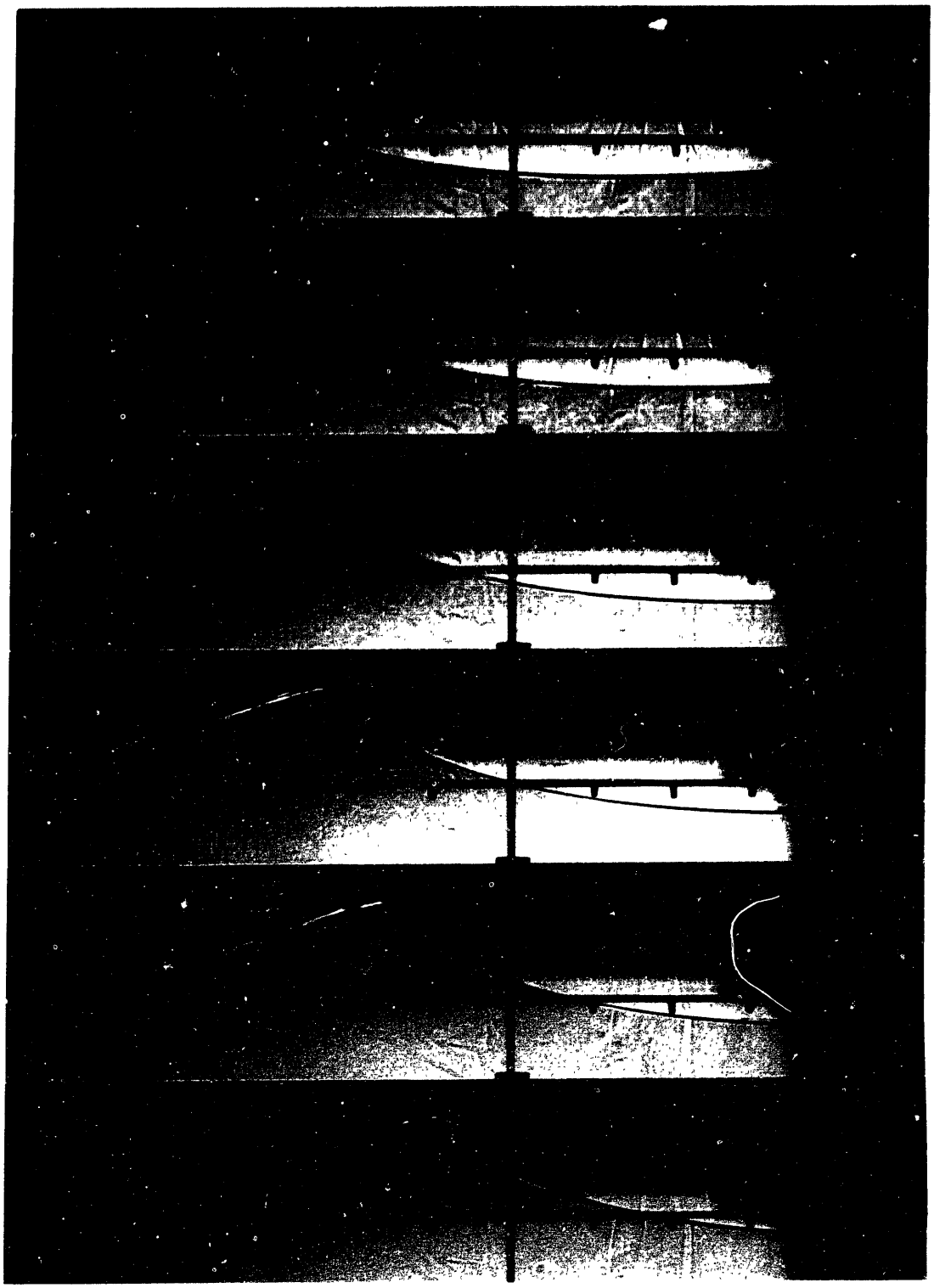

INTENTIONAL DUPLICATE EXPOSURE

Figure 3.1.5b. Photographs of a single spilling wave for f_c=0.88Hz ak_c=0.278, $\Delta f/f_c$=0.73, and $x_b k_c$=27.4. Tick marks are at 10 cm intervals and times at right are referenced from paddle start.

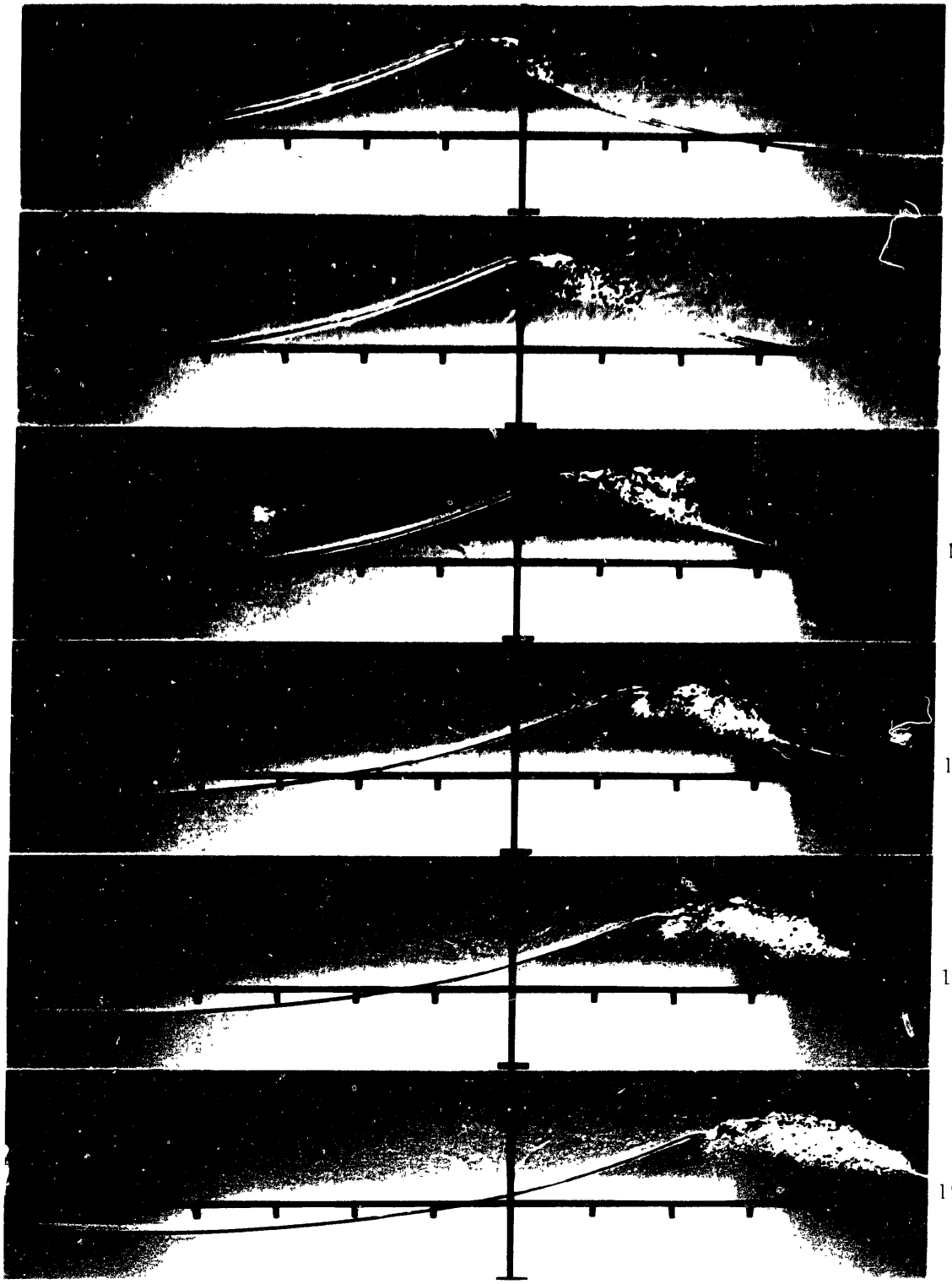
19.30
19.40
19.50
19.55

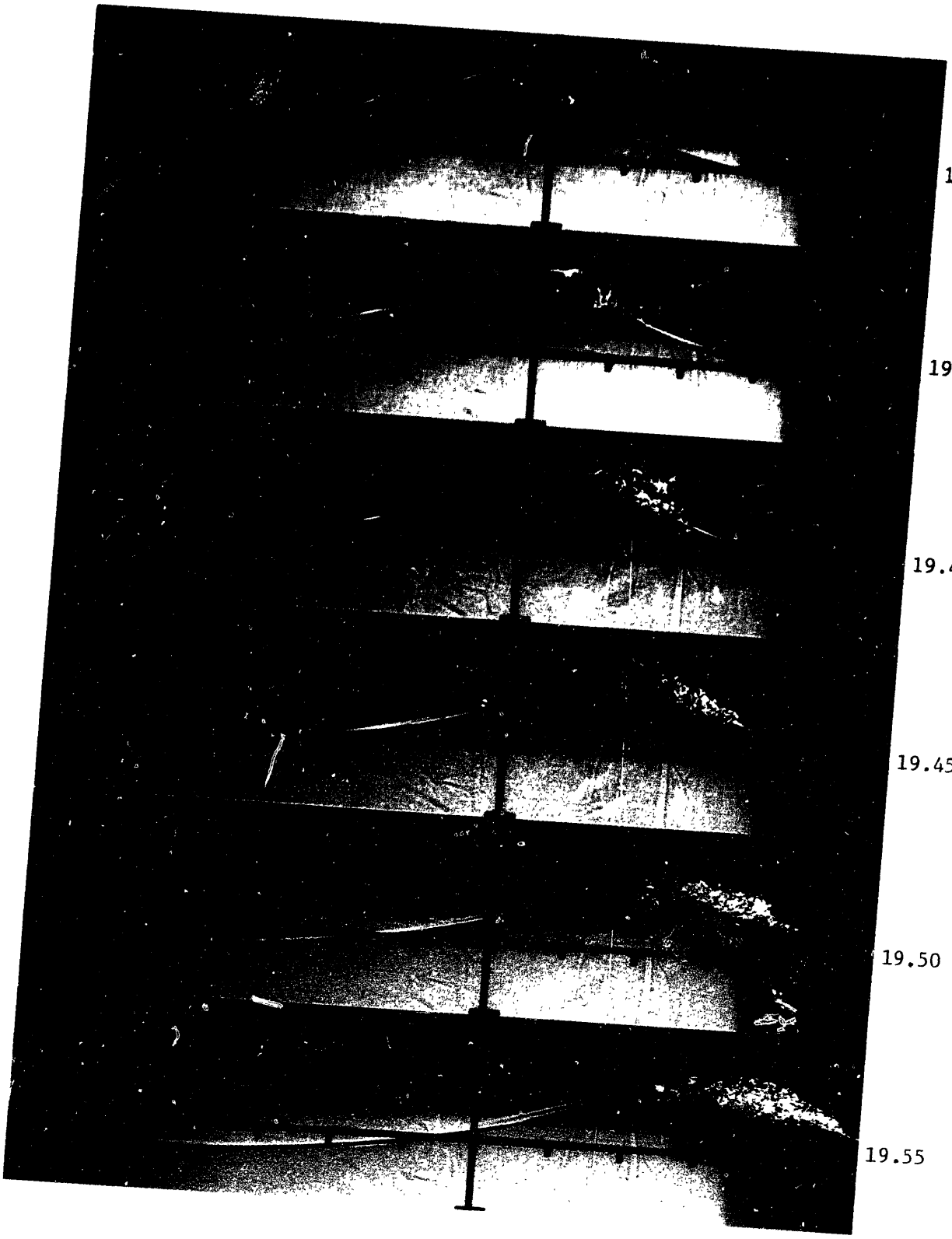

INTENTIONAL DUPLICATE EXPOSURE

Figure 3.1.6a. Photographs of a single plunging wave for f_c=0.88Hz ak_c=0.352, $\Delta f/f_c$=0.73, and $x_b k_c$=27.4. Tick marks are at 10 cm intervals and times at right are referenced from paddle start.

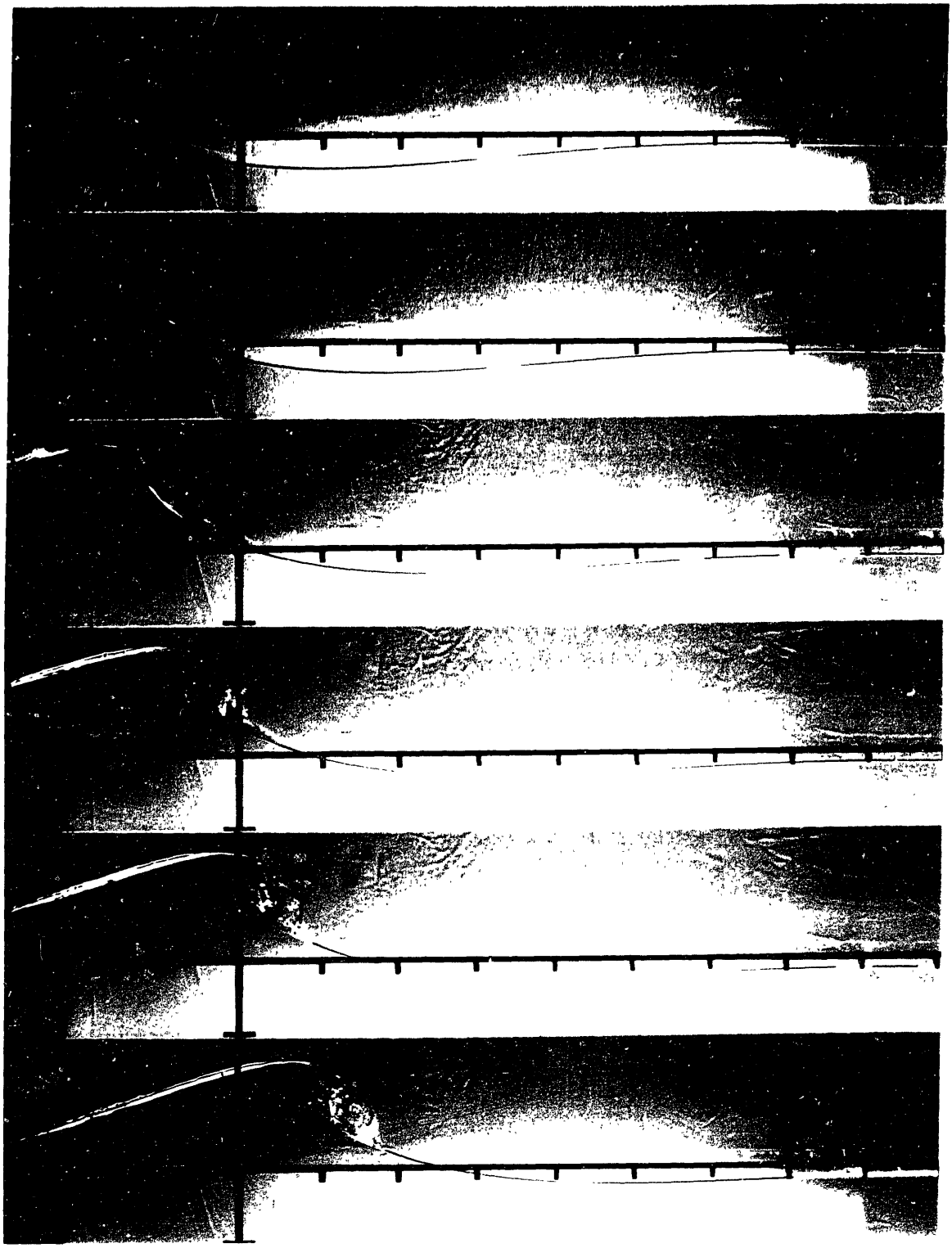

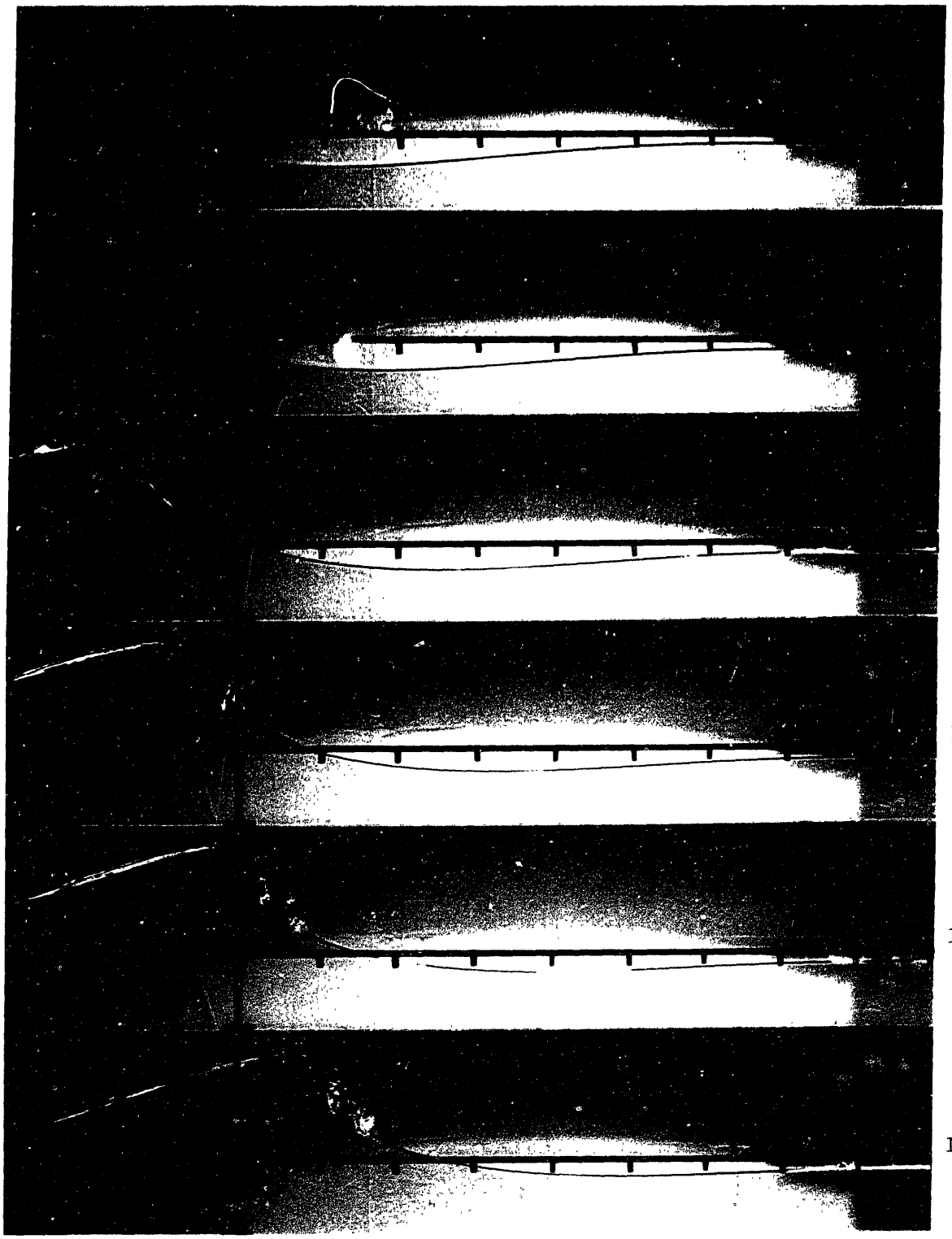

INTENTIONAL DUPLICATE EXPOSURE

Figure 3.1.6b. Photographs of a single plunging wave for f_c=0.88Hz ak_c=0.352, $\Delta f/f_c$=0.73, and $x_b k_c$=27.4. Tick marks are at 10 cm intervals and times at right are referenced from paddle start.

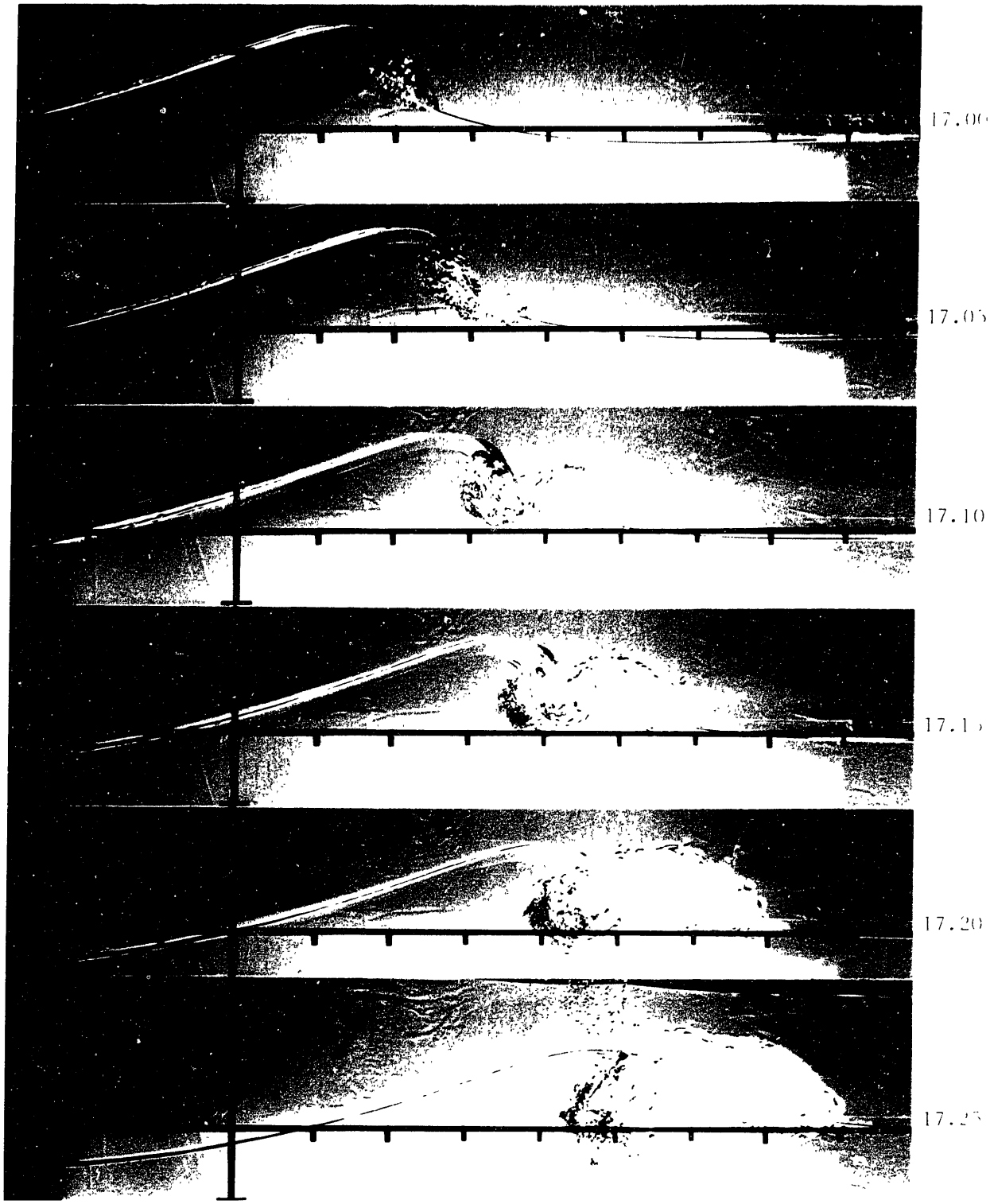
17.00
17.05
17.10
17.15
17.20
17.25

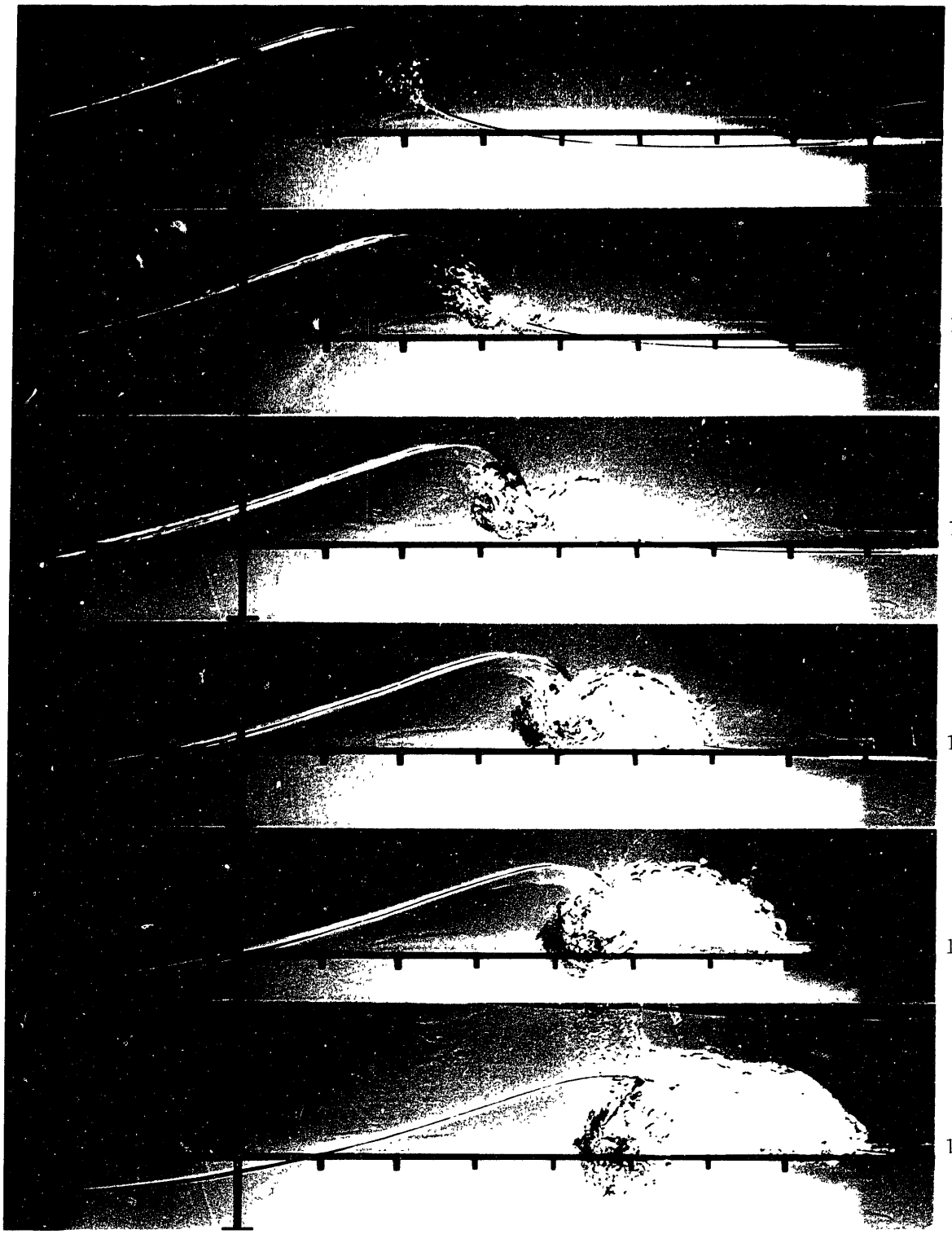

INTENTIONAL DUPLICATE EXPOSURE

Figure 3.1.7. Photographs of a single plunging wave for f_c=0.88Hz ak_c=0.352, $\Delta f/f_c$=0.73, and $x_b k_c$=27.4 showing generation and decay of bubble cloud. Times at right are referenced from paddle startup.

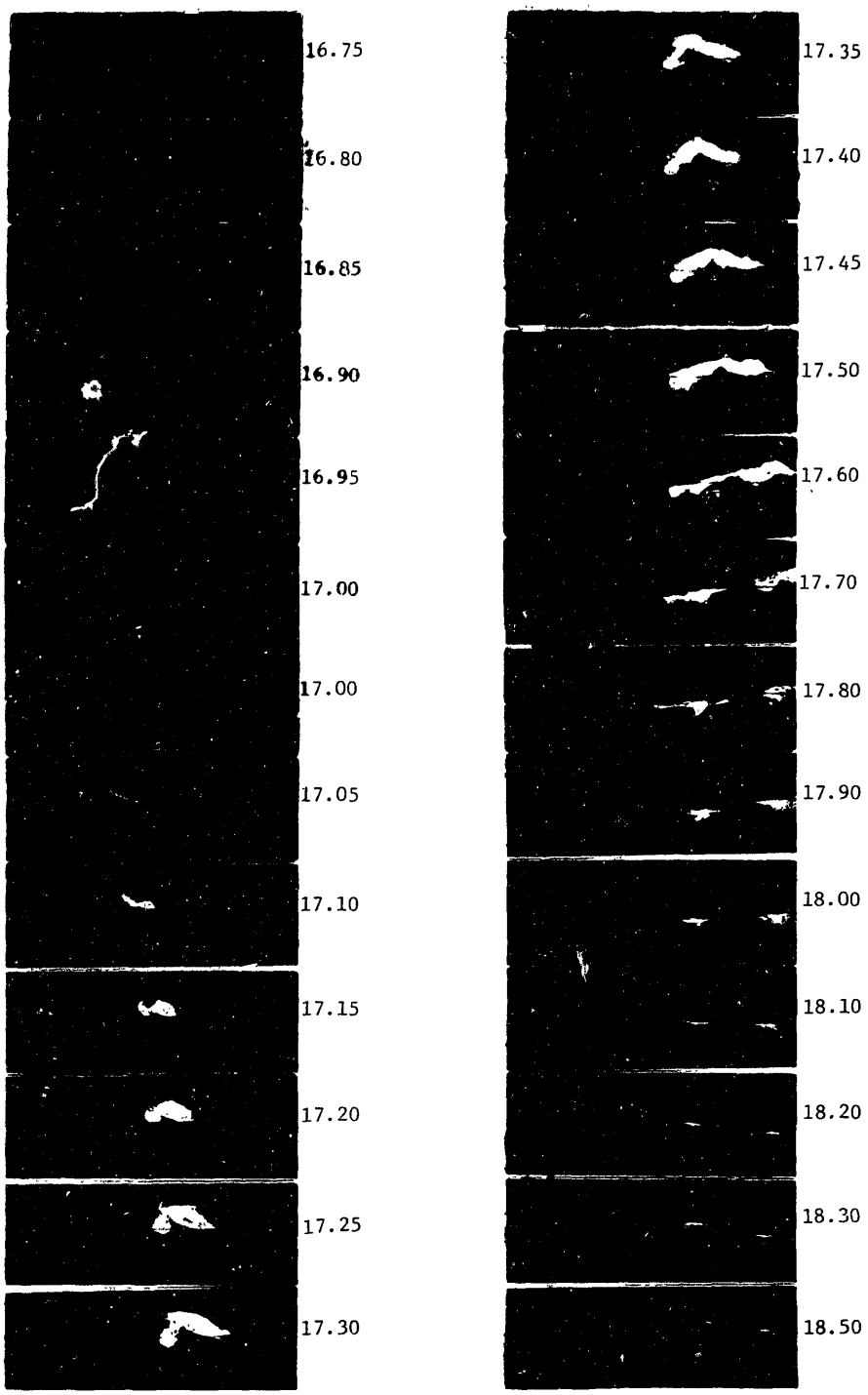
16.75
16.80
16.85
16.90
16.95
17.00
17.00
17.05
17.10
17.15
17.20
17.25
17.30
17.35
17.40
17.45
17.50
17.60
17.70
17.80
17.90
18.00
18.10
18.20
18.30
18.50

with t_b the theoretical time of breaking (20.2 sec in this scale of f_c = 0.88 Hz center frequency). The repeatability of the breaking can be seen in figure 3.1.7 at 17.0 sec which shows two separate runs. We estimate the horizontal variability in the surface displacement to be 1-2 cm between repeats when comparing the same time step. The variability in the time of jet impact on the free surface is 0.01 sec. over 17 seconds from paddle startup.

The large-scale single spilling case of f_c = 0.88Hz ak_c = 0.278, $\Delta f/f_c$ = 0.73, $x_b k_c$ = 27.4 (figure 3.1.5) shows breaking occurring near the predicted location, x_b, but that the breaking process evolves over a distance of almost one wavelength. The wave amplitude, and slope fore and aft, are continuously varying in this unsteady process, making a definition of breaking based on one of these variables ambiguous. The early breaking wave is forward leaning with a steeper front face. Fluid is ejected at the crest, causing bubble generation and air entrainment, although no obvious jet can be observed. Note that breaking occurs first at the walls, leading the center of the wave by less than 0.5 cm. The front slope, locally at the crest, reaches a maximum of 90°, with the horizontal at t = 19.25 sec. The region of entrained air grows forward down the front face of the wave and in depth.

This bubbly region has also been modeled as an accelerating turbulent gravity current (Longuet-Higgins and Turner, 1974). Their model assumes a steady underlying wave with a constant front slope. However, these photographs show the front slope to be decreasing over the breaking process.

The same wave packet, but with the amplitude increased to ak_c = 0.352

resulting in a single plunging wave, is shown in figure 3.1.6. The wave starts breaking one wavelength upstream and two wave periods before the spilling wave. The wave is severely asymetric about the vertical with the front face going past the vertical and a well defined jet being ejected. Again the fluid at the walls leads the center section. The jet encloses a pocket of air and touches down on the forward face shearing up a secondary jet. Two regions of bubbles are generated which are carried down in depth by the next passing wave trough. The evolution of this wave is shown for longer times in figure 3.1.7. Bubbles persist longer than two wave periods after breaking.

The problem of defining a unique breaking time or location is evident from these photographs. For the plunging wave, the location where the wave front becomes vertical to where the jet impacts the free surface is 40 cm or $0.2\,\lambda_c$ (where λ_c is the wavelength computed from the center frequency using the finite depth dispersion relation). The corresponding time of breaking may vary over $0.2\,T_c$, the period of the wave. For the spilling wave the horizontal range is somewhat less but still over 10 cm. To reduce any ambiguity, two points in the breaking process are defined for use in this thesis. For the plunging wave, the time and location where the wave front becomes vertical will be defined as t_{sb}, x_{sb} are defined by t = 19.15 in figure 3.1.5 for the spilling wave and by t = 16.80 in figure 3.1.6. for a plunging wave. A later time in the breaking process that will be referred to in chapter 4 and 5 is the point where significant air entrainment has begun. We call this the time and location of observed breaking t_{ob}, x_{ob}. This corresponds to t = 19.35 see in figure 3.1.5 for the spilling case and t = 17.05 in figure 3.1.6 for plunging. These times and locations are summarized in table 3.1.1.

Table 3.1.1

Definitions of Breaking Times and Locations

f_c = 0.88 Hz	x_b = 8.46 m	t_b = 20.5 s
ak_c = 0.352	x_{sb} = 6.9 m	t_{sb} = 16.80 s
plunge	x_{ob} = 7.3 m	t_{ob} = 17.05 s
f_c = 0.88 Hz	x_b = 8.46 m	t_b = 20.5 s
ak_c = 0.278	x_{sb} = 8.8 m	t_{sb} = 19.15 s
spill	x_{ob} = 9.1 m	t_{ob} = 19.35 s

Refer to figures 3.1.5 and 3.1.6 for wave profiles.

x_b = Theoretical break point or focal point.

x_{sb} = start of breaking defined by profile at

t = 19.15 s figure 3.1.5 spill

t = 16.80 s figure 3.1.6 plunge

x_{ob} = start of significant air entrainment defined by profile at

t = 19.35 figure 3.1.5 spill

t = 17.05 figure 3.1.6 plunge

We call this the time of <u>observed</u> breaking.

Also listed is the theoretical time and location of breaking t_b, x_b that specified in equation 2.3.

These photographs are intended to illustrate the qualitative features of the breaking waves that are analyzed for their loss of momentum flux. This is done in the sections that follow.

3.2 The Excess Momentum Flux Through Breaking

Time histories of the surface displacement, $\eta(t)$, were measured at closely spaced intervals (10-25 cm) along the channel for various wave packets, computed for a range of f_c, $\Delta f/f_c$, $x_b k_c$ and ak_c. A summary of the measurements is given in table 3.2.1. From these measurements, the free surface variance, $\overline{\overline{\eta^2}}$, was computed at each x location by removing the mean and integrating over a period long compared with the packet. This time was typically 40 or 80 seconds. (Program STAT7 in Appendix 3 was used). The computed quantity is defined as:

$$\overline{\overline{\eta^2}} = \int_{t_1}^{t_2} \overline{\eta^2}\, dt = \int_{t_1}^{t_2} \eta^2\, dt \,. \tag{3.1}$$

As was shown in section 2.3, the variance of the free surface displacement defined in this way is approximately proportional to the time integrated excess momentum flux due to the carrier waves crossing this x location. Given by,

$$\int_{t_1}^{t_2} S\, dt = \int_{t_1}^{t_2} \frac{\rho g \overline{\eta^2}}{2} \left[1 + \frac{2kd}{\sinh 2kd}\right] dt + 0\,(\epsilon)^4 \tag{3.2}$$

Table 3.2.1

Measurements of $\eta(x)$ vs x

f_c =	0.88 Hz	1.08 Hz	1.28 Hz
	$\frac{\Delta f}{f_c}$ = 0.73	xk_c = 27.4	
ak =	0.250	0.256	0.264
	0.278	0.296	0.319
	0.352	0.388	0.420
		0.48	
	$\frac{\Delta f}{f_c}$ = 0.5, 1.0	$x_b k_c$ = 27.4	
ak =		0.15	
		0.3	
		0.45	
	$\frac{\Delta f}{f_c}$ = 0.73	$x_b k_c$ = 47.1	
ak =		0.3	
	$\frac{\Delta f}{f_c}$ = 0.73	$x_b k_c$ = 66.0	
ak =		0.15	
		0.3	

Additional terms, proportional to the envelope steepness, $\left|\frac{\partial A}{\partial x}\right|^2$ and the carrier wave steepness, $|A|^4$ where $|A|^2 = \overline{\eta^2}/2$ give higher order corrections to this estimate of the excess momentum flux. Also in shallow depth, the forced wave velocity term $\rho \bar{g} u^2 d$ may be significant. The 4th order term proportional to $\frac{\partial |A|^2}{\partial x}$ will be zero when the integration over the packet

As the focal point is approached where the carrier waves and envelope steepen, these errors increase.

The interpretation of $\overline{\eta^2}$ as being proportional to the energy flux may also cause errors near the energy focal point. The energy flux is given to 2nd order by

$$F = \bar{E}\, C_g$$

where $\bar{E} = \rho g \overline{\eta^2}$ is the local energy density at a particular x. Strictly, this is twice the <u>potential</u> energy flux and we assume kinetic and potential energy are equipartitioned. The energy flux may also be written

$$F = \left[\bar{E}_{\text{kinetic}} + \bar{E}_{\text{potential}}\right] C_g$$

In normalizing the energy flux by dividing by its value at an upstream reference station, two sources of error may result in setting

$$\frac{F}{F_0} = \frac{\overline{\eta^2}}{\overline{\eta_0^2}}.$$

If C_g is not constant in x, $\frac{Cg}{Cg_0}$ may not equal 1. Also, if the energy is not equipartitioned then E will be in error. Some of these errors will be estimated based on the measured data.

3.2.1 Variation in Packet Amplitude, ak_c

Figure 3.2.1(a) shows the variance computed by eq. (3.1) vs. distance from the energy focal point or predicted breakpoint for a packet of f_c = 1.08 Hz, $\Delta f/f_c$ = 0.73 and $x_b k_c$ = 27.4 for three values of ak_c. In this case these amplitudes correspond to an incipient or near breaking packet (ak_c = 0.256), a single spill (ak_c = 0.296) and a single plunging wave (ak_c = 0.388). The variance is normalized by the variance at the upstream reference station approximately three wavelengths from breaking. The x-axis is normalized by k_c.

Three distinct regions are evident. Upstream of the focal point, the variance decays almost linearly with x and at the same rate for all three values of ak_c. Viscous dissipation in the channel sidewall and bottom boundary layers is responsible for approximately one-half of this decay shown by the broken line (see Appendix 2). In the momentum flux interpretation, this is the loss due to the time integrated shear stress at the boundaries. Since no other losses are expected in this region, it is believed that the additional decay is due to errors in using $\overline{\eta^2}$ as estimates of S and F. At the upstream reference station, the packet contains roughly six waves making the envelope steepness of order 1/6 ε. Then the error is

$$\frac{\left|\frac{\partial A}{\partial x}\right|^2}{k_c^2 \left|A\right|^2} = \approx 0.02\text{-}0.03.$$

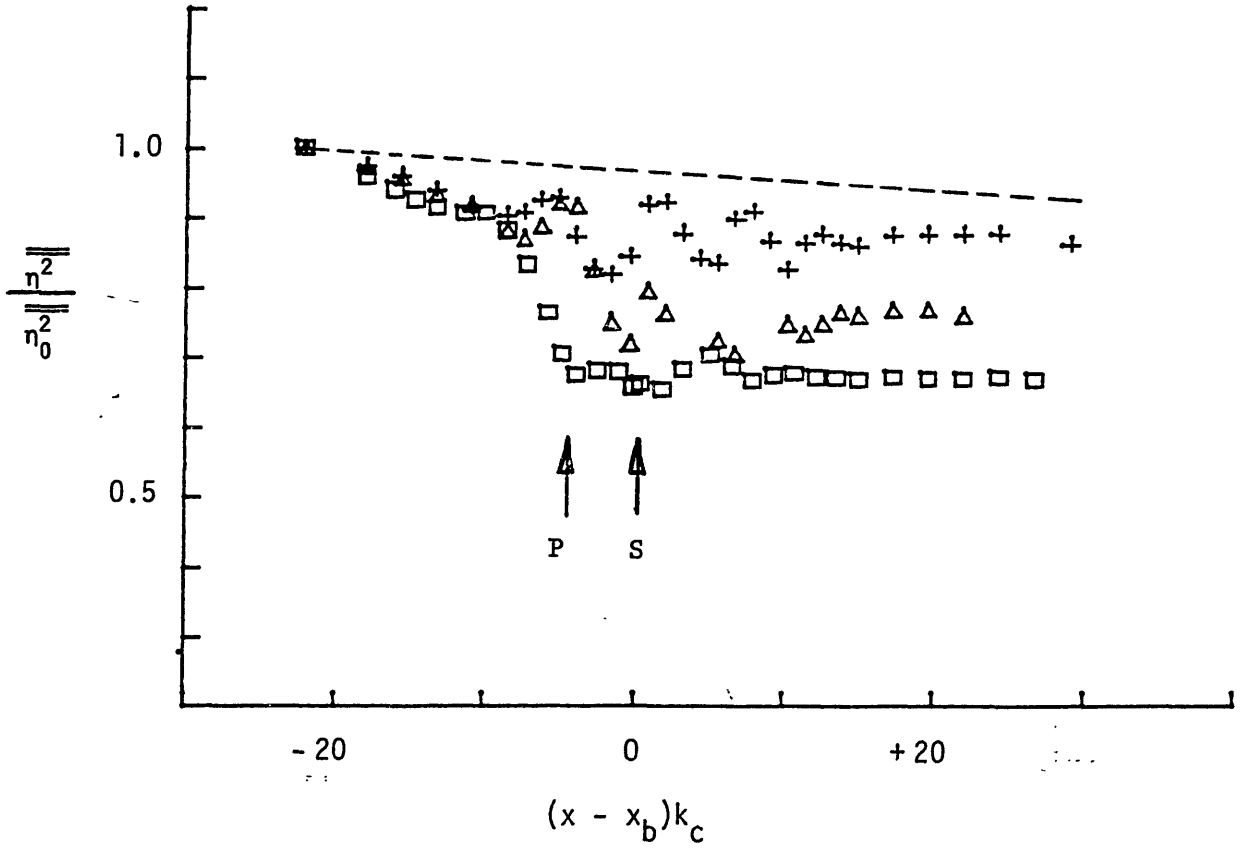

Figure 3.2.1a Measurements of normalized surface displacement variance vs. distance from x_b ($x_b \equiv$ linear prediction of breakpoint or focal point). Wave packet variables are f_c = 1.08 Hz, $\Delta f/f_c$ = 0.73, $x_b k_c$ = 27.4. Incipient breaking ak = 0.256 (+), single spill, ak = 0.296 (△), single plunge, ak = 0.388 (□). P and S mark start of breaking, x_{sb} for plunge and spill (table 3.1.1). Broken line is theoretical dissipation due to tank size walls and bottom (Appendix 2).

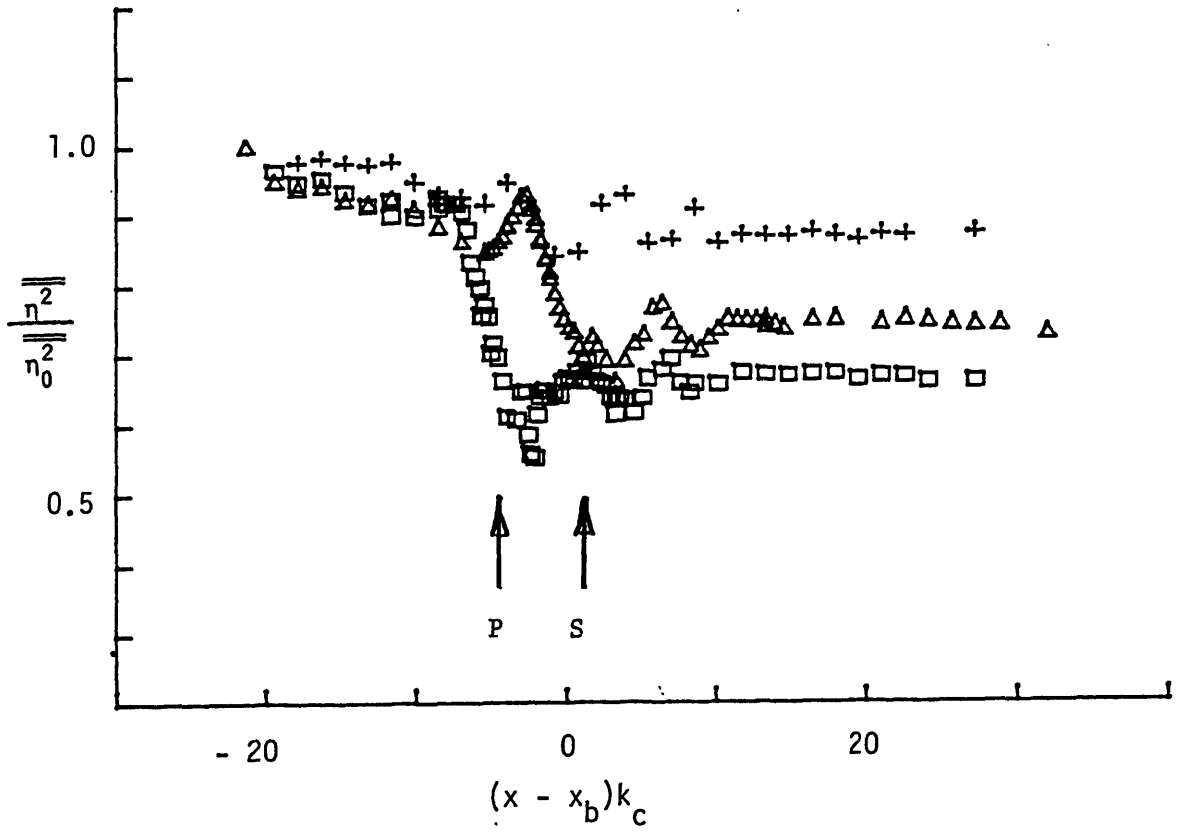

Figure 3.2.1b As for figure 3.4.1a, except f_c = 0.88 Hz, incipient breaking (+), single spill (△), single plunge (□).

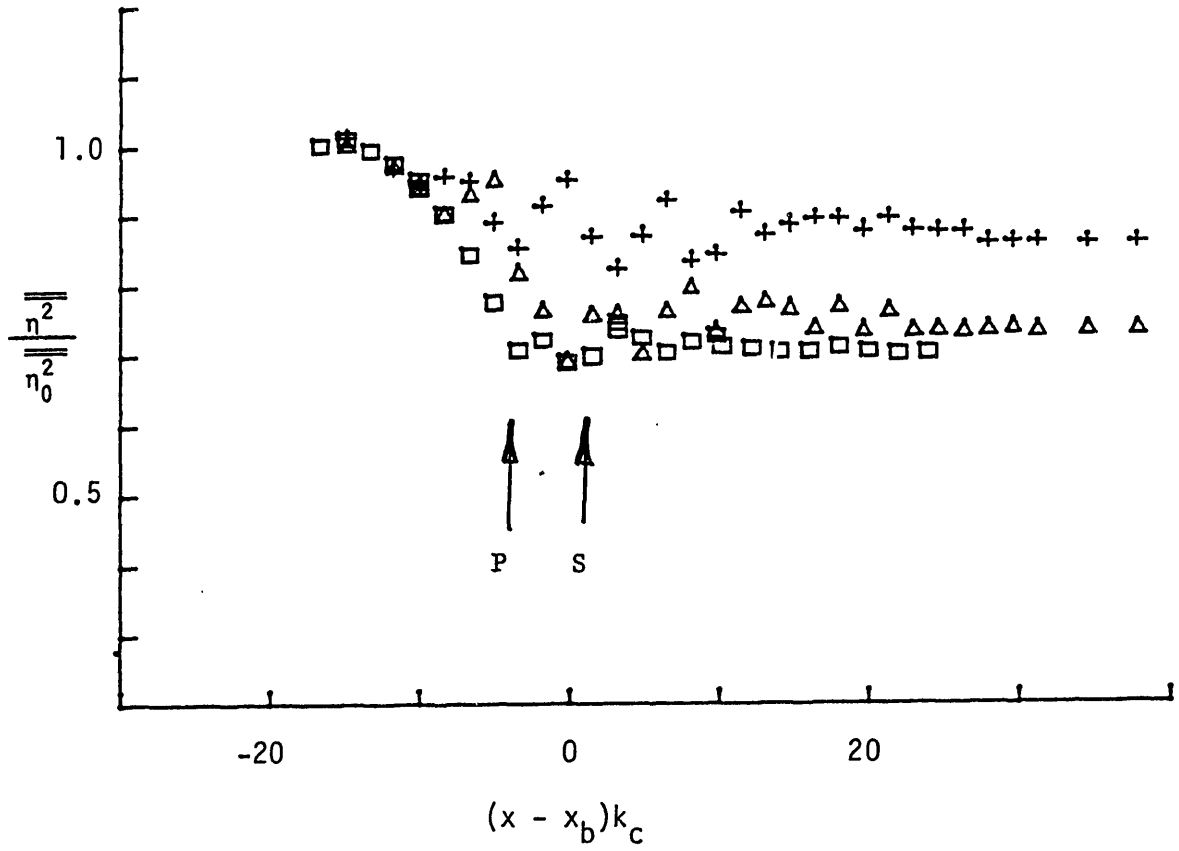

Figure 3.2.1c As for figure 3.4.1a except f_c = 1.28 Hz, incipient breaking, ak = 0.264 (+); single spill, ak = 0.319 (△); single plunge, ak = 0.420 (□).

The steepness of the carrier waves at this location is of maximum ak = 0.25. So the carrier wave steepness error is $\frac{|A|^4}{|A|^2} = \varepsilon^2 \approx 0.06$. The contribution to the forced wave velocity was estimated from mean velocity measurements in Chapter 5, and found to be $u = -.02\ C$, causing the error of $\frac{\rho \overline{u^2} d}{\rho \frac{1}{2}|A|^2} = 0.02 - 0.03$. These errors increase as the focal point is approached and are of the correct magnitude to account for the discrepancy in the slope of $\overline{\eta^2}$ with x.

From an energy flux viewpoint, the discrepancy may be explained by the failure of the surface displacement variance to account for the kinetic energy where equipartitioning is violated as the waves steepen. More energy may be expected to be in the velocity in this case.

As breaking is approached, the incipient breaking case shows oscillations in the variance of magnitude 0.10 $\overline{\eta_0^2}$ occurring at intervals equal to one carrier wave length. Since the measured setup of the mean water level is negligible, the true momentum flux and energy flux should follow the broken line in figure 3.2.1(a), meaning that again the discrepancy is due to the errors in the estimate. Plots of η vs. time show that these oscillations are correlated with the phase of the carrier wave in relation to the envelope. (figure 3.2.2). A minimum in the variance corresponds to the plot in figure (a) where the carrier wave is at the peak of the envelope and very steep. The maximum corresponds to figure (b) where the carrier waves are less steep. The difference in the carrier wave steepness error terms between waves in figures (a) and (b) is

$$\varepsilon_a^2 - \varepsilon_b^2 = 0.4^2 - 0.3^2 = 0.07$$

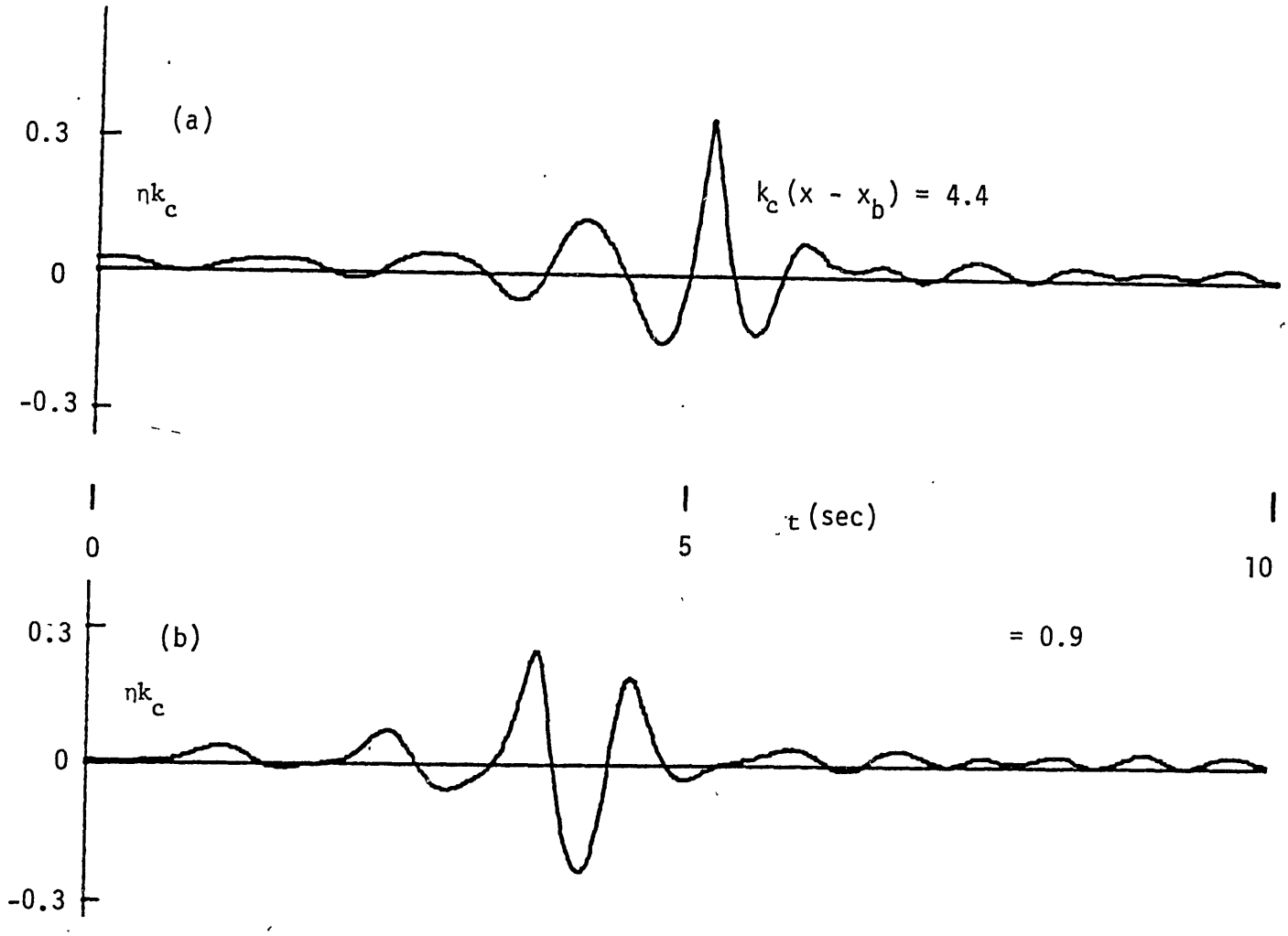

Figure 3.2.2 Wave packet time history corresponding to local maximum (bottom) and minimum (top) of $\overline{\eta^2}$ vs. x curve figure 3.2.1a. f_c = 1.08 Hz, ak_c = 0.256 incipient breaking.

The envelope steepness may also oscillate in this manner with comparable errors which again leads to errors of the magnitude observed in the data. From an energy flux viewpoint it may be expected that the ratio of kinetic to potential energy is greater in the steeper wave of figure (a) than in figure (b) which will explain the oscillation. Also the group velocity C_g may vary throughout the envelope. The above discussion is intended to give possible explanations, and is not meant as a complete verification of these features.

The variance of the two breaking wave cases, spilling and plunging, begins a steep drop approximately one-half wavelength upstream of the location where breaking starts, x_{sb}. This is where the front face of the plunging wave is vertical (Figure 3.1.6, t = 16.8 sec) and for the spilling wave it corresponds to t = 19.15 sec in figure 3.1.5. This drop in the variance, upstream of where any total energy dissipation due to breaking is expected, further supports the fact that potential energy is going into the velocity just at breaking as the wave steepens. In the breaking waves, however, energy and momentum flux is lost from the carrier waves so the variance does not recover up to the non-breaking value. The oscillations are still present downstream for a few wavelengths. The gradient of the loss appears to be equal for all three cases, $\approx$ 25% per wavelength; however, the drop persists over a longer distance for spilling and an even longer distance for plunging (about 1 wavelength), resulting in lower downstream levels of the variance. At the start of breaking location, x_{sb}, and for approximately one wavelength downstream, where the fluid is entrained with air, the gauges may not be expected to give reliable measurements. However, the scatter in the data is small, so this

does not appear to be a large problem.

Downstream of breaking, the packet disperses and the waves again become more linear, the oscillations have died out leaving an almost constant level of potential energy with x. The difference in these levels from the nonbreaking packet may be attributed completely to wave breaking. The results of similar measurements for two other scales of waves or center frequencies f_c = 0.88 Hz and f_c = 1.28 Hz (figures 3.2.1(b), (c)) show good agreement between scales using the wavenumber of the center frequency to scale x. Notice the good agreement between scales in the location where the variance steeply drops. The agreement is seen more clearly in figure 3.2.3 where the three scales are plotted together for each level of breaking. The downstream levels of the surface displacement variance also show good agreement between scales. Note, however, that these results compare packets where the breaking was incipient, a single spill, and a single plunge; and there is a small deviation between scales in the values of ak that correspond to these qualitative classifications (see figure 3.2.3)

3.2.2 Variation in Packet Bandwidth, $\Delta f/f_c$

Similar measurements were made of wave packets computed with two other bandwidths and are shown in figure 3.2.4. The three values of wave amplitude ak_c in these runs do not necessarily correspond to single breaking events. The non-breaking packet of ak_c = 0.15 is well below the incipient breaking case and its decay is in agreement with the predicted viscous loss (Appendix 2) in the channel boundary layers (see also figure 3.2.7). Small oscillations in the variance are still present for this

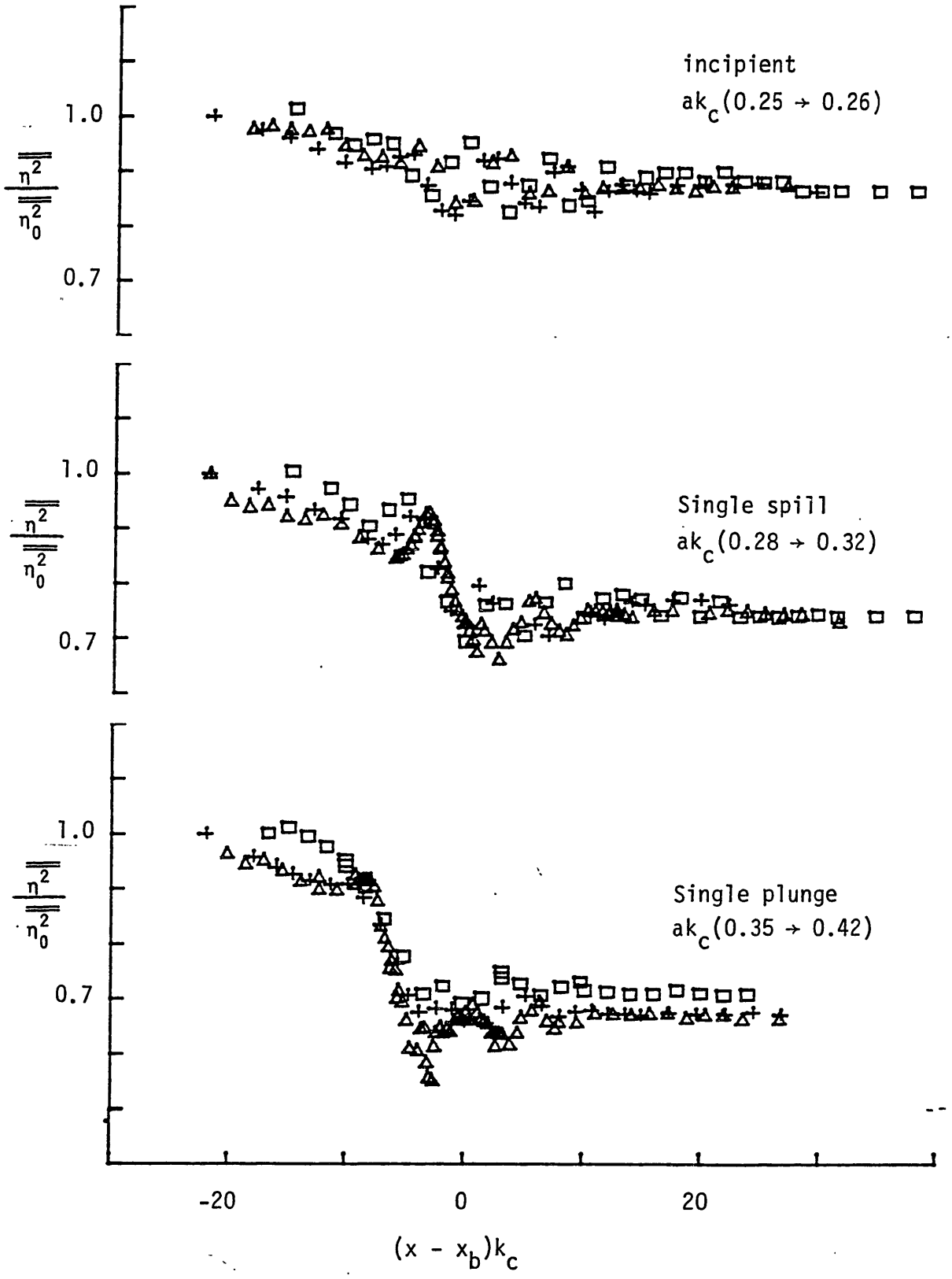

Figure 3.2.3 Surface displacement variance vs. distance from breaking, x_b. A comparison between scales or packet center frequencies. f_c = 1.28 Hz (□), 1.08 Hz (+), 0.88 Hz (△). For $\Delta f/f_c = 0.73$, $x_b x_c = 27.4$.

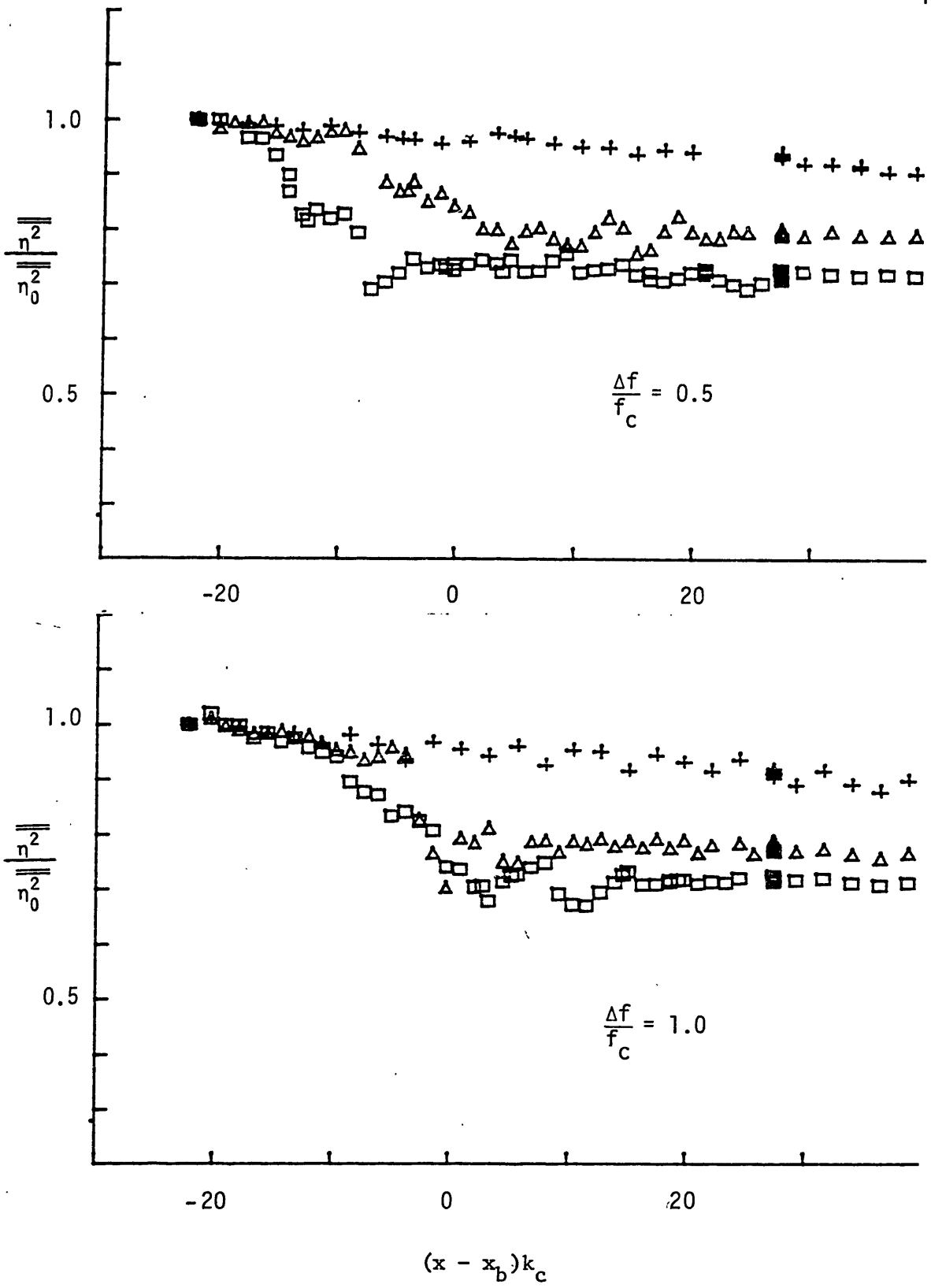

Figure 3.2.4. Surface displacement variance vs. distance from breaking, x_b, for variations in packet bandwidth; top: $\Delta f/f_c = 0.5$; bottom: $\Delta f/f_c = 1.0$. In both, $ak_c = 0.15$ (+), 0.30 (Δ), 0.45 ($\square$), $f_c = 1.08$ Hz, $\Delta f/f_c = 27.4$. The random error between runs is equal to the spread at $k_c(x-x_b) = 28$.

relatively low amplitude packet. In the narrower band case, $\Delta f/f_c = 0.5$, breaking was observed well upstream of the predicted location as is evident by the drop in the variance at $k_c(x - x_b) \approx -18$. Also the intermediate level of ak_c shows a gradual drop in the variance over several wavelengths which corresponds to several gently spilling waves. In this case, the packet is longer and has an envelope steepness less than the previous case at $\Delta f/f_c = 0.73$. The higher bandwidth packet of $\Delta f/f_c = 1.0$ results in a single breaking wave close to the predicted location for $ak_c = 0.3$. This is seen as a steep drop in the variance. The $ak_c = 0.45$ case results in breaking over several wavelengths.

Figure 3.2.5 shows that despite these different local loss rates (i.e.,one vigorous breaking, or three gently breaking waves) the downstream level of the variance is still very well correlated with ak_c. It is possible then, to treat the breaking regions as a "black box" and measure input and output variance to establish the loss due to the breaking packet. The fact that the packet breaks more than once is not important in this type of analysis.

3.2.3 Variations in Breaking Location, $x_b k_c$

The effect of varying the nondimensional breaking location, $x_b k_c$, was found to be small. The case of $ak_c = 0.3$ is shown in figure 3.2.6. The input and output levels of the variance show essentially no change as $x_b k_c$ is varied from 27.4 to 66.0. As the breaking was moved farther from the paddle, however, it became more difficult to obtain a single breaking wave and the loss was spread over several wavelengths, as indicated by the

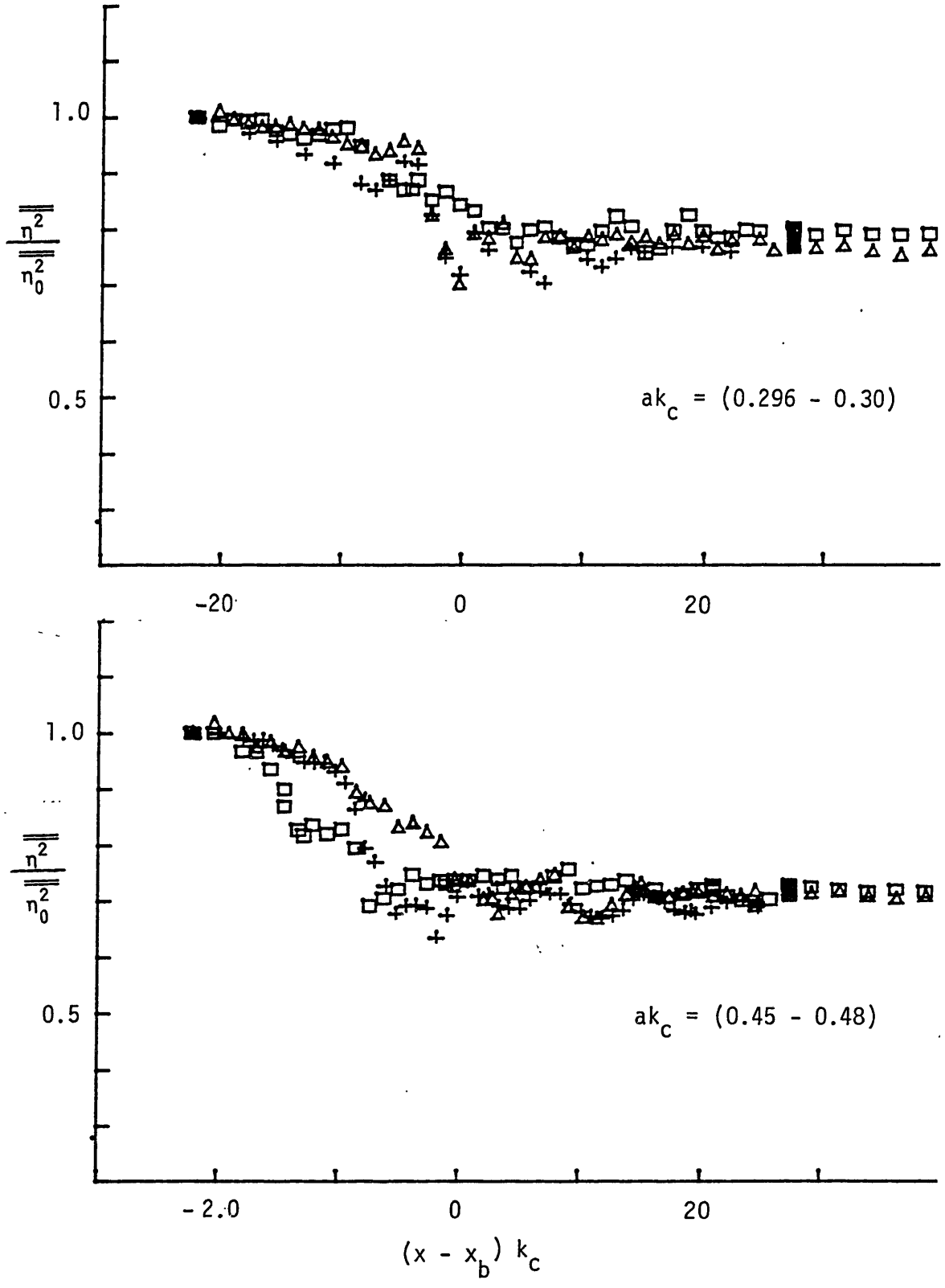

Figure 3.2.5. Surface displacement variance vs. distance from breaking, x_b. A comparison between packet bandwidths for two wave amplitudes. $\Delta f/f_c$ = 0.5 (□), 0.73 (+) 1.01 (△), and f_c = 1.08 Hz, $\Delta f/f_c$ = 27.4.

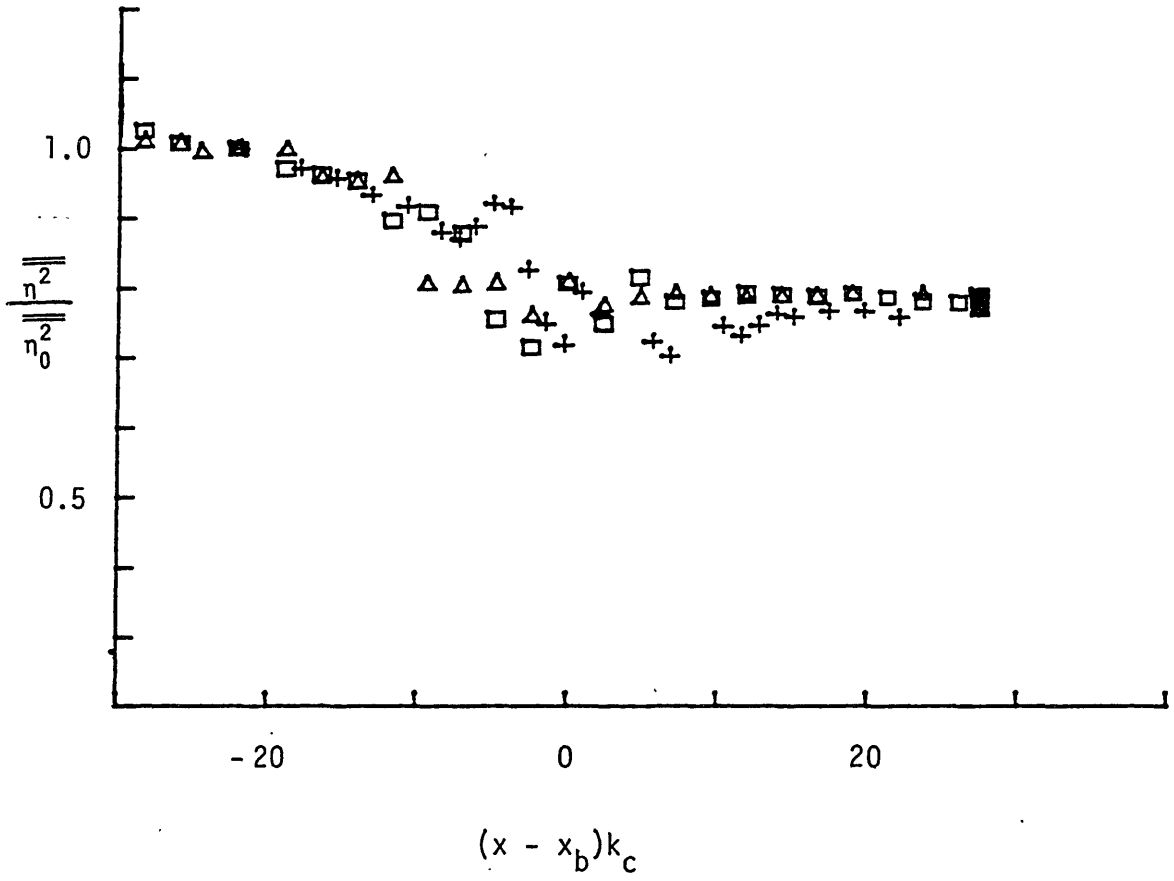

Figure 3.2.6 Surface displacement variance vs. distance from breaking, x_b, for variations in breaking location, $x_b k_c$ = 27.4 (+), 47.1 (△), 66.0 (□); f_c= 1.08, ak_c = 0.03, $\Delta f/f_c$ = 0.73.

shallower slope of the variance in the figure. This can be attributed to phase mismatch between components as the focal point is moved farther from the paddle. Finite depth dispersion effects and nonlinear amplitude dispersion causes this.

The decay in the variance due to the channel sidewalls and bottom is shown in figure 3.2.7 for three wave packets of $ak_c = 0.15$, all below incipient breaking and where linear theory should give good predictions of decay. The comparisons are between packets of different breaking locations bandwidths. The agreement between the three is good with a decay of between 6% and 8% of the variance over about eight center wavelengths. The theoretical prediction of this decay, due to Hunt (1952) and Mei & Lui (1973), (Appendix 2) which results from the viscous decay in the channel sidewall and bottom boundary layers is shown by the broken line. This prediction is slightly less, about 5% - 6% over eight wavelengths, but gives reasonable agreement with the measurements. The theoretical estimate is based on linear wave theory and a wave train periodic in time. Our measurements are made on a finite length packet which may account for some of the difference; nonlinearity and possibly surface tension effects may also be responsible.

3.3 Loss of Excess Momentum Flux and Energy Flux Due to Breaking

At locations greater than three wavelengths from the theoretical break point, x_b, the error in using the surface displacement variance in estimating the momentum flux was shown to be ≈ 5% (section 3.2). In addition, it is expected that the group velocity C_g is the same for the packet far upstream and downstream, so the normalization used in the

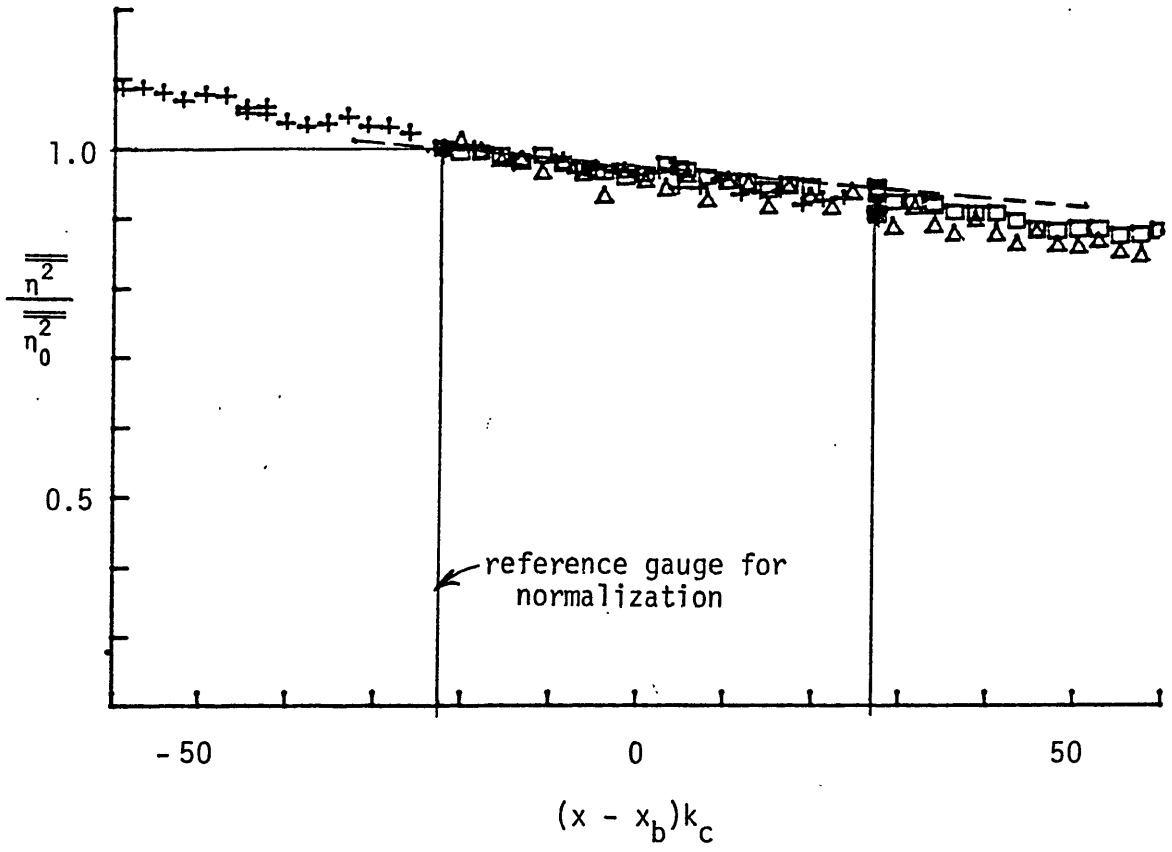

Figure 3.2.7 Surface displacement variance vs. distance from the theoretical break point, x_b, for non-breaking wave packets, $ak_c = 0.15$. Comparison is between $\Delta f/f_c$ = 0.5 (□), 1.0 (△), for $x_b k_c = 27.4$ (+) and $\Delta f/fc$ = 0.73 for $x_b k_c = 66$ (+). All $f_c = 1.08$ Hz. Broken line is theoretical estimate of tank sidewall dissipation. (Appendix 2.)

previous plots will cancel this multiplier in the energy flux equation. With these assumptions and the relatively small errors in mind, the normalized surface displacement variance at these reference stations away from breaking, will be used as a measure of the excess momentum flux. The loss of excess momentum flux will be defined as the difference between the upstream and downstream levels where the momentum flux is nearly constant in x. Viscous decay due to boundary layers can be subtracted out by referencing the incipient breaking case as the zero level.

A similar argument can be made in interpreting the previous plots as the normalized loss of energy flux due to the carrier waves.

A plot of these losses vs. the wave packet amplitude, ak_c, is shown in figure 3.3.1 for the three scales of wave packets. The loss is normalized by the measured variance at the upstream location. At amplitudes less than $ak_c = 0.25$ the loss is due completely to boundary layer dissipation and is in agreement with theory (6 - 8% loss over eight wavelengths). At the critical value of $ak \approx 0.25$, the curve shows a sharp rise, which coincides with the value of ak_c where incipient breaking was observed to occur. Once this transition to breaking is passed, a relatively small increase in amplitude results in energetic breaking up to strong spilling with losses varying from 0 to 20% referenced from the nonbreaking case. Beyond this point, $ak_c \approx 0.3$ a larger increase in ak_c is required to obtain a plunging breaking wave but results in an additional momentum flux loss of only 5 to 10%. The agreement between all three scales is good up to spilling and remains good between the two smaller scales $f_c = 1.08$ Hz and $f = 1.28$ Hz packets beyond. The larger loss at the large scale, $f_c = 0.88$ Hz for high values of ak_c, cannot be

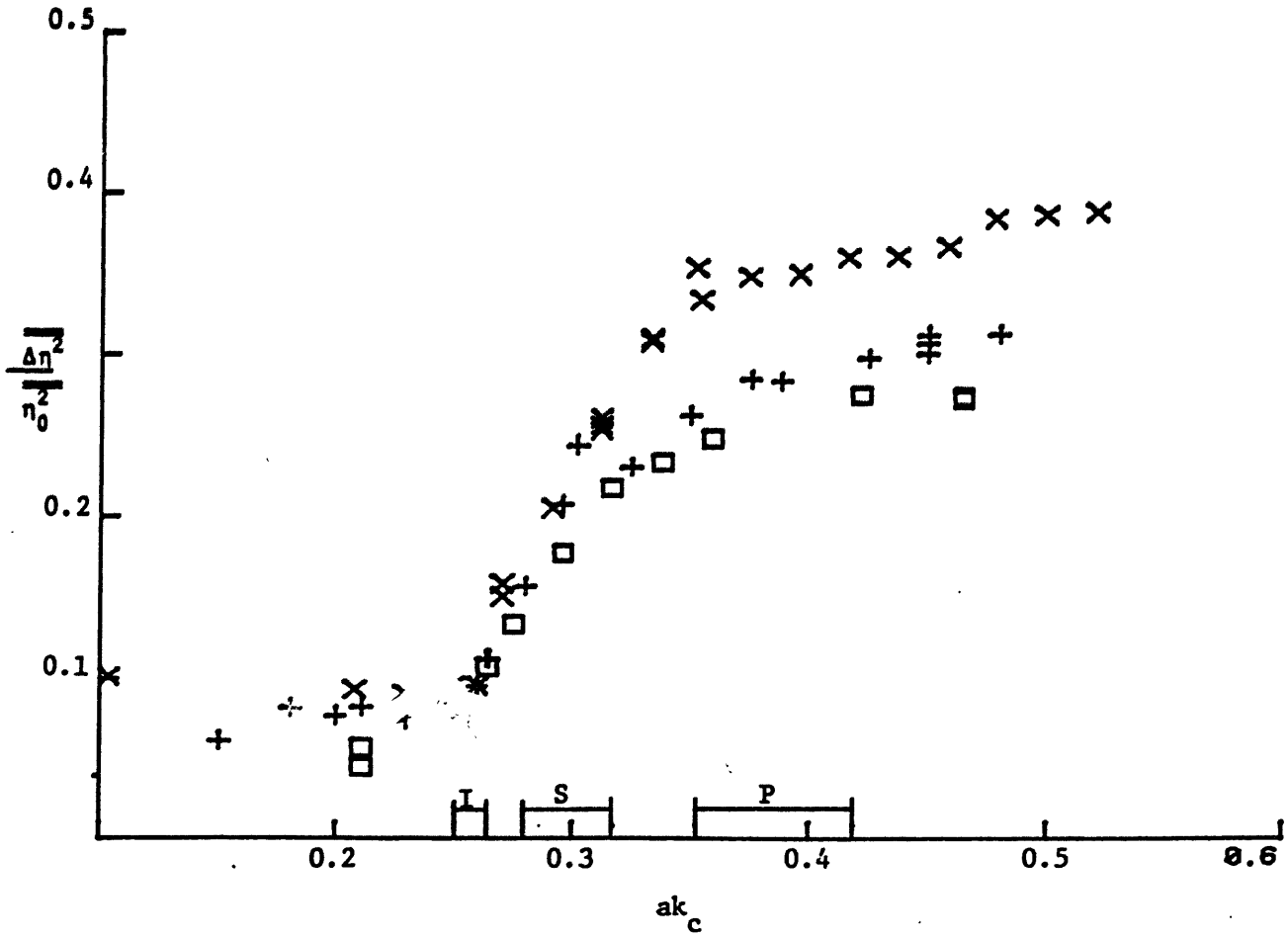

Figure 3.3.1 Loss of excess momentum flux as a function of the wave packet amplitude for three packet center frequencies f_c = 0.88 Hz (x), 1.08(+), 1.28 (□) and $\Delta f/f_c$ = 0.73, $x_b k_c$ = 27.4. Occurrence of incipient breaking, single spilling, and plunging are marked by I, S, P with variations between scales shown by horizontal bars.

explained. It was observed, however, that the plunging jet impinging on on the free surface caused a secondary sheet of fluid to be ejected. This continued in a cascading effect. The nondimensional horizontal extent of this process is greater at the largest scale, leading to the hypothesis that surface tension and the amount of air entrainment does not scale with the wave center frequencies. These factors may affect the total loss; however, larger scale experiments are needed to resolve this discrepancy.

Variation in the packet bandwidth does not appear to strongly affect theoverall loss of excess momentum flux, as can be seen in figure 3.3.2. This fact was also evident in the results of the previous section. The exception to this is noticed at amplitudes near the inception of breaking. The curve corresponding to $ak_c = 0.257$ varies by 10% over the range of packet bandwidths. This value of ak_c corresponds to incipient breaking for $\Delta f/f_c = 0.73$ where the curve is a minimum; however, it was observed that breaking was already occurring at higher and lower values of bandwidth resulting in these larger losses. This result points out two things: first that breaking <u>inception</u> is sensitive to changes in $\Delta f/f_c$ and also that small changes in ak_c quickly lead to losses of up to 10% of the initial momentum flux in the packet. Once ak_c is increased to 0.3, the bandwidth has little effect on the overall loss, however.
The slight bump in the loss for $ak_c = 0.388$ around $\Delta f/f_c = 0.7$ indicates a slight "tuning" effect in the breaking. This corresponds to a single plunging event whereas multiple breaking waves were observed at higher and lower values of $\Delta f/f_c$.

The weak dependence on $\Delta f/f_c$ can also be seen in figure 3.3.3 where the momentum flux loss is plotted against ak_c for five values of $\Delta f/f_c$.

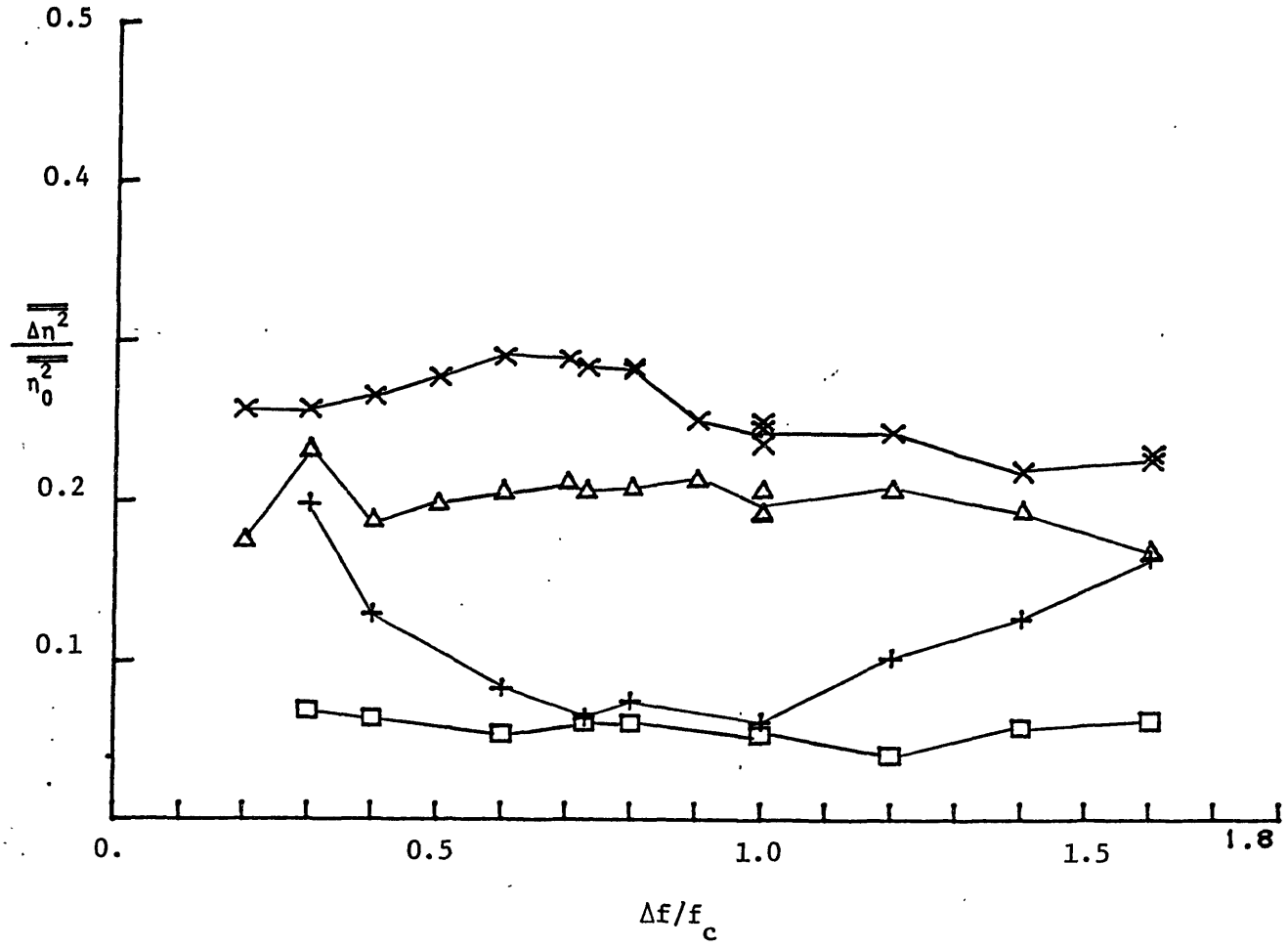

Figure 3.3.2 Loss of excess momentum flux vs. the wave packet bandwidth $\Delta f/f_c$ for four input wave amplitudes, ak_c = 0.151 (□), 0.257 (+), 0.296 (△), 0.388 (×) and f_c = 1.08. These correspond to a nonbreaking packet, incipient breaking, a single spill, and a single plunging wave, respectively, for f_c = 1.08, $x_b k_c$ = 27.4 and $\Delta f/f_c$ = 0.73.

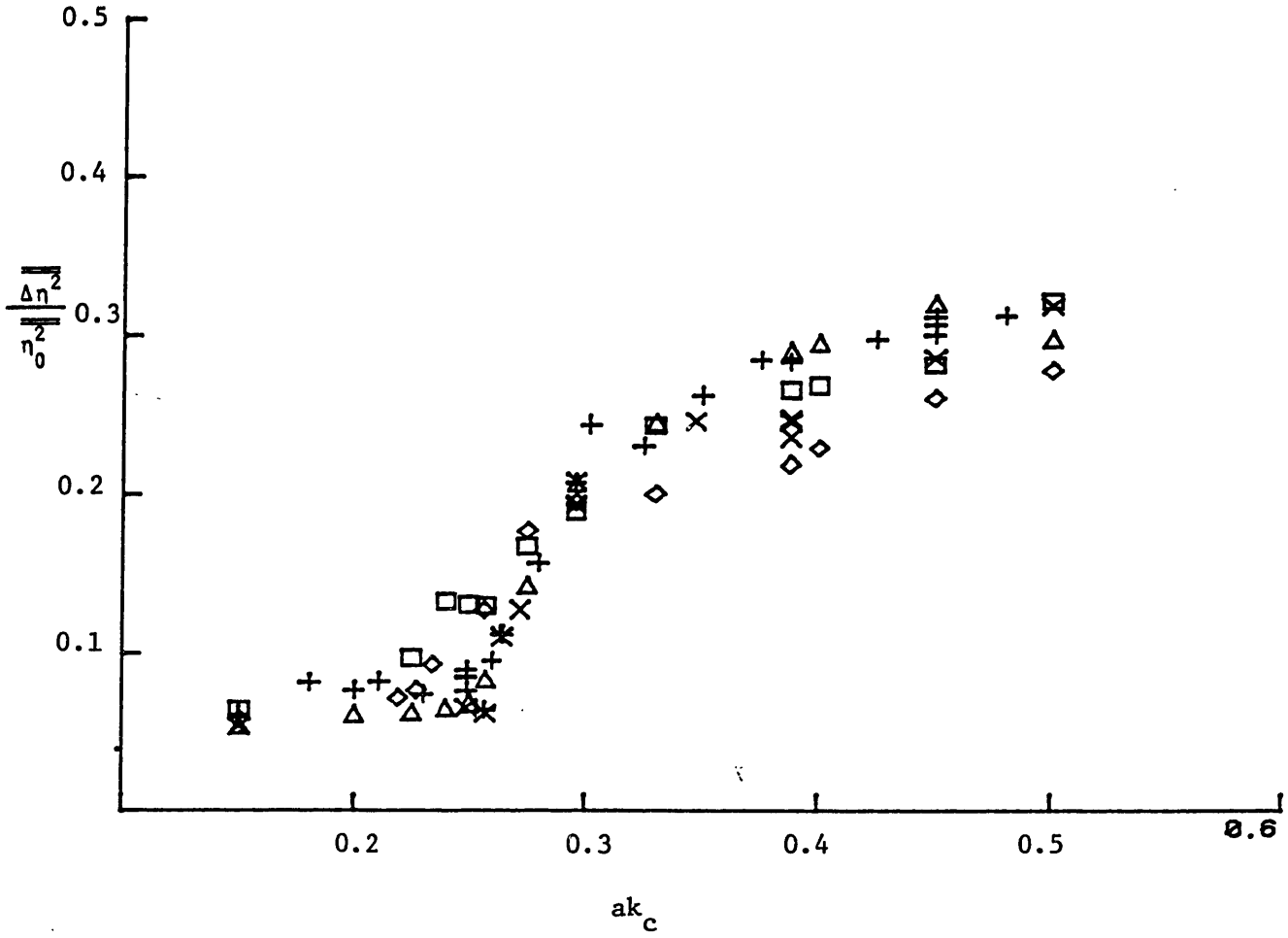

Figure 3.3.3 Loss of excess momentum flux vs. ak_c for five packet bandwidths, $\Delta f/f_c$ = 0.4 (□), 0.6 (△), 0.73 (+), 1.0 (×), 1.4 (◇). Also, f_c= 1.08 Hz, $x_b k_c$ = 27.4

The shapes of the curves are all very similar. However, the sharp break in the curve at breaking inception ak ≈ 0.25 is smoothed out as $\Delta f/f_c$ is increased or decreased from 0.7 and breaking inception was observed to occur at lower values of ak_c . All curves cross at ak = 0.3 with the highest and lowest bandwidths falling below at higher amplitudes. At the high and low bandwidths, the curve approaches a straight line.

Similar plots are shown for measurements made of wave packets where the theoretical energy focal point x_b was varied (figures 3.3.4 and 3.3.5). These results show that the loss of excess momentum flux is also rather insensitive to changes in this parameter, $x_b k_c$, at wave amplitudes up to $ak_c = 0.3$. Where x_b is not too far from the paddle, the agreement at higher values of ak_c is also good. As the breaking location is moved farther downstream, the energy focusing does not appear as good and the loss falls off as is shown in figure 3.3.5 for $x_b k_c = 66.0$. The larger propagation length could allow amplitude dispersion and certainly allows the finite depth dispersion to cause phase mismatch at this downstream location since the starting phases were computed assuming deep water. The curve of the momentum flux loss vs. ak_c is seen to retain its shape; even the agreement in the point of breaking inception is good.

3.4 Locally Measured Wave Amplitude and Steepness at Breaking

Given the nondimensional parameters that specify a particular wave packet prior to breaking, it is of interest to know the geometry of the resultant wave at breaking and if these local parameters can be used to parameterize the breaking intensity or the momentum flux loss. From observation there is a strong correlation between the type and strength of

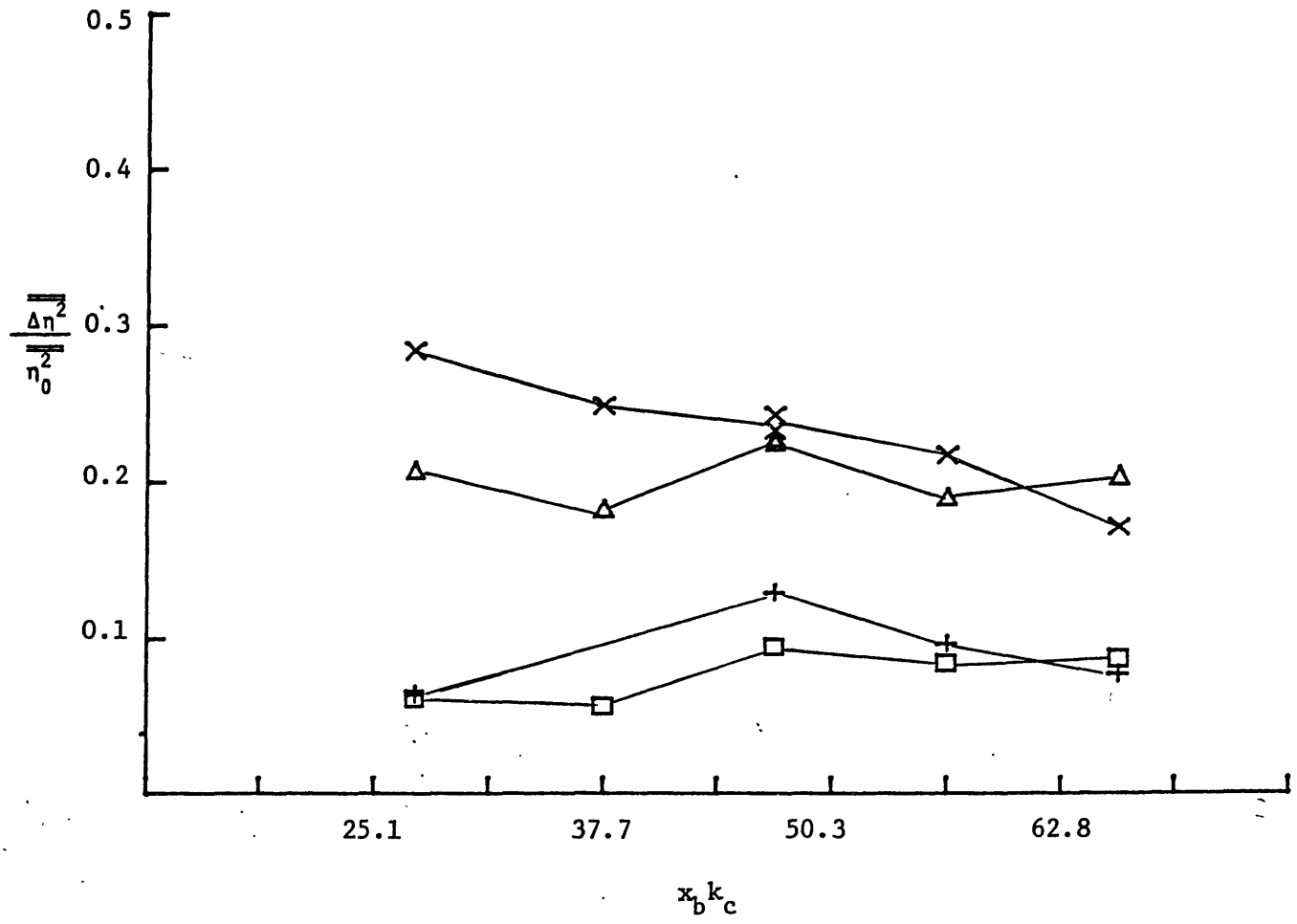

Figure 3.3.4 Loss of excess momentum flux as a function of the theoretical breaking location $x_b k_c$ for four values of wave amplitude ak_c = 0.151 (□), 0.257 (+), 0.296 (△), 0.338 (×). f_c = 1.08 Hz, $\Delta f/f_c$ = 0.73.

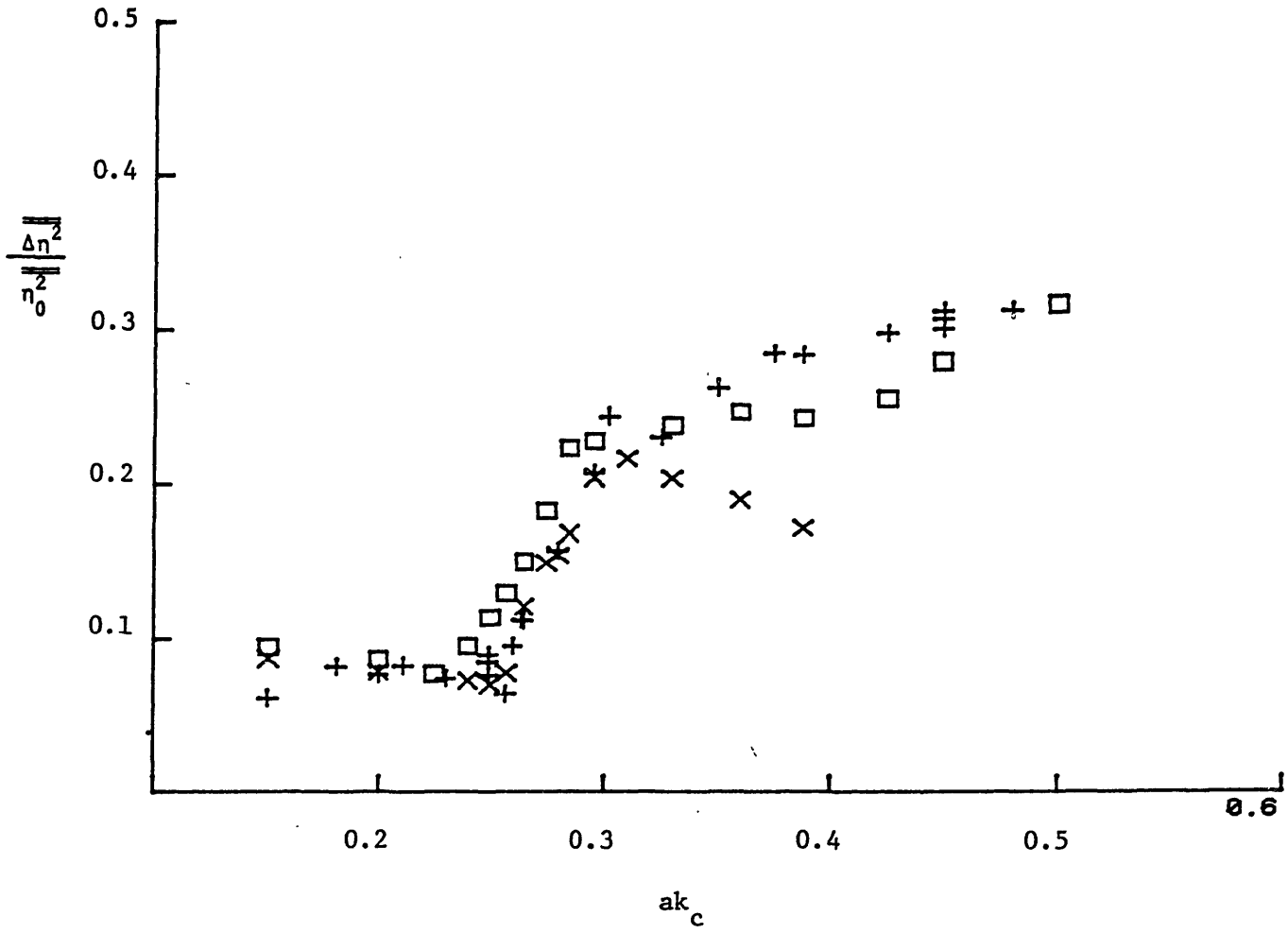

Figure 3.3.5 Loss of excess momentum flux vs. ak_c for three predicted breaking locations, $x_b k_c$ = 27.4 (+), 47.1 (□), 66.0 (×). f_c = 1.08 Hz, $\Delta f/f_c$ = 0.73.

breaking (i.e., incipient breaking, spilling, plunging) and its normalized momentum flux loss. With practice, one could almost predict the momentum flux loss from visual observation alone. The goal, then, is to quantify what is observed locally.

Measurements of the local spatial parameters at breaking were made from 16 mm films taken of the wave at breaking. The movie camera (Bolex H16 REX) was run at 64 frames/sec. In addition, wave gauges were located at closely spaced intervals (12.5 cm) around breaking to obtain a coarse spatial profile of the wave to check against the films.

Breaking inception

Breaking inception or incipient breaking describes a wave that, at no time during its evolution, ever breaks. The carrier wave propagates through the envelope, forms a cusp at the crest, then propagates onward. The wave profile at the time when this cusp forms is measured for a_{sb}, λ, H, and L_f as shown in figure 3.4.1. This point also corresponds to the maximum wave amplitude.

The input wave amplitude ak_c that was observed to cause incipient breaking is plotted against $\Delta f/f_c$ in Figure 3.4.2. This value is almost constant for all bandwidths. The measured wave amplitude, a_{sb}, at breaking, normalized by k_c, is also plotted. This parameter decreases with increasing bandwidth indicating that relatively low waves with low steepness are still near breaking. The measured steepness at breaking, H/λ, also decreases with increasing bandwidth.

These results indicate that breaking criteria such as given by Michell (1893) where $H/\lambda = 1/7$ do not universally apply. Another parameter, defined as the wave front steepness, $\alpha = a_{sb}/L_f$ (figure 3.4.2),

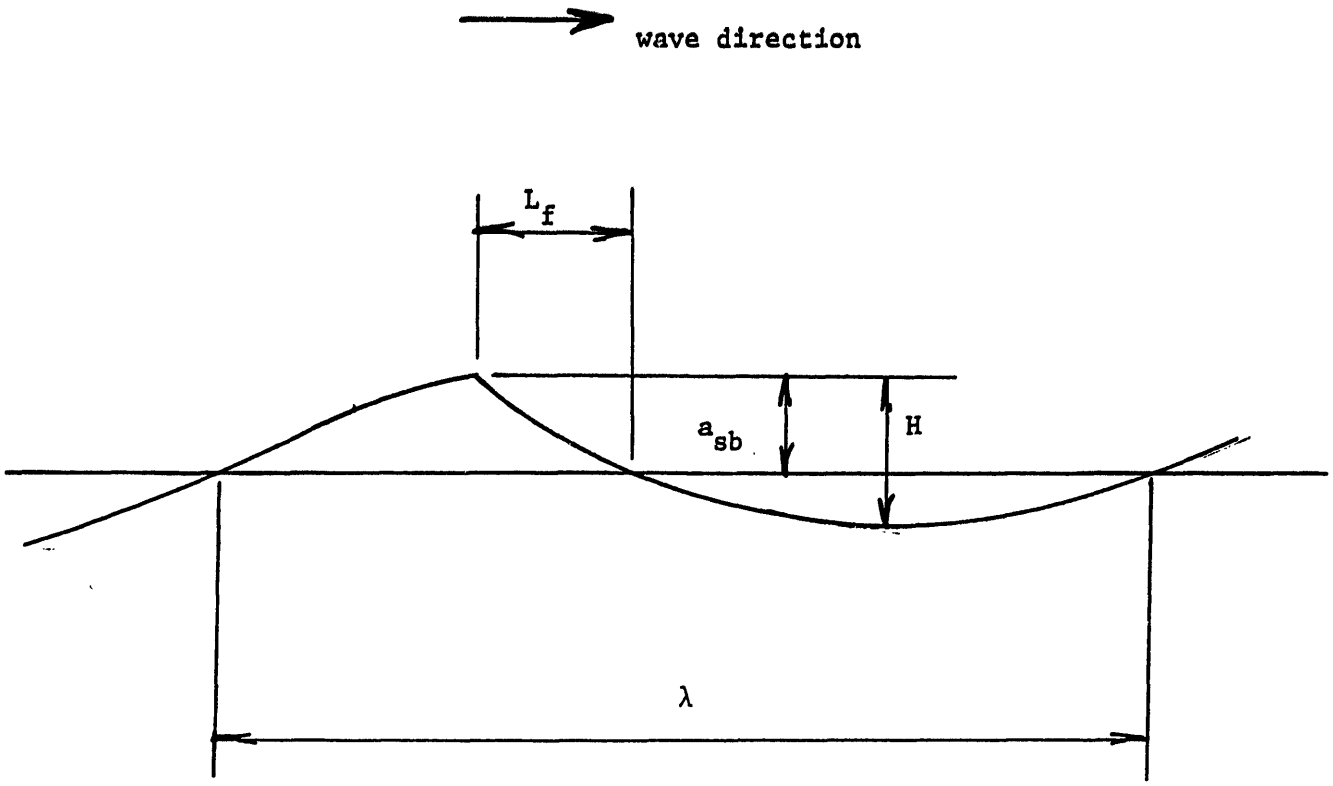

Figure 3.4.1. Definition sketch of wave geometry in space. $\alpha = a_{sb}/L_f$, $\beta = \pi H/\lambda$

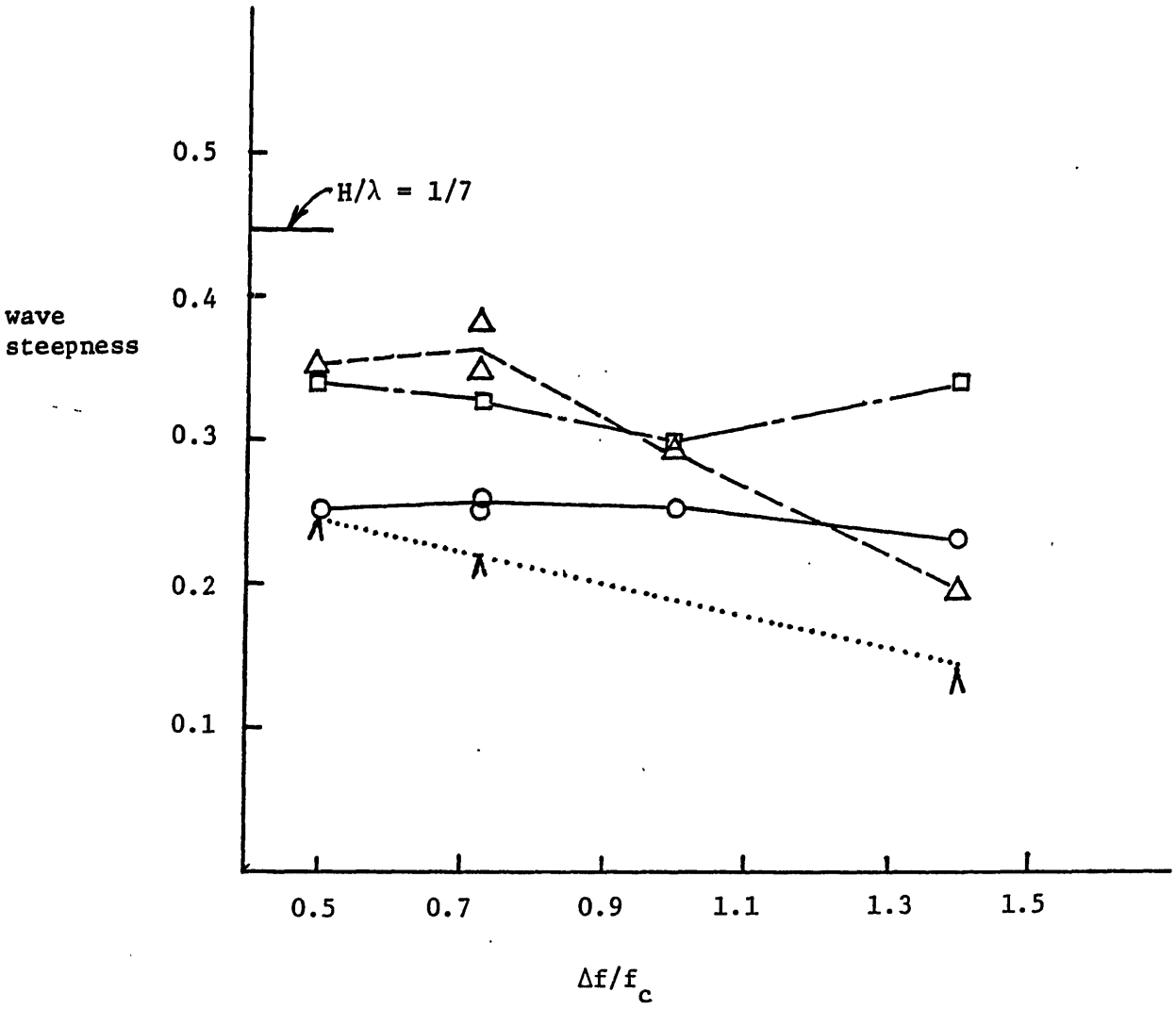

Figure 3.4.2 Spatial wave steepness measurements for incipient breaking. $ak_c(0)$, $a_{sb}k_c$ (△), $\alpha = a_{sb}/L_f$ (□), $\beta = \pi H/\lambda$ (⋀). Refer to figure 3.4.1.

is plotted. This parameter remains constant for all the incipient breaking cases, indicating that it gives a better indication of incipient breaking.

Single spilling, plunging

The same measurements are shown for packets that result in single spilling and single plunging waves (figures 3.4.3 and 3.4.4). Again, the input wave amplitude, ak_c, causing a single spill remains constant for all bandwidths; likewise, the locally measured amplitude decreases with increasing $\Delta f/f_c$. Here a_{sb} was measured at a profile where it was a maximum which corresponds to the start of breaking defined in section 3.1. The measured front steepness of breaking starts out constant at low values of $\Delta f/f_c$, but varies widely at larger bandwidths. From the films, it was observed that the front steepness varied throughout the breaking process and the actual measure of front steepness at breaking depends upon how the breakpoint is defined. Also, it is possible that the horizontal length, L_f, measured from the crest to the forward zero crossing is still too coarse to predict breaking, especially if there are short waves riding on long waves. Breaking is very localized at the crest.

The punging wave suffers the same problems in defining a front steepness. The results of the thesis by Chan (1985) also show how the steepness varies through breaking.

Correlation between input nondimensional amplitude ak_c and local spacial parameters

Figure 3.4.6 shows the poor correlation between the local wave amplitude and the wave packet input amplitude ak_c. While ak_c is a good

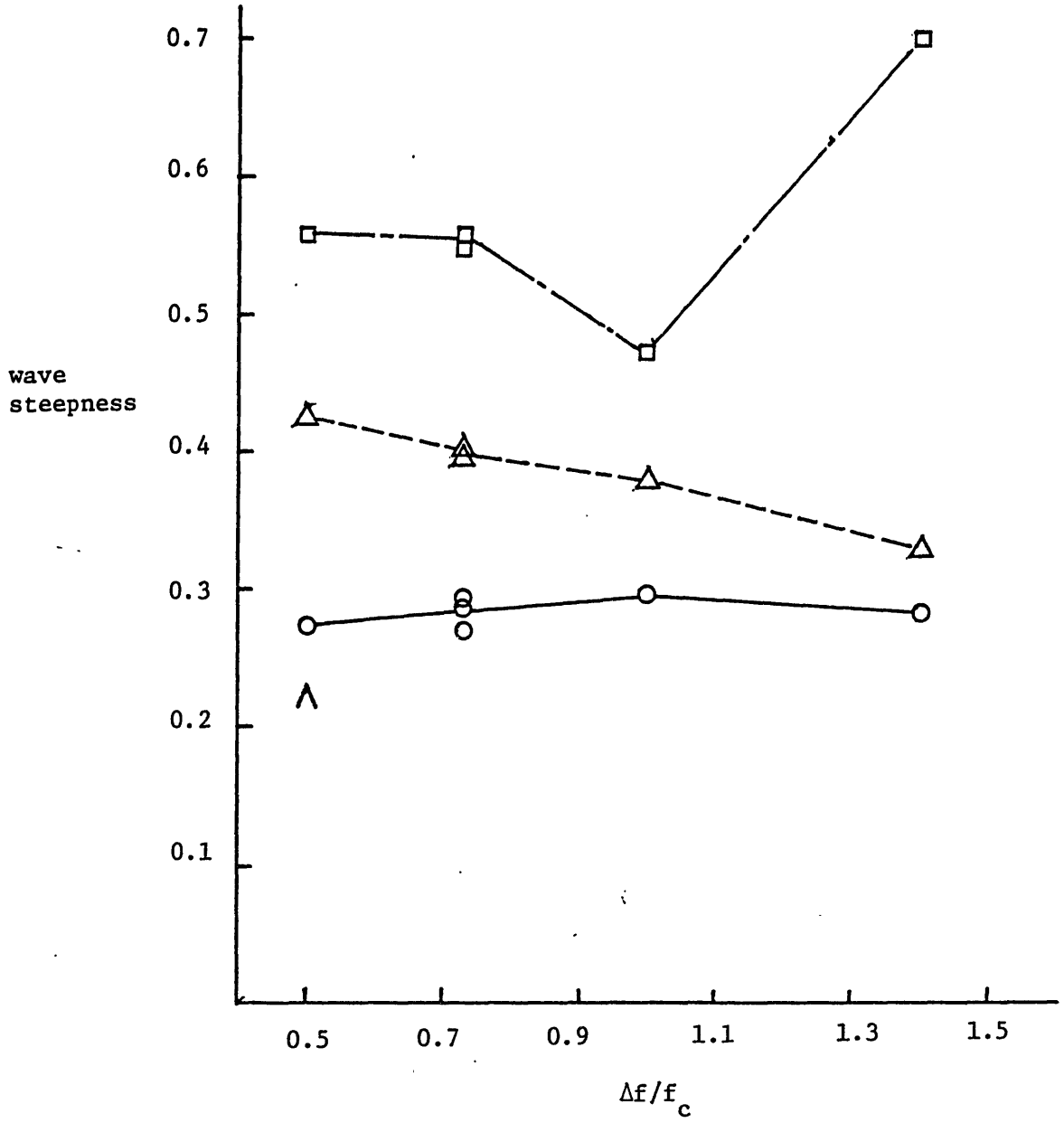

Figure 3.4.3 Spatial wave steepness measurements for spilling breaking as for figure 3.4.2.

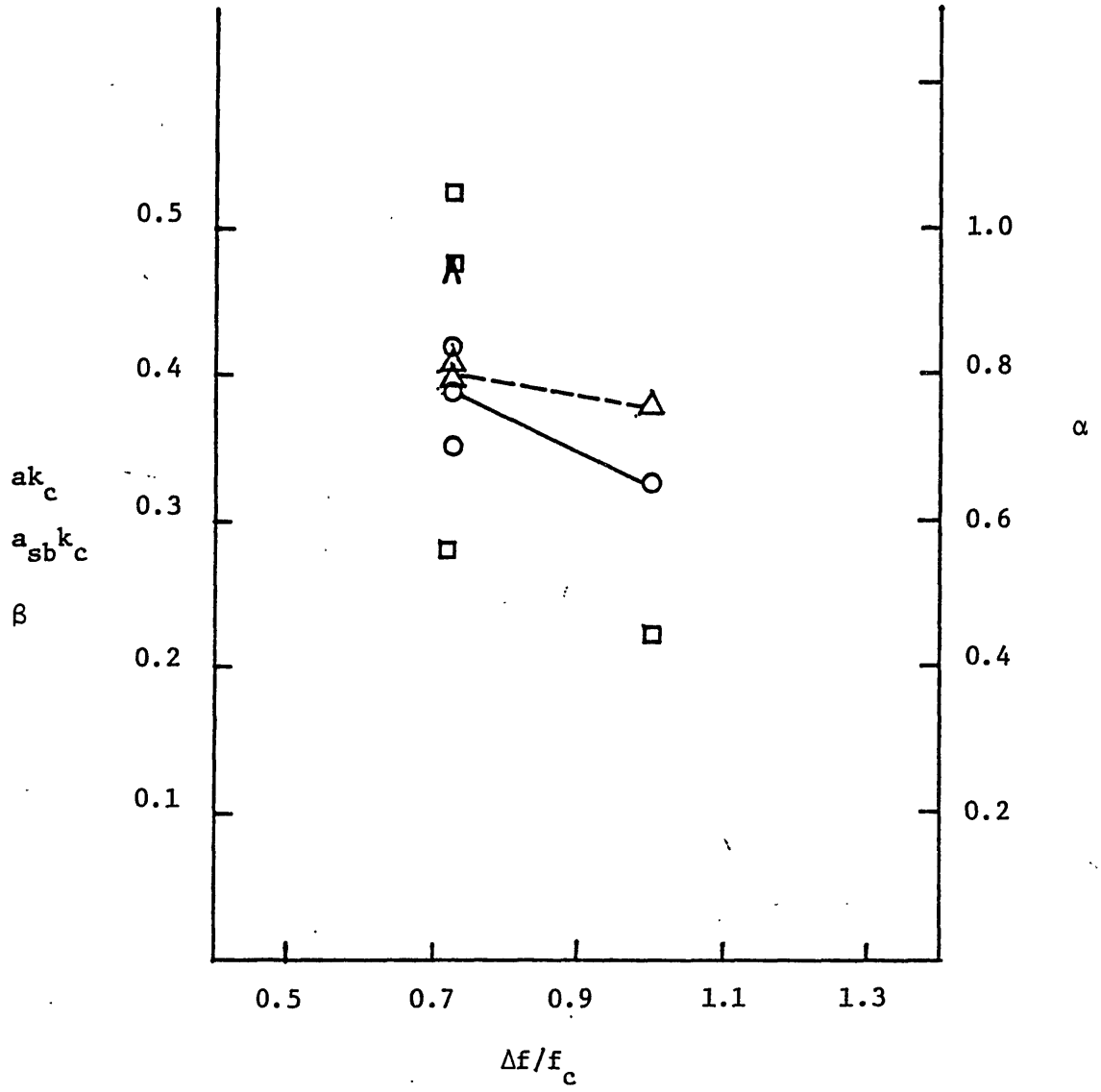

Figure 3.4.4 Spatial wave steepness measurements for plunge breaking as for figure 3.4.2.

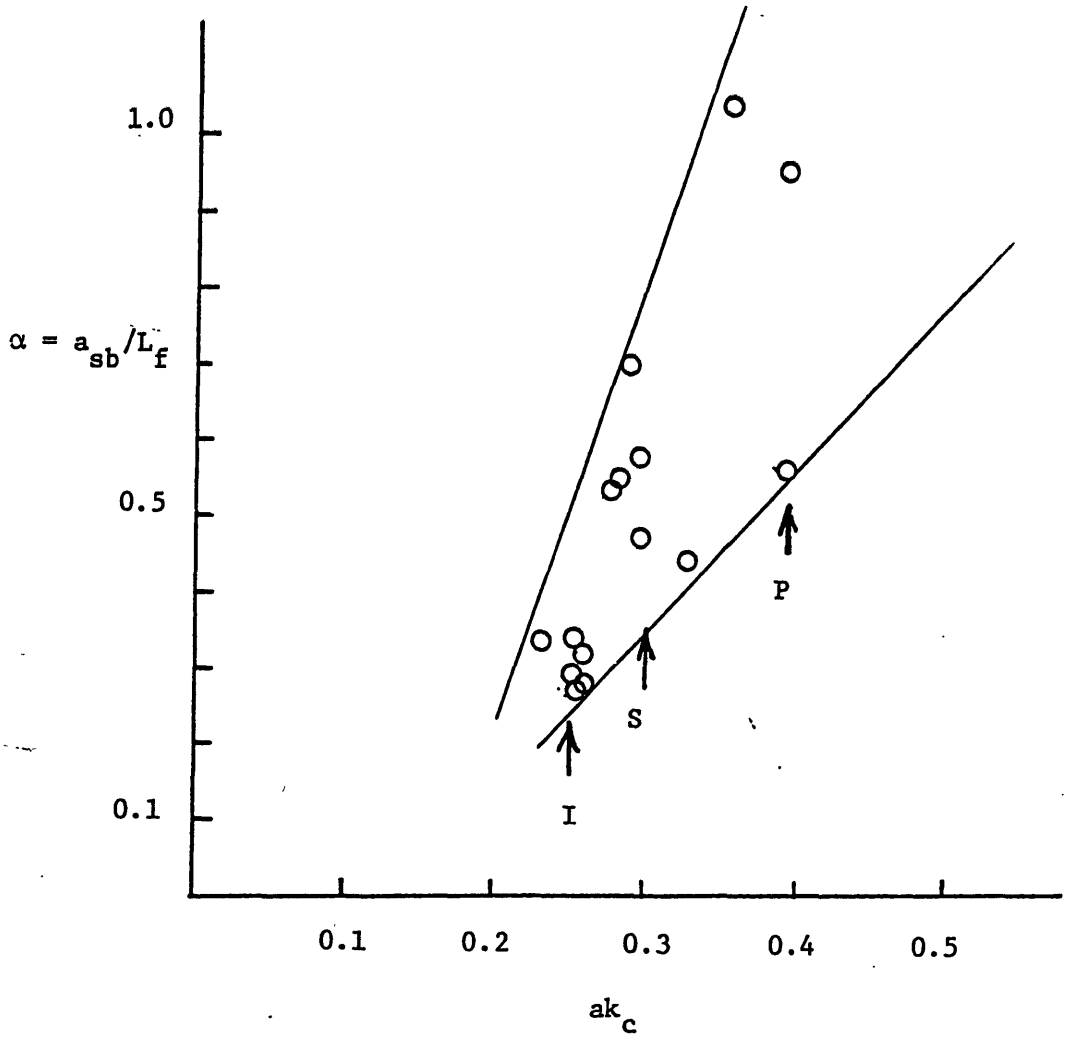

Figure 3.4.5 Correlation between input packet amplitude, ak_c, and front steepness α. Refer to figure 3.4.1. Incipient breaking waves, I; spilling, S; Plunging; P.

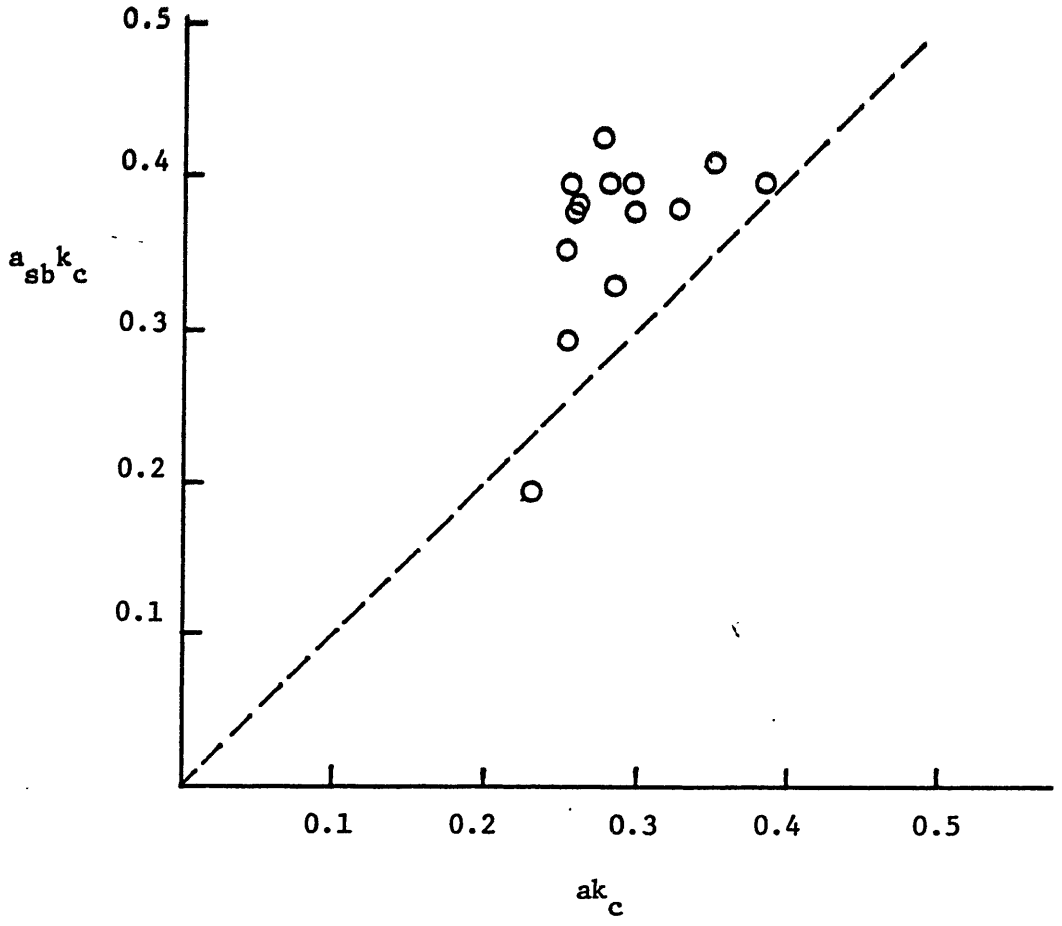

Figure 3.4.6 Correlation between input packet amplitude, ak_c and locally measured amplitude, $a_{sb}k_c$. For all intensities of breaking. Broken line is ideal linear superposition.

predictor of breaking, the local amplitude $a_{sb}k_c$ is not. Figure 3.4.5 that the front steepness parameter does a better job of predicting a unique type of breaking for the incipient case, but becomes less reliable as the front slope increases and the breaking becomes more vigorous.

From these results, it appears that a "snapshot" of the local geometry just before breaking is insufficient to predict spilling or plunging, but spatial derivative or rate of change of the steepness, for instance, maybe needed to better predict breaking. This finding is consistent with that of Van Dorn and Pazan (1975) where the wave growth rate was found to be important in predicting breaking.

3.5 Evolution of the Frequency Spectrum

The measurements of the surface displacement variance have provided a measurment of the loss of the momentum flux and energy flux from the carrier waves due to breaking. It is of interest to determine the form of this dissipation spectrum, that is, which frequencies are losing the most momentum flux.

In this section the spectra of the surface displacement are shown as the packet evolves to the energy focal point and disperses downstream.

A Fast Fourier transform (FFT) was performed over the packet, windowed as shown in figure 3.5.1. The window is smoothly brought to zero with cosine bells over the end 10% of the window. In the large scale case (f_c = 0.88 Hz) the window length is 23.5 seconds, 1175 data samples, sampled at 50 Hz frequency. The program adds zeros to perform a 2048 point FFT. Only one realization at each x location was available, so smoothing was done by averaging over four adjacent spectral estimates,

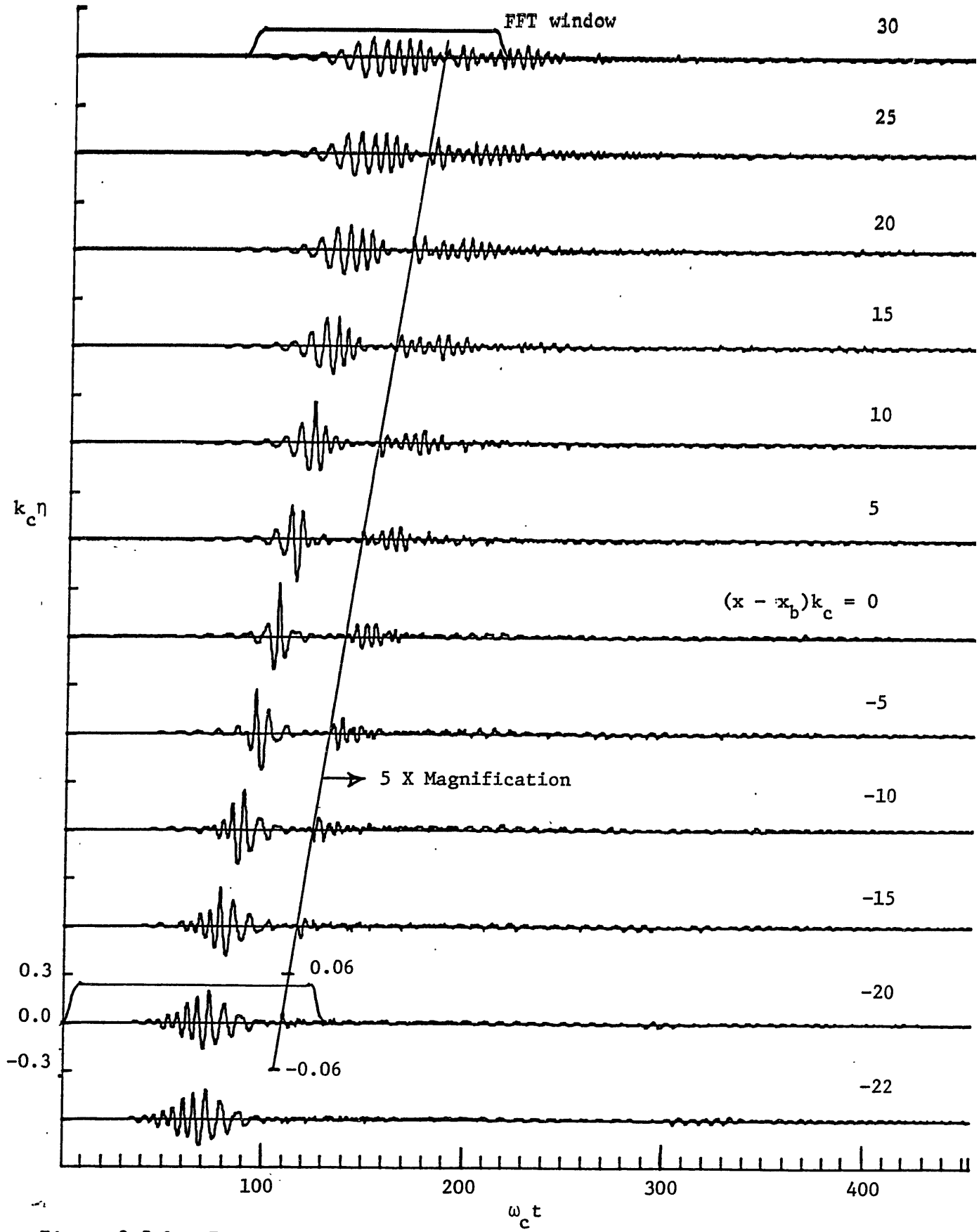

Figure 3.5.1 Time histories of surface displacement vs. distance from the energy focal point, x_b, emphasizing the waves trailing the packet. The scale to right of slant line is magnified five times. Packet f_c = 0.88 Hz, ak_c = 0.257 (incipient breaking). $\Delta f/f$ = 0.73, $x_b k_c$ = 27.4.

giving eight degrees of freedom. The spectrum over the input band of frequencies is deterministic so these spectral estimates do not have errors associated with stochastic processes.

The spectra for the large scale (f_c = 0.88 Hz) incipient breaking packet (ak_c = 0.257) is shown in figure 3.5.2. The corresponding time histories are shown in figure 3.5.1. The momentum flux density is normalized by $k_c^2 \cdot f_c$ and the frequency by f . The spectrum at the upstream reference station $k_c(x - x_b) = -22$ shows the top hat input spectrum. Also evident is the energy in the second harmonic band. This spectrum is plotted as a dashed line in subsequent spectra for reference. As the packet evolves to the energy focal point, the spectra loses its top hat shape, and energy is spread to higher frequencies. Note that these are log plots and one order of magnitude is represented by one tick mark on the left margin, so the energy in the high frequencies has increased by almost 10 times. The corresponding time history is the steep carrier wave at the energy focal point. Even though the wave is not breaking, the spectra hasbecome quite changed. Note also the growth of the forced wave at the low frequencies as the packet approaches breaking.

As the packet disperses again downstream, the wave becomes more linear and the spectrum at $k_c(x - x_b) = 30$ returns to almost its initial top hat shape. Note the slight loss at the higher end of the first harmonic band, and in the second harmonic band (boundary layer losses).

The plunging wave results are shown in figure 3.5.3. Here again, near the paddle the spectrum is very much like the theoretical input spectrum. Also plotted here with a long-short broken line is the small scale plunging packet also normalized by $k_c^2 \cdot f_c$. The agreement

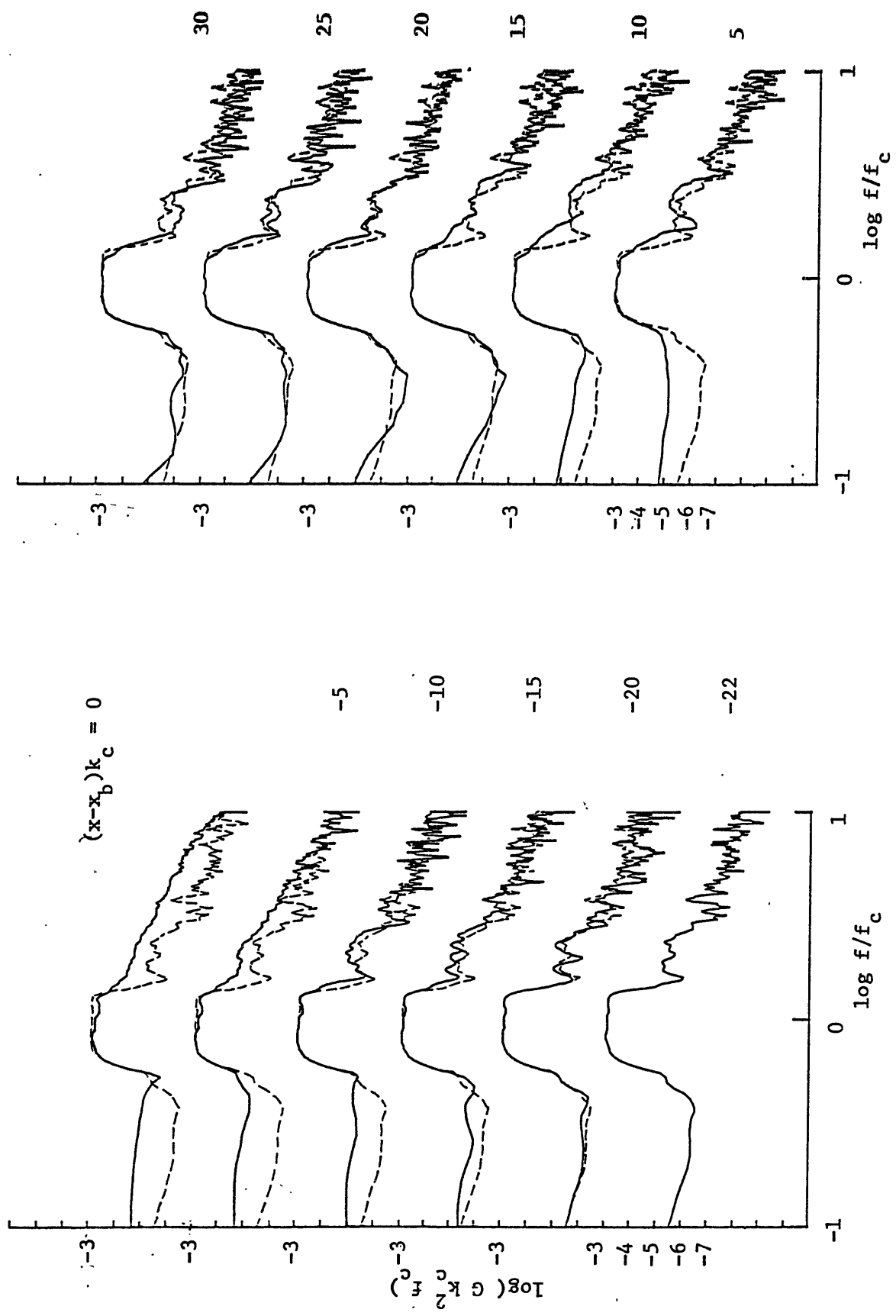

Figure 3.5.2 Spectra of incipient breaking wave packet. f_c = 0.88 Hz, ak_c = 0.257, $\Delta f/f_c$ = 0.73, $x_b k_c$ = 27.4. Dashed line is spectrum at reference station $k_c(x - x_b)$ = 22.

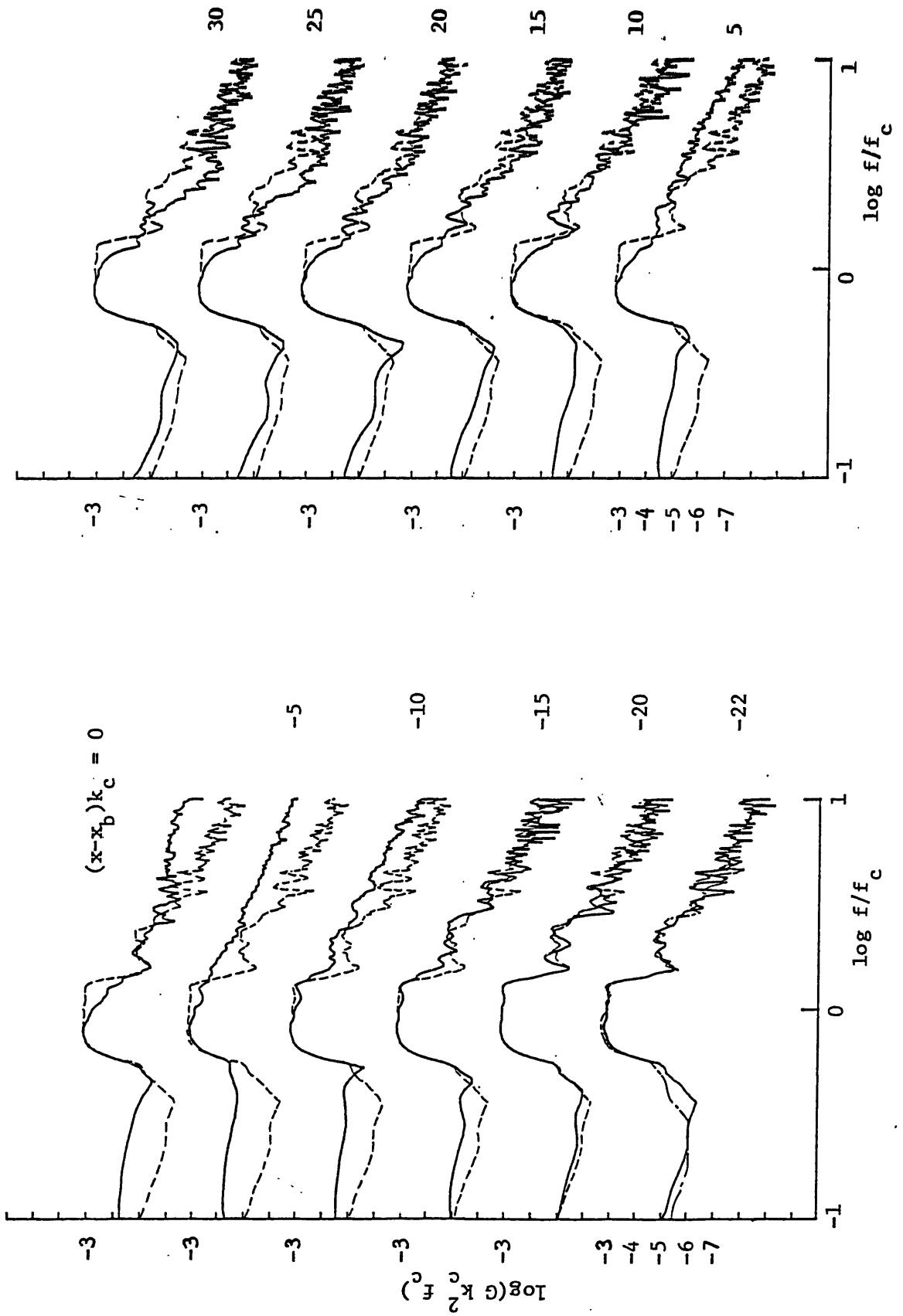

Figure 3.5.3 Spectra of plunging breaking wave packet. As for figure 3.5.2 except $ak_c = 0.352$. Broken line at $k_c(x - x_b) = -22$ is for small scale plunging $f_c = 1.28$ Hz, $ak_c = 0.420$.

between the scales is very good. The spectra evolve as for the nonbreaking case, but here the packet is steepest at $k_c(x - x_b) = -5$. Breaking occurs between $k_c(x - x_b) = -5$ and 0 and the loss in the high frequency end of the first harmonic and in the second harmonic band between these stations is appreciable. The packet continues downstream, dispersing into linear waves but note the spectra far downstream. Essentially all the momentum flux loss from the packet (24%) is lost from the high frequency end of the first harmonic band. About a 90% reduction is seen in the second harmonic band.

A similar behavior is observed for the spilling breaker (figure 3.5.4) but here only 10% of the momentum is lost from the packet, but still comes from the high end of the first harmonic band of frequencies.

The scaling of this behavior is justified in figure 3.5.5 where the small scale ($f_c = 1.28$) plunging ($ak_c = 0.420$) wave spectra is plotted. It agrees very well with the large scale plunging case.

Thus it seems that the low frequency waves in all cases propagate through breaking, even the intense plunging, without significant loss of energy.

3.6 Radiated waves due to the Breaking Disturbance

In the course of these experiments, it was observed by eye that waves were radiated back upstream as a result of the more intense plunging breaking. It is reasonable that the impact of the plunging jet into the free surface can radiate waves in both directions.

Measurements at the free surface displacement through the channel were made to measure these waves. Time histories for the large scale

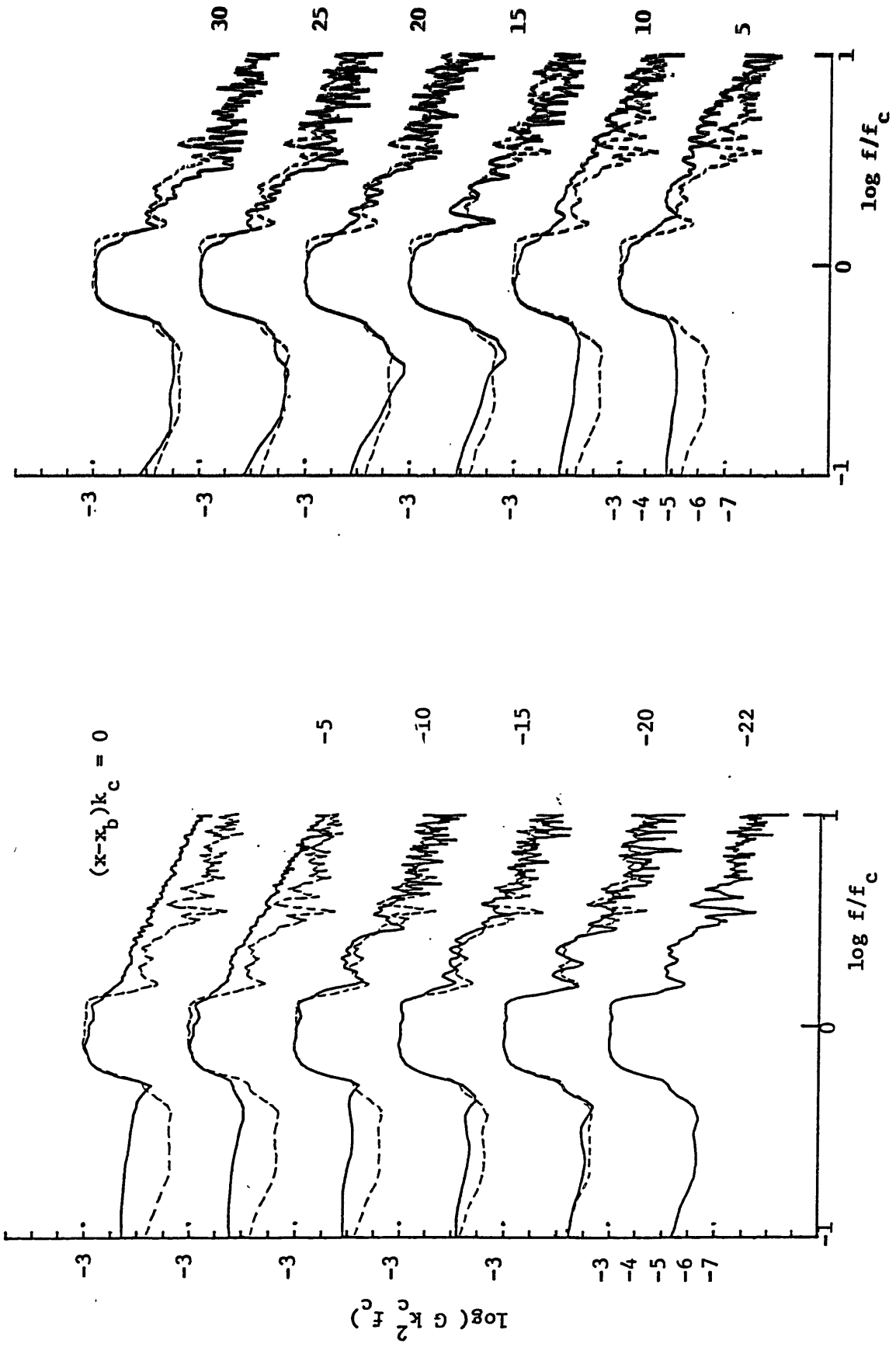

Figure 3.5.4 Spectra of spilling breaking wave packet. As for Figure 3.5.2 except $ak_c = 0.278$.

This is the most complete text of the thesis available. The following page(s) were not included in the copy of the thesis deposited in the Institute Archives by the author:

Pg. 145

plunging wave are shown in figure 3.6.1, where the signal to the right of the solid line at the end of the main packet has been magnified five times. High frequency waves ($\sim 2 f_c$) are noticed at later times, $\omega_c t = 100 \rightarrow 300$ at breaking. These waves are not present for the incipient breaking case of figure 3.5.1. (In that figure, the signal is also magnified five times.) The dashed line in figure 3.6.1 show the predicted group velocity of waves with frequency $2f_c$, radiated from the break point. They propagate upstream and are reflected off the wavemaker paddle. Likewise, using this same group velocity, waves may be transmitted downstream. Downstream, however, there is not a clear separation in time between these transmitted waves and waves trailing the packet that are also present in the incipient breaking case (figure 3.5.1). (The source of these trailing waves has not been determined, but they may have been generated upon stopping the paddle motion, even though this was done smoothly.). Also drawn in figure 3.6.1 is the expected propagation of waves from the main packet reflecting from the beach at the end of the tank.

The spectra at the signal to the right of the solid line was computed by FFT methods. The FFT window of 2048 samples in 40.96 seconds was tapered with cosine bells at the end 10%. The data was sampled at 50 Hz. Only one realization was recorded and frequency smoothing of four adjacent estimates was used to improve the accuracy giving eight degrees of freedom.

The resultant spectra for the large scale ($f_c = 0.88$ Hz) plunging ($ak_c = 0.352$) is shown in figure 3.6.2 as a solid line and the dashed line is for the incipient breaking wave packet ($ak_c = 0.257$). Note

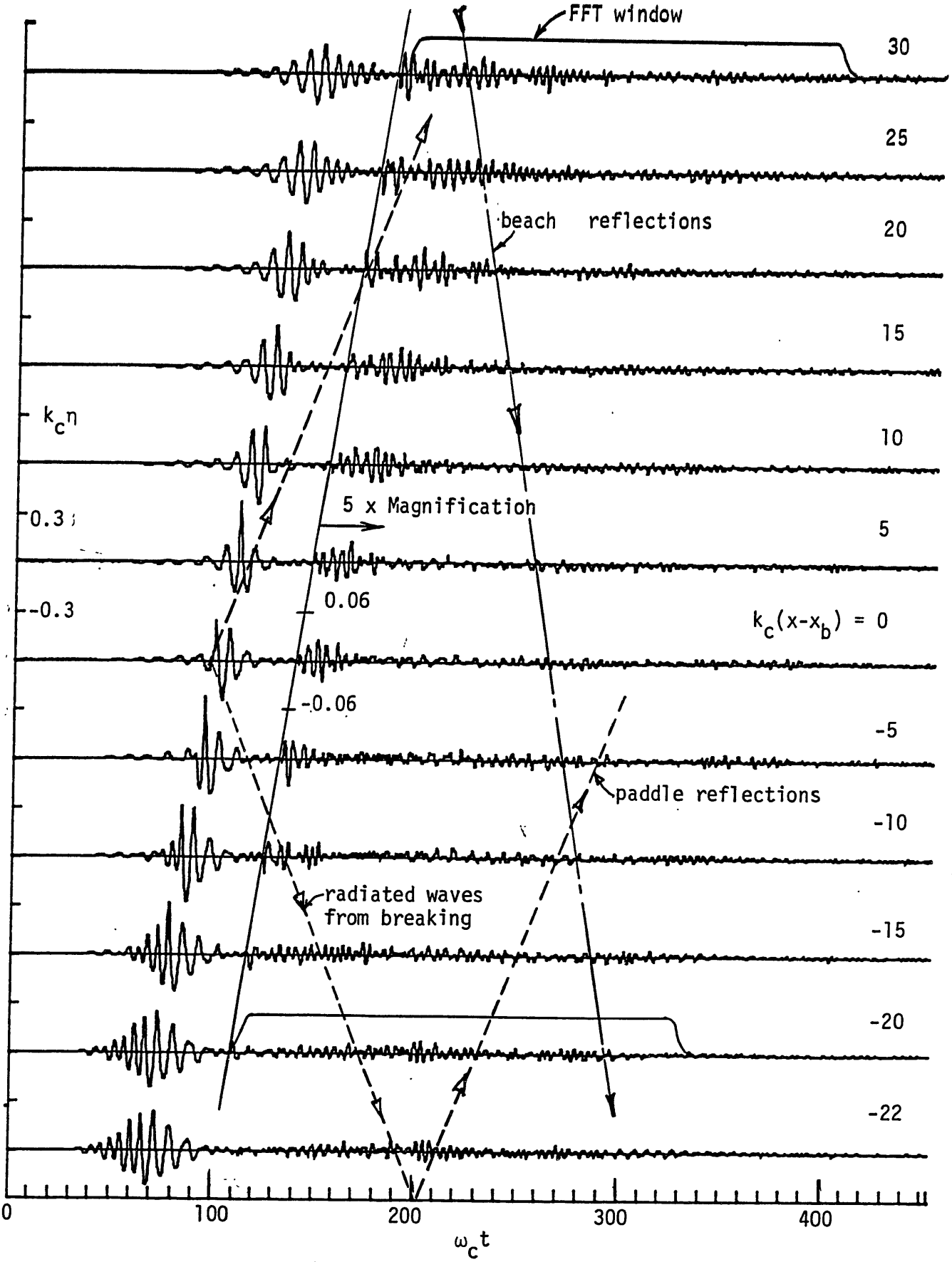

Figure 3.6.1 Time histories of surface displacement showing high frequency waves radiated from the breaking point. Same as Figure 3.5.1, except $ak_c = 0.352$, plunge breaking between $k_c(x - x_b) = -5$ and 0. Scale is magnified 5 × to right of slant solid line.

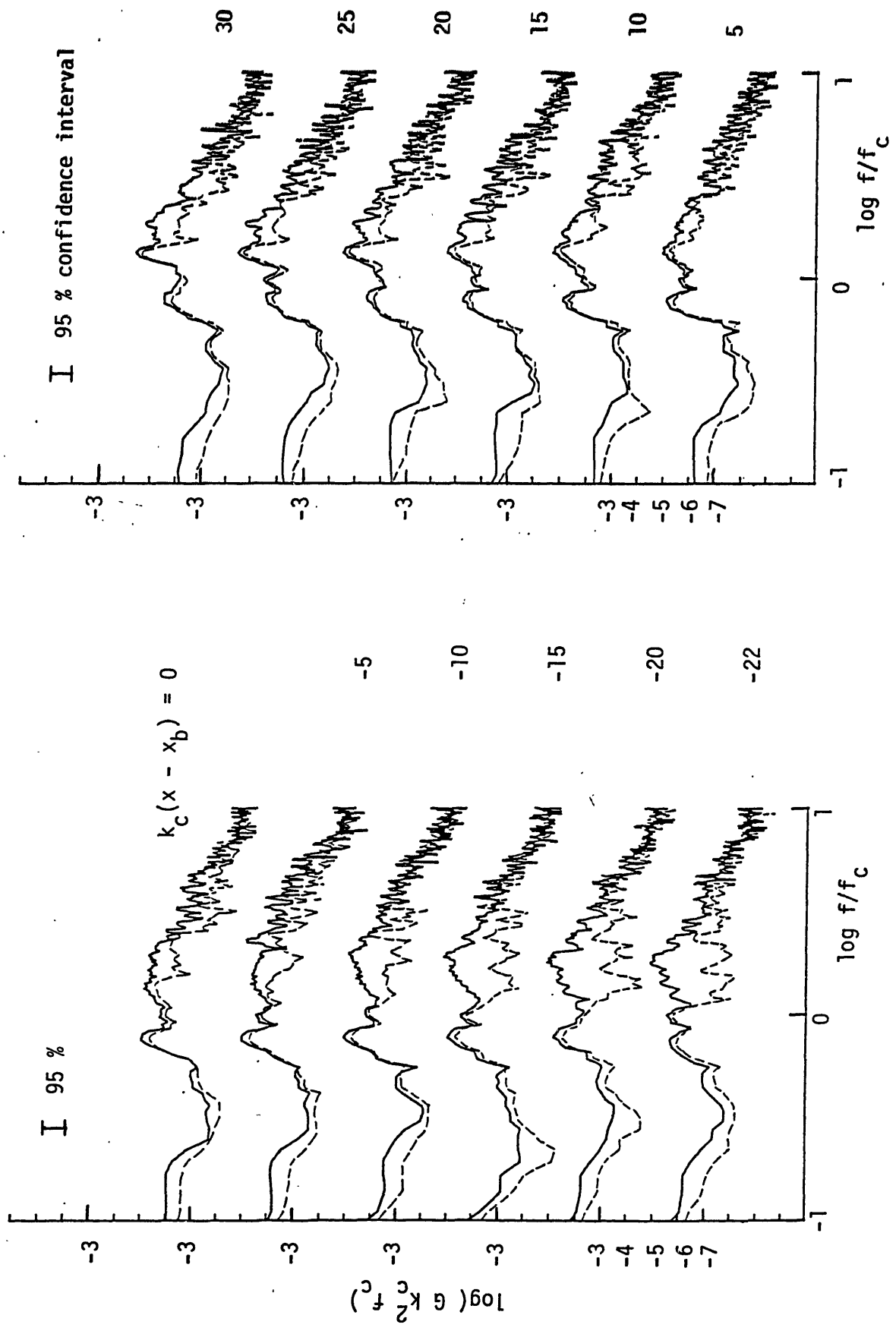

Figure 3.6.2 Spectra of waves radiated away from breaking disturbance f_c = 0.88 Hz, ak_c = 0.352 plunging ——, ak_c = 0.257 incipient breaking - - - . 95% confidence interval for spectral estimates is shown by vertical error bars.

the obvious difference between the two cases in the energy around the second harmonic band, particularly for the locations upstream of breaking. A comparison with the spectra of the main packet shows that these radiated waves contain approximately 1% of the energy in the main packet. These data suggest, then, that second harmonic waves are reflected from the breaking region or generated there. Whether or not these waves are random or deterministic cannot be seen here. Results of the ensembled averaged surface displacement over 10 repeats tend to show that these may in fact be deterministic, surviving the averaging (figure 5.2.4).

Downstream of breaking, the difference in the spectra between the incipient and plunging waves is not as large but still evident, suggesting that there are also second harmonic free waves generated by breaking which travel downstream.

These waves are seen to scale with the waves of the incident wave packet by the comparison between the spectra of the radiated waves due to the large and small scale plunging waves (figure 3.6.3).

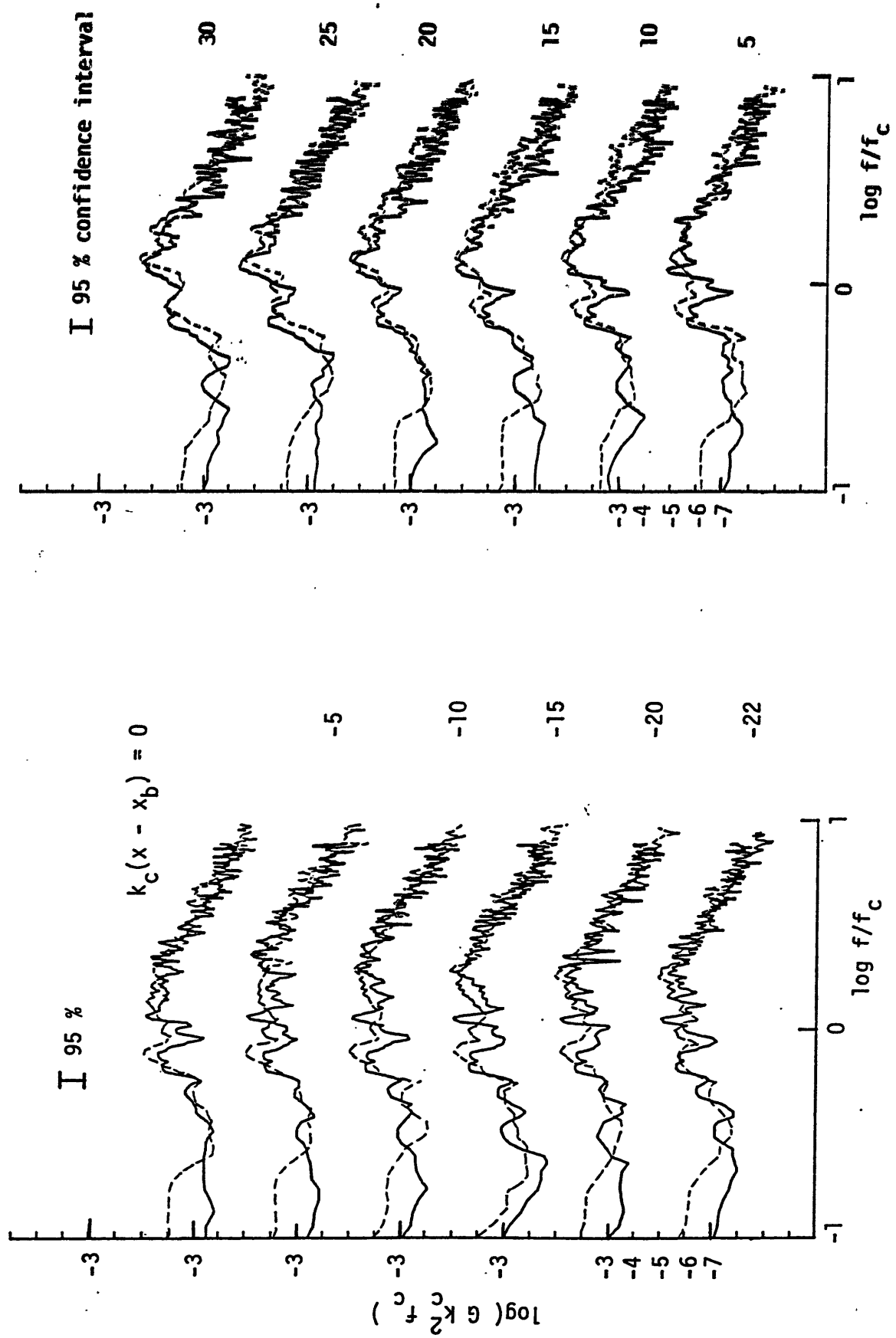

Figure 3.6.3 Comparison of radiated waves for two scales of packets. f_c = 0.88 Hz ---- , f_c = 1.28 Hz ——— , both plunge breaking.

Chapter 4

4. Flow Visualization Experiments of Mixing in the Breaking Region.

4.0 Summary

Flow visualization experiments of the mixing of a dye slick, floated on the water surface, were performed to quantify the rate and spatial extent of turbulent mixing of fluid initially at the free surface. The intent of these experiments is to determine if the mixing, specifically, the time rate of lengthening, deepening, and increase in area of the mixed region, scale with the length scale of the input wave packet and also how these quantities depend upon the packet wave amplitude, ak_c, which was shown to strongly influence the wave breaking momentum flux loss. The momentum flux lost from the wave field may then be related to these mixing rates.

The results show that, indeed, the mixed region, as defined by the dye length, maximum depth, and area, scale with the wavenumber of the packet center frequency over the scales tested, and that the rate of increase of the quantities can be described by certain power laws. The maximum depth grows initially (in 0 - 1 wave periods) as the wave orbital velocity, then as $\omega_c(t - t_{ob})^{1/4}$. The mixed area grows as $\omega_c(t - t_{ob})^{1/2}$ were the time t_{ob} is the time of observed air entrainment. The length, near the surface, grows initially as the wave phase speed, then at a rate of ≈ 1% of the phase speed. The coefficients multiplying these power laws are roughly constant over the scales tested and increase with increasing wave amplitude, ak_c, in a similar manner to the momentum flux loss. After a long time (10 wave periods), the dyed region is roughly one

wavelength in horizontal extent and 3 - 4 waveheights in vertical extent for spilling and plunging, respectively. As was observed for the excess momentum flux loss, once ak_c is increased above a breaking threshold, the resulting mixing is of the same order as the more vigorous plunging. It appears that the input packet wave amplitude, ak_c, is a good predictor of the momentum flux loss as well as of the region and rate of mixing.

The turbulent flow in the breaking region (which is roughly defined by the dye boundary) is strictly non-stationary, since it is decaying, and nonhomogeneous in x and z. The trajectory of a single fluid particle initially at the free surface will be random from one run of the experiment to the next owing to the turbulent flow. To analyze a turbulent flow, statistical averages are taken as a description of the turbulent flow. Time and spatial averages are not relevant in the nonstationary and nonhomogeneous flow since the flow is changing over the averaging time. Ensemble averages over many runs of the experiment must then be made. If many dyed particles are placed close together at some point in the free surface, the average motion of all these particles will form an ensemble average with just one run of the breaking wave.

In these experiments we measure the <u>maximum</u> excursion (from breaking) of a continuous sheet of dyed particles with time. The concentration of the dye varies with depth and distance from breaking and the concentration may be interpreted as a probability of a particle from the surface reaching a certain depth or horizontal location. In analyzing the films, the dye "boundary" is traced by eye. At short times after breaking the boundary is well defined and the traced contours represent lines inside of

which, the probability of a surface particle appearing there is near 100%. At later times, the boundary becomes less sharp and the traced contours may represent a probability contour of less than 100%, however it is estimated by eye that at least 90% of the dye will be contained in the traced contour.

4.1 Procedures

A surface dye slick was formed by placing small amounts (1/4 teaspoon) of blue powdered vegetable dye (FD & C Blue No. 1, H. Kohnstamm & Co., New York) on the water surface at equally spaced intervals along the channel centerline. Care was taken to apply the dye gently so as not to break the water surface. The water surface was first skimmed clean of any contaminants. This allowed the dye to spread evenly and the dye slicks to merge and form a uniform and continuous slick over a length of approximately twice the expected mixed region (i.e., about two center wavelengths). The dye remained on the surface even under the action of near breaking waves. Mixing was observed only when the free surface was broken. Even a very gentle breaking, with no visible air entrainment was observed to trigger mixing.

The dye mixing was recorded with a 16 mm Bolex REX cine camera at 48 and 24 frames/second for 12 and 25 seconds after breaking. A back-lit white cloth background provided good contrast between the mixed and unmixed region when filmed with color reversal film (see section 2.1 for details and figure 2.1.5a). At the same time as the cine' films were made, 35 mm slides were also taken as examples. These photographs are shown in figure 4.1.1 for a plunging breaking and 4.1.2 shows a spilling breaker. These correspond to f_c = 0.88 Hz, the large scale. Time (in

Figure 4.1.1. Photographs of dye mixing under a plunging breaker for f_c=0.88Hz ,ak_c=0.352, $\Delta f/f_c$=0.73, and $x_b k_c$=27.4
Tick marks are 10cm intervals. Numbers at right are elapsed times in sec from top frame.

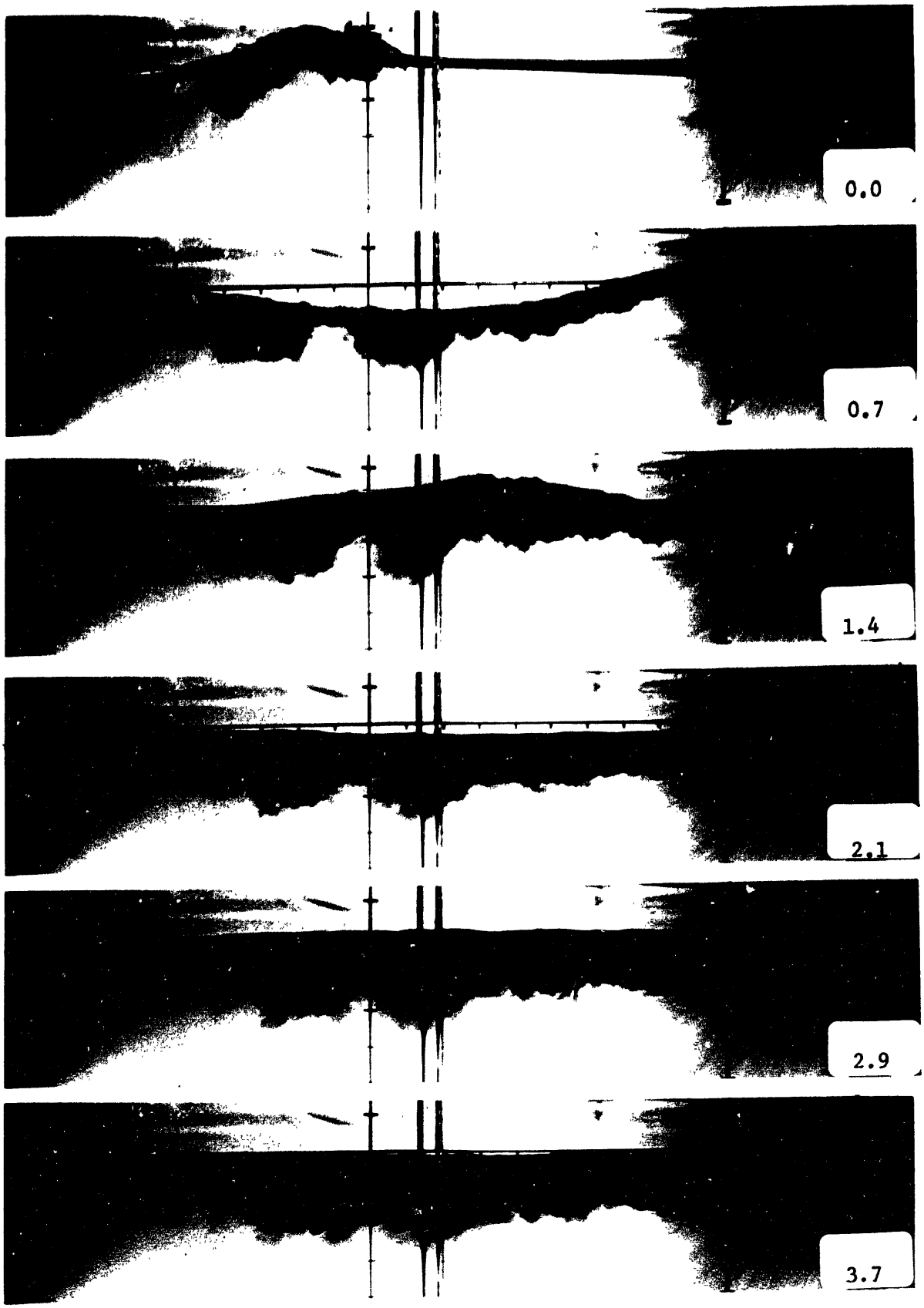
0.0
0.7
1.4
2.1
2.9
3.7

Figure 4.1.2. Photographs of dye mixing under a spilling breaker for f_c=0.88Hz, ak_c=0.278, $\Delta f/f_c$=0.73, and $x_b k_c$=27.4
Tick marks are 10cm intervals. Numbers at right are elapsed times in sec from top frame.

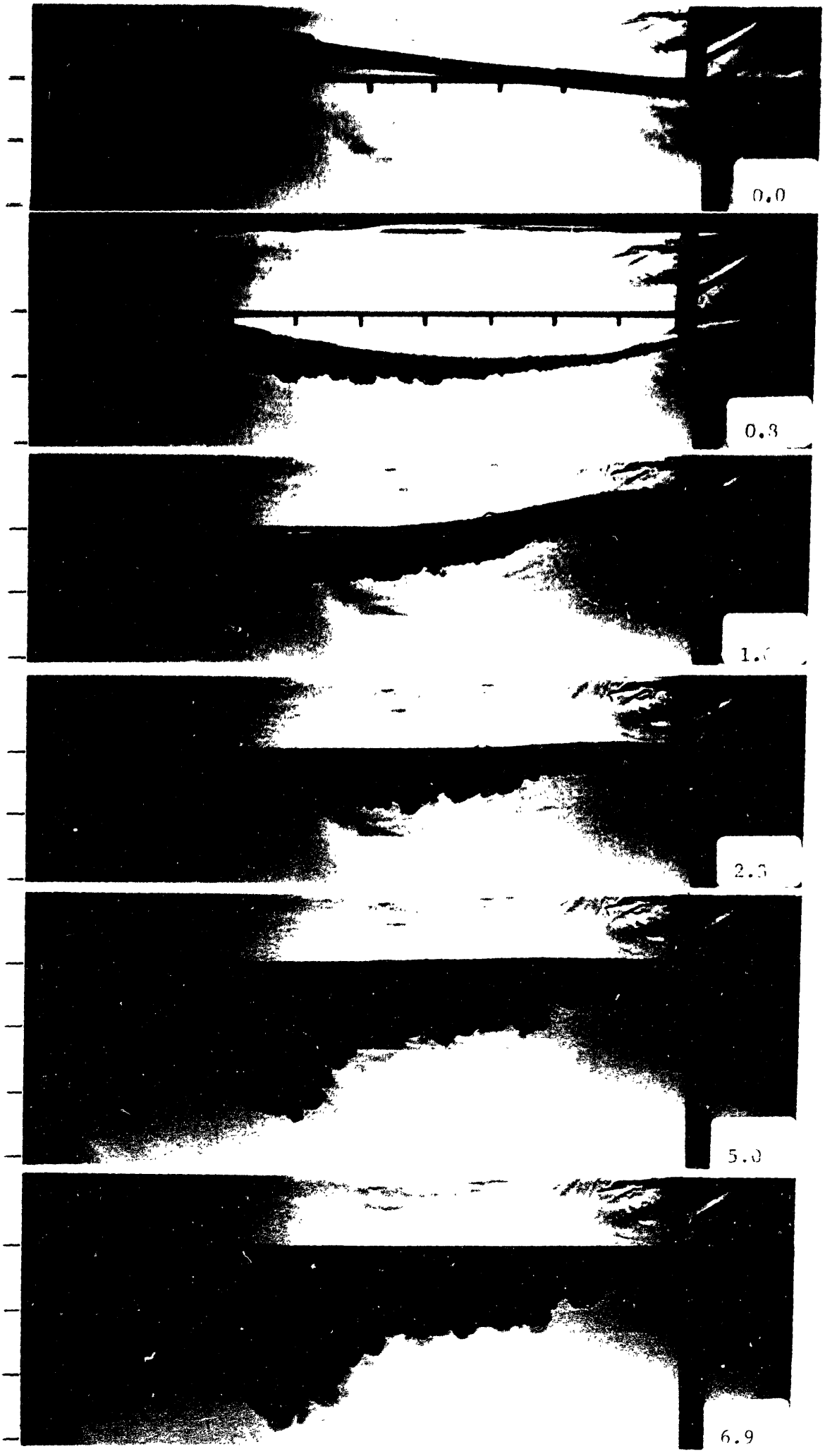
0.0
0.3
2.3
5.0
6.9

seconds) referenced from the top photograph, are shown in the bottom right corner. Tick marks are at 10 cm intervals.

The plunging breaking starts at x = 6.9 m which is just off the left margin (7.0 m is at the left edge of the frame). Dye is carried down by the initial jet and the turbulent front mixes dye ahead. Two regions of dye are evident. Photographs of bubbles in Figure 3.1.7 show this same behavior. Notice the role of the next passing trough in pumping the dye down. Within two wave periods from breaking the dye has mixed to ~1-1/2 wave heights. The dye continues to be mixed down by the turbulence generated by breaking. The dye under the spilling breaker (figure 4.1.2) is mixed down by the turbulent region propagating at near the wave phase speed. Again the following wave assists in displacing the dye downward after which the generated turbulence takes over in mixing down the dye. A quantitative analysis of the motion follows.

In photographing this wave the cine camera axis was perpendicular to the length of the channel and recorded a transversely integrated measure of the dye concentration as a function of depth, length, and time. Although the wave was very nearly two-dimensional (i.e., little transverse variation), the turbulent mixing process is three-dimensional. However, it was observed that the dye front varied little across the tank and the bottom boundary varied by about 20% of the mean depth of the dye region across the tank. Since the length and depth reference marks were located on the front glass wall of the channel, camera parallax could cause the location of the dye boundary to be underestimated if the boundary is not two-dimensional across the tank.

Since the boundary was nearly two-dimensional, the error in the length measurement, is less than -10%. In the depth measurement, the parallax angle was small, so even though the depth boundary was not two-dimensional, and the error is also less than -10%. In both cases the errors cause the quantities to be underestimated.

The cine films show a relatively sharp, well defined boundary between the dyed and undyed region even though the dye density tends to decrease with depth. Cine film records were made for single plunging and single spilling for the three scales of the input wave packets (f_c= 0.88, 1.08, 1.28 Hz) (see table 4.1). Two repeats were made for each wave packet. The wave packet bandwidth and breaking location were held constant at $\Delta_f/f_c = 0.73$, $x_b k_c = 27.4$.

The films were analyzed by projecting on a CALCOMP 9000 digitizing table and tracing the dye boundary for each frame (Program RDIGT2 in Appendix 3). Tick marks on the channel glass wall were used to calibrate the digitizer. A third-order polynomial was fit to te digitizer output of readings of the tick marks in the film frame. This corrects for distortion due to the lens focal length mismatch between the camera and projector and any lens nonlinearity. A resulting accuracy of ±1 cm was realized which is within the parallax errors.

Examples of the digitized evolution of the dye boundary in time are shown in figures 4.1.3 for a spilling wave and 4.1.4 for a plunging wave. Note that these correspond to the medium scale f_c = 1.08 Hz. The top trace is of the free surface just after breaking. The wave period is 0.93 sec in these examples, so appreciable mixing has taken place within one wave period. The trough of the following wave can be seen pushing the dye

Table 4.1

Summary of Dye Mixing Experiment
Packet Parameters

				Symbol	Film Run #
Single Plunging	f_c = 0.88 Hz	ak_c = 0.352	2 repeats	X	14,15
	1.08	0.388	2	+	6,7
	1.28	0.420	2	□	1,2
Single Spilling	f_c = 0.88	ak_c = 0.278	1	X	16,18
	1.08	0.296	2	+	9,11
	1.28	0.319	1	□	3

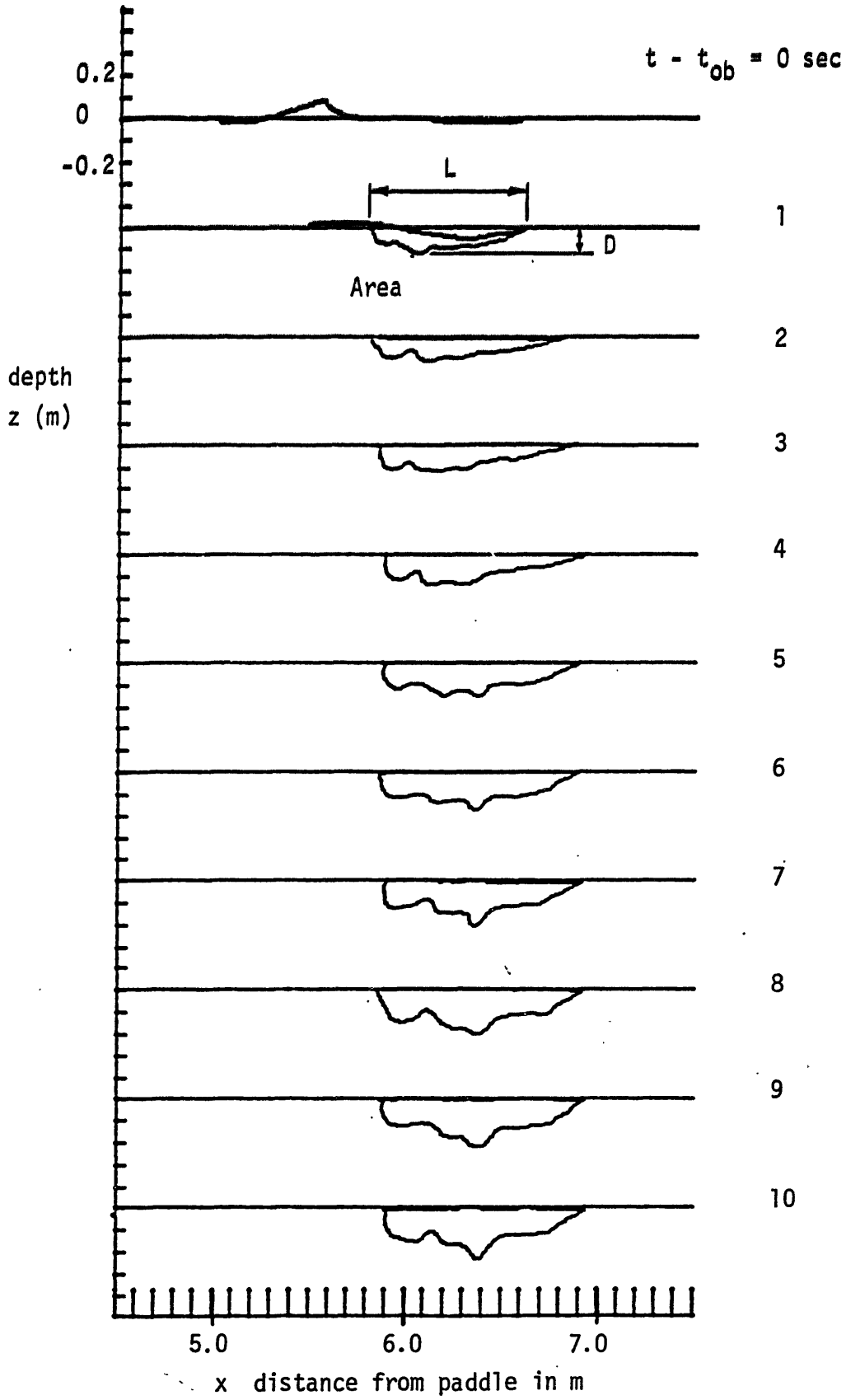

Figure 4.1.3 Digitized data of dye boundary taken from cine' films. Wave packet with f_c = 1.08 Hz, k_c = 4.72 1/m, ak_c = 0.296 (spilling). $\Delta f/f_c$ = 0.73, $x_b k_c$ = 27.4. Time steps are referenced from t_{ob}, time of observed breaking in seconds. Top contour is the free surface at breaking. Refer to table 3.1.1 for definition of t_{ob}.

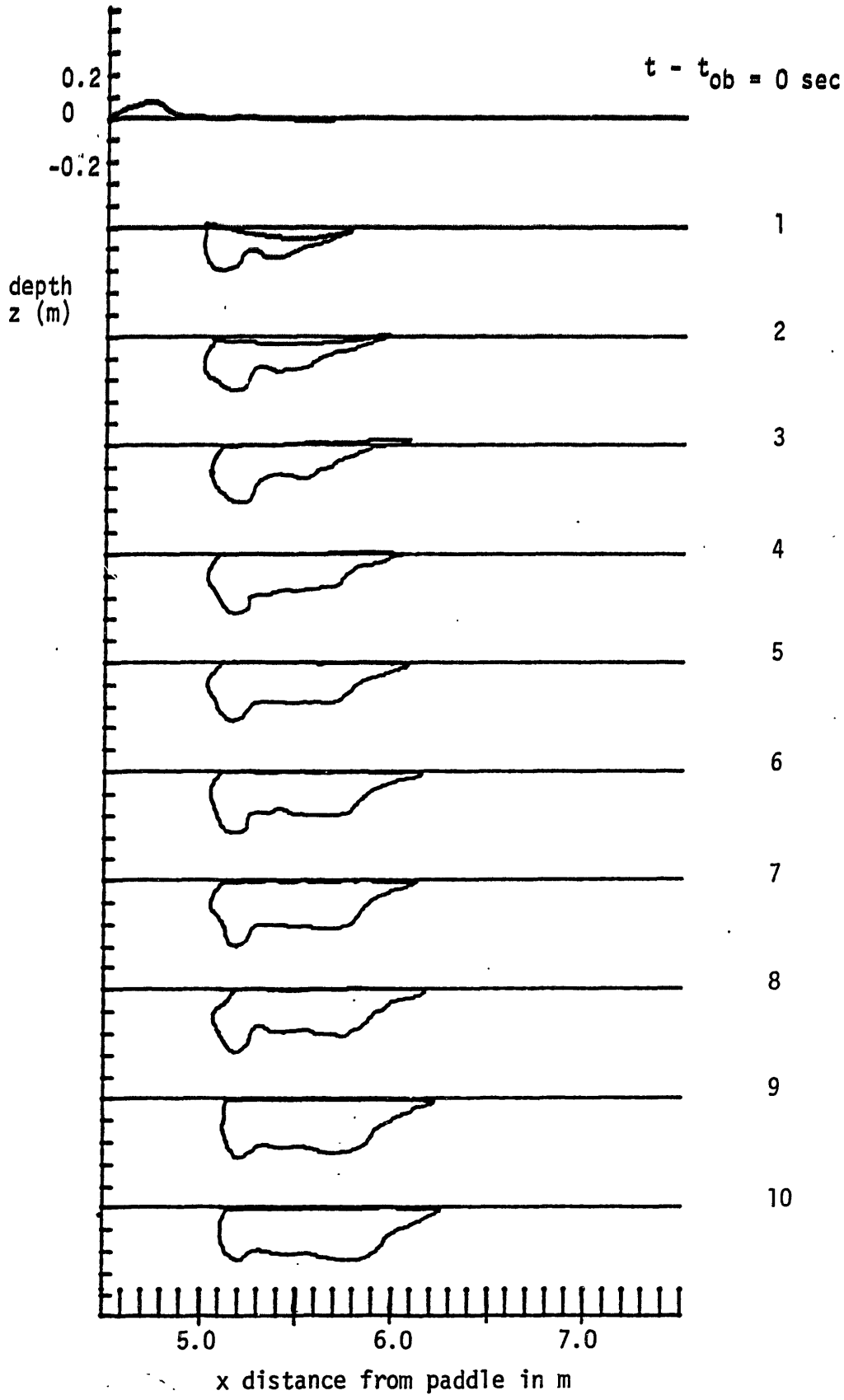

Figure 4.1.4 Digitized data of dye boundary taken from cine' films
As for figure 3.1.3 except $ak_c = 0.388$ (plunging).

down further. The tracing of figure 4.1.4 can be qualitatively compared with the photographs of the bubble cloud in figure 4.1.1 where two clouds are formed by the plunging. Note that they represent different scales of the wave packet, however.

The digitized data was analyzed for the dye length at the surface, L, the maximum depth, D, and the area (see figure 4.1.3). These quantities are nondimensionalized by k_c,k_c, and k_c^2, respectively and plotted against nondimensional time $f_c t$ (Program ANLDIG in Appendix 3.)

4.2 Horizontal Extent of Mixing

The results plotted in figures 4.2.1 show the maximum dye cloud length vs. time for a single spilling wave (top) and a single plunging wave (bottom). The results of the three scales of wave packets are overplotted with the indicated symbols. The time scale (horizontal axis) is expanded in figure 4.2.2. The time scale is referenced from t_c which is the observed time (from cine films) of the wave crest crossing the theoretical breaking location or focal point. This was done to compare the observed time of breaking between scales. The original intention was to reference the time from t_b (equation 2.3) by starting a clock at paddle startup. However, the clock face was difficult to resolve in the films so the former method of time referencing was used.

These plots show a rapid increase in the dye length, that is linear in time, at a rate of 0.7 - 0.8 C, where C is the linear wave phase speed computed for finite depth from f_c. The dye length increases to $k_c L \approx 4$ ($k L = 2\pi$ is one wavelength) in two wave periods. During this time, the rear boundary of the dye is essentially stationary (Figures

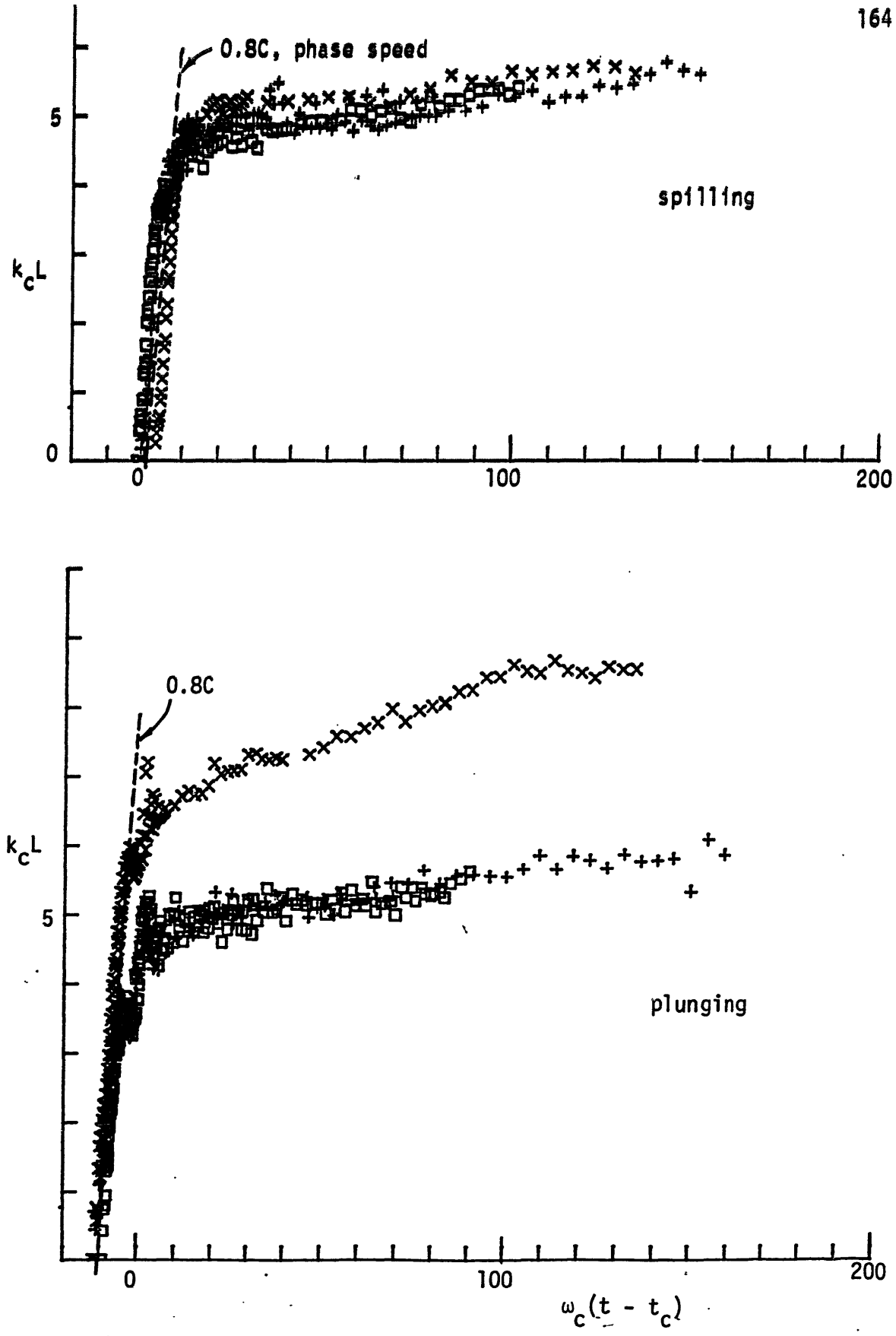

Figure 4.2.1 Length of dye boundary vs. time from t_c (refer to page 163 in text) for spilling wave (top) and plunging wave (bottom). Wave group center frequency f_c = 0.88 Hz (X), 1.08 (+), 1.28 (□) and $\Delta f/f_c$ = 0.73; $x_b k_c$ = 27.4.

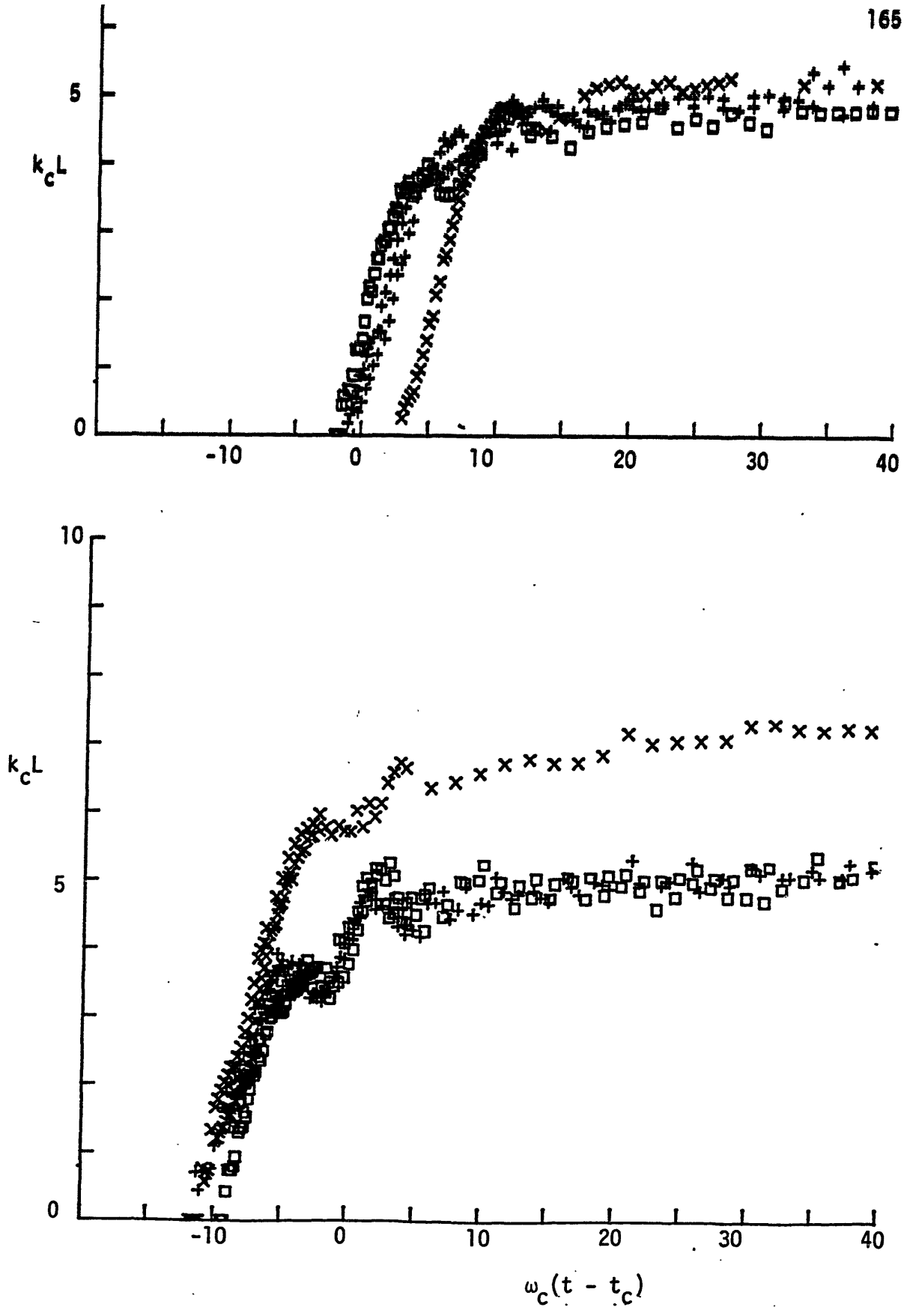

Figure 4.2.2 Length of dye boundary vs. time. As for figure 4.2.1 but with expanded time scale.

4.1.1 and 4.1.2) and the front is being defined by the turbulence at the free surface at the leading edge of the breaking. The oscillations in L (best viewed in figure 4.2.2) indicate the next passing wave trough (minimum of k_cL) and the next crest whose orbital velocity displaces the dye front forward to $k_cL \approx 5$. There is apparently a velocity contribution due to induced streaming from breaking since the wave orbital velocity is ~0.4 C at most and the speed of the dye is 0.7 - 0.8 C. Essentially, then, the trailing waves act to pump the dye ahead an additional amount. Good agreement can be seen between scales and between repeats of the same scale packet. Also, the length of the dye is the same for spilling and plunging, except for the case of the large scale plunging wave $f_c = 0.88$ Hz. This discrepancy appears to result from the increased air entrainment in the large scale. The sequence of photographs (figures 3.1.6) shows a secondary jet causing mixing further downstream, which was not as pronounced in the smaller scales. The Froude scaling used in these results apparently does not scale this phenomenon.

After three wave periods and after the waves have passed, the rate of lengthening is much slower at ≈ 0.005 - 0.01 C which indicates a slow drift current at the surface.

4.3 Vertical Extent of Mixing

The maximum depth of dye excursion, D, vs. time is plotted in figures 4.3.1 and 4.3.2. In the spilling wave, the free surface is initially broken nearthe crest which is above the still water line. The jet impacting the free surface initiates mixing in the plunging wave and occurs closer to the still water line. This observation is manifested in

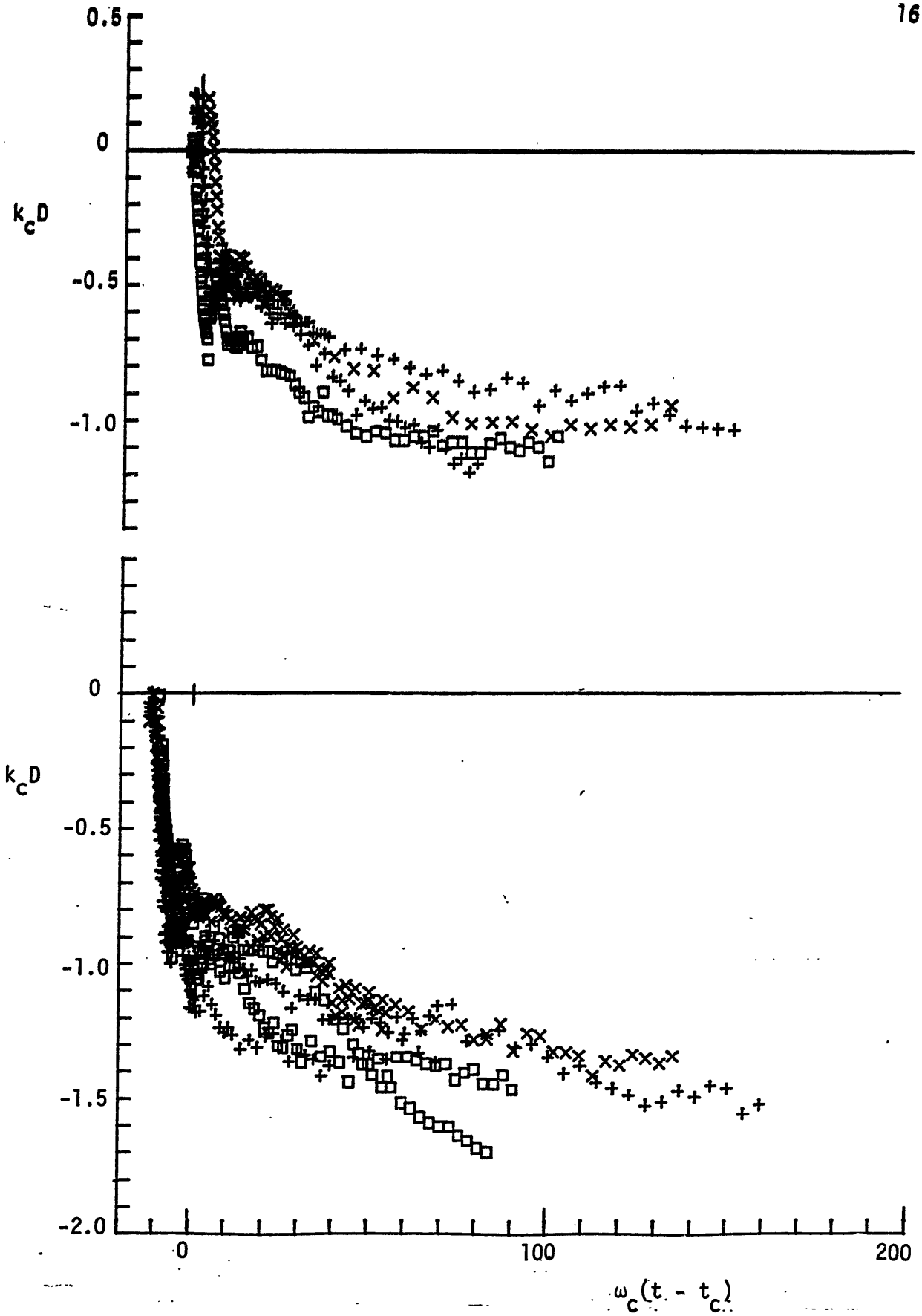

Figure 4.3.1 Maximum depth of dye boundary below still water level vs. time for spilling wave (top) and plunging wave (bottom). Wave group center frequency f_c = 0.88 Hz (×), 1.08 (+), 1.28 (□) and $\Delta f/f_c$ = 0.73, $x_b k_c$ = 27.4.

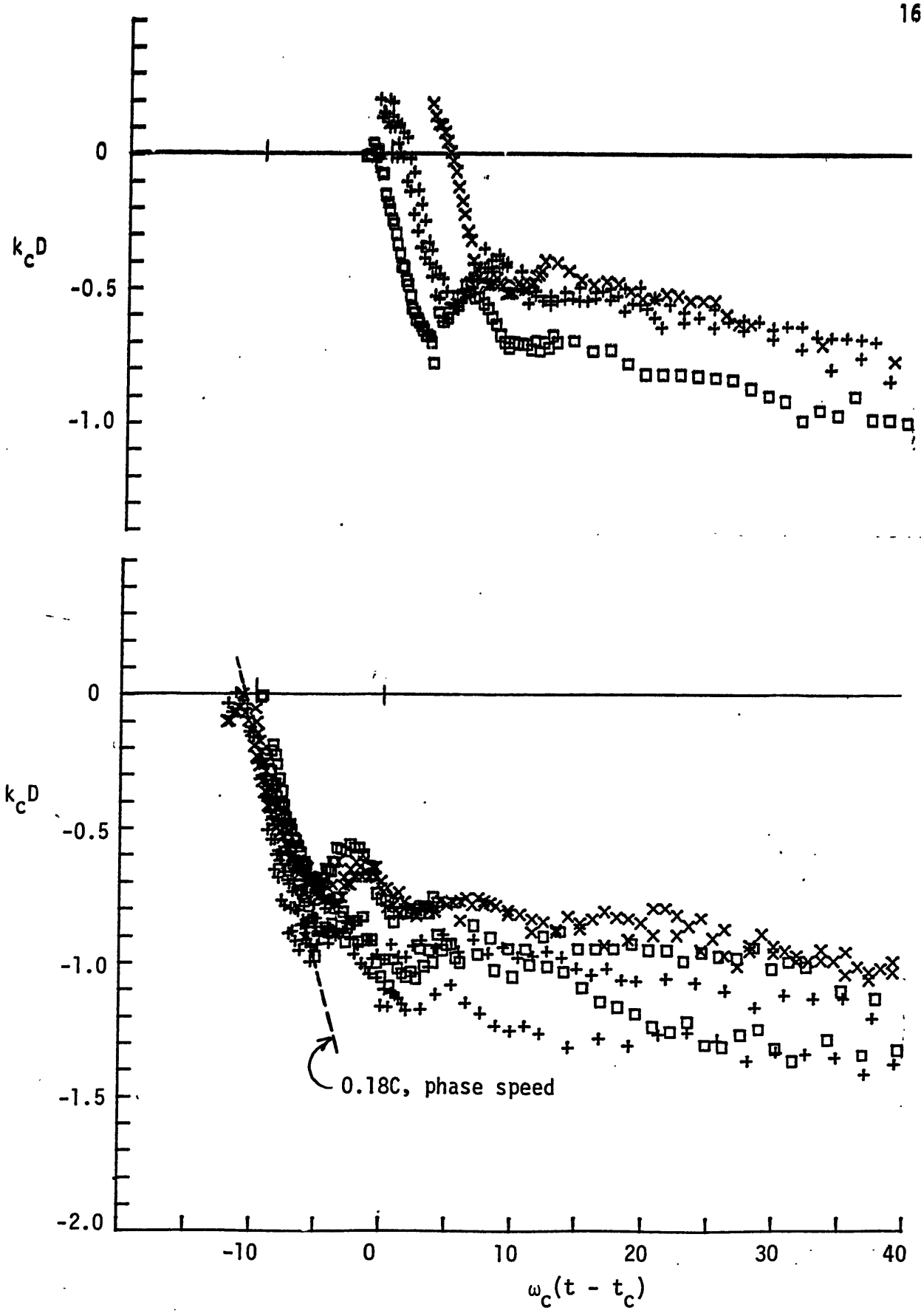

Figure 4.3.2 Maximum depth of dye boundary vs. time. As for figure 4.2.3 but with expanded time axis.

these figures where the maximum depth starts above the still water line for the spilling wave. The initial rate of deepening is of the order of the wave orbital velocity, 0.18Cand again emphasizes the role of the following wave trough in carrying the dye down. Based on observations of cine films, the following description is offered. The breaking turbulence carries the dye down to $k_cD \approx 0.3$ for spilling and $k\,D \approx 0.5$ for plunging within 1/2 wave period from breaking. The next passing wave the dye down an additional $k_cD \approx 0.3$, to $k_cD \approx 0.6$ for spilling and $k_cD \approx 0.8$ for plunging. Again, because the next crest is of lower amplitude the dye depth does not recover to its original level. The oscillations in the maximum depth are due to these following few waves.

After approximately three wave periods, the waves have passed and further deepening is due to turbulent diffusion in the highly turbulent flow generated after breaking. Following the practice of analyzing various turbulent flows, an attempt is made to fit this data to a power law in time of the form

$$k_cD = C_1[\omega_c(t - t^*)]^p. \tag{4.1}$$

To empirically determine p the data is plotted on a log-log scale. The equation becomes

$$\log(k_cD) = \log C_1 + p \log[(\omega_c(t - t^*)] \tag{4.2}$$

where p is the slope of a straight line that fits the data and $\log C_1$ is the y intercept. Since the data may not be expected to follow this

equation in the immediate vicinity of the time origin a virtual time origin is usually determined by iteration. Since p is dependent upon t^*, the proper choice of t^* is critical. The value of t^*, time origin, which gives the longest straight line fit to the data is the usual choice for t^* (Compte-Bellot and Corsin 1966). The value of t^* which gave this result turned out to be very close to the observed time of breaking, t_{ob}, as defined in section 3.1. To eliminate any ambiguity over the choice of time origin, the time of observed breaking was used as the origin. Note that only the data at times after one wave period from breaking were considered in this curve fitting, since the dye motion is dominated by the

The log-log plot corresponding to the maximum depth (figure 4.3.3) show that a slope of p = 1/4 fits the data reasonably well. The range of the coefficient, C_1, is determined graphically by drawing two p = 1/4 slope lines enclosing the spread of data at the later times. The y intercept of these lines give the following range of C_1:

$$C_1 = (0.28 - 0.43) \text{ for spilling} \qquad (4.3a)$$

$$= (0.38 - 0.57) \text{ for plunging} \qquad (4.3b)$$

The value of p is very well followed for the three scales in these experiments. The spread of C_1 is due to scale effects and due to the random error between runs.

4.4 Area of Mixing

The two-dimensional mixed area is similarly plotted for the spilling and plunging wave in figure 4.4.1. The log-log plot of this data (figure

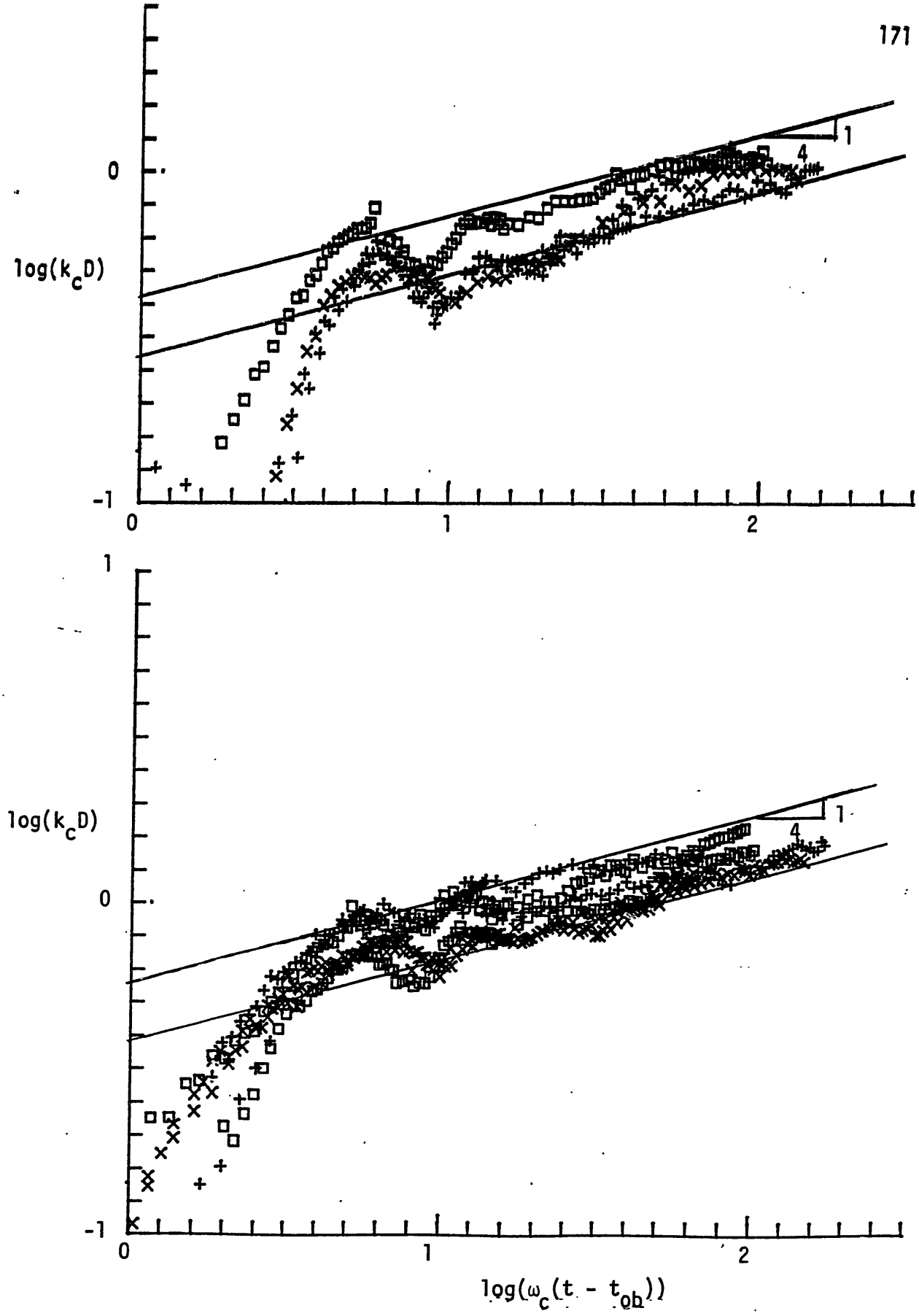

Figure 4.3.3 Log-log plot of maximum depth vs. time from observed breaking. Same symbols as figure 4.2.3. Plot shows fit of data to $\omega_c(t - t_{ob})^{1/4}$ power law.

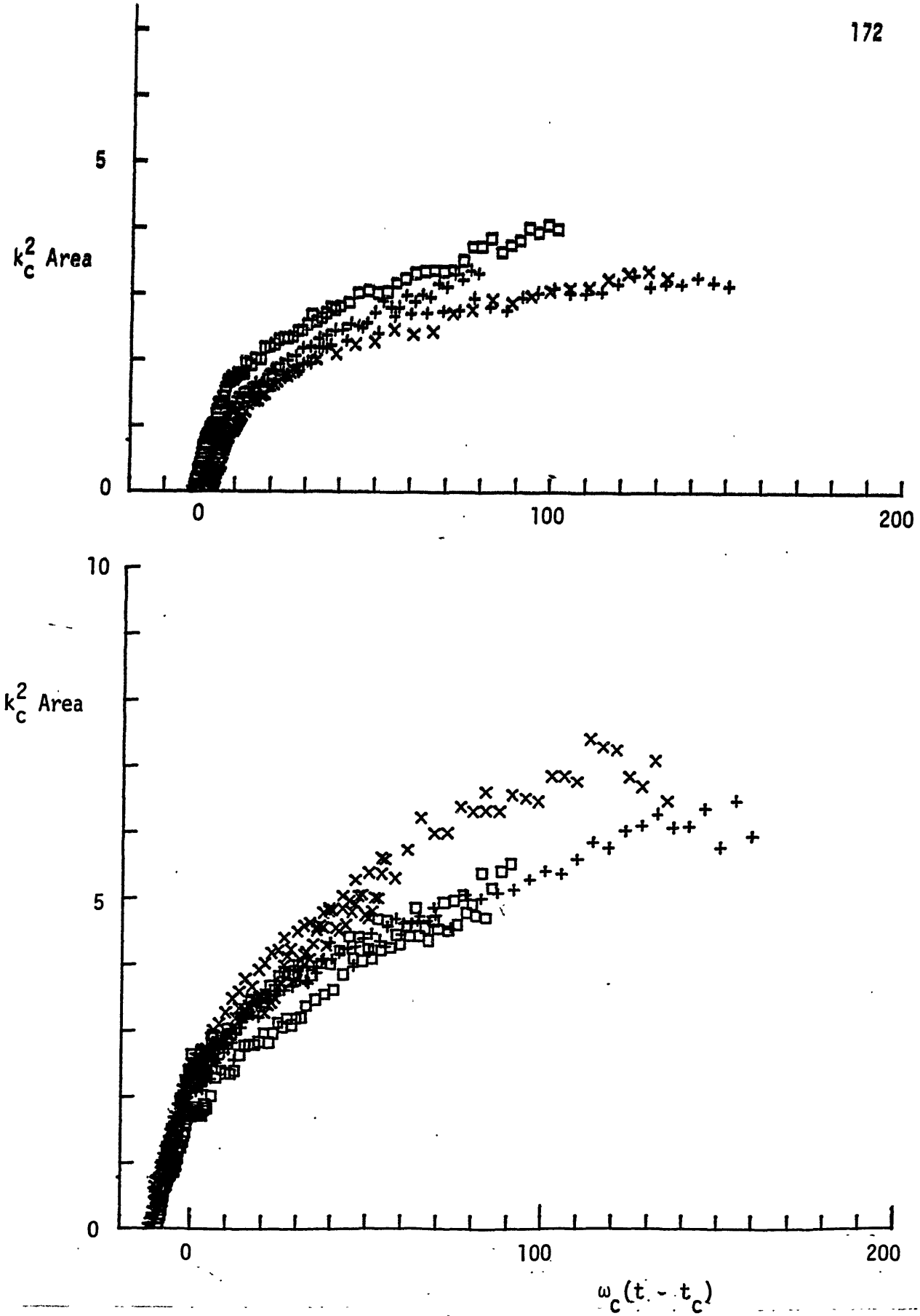

Figure 4.4.1 Dyed area vs. time from t_c for spilling wave (top) and plunging wave (bottom). Wave group center frequency f_c = 0.88 Hz (×), 1.08 (+), 1.28 (□), and $\Delta f/f_c$ = 0.73, $x_b k_c$ = 27.4.

4.4.2) shows that after one wave period from the observed breaking time, nondimensional area grows as $\omega_c(t-t_{ob})^{1/2}$ for both levels of breaking. As for the maximum depth, the time origin is the time of observed breaking. Given that the area is normalized by k_c^2, the agreement between scales is quite good and within the scatter of repeated runs of the same wave. Note that the large scale (f_c = 0.88 Hz) plunging wave case grows fastest, which is consistent with the fast growing length measurement due to the additional spray generated (section 4.2). The coefficients for the power law were graphically estimated as

$$C_2 = (0.32 - 0.45) \text{ for spilling} \tag{4.4a}$$

$$(0.48 - 0.74) \text{ for plunging} \tag{4.4b}$$

and the area is given by

$$k_c^2 \text{ Area} = C_2[\omega_c(t - t_{ob})]^{1/2} \tag{4.5}$$

4.5 Variation of the Mixed Region with Wave Packet Amplitude

The nondimensional amplitude, ak_c, was found to be the most sensitive wave packet parameter affecting the loss of momentum flux from the wave field. It also has been found to be important in determining the rate of mixing, through the coefficients C_1, C_2 in the power laws for mixed depth and area. These coefficients are plotted against ak_c in figure 4.5.1. The shape of these estimated curves looks similar to the plots of momentum flux loss vs. ak_c (figure 3.3.1) where once incipient breaking is triggered at $ak_c \approx 0.25$, there is a steep rise in the depth and area of mixing. The curve then starts to level off in the plunging region. The

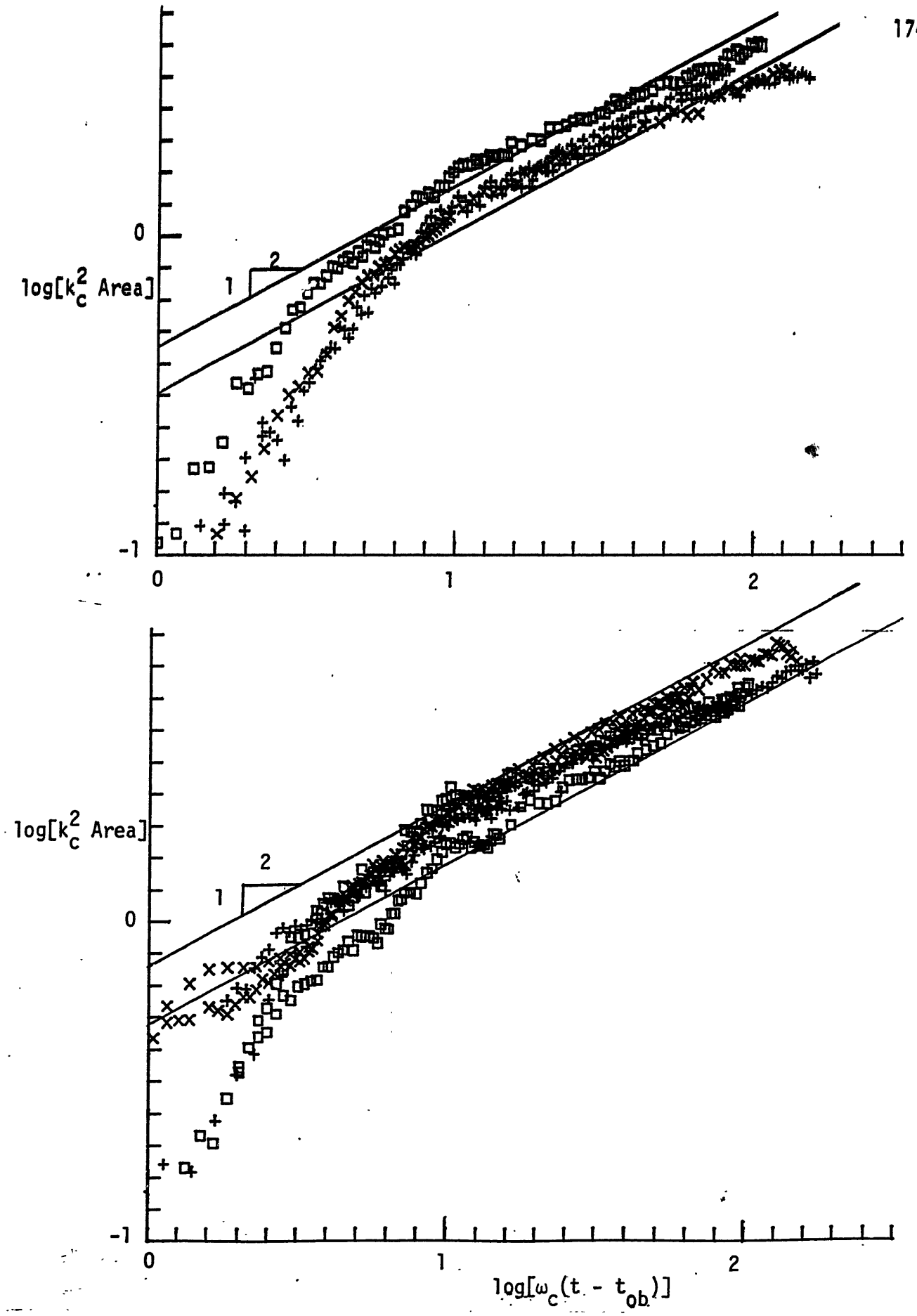

Figure 4.4.2 Log-log plot of dyed area vs. time from observed breaking. Same symbols as figure 4.2.6. Plot shows fit of data to $[\omega_c(t - t_{ob})]^{1/2}$ power law.

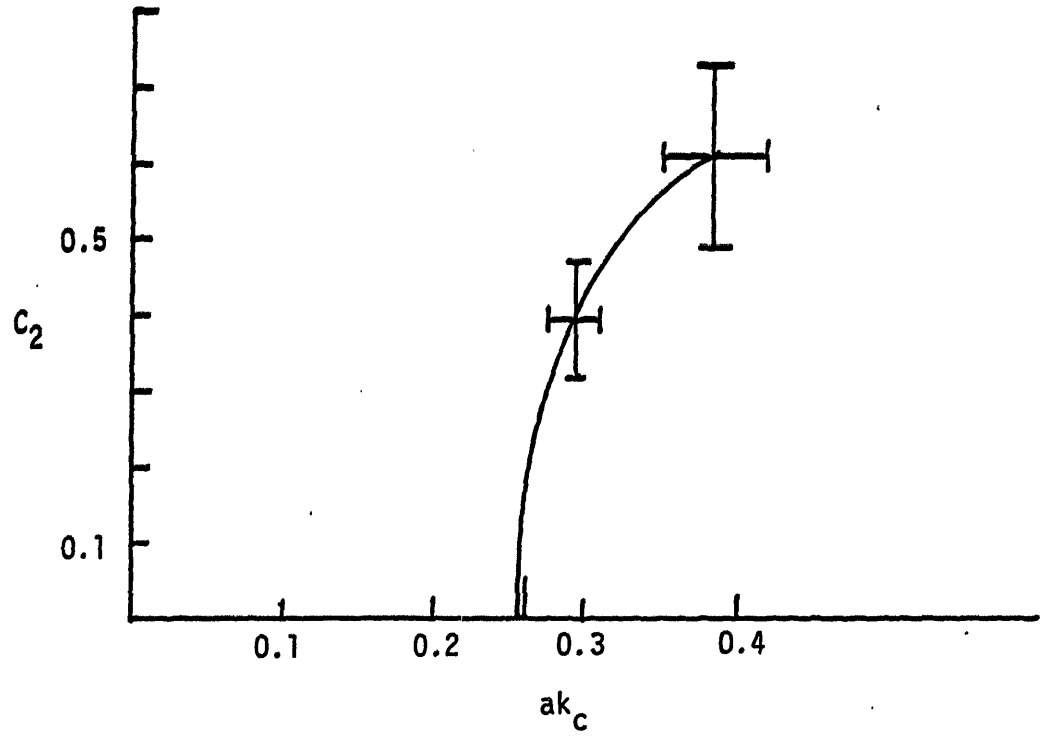

Figure 4.5.1b Dyed Area Coefficient, C_2, as a function of wave packet amplitude, ak_c. Dyed area is given by k_c^2 Area = $C_2[\omega_c(t - t_{ob})]^{1/2}$.

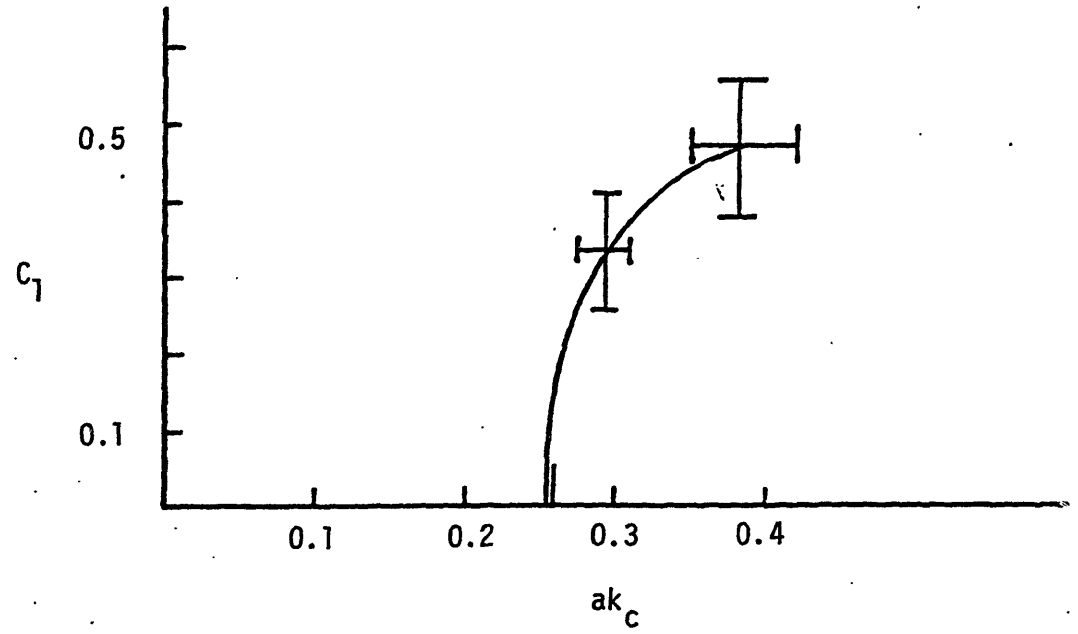

Figure 4.5.1a Dyed Depth Coefficient, C_1, as a function of wave packet amplitude, ak_c. Dyed Depth is given by k_c D = $C_1[\omega_c(t - t_{ob})]^{1/4}$.

vertical error bars are indicative of the scatter in the measurements between repeats of the same wave. This is also the error between scales of packets. The horizontal "error" bars indicate the range of ak_c over which a single spilling or plunging wave was generated for the three scales of wave packets. (Note that for each scale, the value of ak_c producing an incipient spilling or plunging breaking wave does not change from run to run).

The measurements made here were on one breaking wave in the packet. At intermediate values of ak_c more than one breaking wave is generated, so it is not clear how the total area or maximum depth will be affected if all breaking regions are summed. Certainly the length can grow to three wavelengths if three waves in the packet break. The depth may appear steplike, or oscillating as the number of breaking waves varies between, say one and three. The total area, on the other hand, may still follow the indicated curve. Additional measurement should be made to study this. Since the mixed area and depth are nicely correlated with ak_c, they should also be correlated with the loss of momentum flux from the waves. The plots in figure 4.5.2 show this correlation.

The horizontal length of mixing and the surface was found to be independent of ak_c, except where appreciable spray is generated at plunging. It can be expected that this quantity will grow at ~0.8 C to 0.8 - 0.9 of a wavelength for any value of $ak_c > 0.25$. These dependencies on ak can also be seen in figure 4.5.3 where the dye length, maximum depth and area are plotted for three values of ak_c. The two lower values correspond to different levels of spilling. Note the length remaining nearly constant for all three values of ak_c.

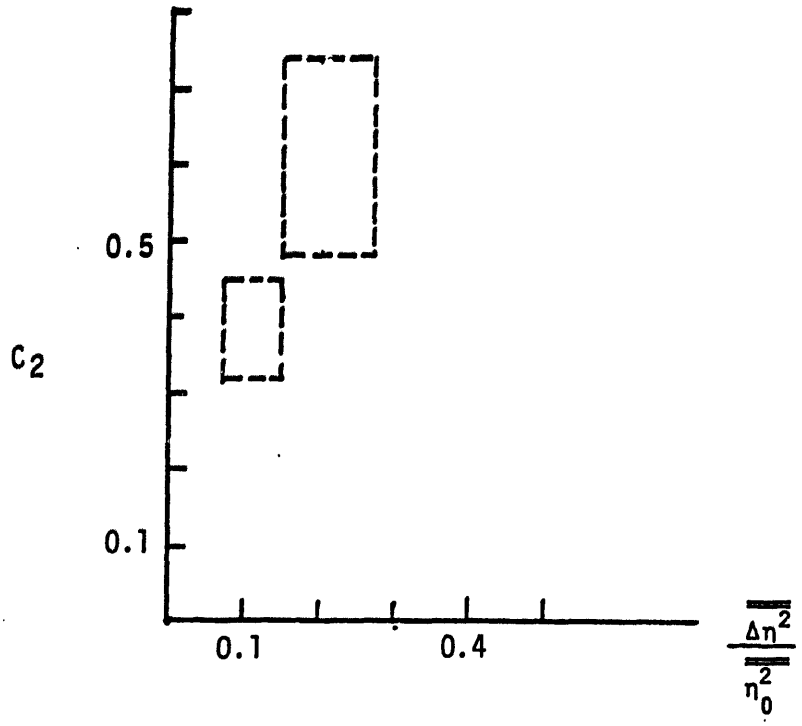

Figure 4.5.2b Dyed Area Coefficient, C_2 as a function of momentum flux lost from carrier waves in a breaking event.

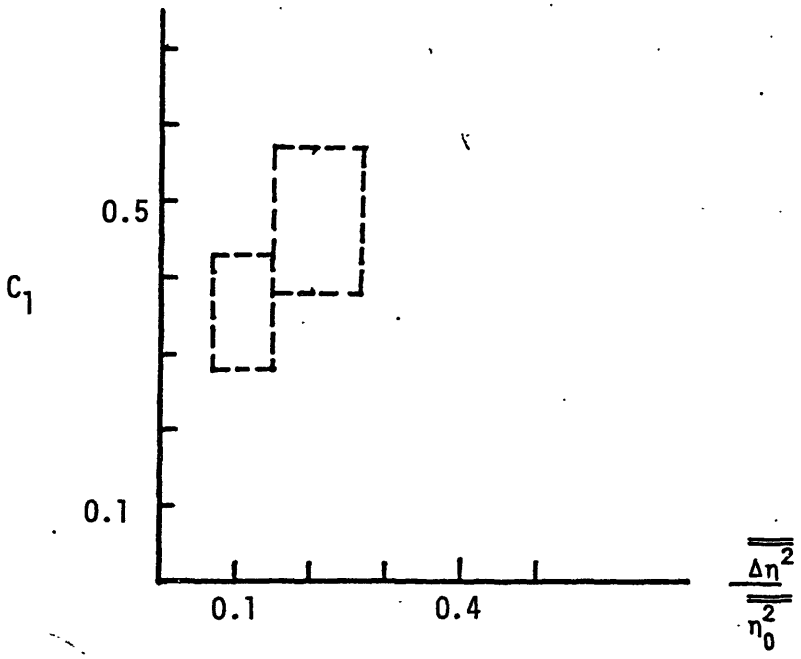

Figure 4.5.2a Dyed depth Coefficient, C_1 as a function of momentum flux lost from carrier waves in a breaking event.

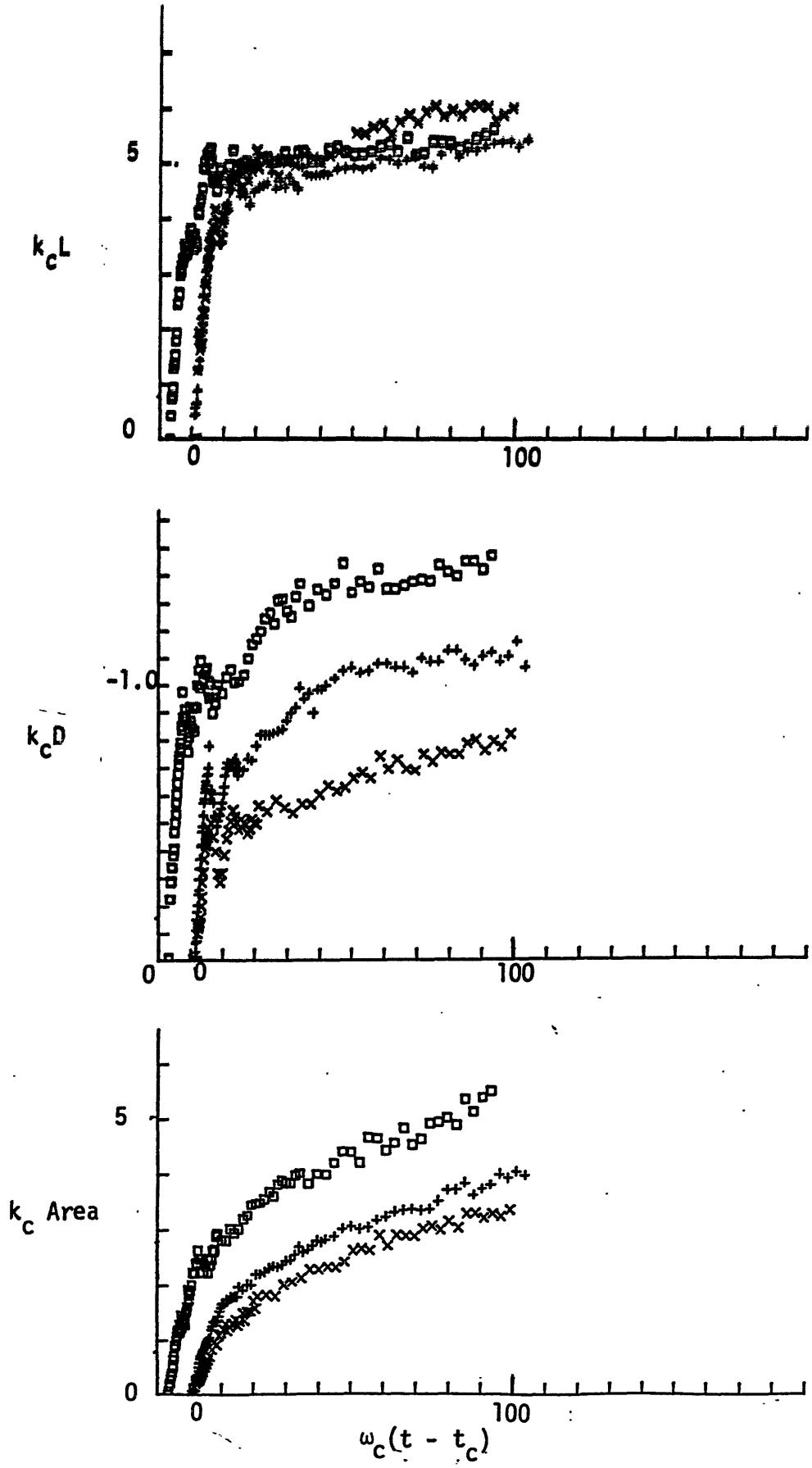

Figure 4.5.3 Dye length (top), depth (center), and area (bottom) for f_c = 1.28 Hz and three different wave amplitudes ak = 0.296 (×), 0.319 (+), 0.420 (□). $\Delta f/f_c$ = 0.73, $x_b x_c$ = 27.4.

4.6 The Integral Length Scale of Turbulence

A continuous range of length scales are present in turbulent flows, the largest being at the size of the width of the flow field. The integral length scale, ℓ, of the turbulence is very useful in describing the turbulence through such parameters as the eddy diffusivity $K \sim u\ell$ and Reynolds number. Here u is a characteristic velocity, usually the rms velocity. Also dissipation can be estimated by $\varepsilon \sim U^3/\ell$ (Taylor, 1935). The integral length scale is defined as the area under the autocorrelation function, divided by the autocorrelation at a separation of 0.

$$\ell = \int_0^\infty \frac{\overline{u(\xi)\, u(\xi + x)}\; dx}{\overline{u^2}}$$

Hinze (1959), pg. 37.

This length scale is roughly a measure of the width of the turbulence if the flow is not periodic (Hinze, 1959). In our measurements, D, the maximum dye depth, will be considered to be roughly comparable to ℓ. We found $\ell \sim t^{1/4}$. Also the dye area went as $t^{1/2}$, so $(\text{area})^{1/2} = \sim t^{1/4}$ which is consistent with our results. We would also expect the horizontal length to go as $t^{1/4}$, but at the surface it was found to be nearly constant. From observations of dye mixing films and as can be seen in figures 4.1.1 and 4.1.2, the horizontal length at some depth below the surface appears to grow faster than at the surface, however. With measurements of turbulent velocities (Chapter 5), the time variation of ℓ will be used to estimate the time dependence of K and ε.

Chapter 5

Velocity Measurements in the Breaking Region

5.0 Summary

Having measured the loss of momentum flux and energy flux from the carrier wave field (Chapter 3), an attempt is made to account for this loss by measuring the velocity of the flow field in the breaking region during breaking and after the waves have passed. The dye measurements serve as a guide in defining the region over which a detailed velocity survey is done. It is expected that the net horizontal momentum loss from the carrier waves will result in a surface current and that the loss of energy will go largely into turbulence and be dissipated. Since the net horizontal momentum density of the carrier waves plus the forced wave integrated over depth is nearlyzero upstream and downstream of breaking (Chapter 2, page79), the net momentum integrated over depth in the breaking region must also be zero. It is of interest, however, to understand how the momentum or current is distributed in depth. The turbulent kinetic energy depth penetration and decay in time is also obtained from the velocity measurements.

Crucial to any analysis of this type, be it with field or laboratory data, is our ability to distinguish various velocity contributions. We expect the motion to be the sum of the carrier wave orbital velocity, the nonlinearly generated forced wave, the current generated by breaking, turbulent velocities, and noise due to the instrumentation. Ensemble averaging over many runs of the experiment was found to be the only method of determining the mean and turbulent quantities in this nonstationary flow generated breaking. This averaging also effectively separates the deterministic wave orbital velocities (carrier wave and forced waves) from

the nonrepeatable turbulence. The velocity of the random waves, generated by breaking, is shown to be small in comparison to the random turbulent velocities, particularly away from the free surface where the motion had decayed to low levels. The ensemble averaged signals of the mean velocity are low pass filtered to remove the carrier waves, resulting in a signal of the forced long wave and the currents generated at breaking. Since the currents are long lived and the forced wave passes the probe relatively quickly, these two contributions are separable in time. The ensembled averaged variance of the turbulence is also filtered to remove the high frequency random errors in the averaging.

The results show the generation of a slowly decaying current, initially equal to 0.02 C, near the surface, penetrating to depths of $k_c z = 0.5$. A return flow, at lower depths and extending to the tank bottom was measured which balances the mass flux near the surface. This flow appears to be the remnants of the forced long wave. Combined, these flows form a large eddy slowly decaying in time. The formation of this eddy was observed for both plunging and spilling wave packets and at both scales measured. The turbulent rms velocities of 0.02 C, show turbulence penetration to several wave amplitudes in ~10 wave periods. This turbulent region is very well defined by the dye boundary measurements of Chapter 4.

The total kinetic energy integrated over the volume is seen to decay as ωt^{-1}. Only about three percent of the wave energy lost from the packet is accounted for in the breaking region after four wave periods from breaking. On the other hand, 60 - 90% of the momentum lost from the carrier waves shows up in currents.

5.1 Procedures

The two component velocity measurements were made using the laser doppler anemometer described in Chapter 2. Data was typically sampled at 50 Hz for 81.96 sec. A coincident surface displacement measurement was also made. The wave gauge was slightly displaced downstream by 1 mm, and transversely by 10 mm in order not to interfere with the laser beam paths. Data was calibrated and processed between repeats of the experiment. The time between breaking events was approximately 10 minutes which was found to give sufficient time for the mean motions to decay out to negligible levels.

5.2 Analysis of the Velocity Measurements

A typical 81.96 sec time history of the measured surface displacement η and subsurface Eulerian velocity u, and w is shown in figure 5.2.1. These are the unfiltered raw signals. Note the clean velocity signal, particularly in the non-turbulent flow before breaking and how well η and u follow one another. The velocity resolution here is better than 0.5 cms, within the thickness of the plot line. The dropout in the velocity signal is due to the wave trough passing the measurement point; the signal is quickly picked up as the next crest crosses the beam intersection point. At times after breaking, the signal is seen to become quite turbulent at all frequencies, almost swamping out the underlying wave velocities. There is also evidence of a mean horizontal velocity after breaking. The measurements of 10 repeats of the same breaking wave made at the same measurement point (figures 5.2.2, 5.2.3) show the variability of the low frequency motion downstream of breaking. From this set of data it is obvious that one measurement is a poor indicator of the

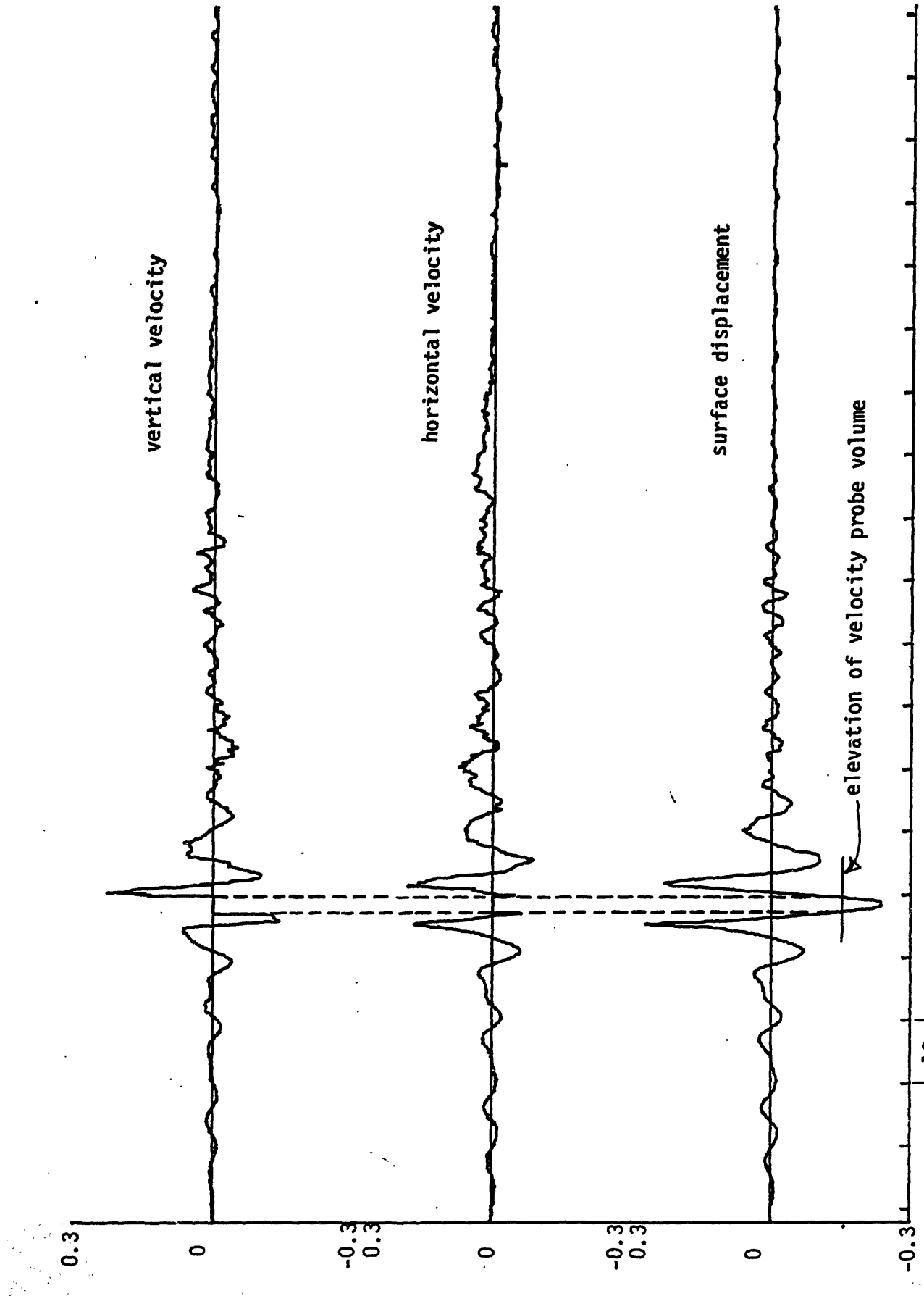

Figure 5.2.1 Coincident surface displacement and subsurface velocity measurement at $k_c(x - x_{ob}) = 3.80$ and $k_c z = -0.16$ downstream of plunging break. For $f_c = 0.88$ Hz, $ak_c = 0.352$, $\Delta f/f_c = 0.73$, $x_b k_c = 27.4$. C is the linear phase speed, k_c is the wave number corresponding to f_c for finite depth.

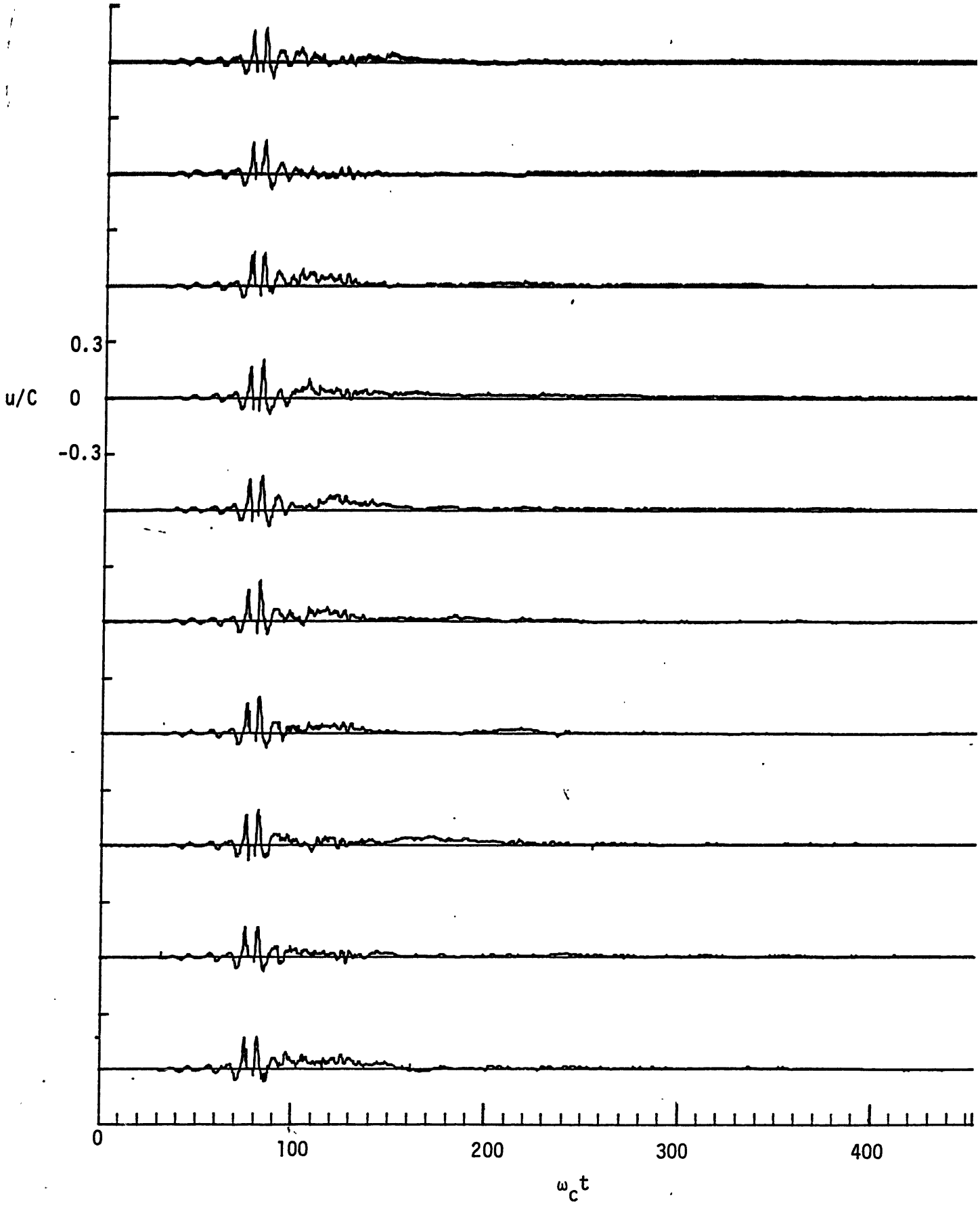

Figure 5.2.2 An ensemble of horizontal velocity measurements repeated at the same point as in figure 5.2.1. Note variation in low frequency motion after breaking.

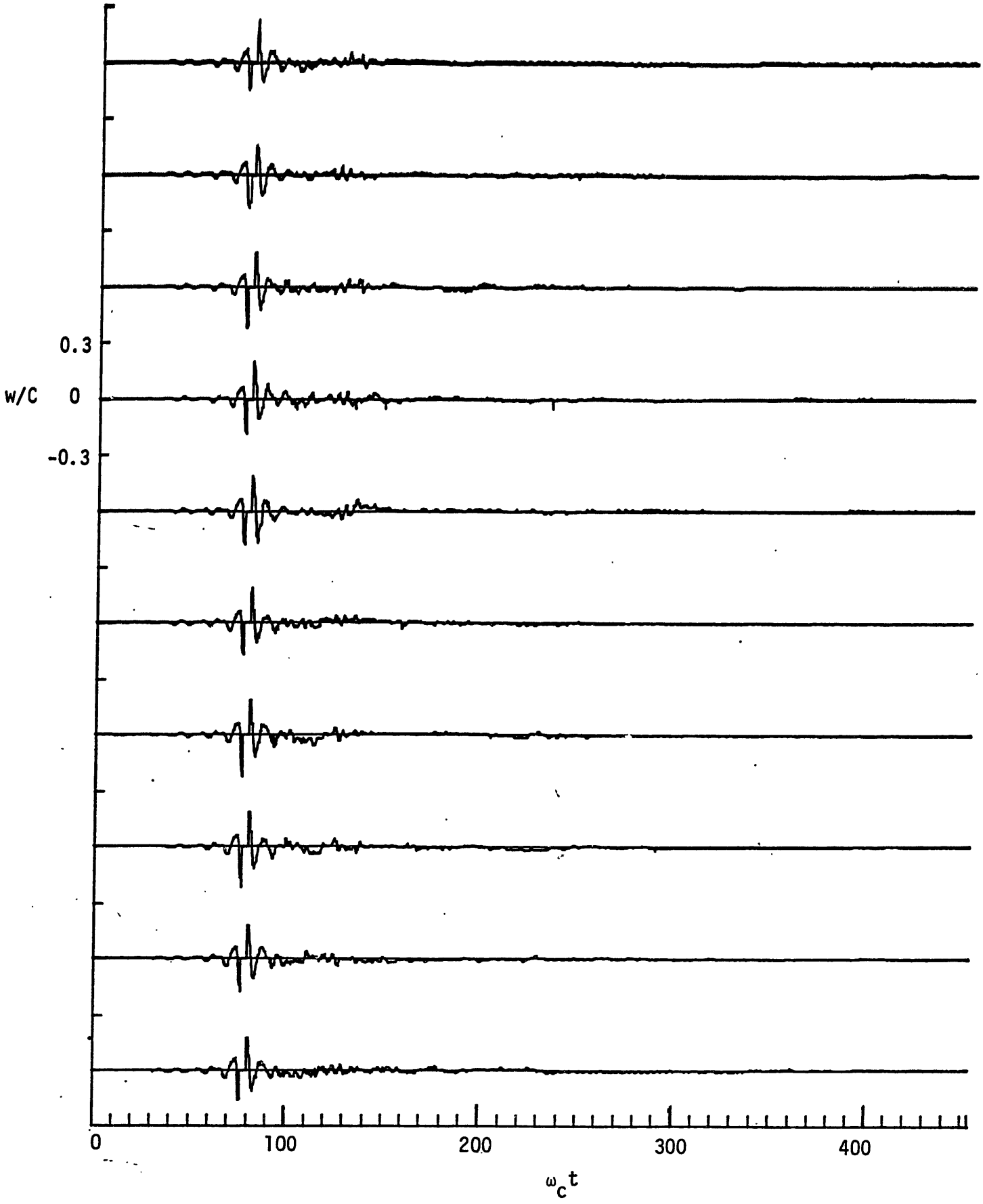

Figure 5.2.3 An ensemble of vertical velocity measurements repeated at the location as in figure 5.2.1.

mean motion. Note that many of the small irregularities in these plots are due to plotter resolution. The top time history, expanded in figure 5.2.1, shows the true quality of the data.

The data is analyzed by forming ensemble averages of measurements from many repeats of the experiment with "identical" initial and boundary conditions. The averages are taken over data at constant times from paddle startup and no attempt is made to adjust the starting phase for best agreement. The ensemble mean is defined as:

$$\langle u(x,z,y,t)\rangle = \frac{1}{Q} \sum_{q=1}^{Q} u_q(x,z,y,t) \tag{5.1}$$

where Q is the number of repeats. The same is done for the vertical velocity w and surface displacement η. The raw velocity is then

$$u = \langle u\rangle + u' \tag{5.2}$$

where u' is the fluctuation from the ensemble mean. The variance of the signal is computed as

$$\langle [u'(x,z,y,t)]^2\rangle = \frac{1}{Q} \sum_{q=1}^{Q} [u'(x,z,y,t)]^2 \, . \tag{5.3}$$

In the plots that follow it is convenient to take the square root of this quantity which will be defined as

$$u_{rms} = \left[\langle [u'(x,z,y,t)]^2\rangle\right]^{1/2} \, . \tag{5.4}$$

Examples of these ensemble averages of the data presented in the previous figures are shown in figure 5.2.4. Here the number of repeats is Q = 10.

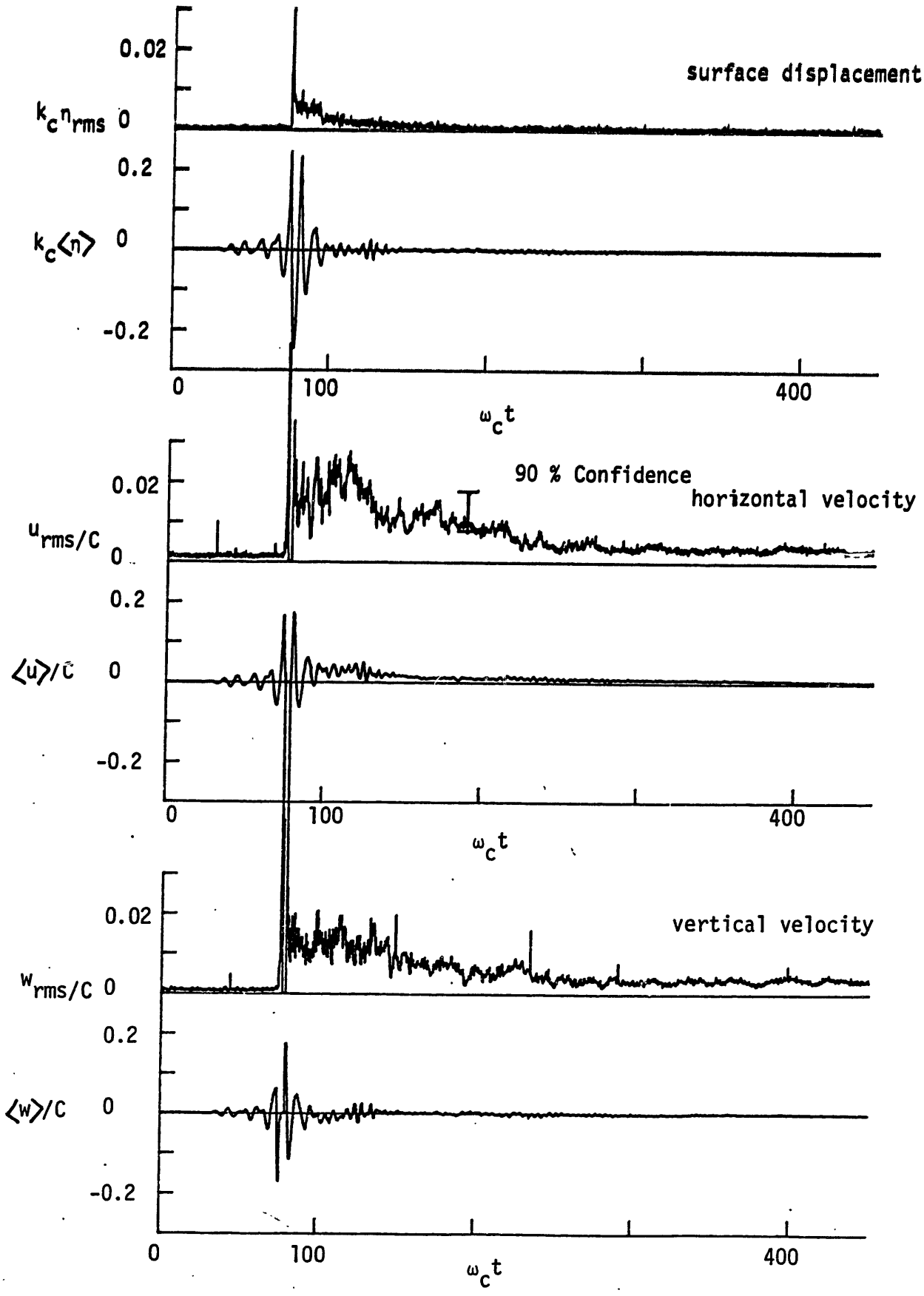

Figure 5.2.4 Ensemble averaged velocities <u>, <w> and surface displacement <η>. Also the corresponding rms velocities, and surface displacement. Average of 10 repeats; same location as figure 5.2.1.

The ensemble mean velocities are composed of contributions due to the carrier waves $u_{c.w.}$, a forced long wave, $u_{f.w.}$, and a current, u_c which are all functions of time. Then

$$\langle u \rangle = u_{c.w.} + u_{f.w.} + u_c \tag{5.5}$$

The fluctuating velocity is considered to be composed of random waves u'_w, turbulence u'_t, and instrument noise u'_n.

Then

$$u' = u'_w + u'_t + u'_n \tag{5.6}$$

The square of u' will give cross terms of $u'_w u'_t$, $u'_w u'_n$, and $u'_t u'_n$ which when averaged over the ensemble, are assumed to be negligible since any correlation between these motions is weak. Then

$$\langle u'^2 \rangle \simeq \langle u'^2_w \rangle + \langle u'^2_t \rangle + \langle u'^2_n \rangle \tag{5.7}$$

The magnitude of $\langle u'^2_n \rangle$ can be seen in figure 5.2.4 at times before breaking where

$$u_{rms} = [\langle u'^2_n \rangle]^{1/2} . \tag{5.8}$$

This shows u_{rms} due to noise = 0.34 cms and w_{rms} = 0.2 cms, which reflects the lower intensity blue laser beam used for the u measurement and higher noise level. This noise level is relatively small when compared to the variance after breaking. (See also figure 5.2.5. where 40 repeats are averaged). The noise in the wave gauge measurement is also small.

The large spikes in the variance at breaking are largely due to the nonrepeatability of the wave-phase, of measurement noise due to bubbles,

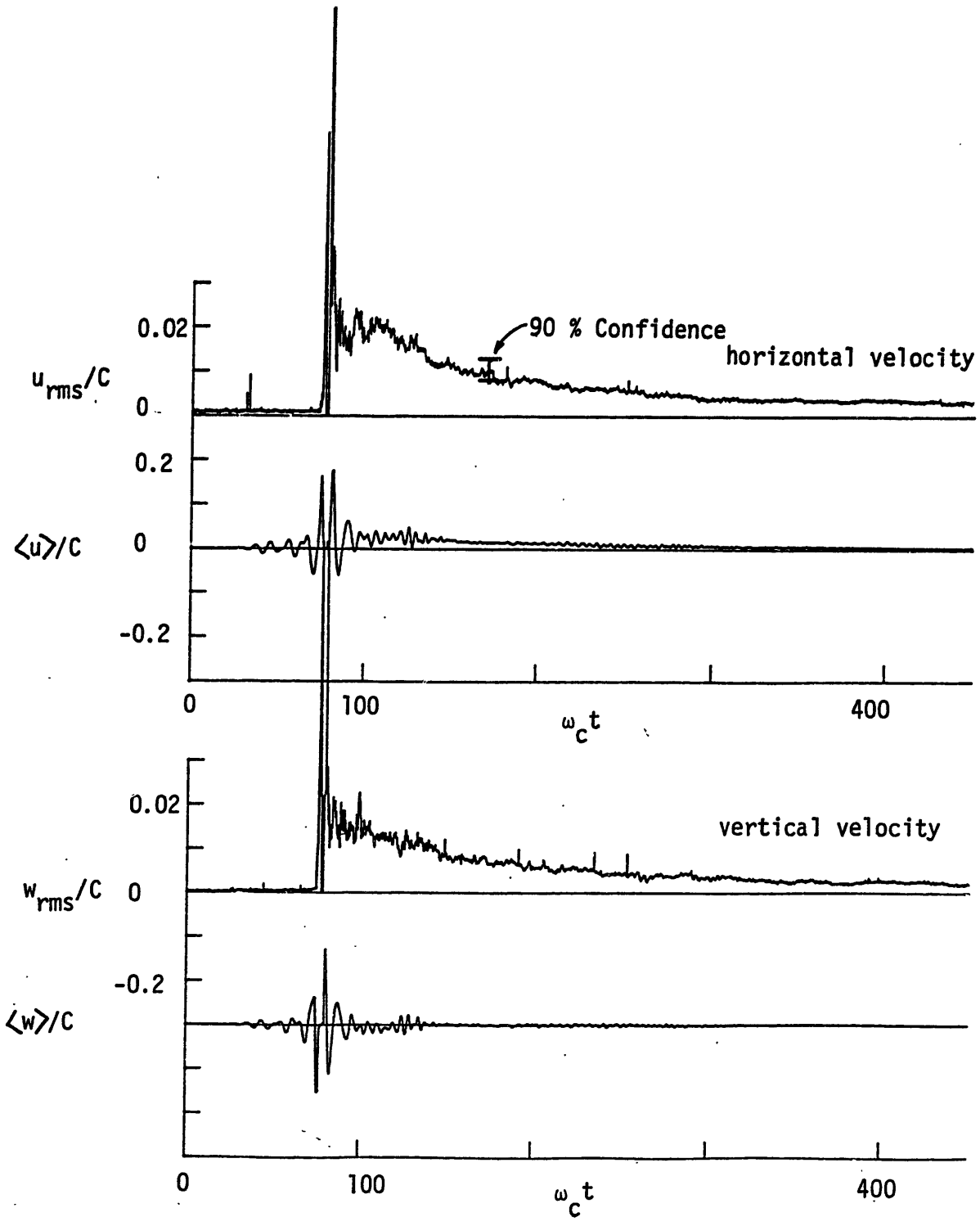

Figure 5.2.5 Ensemble averages as in figure 5.2.4 for 40 repeats.

and dropout in the wave trough. It is unlikely that dropout will occur at exactly the same time for each run, and thus variability shows up as spikes in the variance. After the wave packet has passed the velocity probe, the variance level is still quite high at $u_{rms} \approx 0.02C$. The question still remains as to how much of this is turbulence and what do the random wave orbital velocities contribute. The maximum contribution from random waves can be seen in the curve of η_{rms} (figure 5.2.4, 5.2.5). If the random waves are of frequency ω_c, then $k_c\eta_{rms}$ represents the velocity, u_{rms}/C due to waves at the free surface as given by linear theory.

This contribution will decay out in depth. If the random waves are of frequency $2\omega_c$ then the contribution will be twice that shown in the figure; however, it will decay out even faster with depth. With this in mind, the contribution of random waves to the variance is ~10%.

At times after the wave packet has passed we will interpret the variance of the fluctuating velocity as being due to turbulence with an error of -10%.

Then

$$\langle u_t'^2 \rangle \approx \langle u'^2 \rangle \tag{5.9}$$

The ensemble means in these figures show a slowly varying horizontal current of 0.03 C, generated after breaking, trailing waves show a small packet separating from the main group. At later times $\omega_c t$ (200-300) a very low amplitude, high frequency wave train is passing. The phase of u follows the phase of η, indicating that they are traveling downstream. These waves have sustained an averaging over 40 repeats (figure 5.2.5)! They are believed to be second harmonic waves radiated upstream from the

breaking region, then reflected back off the paddle. (See Section 3.6.)

The vertical mean velocity shows a negative flow just after the packet has passed, then essentially zero. No mean set down in the free surface can be seen in this figure, after the packet has passed. This indicates that the mass flux in the horizontal current is being supplied from below or from upstream since, by conservation of mass

$$\rho \frac{\partial \bar{\eta}}{\partial t} + \frac{\partial M}{\partial x} = 0$$

and $\partial \bar{\eta}/\partial t = 0$.

The extent to which these averages of 10 repeats converge to the true mean can be seen by comparing with the averages taken over 40 repeats (figure 5.2.5). The differences between the mean computed with Q = 10 and Q = 40 is negligible. The effect on the variance is to reduce the random error and oscillations evident in figure 5.2.4. At times after the waves have passed, this comparison shows that the oscillations in the variance over 10 repeats are in fact random errors and may be smoothed with time averaging which will closely approximate the more time consuming 40 repeat averaging. At the rear of the packet, however, there appears to be a correlation between the turbulence, u_{rms}, and the carrier wave. u_{rms} is approximately 180° out of phase with $\langle u \rangle$. An explanation of this may be that a region of higher turbulence near the surface is advected down to the fixed measurement point by the wave orbital velocity. This explains why the turbulence is greater when the wave trough passes the measurement point.

The error in these means from the true mean may be estimated by assuming that the turbulence has a Gaussian probability distribution about

the mean value for each time. Adjacent times may be considered as independent random processes. The 90% confidence interval for the mean value where the variance is 0.01 is

$$\frac{\langle u \rangle}{C} \pm 0.005 \quad \text{for} \quad Q = 10$$

$$\pm 0.002 \quad \text{for} \quad Q = 40$$

The 90% confidence interval for the square root of the variance is

$$(0.73 \rightarrow 1.64)\frac{u_{rms}}{C} \quad \text{for} \quad Q = 10$$

$$(0.836 \rightarrow 1.21)\frac{u_{rms}}{C} \quad \text{for} \quad Q = 40$$

If adjacent times are averaged, the effect is to average over more samples and thus reduce these confidence intervals.

The data was further processed by filtering the repeatable, carrier wave velocity from the ensemble mean velocities. This was done by low pass filtering the ensemble mean with a filter having a cutoff frequency $f_{cut}/f_c = 0.34$ or $f_{cut} = 0.3$ Hz for $f_c = 0.88$ and $f_{cut} = 0.436$ for $f_{cut} = 1.28$ Hz. The filter was designed by specifying an ideal boxcar frequency response. The Fourier transform was then taken resulting in the impulse response of the filter. To improve the stop band attenuation the impulse response was multiplied by a Hamming window of length 511 samples. The frequency response H(f) and impulse response h(t) of this filter is shown in figure 5.2.6. The program FILDES was used to design the filter. The filter was implemented using the overlap-add method (Oppenheim & Shaffer,1977) which effectively does the linear convolution (Program RJFIL2, Appendix 3.)

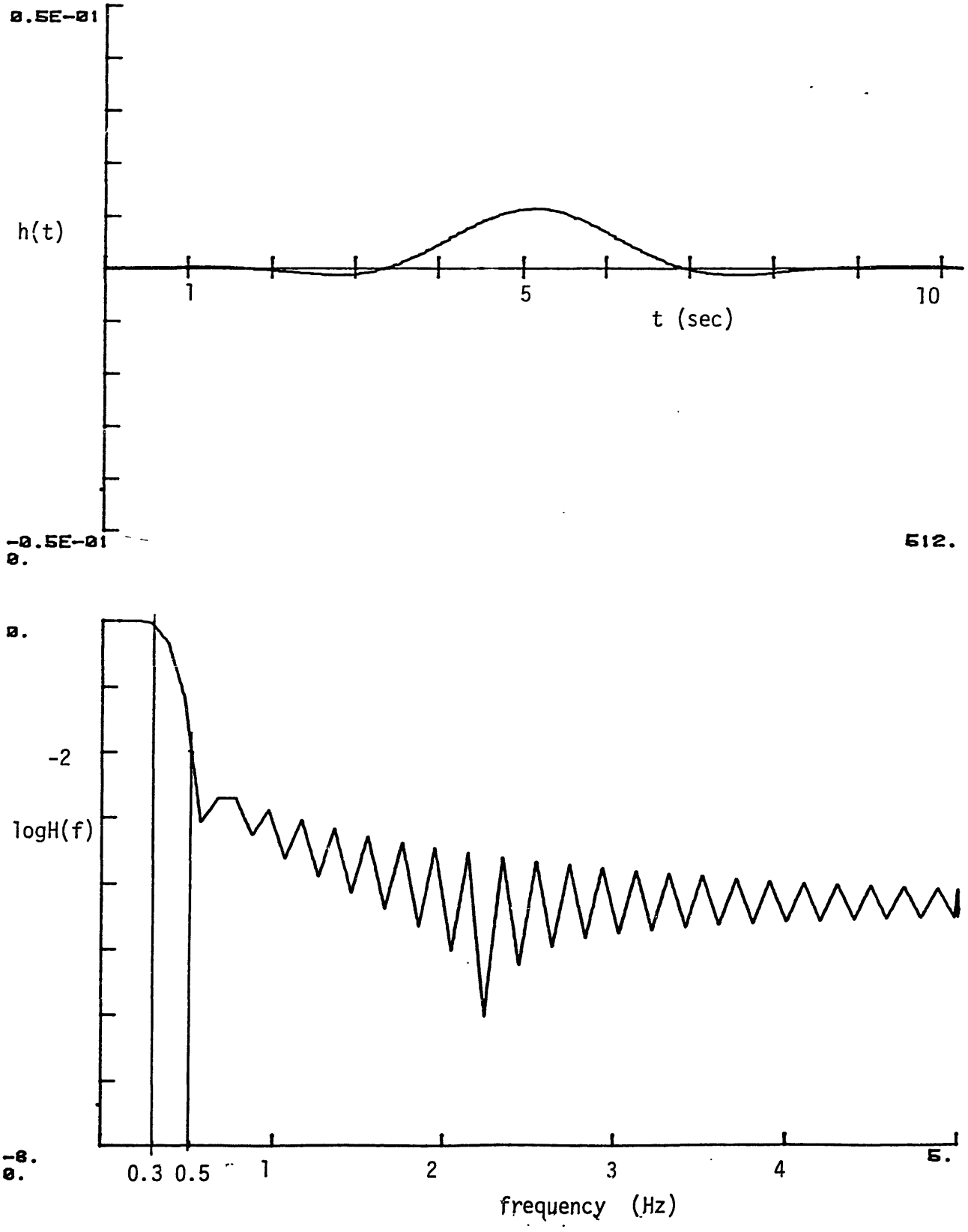

Figure 5.2.6 Low pass filter design using Hamming window for f_{cut} = 0.3 Hz. Impulse response (top), frequency response (bottom). For f_c = 0.88 Hz center frequency packet.

$$\langle u \rangle = \langle u \rangle * h(t) \tag{5.10}$$

An example of the filtered data can be seen in figure 5.3.1.

The ensemble averaged variance was filtered in the same manner. Note that the filtering was done on the squared velocity, then the square root was taken. Examples of this data are shown in figure 5.4.1. This is consistent with taking short time averages on u'^2 if the process is stationary over short time segments.

5.3 Mean Velocities Induced by Breaking

The low pass filtered ensemble mean horizontal $\langle \bar{u} \rangle$ and vertical velocity $\langle \bar{w} \rangle$ were obtained at seven elevations and seven x locations from the observed breaking location. The three wave packets measured in this way were the large scale (f_c = 0.88 Hz), plunging (ak_c = 0.352) and spilling (ak_c = 0.278) and the small scale (f_c = 1.28 Hz) plunging (ak_c = 0.420) wave packets. The measurement at each grid point represents 10 repeats of the packet; a total of 490 runs were made for each of the three cases.

Figure 5.3.1 shows the case of the large-scale plunging. The first box shows measurements just downstream of observed breaking ($x-x_{ob}$) = 0.29 m. The positive mean horizontal velocity at elevations above the trough represent the mass flux in the carrier waves. This is consistent with the Eulerian description which gives all the carrier wave mass flux and momentum density in the trough to crest region of the waves. At depths below the wave trough the forced long wave velocity is evident, and can be seen to remain nearly constant with depth. The vertical mean velocity decays to zero near the bottom. The magnitude of this velocity, -0.025 C, compares with the estimate from equation (A1.41) based on weakly

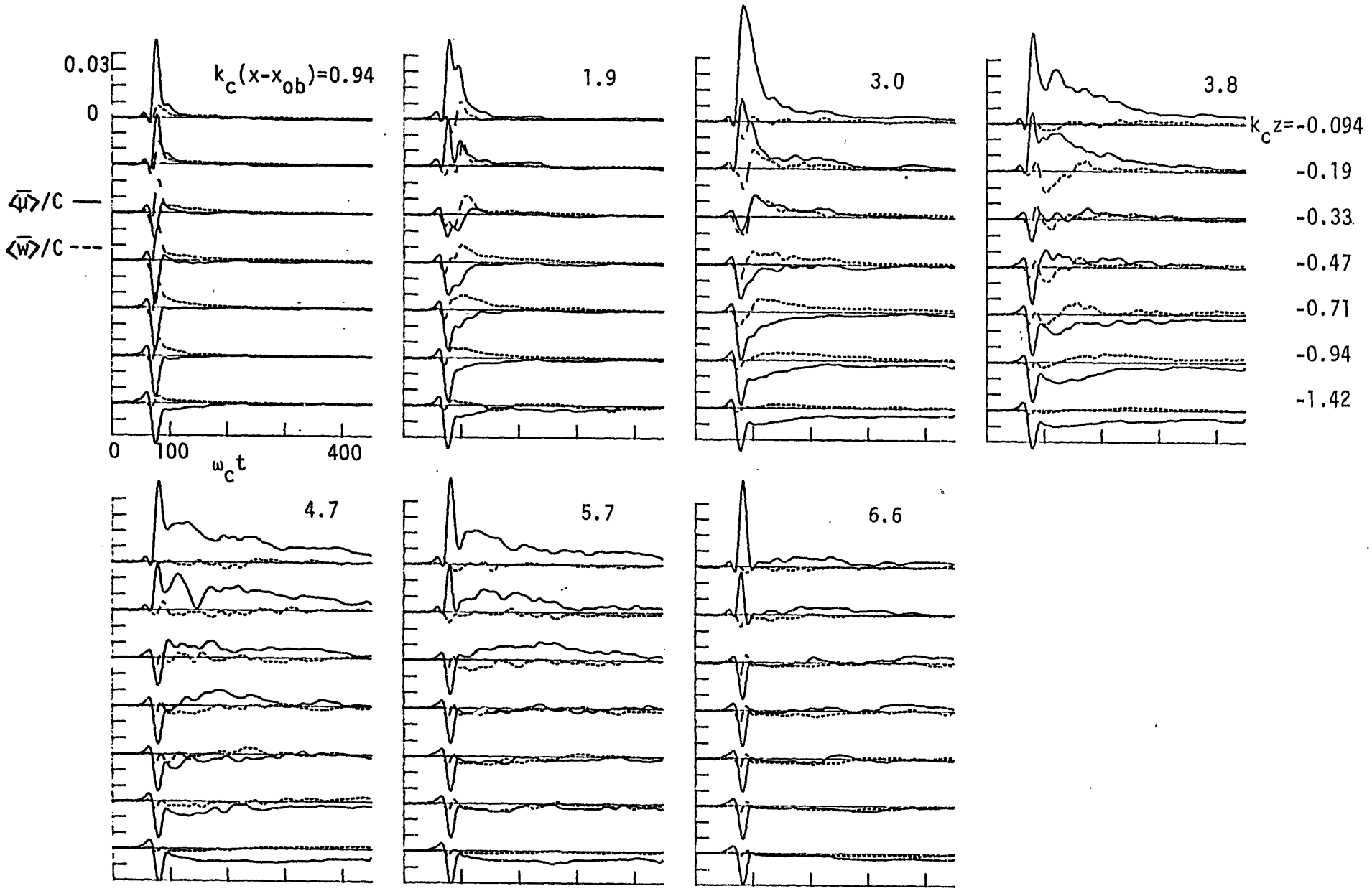

Figure 5.3.1 Time series of mean horizontal $\langle\bar{u}\rangle/C$ —— and vertical $\langle\bar{w}\rangle/C$ velocity measured at stations downstream of breaking. Each curve is an ensemble average of 10 repeats which was then low pass filtered. f_c=0.88 Hz, ak_c = 0.352 (plunging).

nonlinear wave theory of $\bar{u} = -0.026$ C. The long transient wave ahead of the packet can be seen as the positive mean velocity at times before the packet has arrived at the probe. At later times, after the packet has passed, there remains a positive horizontal streaming which, at this x location, is advected downstream. This flow is supplied from below as seen by the upward vertical mean velocity at lower depths. Below an elevation of one wave amplitude $k_c z \sim 0.33$, there is a return flow set up after the packet has passed. At stations further downstream these features are all magnified and are longer lived. At $k_c(x - x_{ob}) = 3.8$ the surface current induced by breaking is initially 0.03 C decaying to 0.01 C only after 60 carrier wave periods. The deeper return flow is also accentuated. The depth of penetration of the positive going flow has reached almost 1-1/2 wave amplitudes at this station. Finally at stations ~1 wave length from breaking, the current has decayed to less than 0.005 C but is still significant.

The spatial flow field corresponding to these measurements is illustrated with the vector diagrams in figure 5.3.2. The time steps are referenced from the observed time of breaking. The top diagram illustrates the measured flow field as the wave group passes through the region. Note the mass flux due to the carrier waves near the surface and the return flow in the long forced waves. The bottom of the channel is at $k_c z = -1.95$ at this scale. After four wave periods from breaking, the group has passed the region and a large eddy is left behind. At the ends of the breaking region the horizontal velocity is near zero. The surface flow velocity is ~0.02 C and the deeper return velocity ~0.01 C. The rotational motion is still significant after 50 wave periods from breaking.

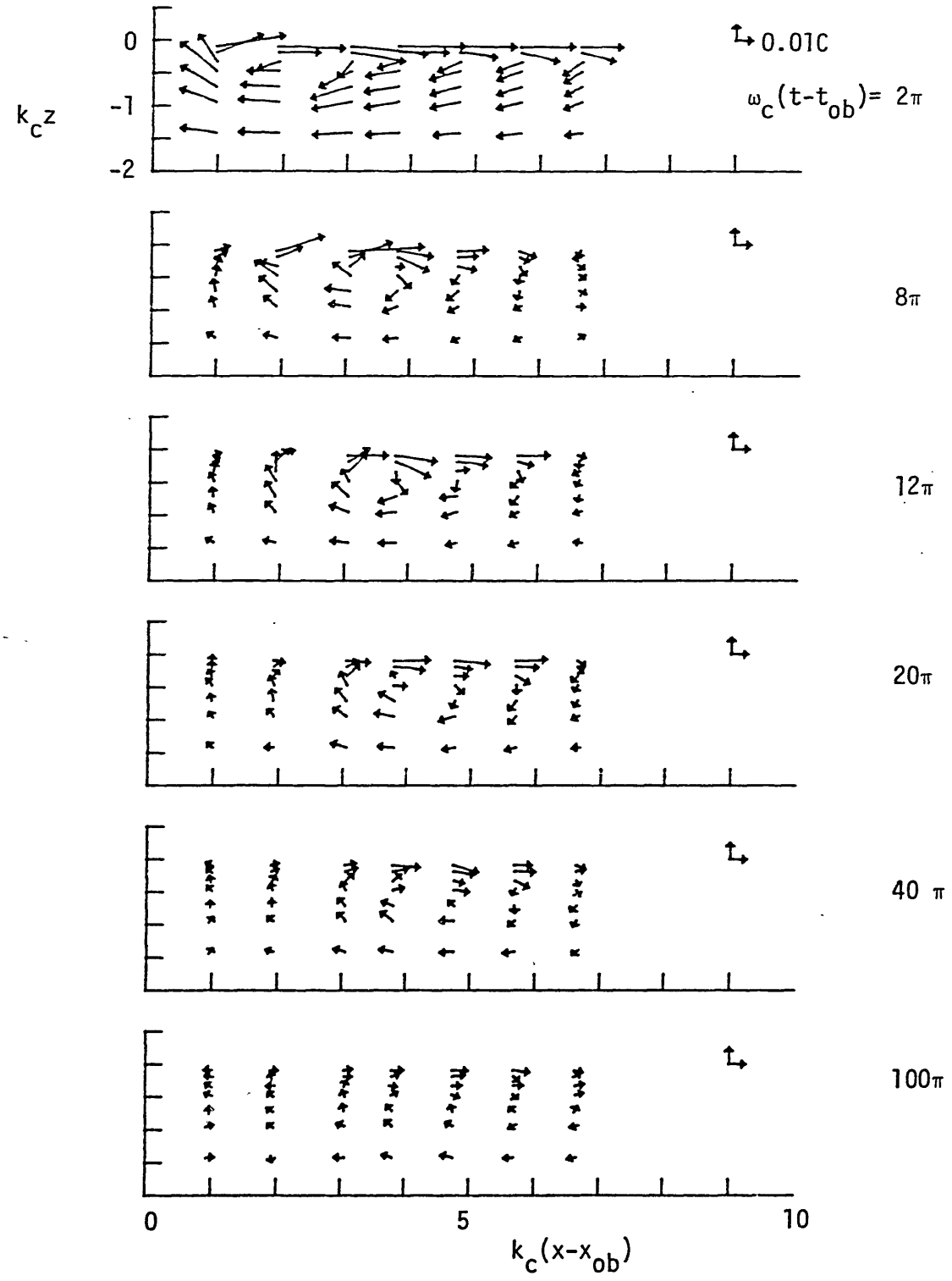

Figure 5.3.2 The mean velocity field at times after breaking for f_c = 0.88 Hz, ak_c = 0.352 (plunging), $\Delta f/f_c$ = 0.73, $x_b k_c$ = 27.4. Derived from ensemble averaged, low pass filtered measurements. Each vector is the average of 10 repeats. Channel bottom is at $k_c z$ = -1.95 for this scale.

Similar results are shown for the large scale spilling wave in figures 5.3.3 and 5.3.4. The filtered time history show the forced long wave under the packet to be $\bar{u}$ ~0.015 C and due to the lower envelope amplitude compared to the plunging case. The surface currents generated by this spilling breaking are still appreciable, initially at 0.02 C and decaying slowly. The positive currents penetrate to depths comparable to the plunging wave. The return flow after the packet has passed, is smaller but still present and a similar eddy is generated. It appears that the forced wave under the packet is important in setting up this large vortex. One may have attributed it to the overturning in the plunging wave; however, the size of the measured eddy is larger than the plunging curl. Also the fact that it is set up in a spilling wave supports the idea that the group is important in generating it and not the curling of the wave itself.

Some verification that this breaking induced flow does scale with the wave packet center frequency can be seen in the results for the small scale plunging wave $f_c = 1.28$, $ak_c = 0.420$ (figures 5.3.5 and 5.3.6). These velocities scale very well with the large scale case. The differences are suspected to be due to the larger nondimensional depth of the channel in the small scale $k_c d = -3.96$. This situation reduces the forced long wave velocity since now the required return mass flux (to balance that in the carrier waves) is distributed over a larger effective depth. Also, the forward flowing induced flow penetrates about 20% deeper than in the large scale case. Otherwise the nondimensional values of the breaking induced flow of ~0.02-0.03 C agree with the larger scale case. The same large eddy is also generated.

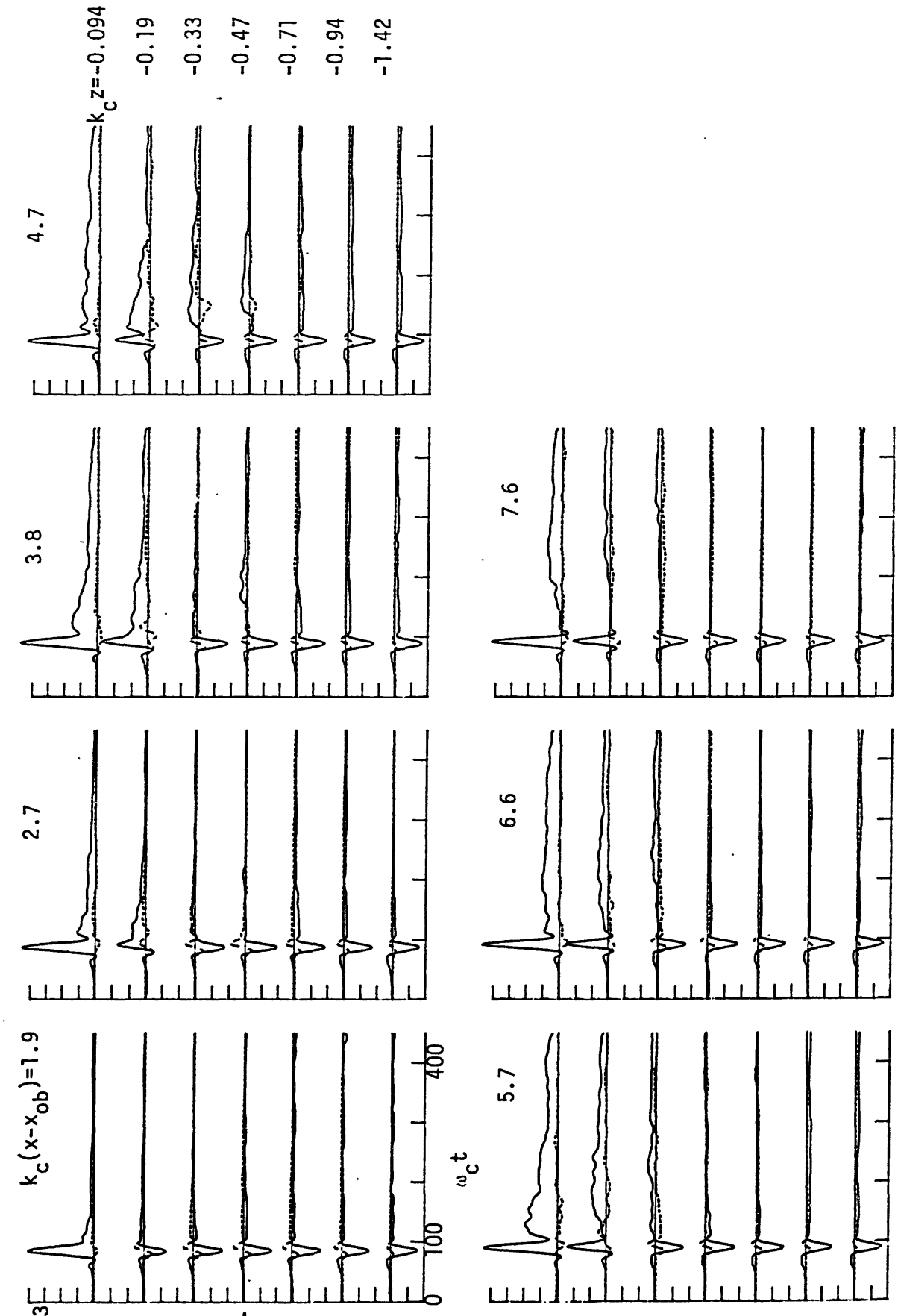

Figure 5.3.3 Time series of mean horizontal $\langle\bar{u}\rangle/C$ and vertical $\langle\bar{w}\rangle/C$, ---- velocity for f_c = 0.88 Hz. Same as figure ak_c = 0.278 (spilling).

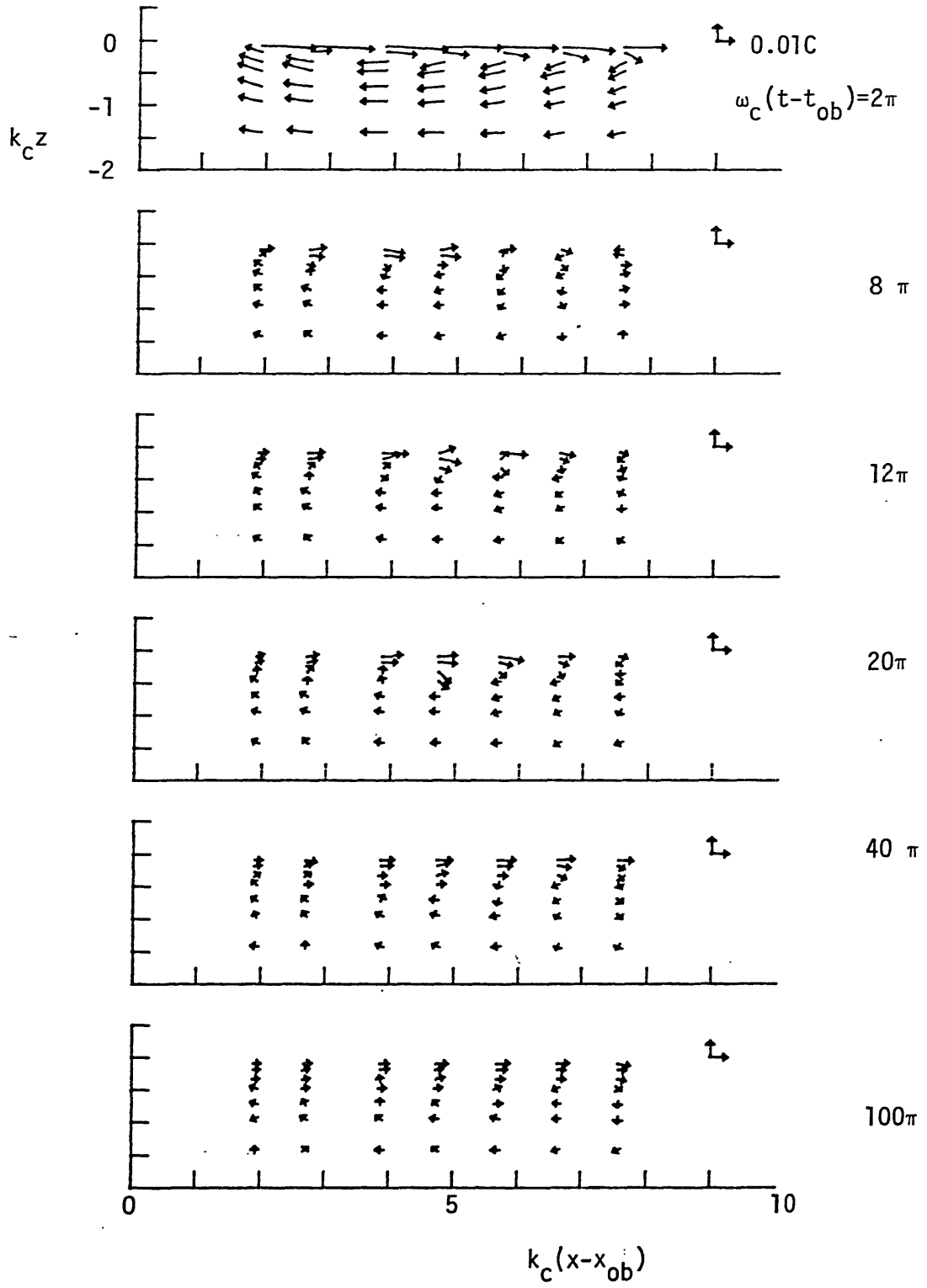

Figure 5.3.4 Mean velocity field for f_c = 0.88 Hz, ak_c= 0.278 (Spilling)
As for figure 5.3.2

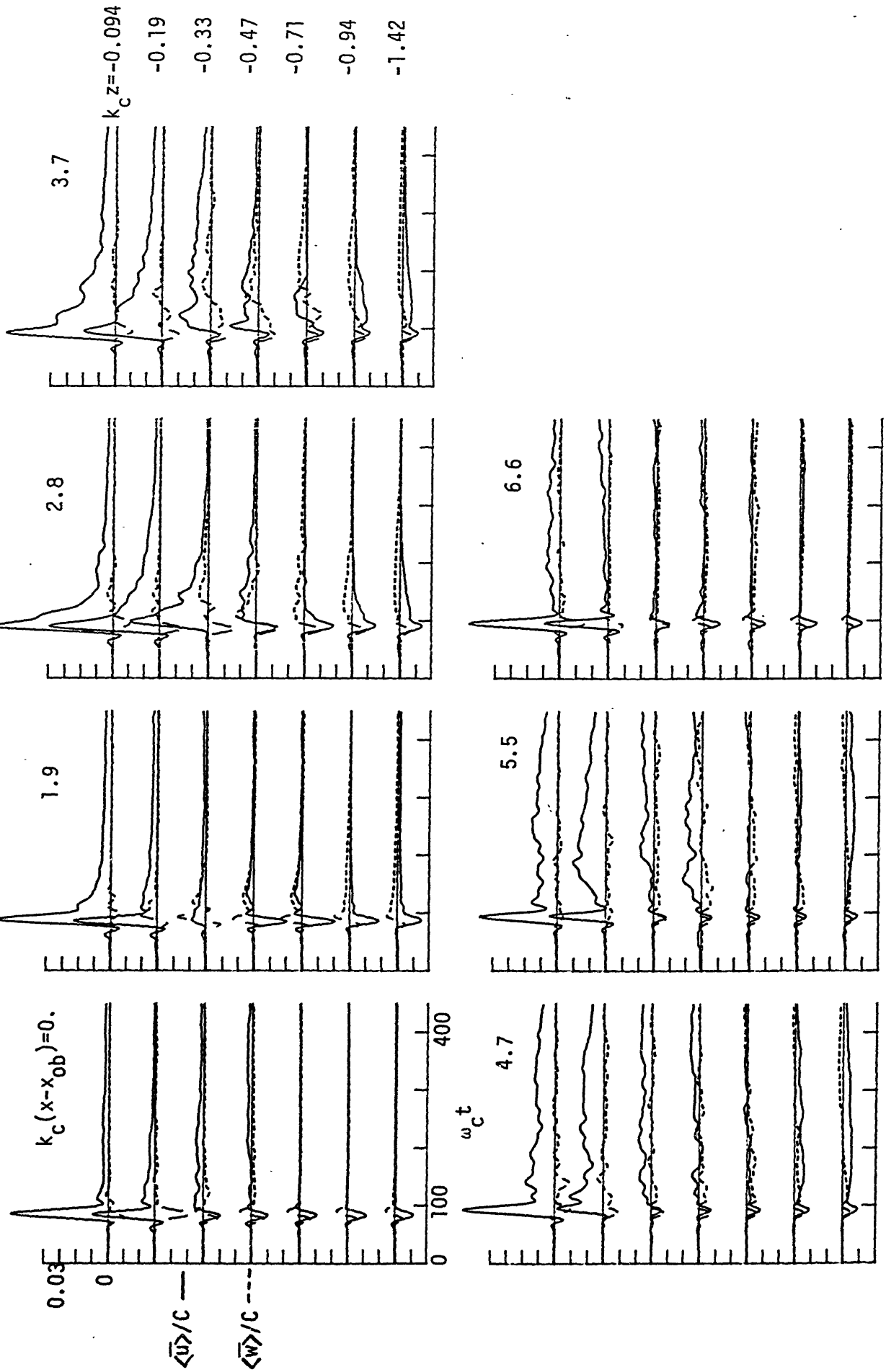

Figure 5.3.5 Time series of mean horizontal $\langle\bar{u}\rangle/C$ and vertical $\langle\bar{w}\rangle/C$ ---- velocity for f_c = 1.28 Hz. ak_c = 0.420 (plunging).

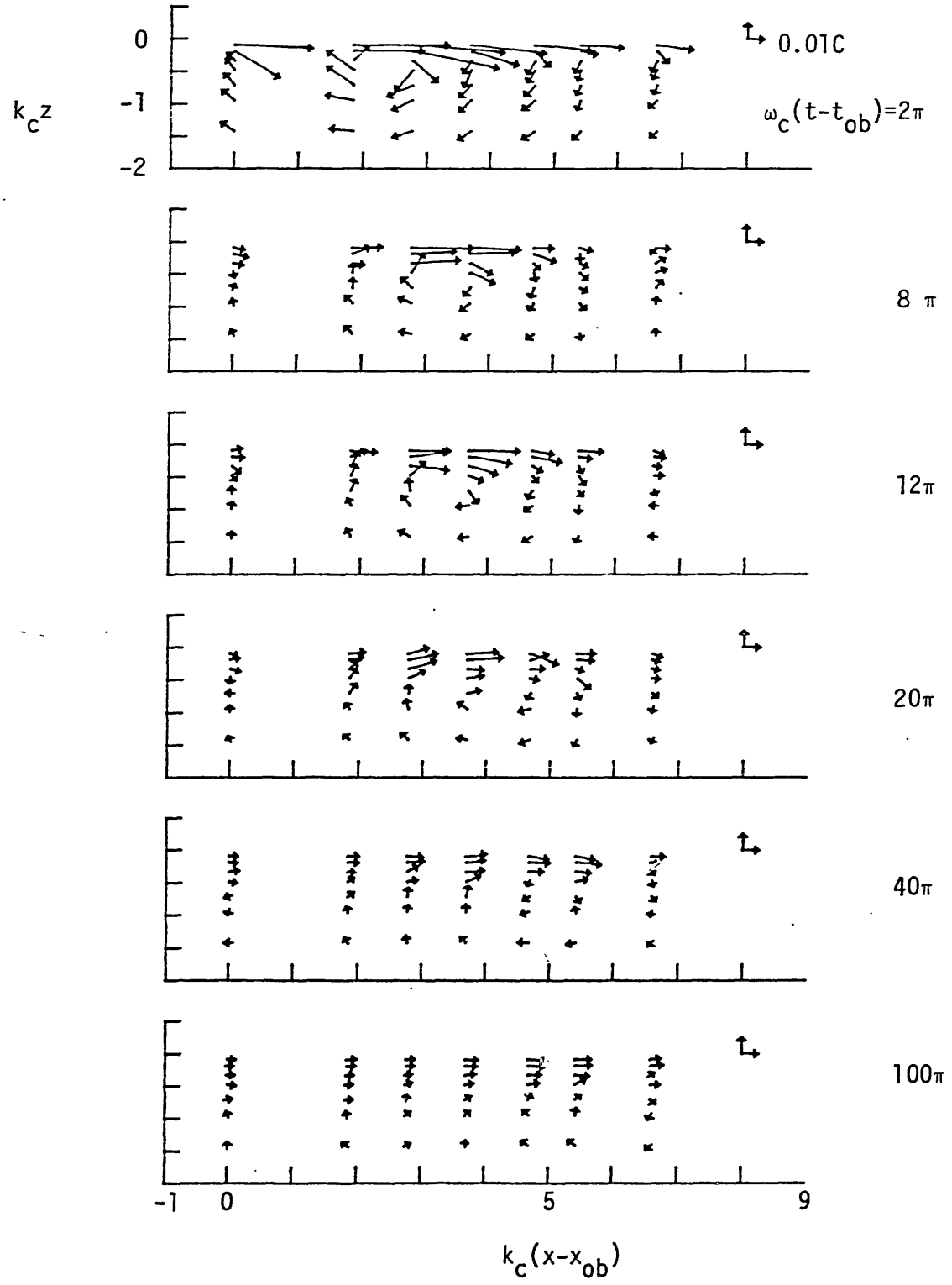

Figure 5.3.6 Mean velocity field for f_c = 1.28 Hz, ak_c = 0.420 (plunging). As for figure 5.3.2 . Channel bottom is at $k_c z$ = -3.96 at this scale.

5.4 Turbulent Velocities Induced by Breaking

The measurements of horizontal and vertical turbulent velocities in the breaking region are shown in Figures 5.4.1 through 5.4.6. As was discussed in section 5.2, these signals represent the ensemble mean of the square of the fluctuating velocity. The squared signal was lowpass filtered and then the square root was taken and plotted. For times after the wave packet has passed, this signal represents the turbulent mean square velocity to within an error of -10%. The instrument noise and random waves contribute at most 10%. Measurements at times very close to breaking show a large increase in these turbulent velocities. Here, signal spikes due to bubbles crossing the measurement point, contribute to the variance (noise) in the signal which may be larger than previously discussed. It is not possible to resolve the accuracy of this measure of turbulence right at breaking in the bubbly flow. After several wave periods, however, the turbulent measurements are very reliable and show intensities of ~0.02 C. The plots in figure 5.4.1 correspond to the large scale plunging wave. Just downstream of breaking, at $k_c(x - x_{ob}) = 0.94$, the turbulence levels after breaking $\omega_c t > 100$ are relatively small, about 0.005 C, and decay to nearly zero. The turbulence appears to be nearly isotropic in that the vertical and horizontal velocities are nearly equal for all time. From these measurements and observations, it seems that the turbulent region generated at breaking is advected further downstream. Measurements at these downstream stations show levels of turbulence initally of 0.02 C and decaying slowly to 0.005 C after over 60 wave periods. The depth of penetration is seen to increase further downstream showing turbulent rms velocity levels of 0.005 C at $k_c z = -0.94$

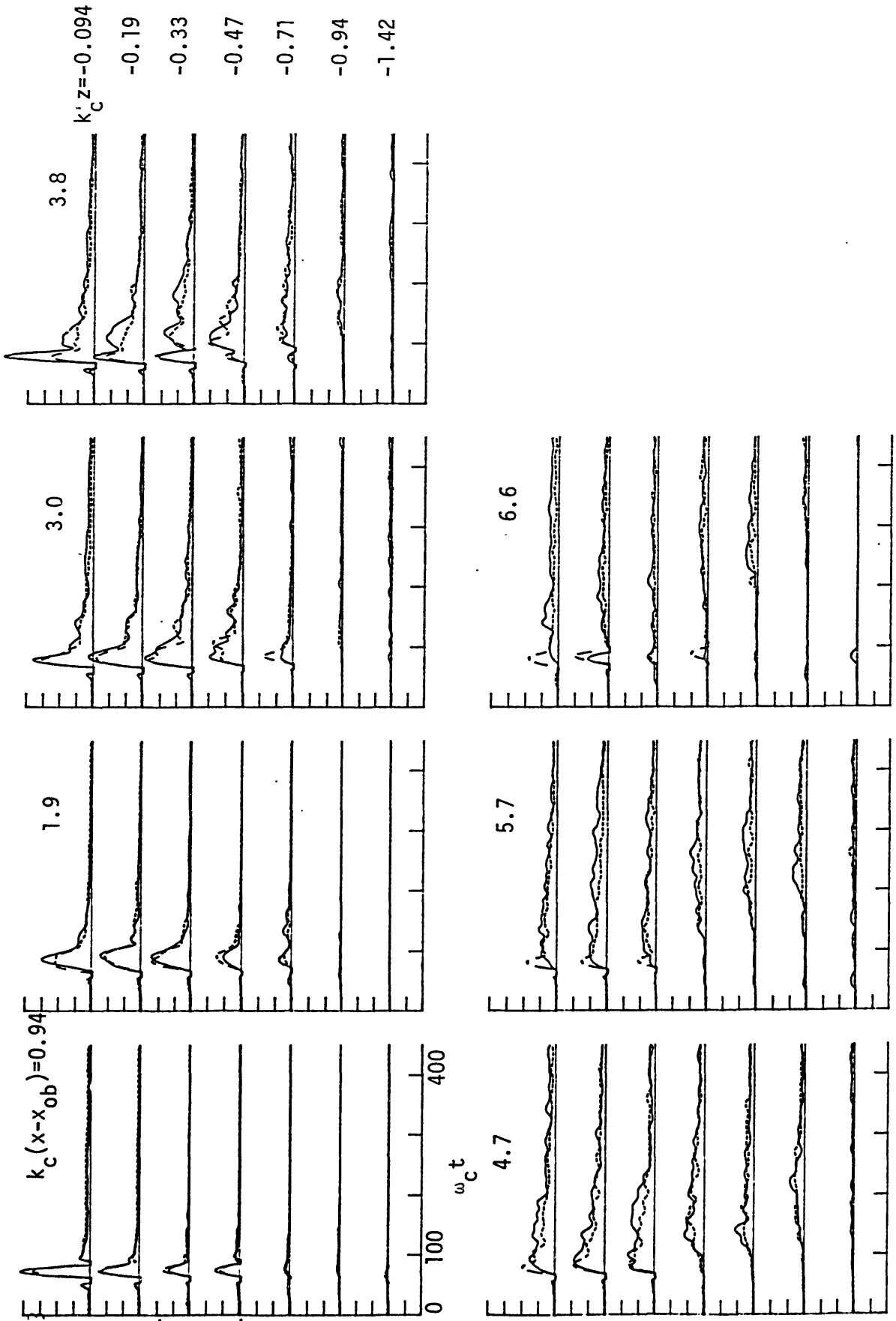

Figure 5.4.1 Time series of horizontal and vertical rms turbulence velocities For f_c = 0.88 Hz, ak_c = 0.352 (plunging).

(~2-3 wave amplitudes) after 60 seconds. At $k_c(x - x_{ob}) = 6.6$ or 1 wavelength from breaking, turbulence rms velocities are still near 0.006 C to depths of three wave amplitudes. The rate of vertical advance of the turbulent front is estimated from the slope of the lines drawn in measurements at $k_c(x - x_{ob}) = 4.7$ and 5.7. The line is drawn to intersect the front of the velocity signal, where the signal initially increases from zero. This rate of ~0.01 - 0.02 C is on the same order as the turbulent rms velocities.

The spatial distribution of the rms fluctuations is shown in figure 5.4.2 at various time steps from observed breaking. Also plotted in this figure is the traced dye boundary digitized from films as described in Chapter 4. These boundaries correspond to the indicated time step after breaking. The horizontal extent of the turbulent region is established within 1 - 2 wave periods. Although the turbulence levels decay with depth, it is possible to define some spatial boundary where the turbulence is below 0.002 C, say. This depth of the turbulence increases in time and follows the dye boundary quite well. Note that in the top time step, high turbulence velocities are seen downstream of breaking, ahead of the instantaneous dye boundary. This is because the turbulence rms signal is low pass filtered over several wave periods, while the dye boundary is moving rapidly here. At later times, where the motion is slowly changing in time, the dye boundary and extent of turbulence is in agreement. The results for the large scale spilling wave (figures 5.4.3, 5.4.4) show a similar growth of the turbulence in x and z and decay in time. The initial levels, however, are ~0.01 C for this case, somewhat lower than in the plunging wave. The depth penetration is still appreciable for this less intense breaking, reaching two wave heights. Again, the dye boundary

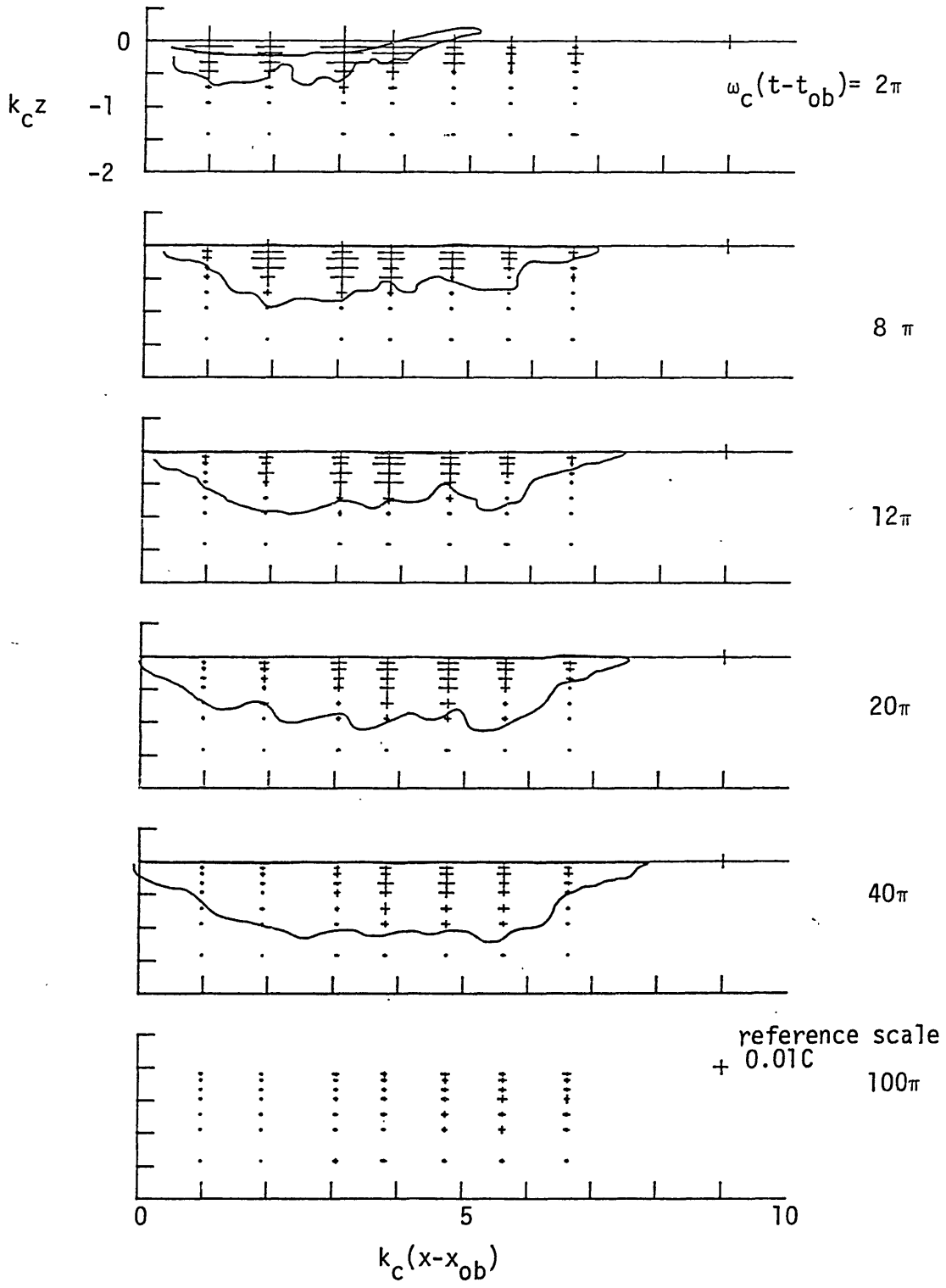

Figure 5.4.2 Turbulence rms velocities in the breaking region. u_{rms}/C (horizontal bar), w_{rms}/C (vertical bar) for f_c = 0.88 Hz, ak_c = 0.352 (plunging). Also shown is digitized dye trace at corresponding time after breaking. Bottom is $k_c z$ = -1.95.

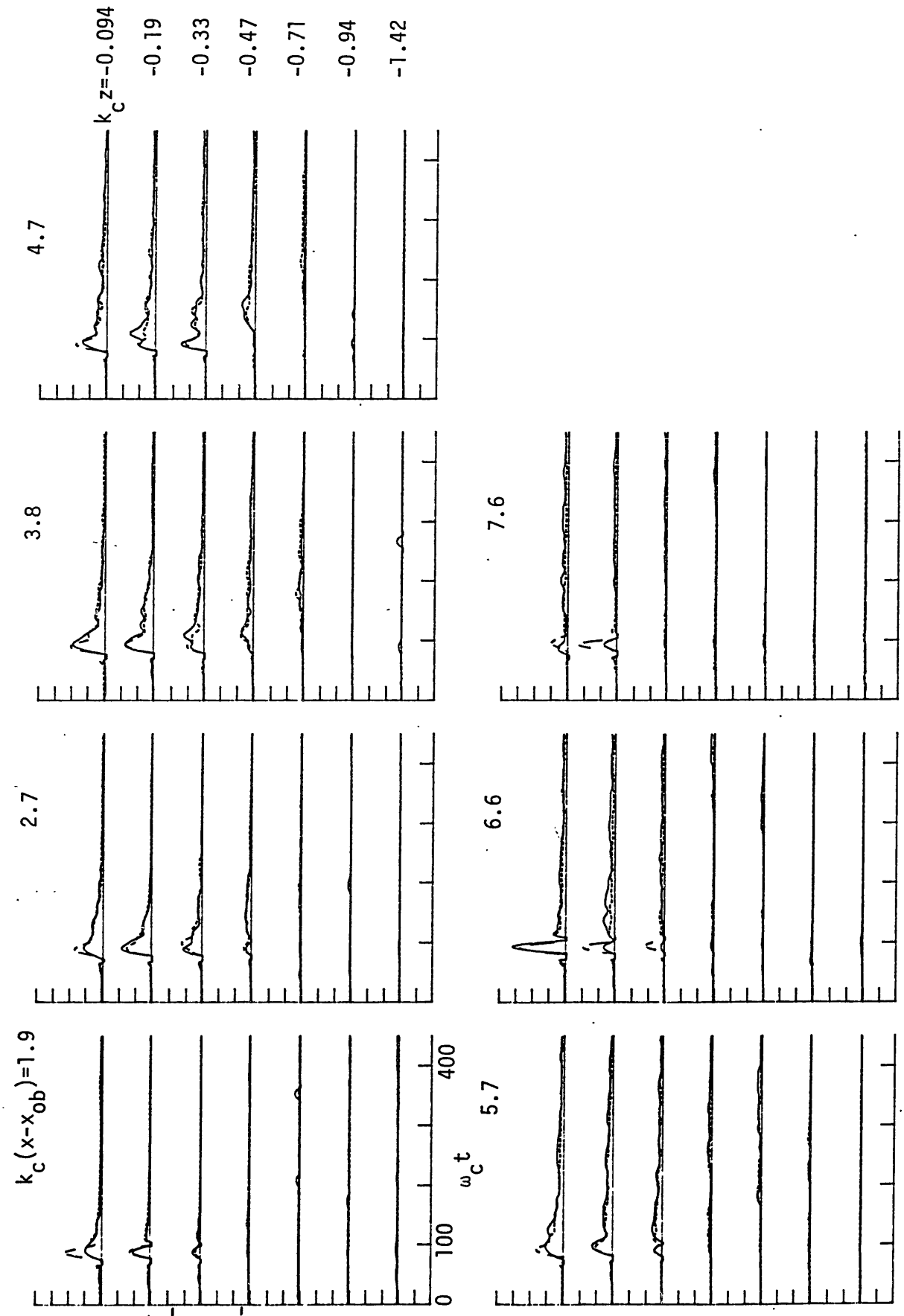

Figure 5.4.3 Time series of horizontal and vertical turbulence rms velocities as for figure 5.4.1 except $ak_c = 0.278$ (spilling).

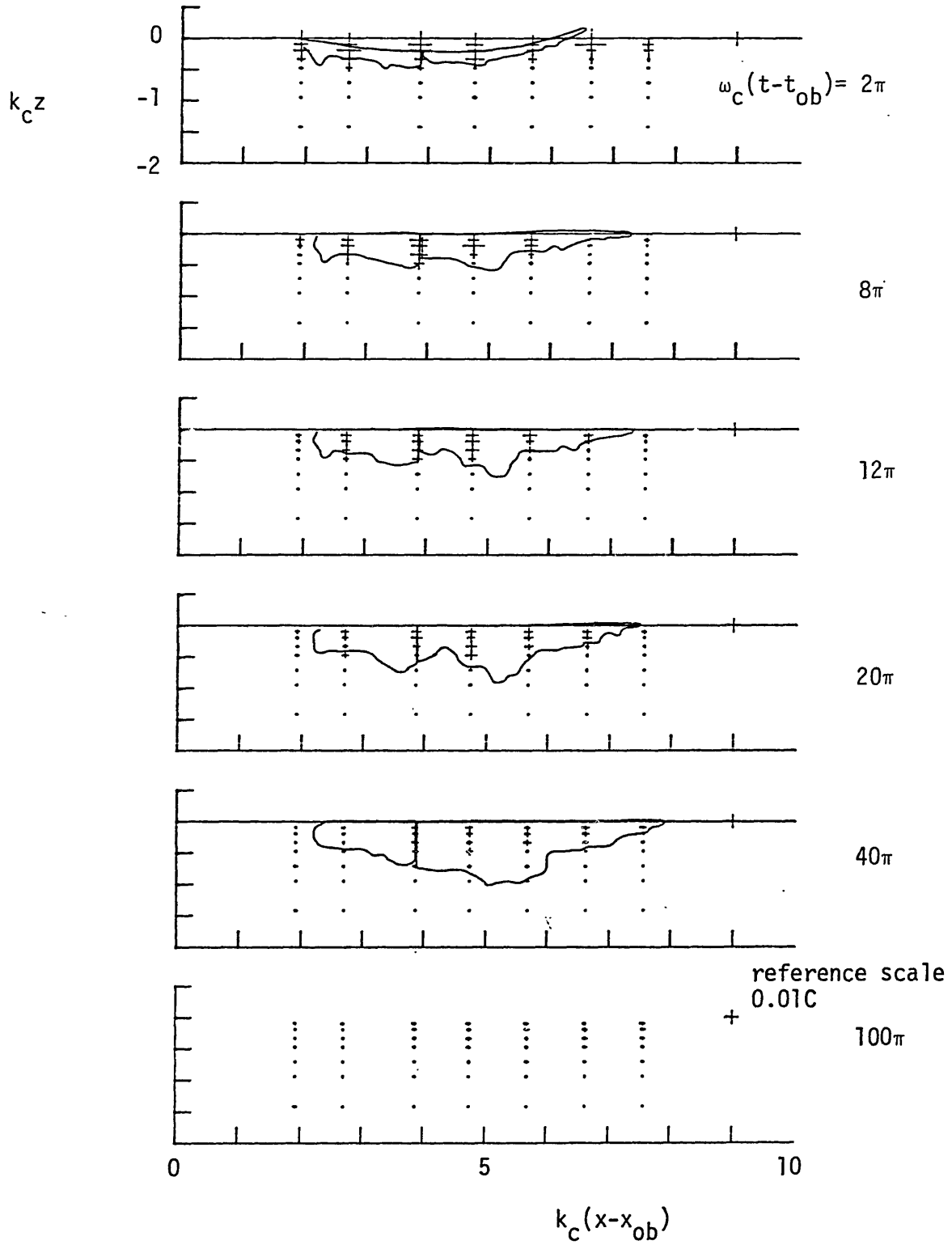

Figure 5.4.4 Turbulence rms velocities for f_c = 0.278 (spilling). As for figure 5.4.2. Contour is two dye tracings spliced together from separate runs of the breaking wave.

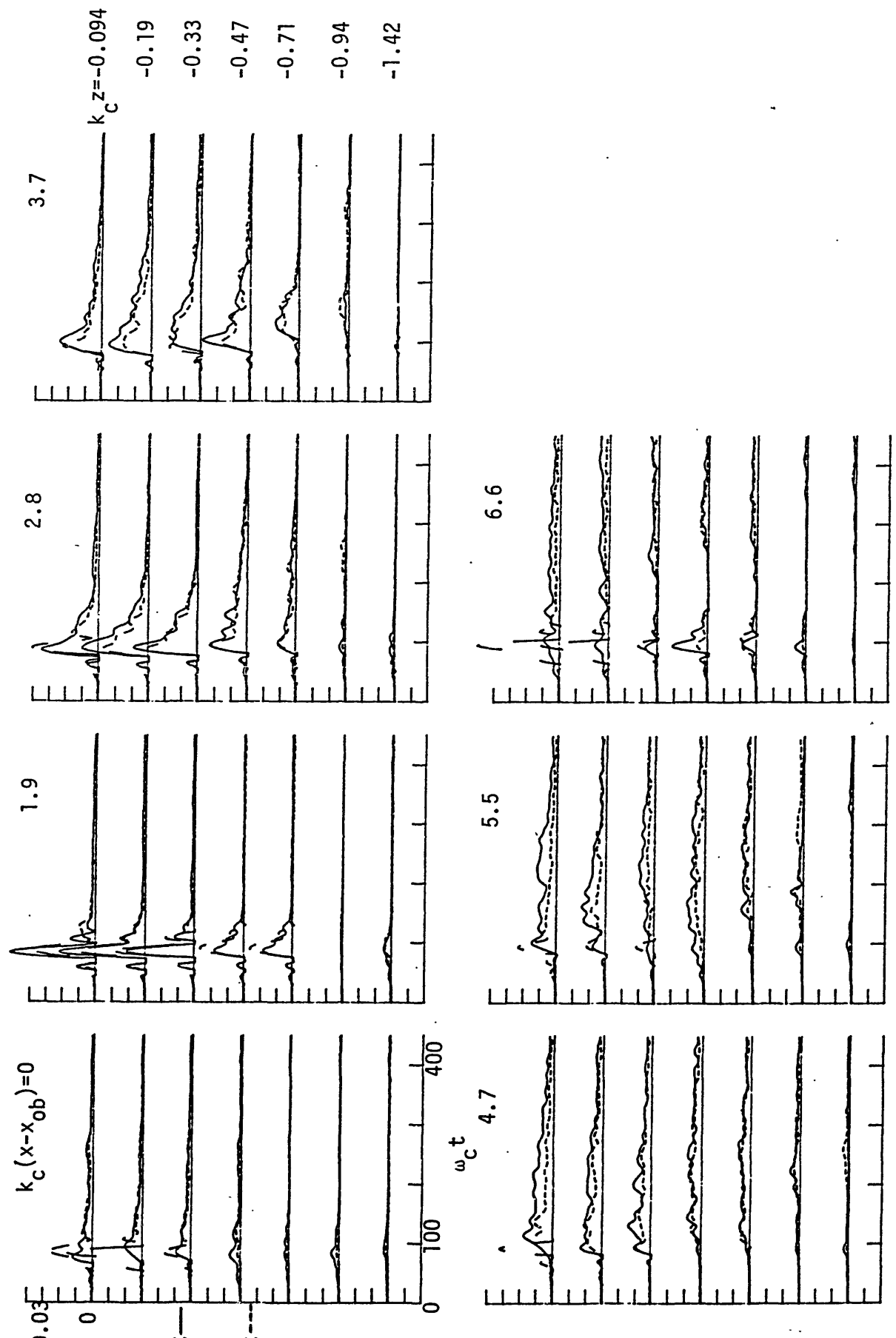

Figure 5.4.5 Time series of horizontal and vertical turbulence rms velocities. f_c = 1.28 Hz, ak_c = 0.420 (plunging).

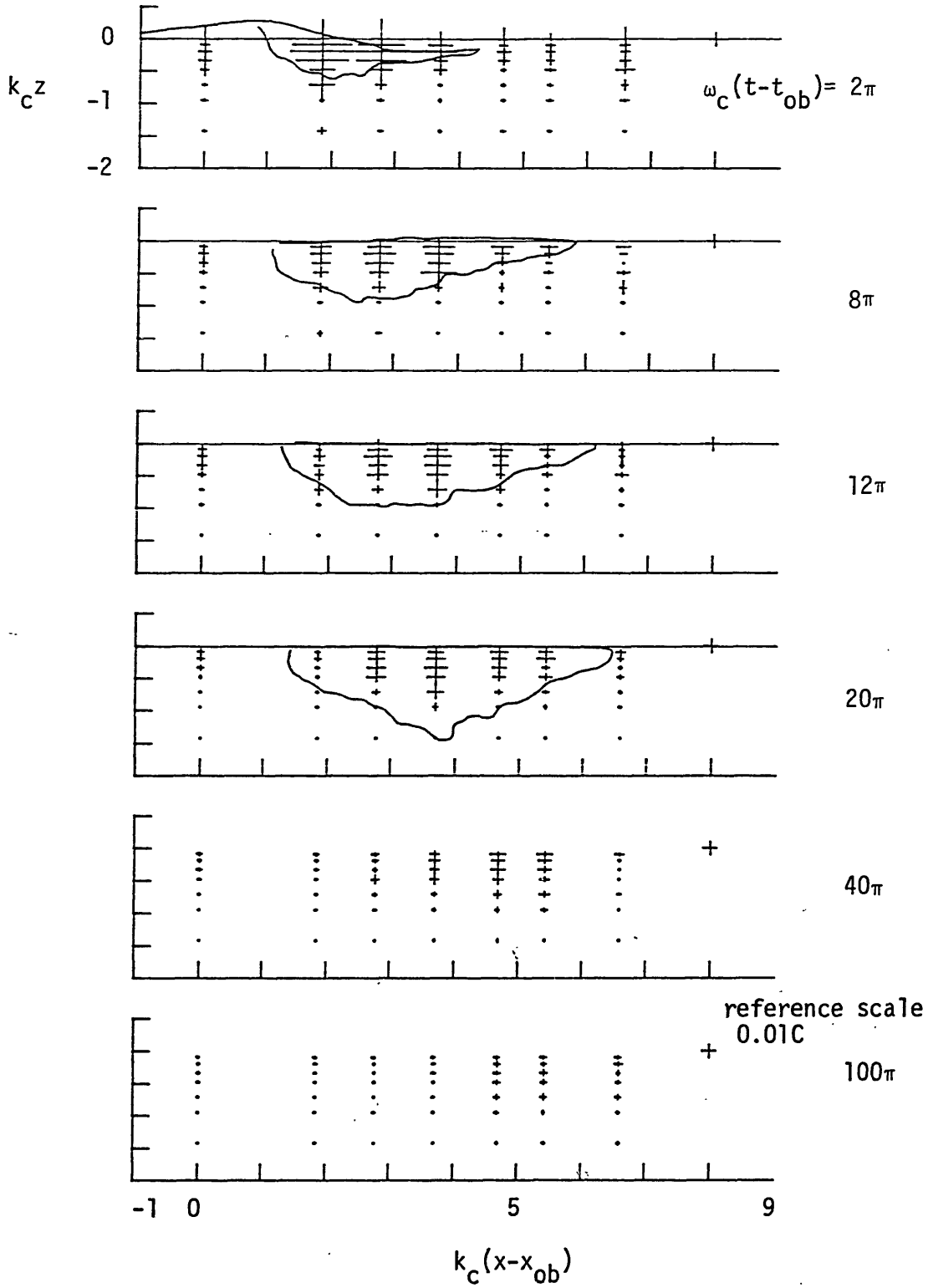

Figure 5.4.6 Turbulence rms velocities for f_c = 1.28 Hz and ak_c = 0.420 plunging. Otherwise as for figure 5.4.2. Bottom is $k_c z$ = -3.96.

does a good job of indicating the extent of the turbulent velocities greater than 0.002 C. Some discrepancy is noted at 20 wave periods after breaking where the dye appears deeper than the high levels of turbulence. Also, at the rear of the dye cloud, turbulence has decayed to negligible levels, while the dye remains.

The magnitude of the turbulent rms velocity, the depth of penetration, and the time of decay, all appear to scale reasonably well with the length and time scales of the waves. This is indicated by the results of the small scale (f_c = 1.28 Hz) plunging wave group. The comparisons between figures 5.4.1 and 5.4.5 are quite good. The spatial plots of the rms turbulence and corresponding dye boundary (figure 5.4.6) shows again the region influenced by breaking and how well the dye boundary defines this region.

5.5 Shear Stresses Induced by Breaking

The shear stresses, generated by breaking, represent the vertical flux of horizontal momentum into the water column. These fluxes are derived from the measured velocity. The contribution from the mean motion and that from the turbulent motion are computed separately as:

$$\langle uw \rangle = \langle u \rangle \langle w \rangle + \langle u'w' \rangle \tag{5.11}$$

where

$$\langle u'w' \rangle = \frac{1}{q} \sum_{q=1}^{Q} [u'_q w'_q] \tag{5.12}$$

These signals were then low pass filtered as for the turbulent normal stresses as described in Section 5.2. In the following plots a negative flux represents a downward flux of positive horizontal momentum (or upward flux of negative horizontal momentum).

Figure 5.5.1 shows the shear stress time history for the large scale spilling wave. At the upstream station and at depths below the trough ($k_c z > -0.33$) the flux is dominated by that of the forced wave showing the downward flux of negative horizontal velocity (positive $\overline{\langle u\rangle\langle w\rangle}$) and then an upward flux of negative horizontal momentum (negative $\overline{\langle u\rangle\langle w\rangle}$). The average of this over the packet period appears to be nearly zero. Further downstream, the net flux is negative over the packet apparently due to the large vertical currents induced by breaking (u_c in equation 5.5). Close to the surface, a slight negative flux is observed in the turbulent contribution. These turbulent shear stress values of $\overline{\langle u'w'\rangle} \simeq -1\times10^{-4}\ C^2$ are comparable to the corresponding normal stresses of $\langle u'\rangle^2 \sim (0.01C)^2 \sim 1\times10^{-4}\ C^2$. Near the downstream end of the breaking region at $k_c(x - x_{ob}) = 7.6$, the momentum flux due to the turbulence has decreased. The momentum flux due to the mean motion now shows a net positive flux averaged over the packet in contrast to the upstream case.

The large scale plunging wave (figure 5.5.2) shows a large negative mean flux of momentum at the upstream x location below a depth of $k_c z = -0.47$. The directions of these fluxes are consistent with the mean velocity vector diagrams of figure 5.3.1. Above this depth there is an upward flux of the positive horizontal momentum. Further downstream at $k_c(x - x_{ob}) = 3.0$ the situation is reversed; the lower depths show a downward flux of negative momentum possibly resulting from the negative vertical velocity in the plunging jet acting on the negative forced wave flow. At these center stations there is an appreciable downward momentum flux after the packet has passed in both the mean motion and the turbulent motion. Again the depth of noticeable negative momentum flux agrees with that of the turbulent rms velocities, going to depths of 2 - 3 wave

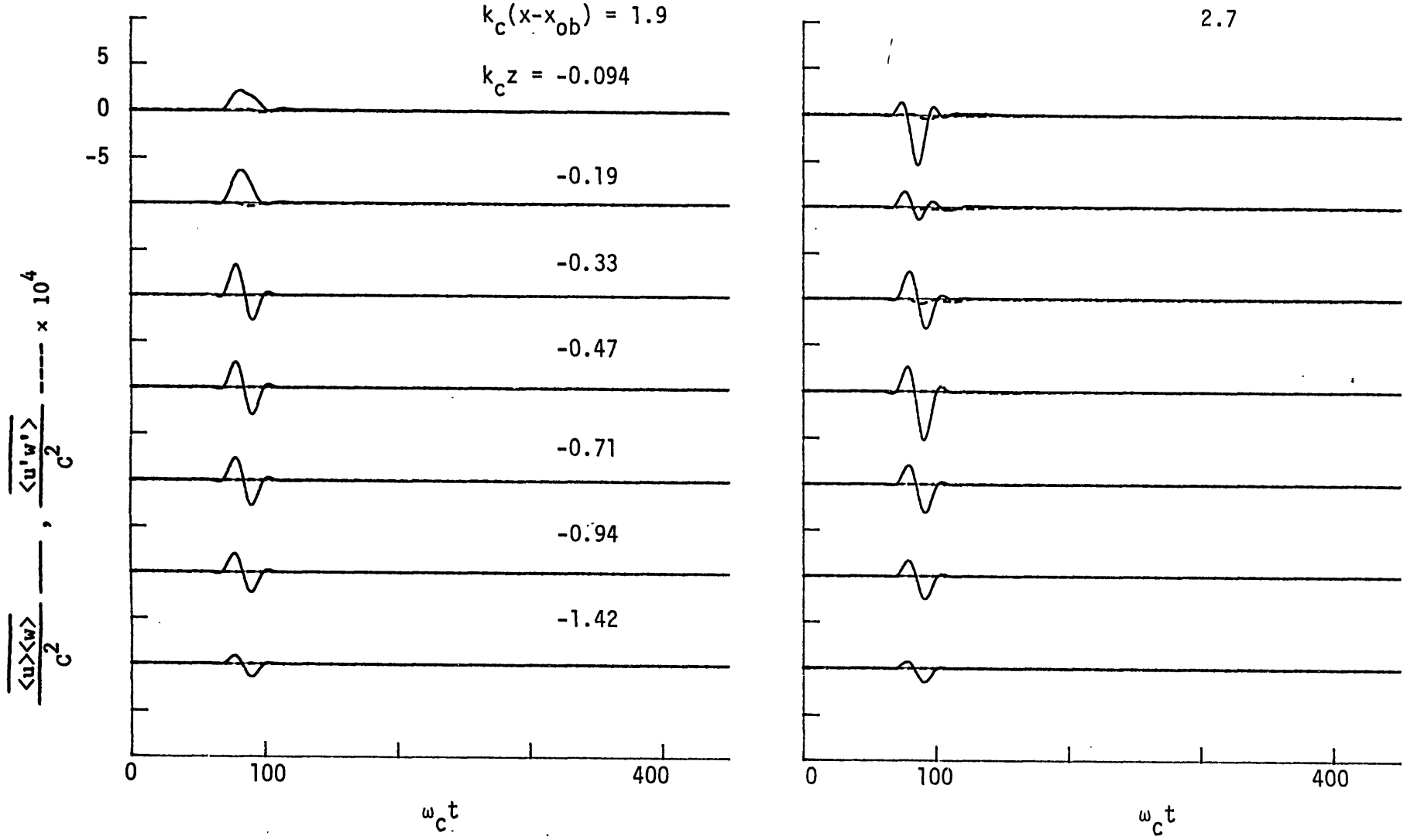

Figure 5.5.1a Time history of shear stress in the breaking region. $\overline{\langle u \rangle \langle w \rangle}$ ——— , $\overline{\langle u'w' \rangle}$ ---- . For f_c = 0.88 Hz, ak_c = 0.278 (spilling).

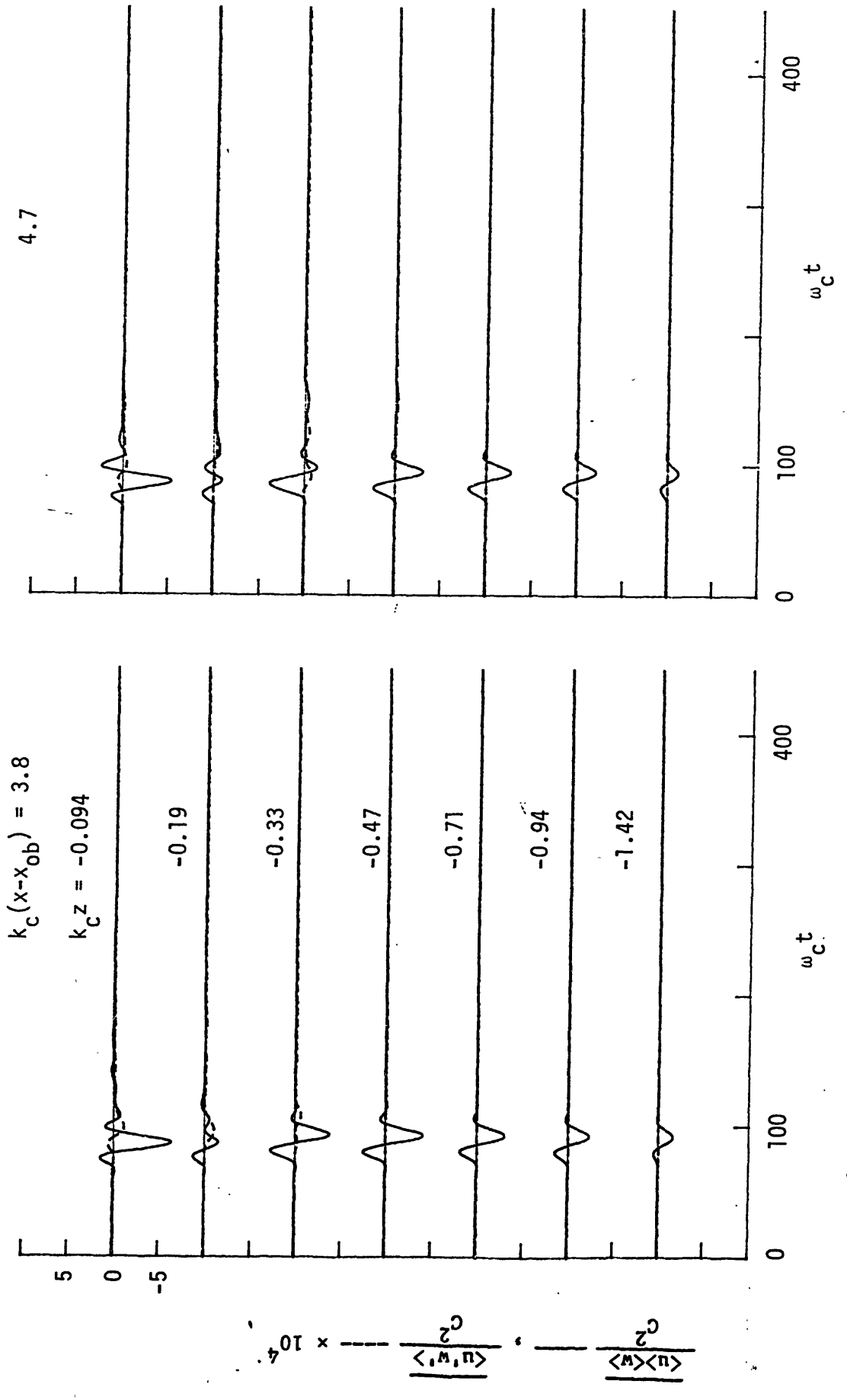

Figure 5.5.1b Shear stress, Continued from figure 5.5.1a.

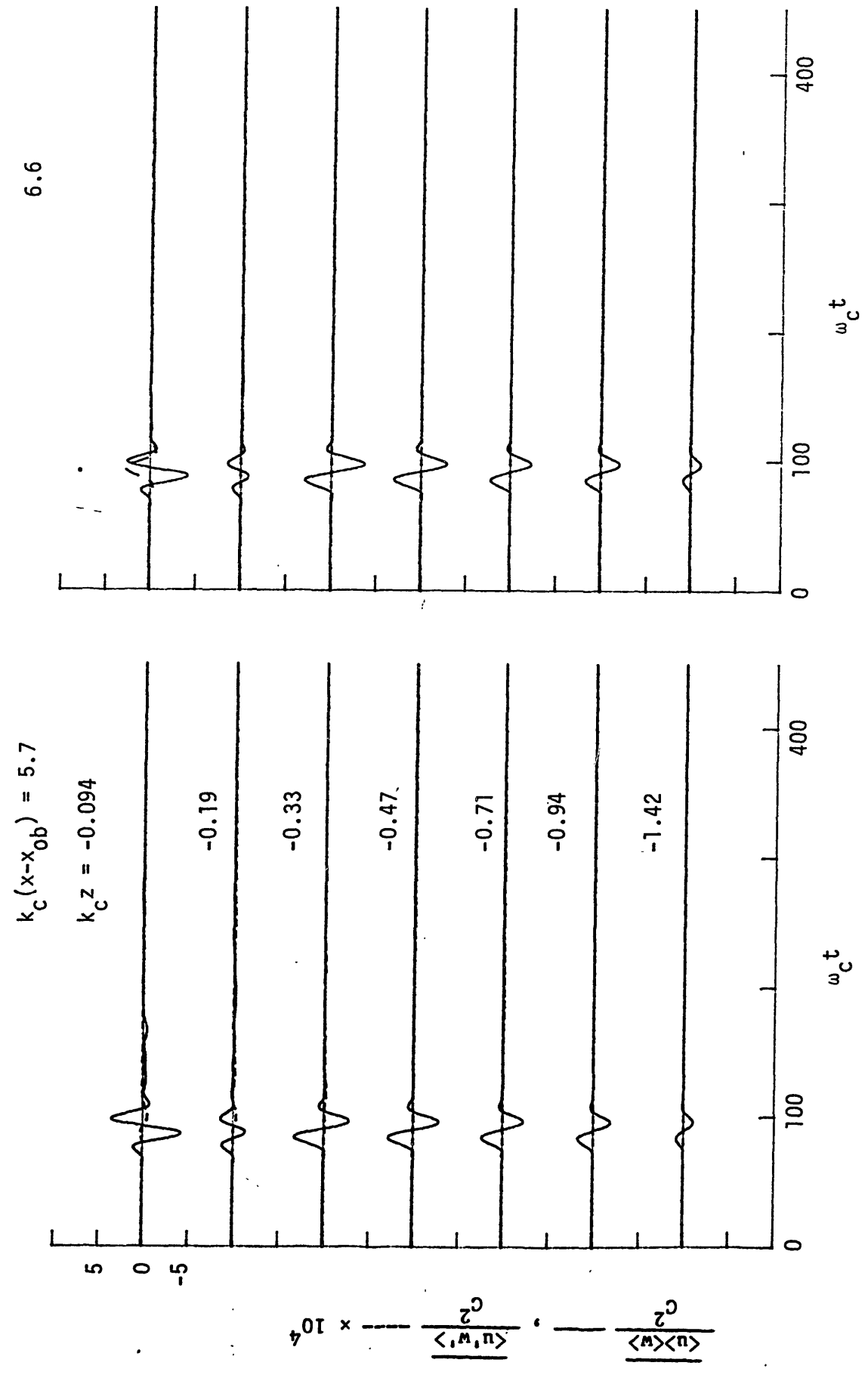

Figure 5.5.1c Shear stress. Continued from figure 5.5.1b.

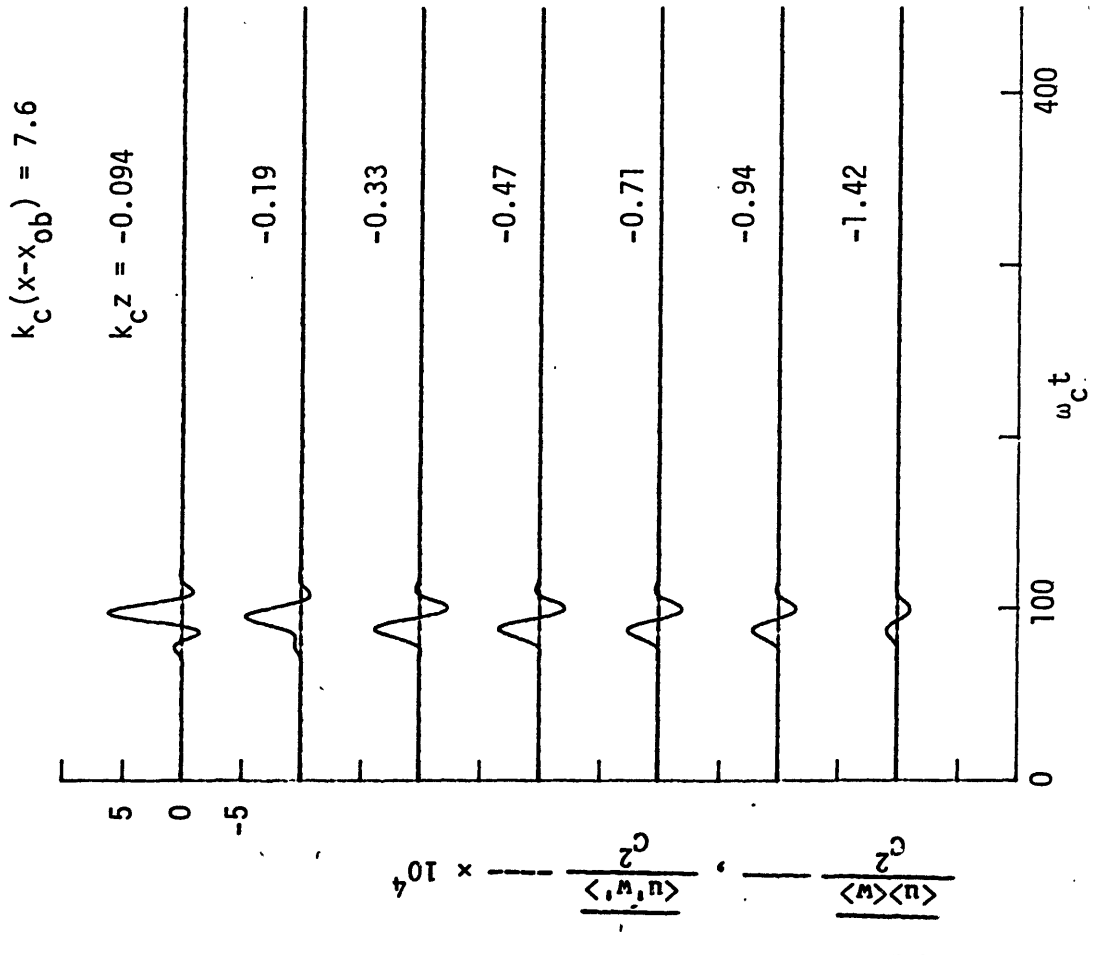

Figure 5.5.1d Shear stress. Continued from figure 5.5.1c.

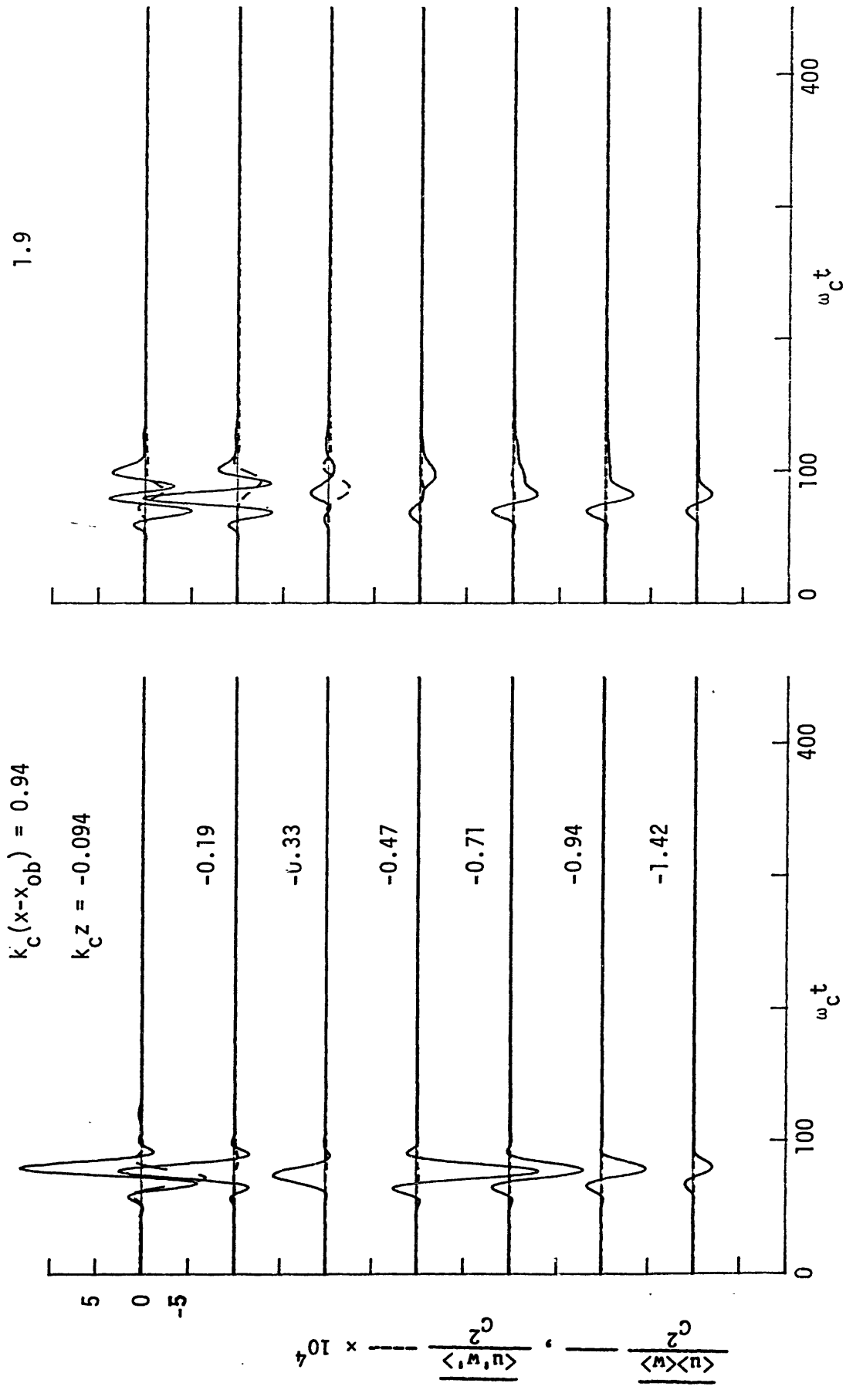

Figure 5.5.2a Time history of shear stress in the breaking region $\frac{\langle u\rangle\langle w\rangle}{c^2}$ ——— , $\frac{\langle u'w'\rangle}{c^2}$ ---- . For f_c = 0.88 Hz, ak_c = 0.352 (plunging).

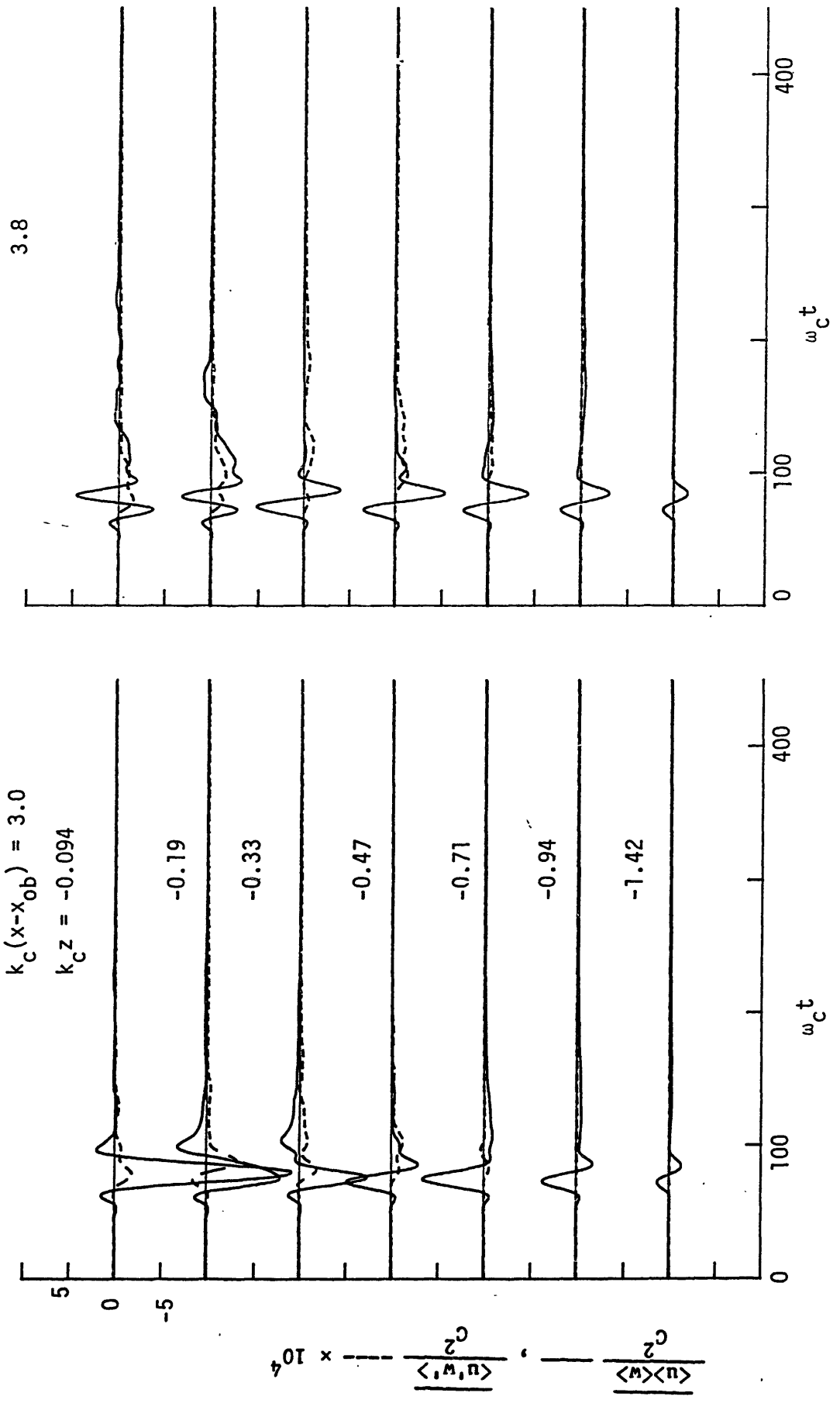

Figure 5.5.2b Shear stress. Continued from figure 5.5.2a.

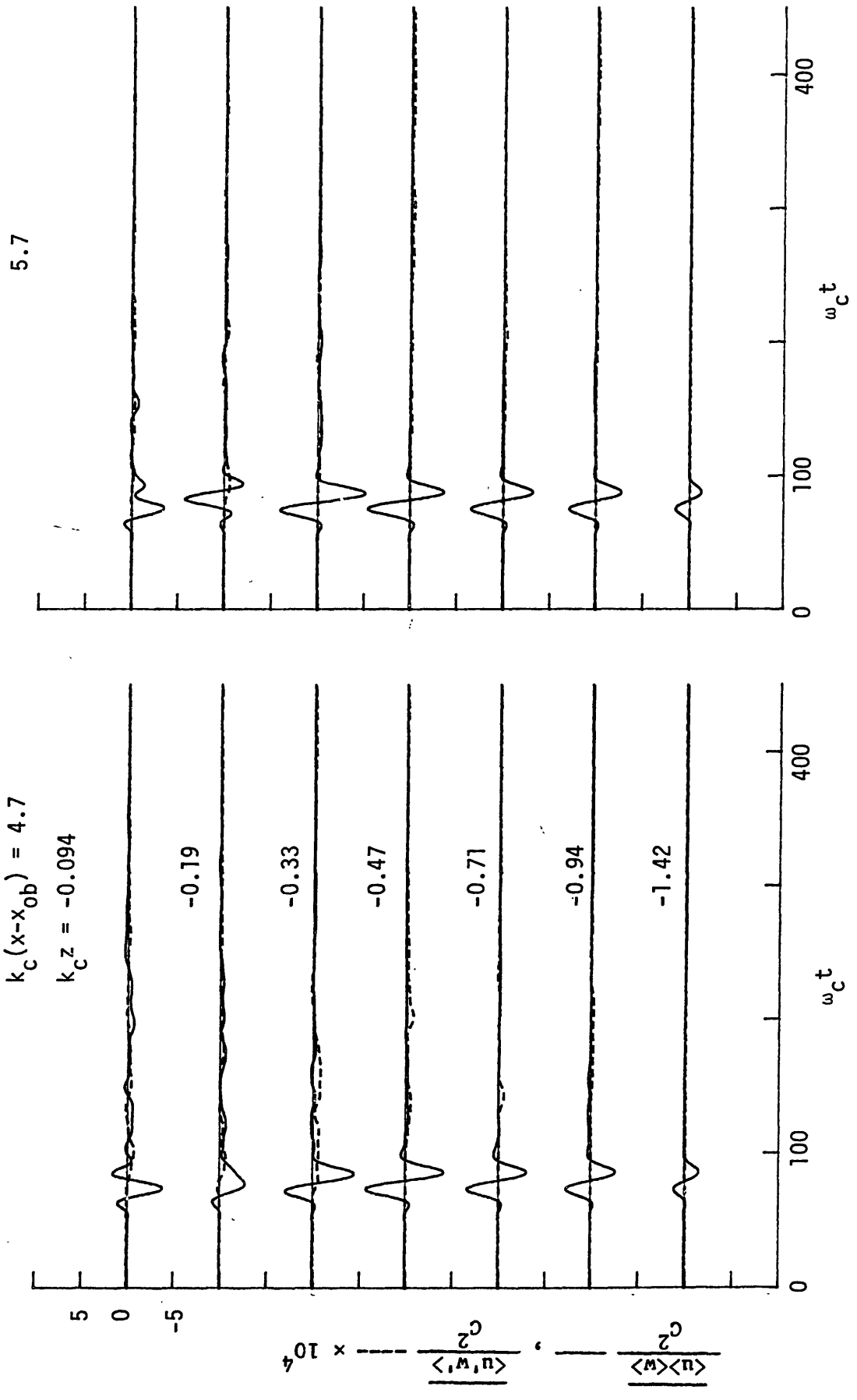

Figure 5.5.2c Shear stress. Continued from figure 5.5.2b.

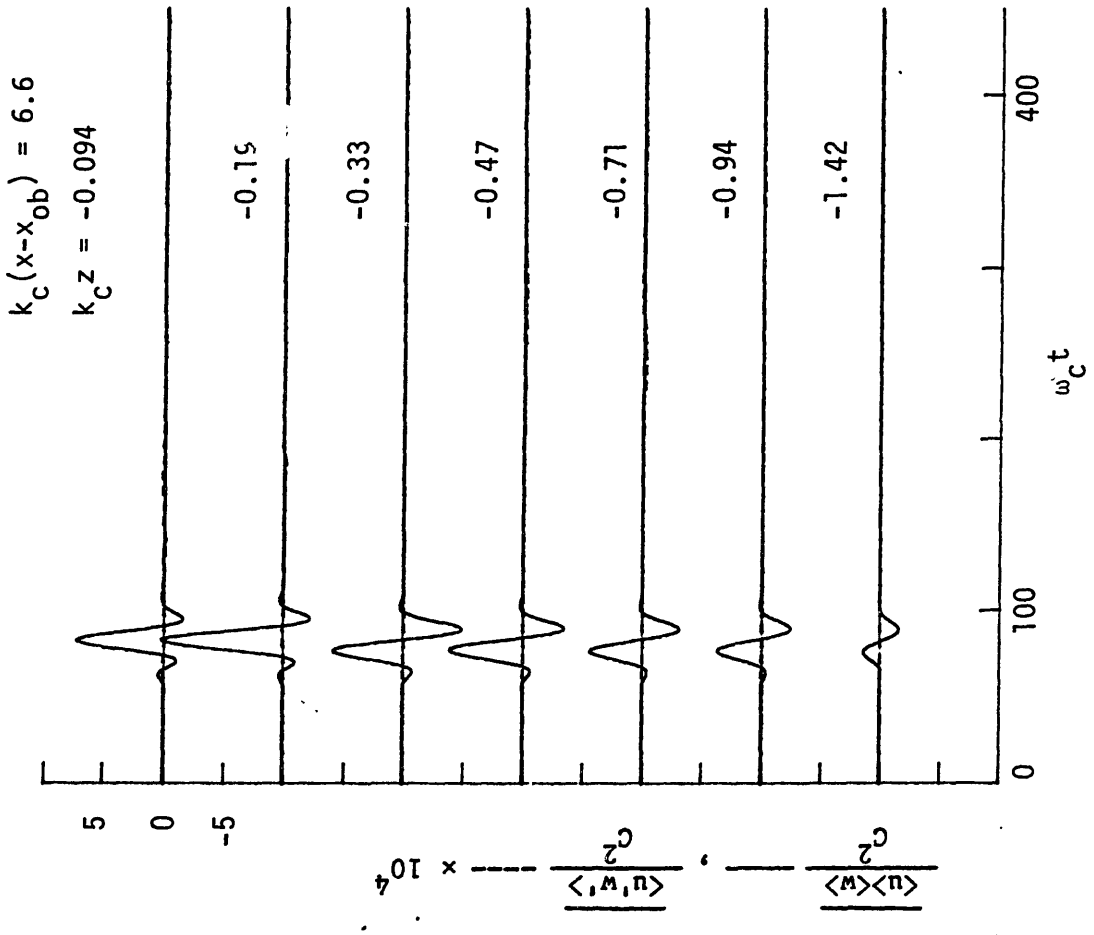

Figure 5.5.2d Shear stress. Continued from figure 5.5.2c.

amplitudes. At the downstream end of the breaking region the mean fluxes look more like an unbroken symmetric wave packet but with a slight net positive flux as was noticed for the spilling wave.

The measurements of the small scale plunging wave (figure 5.3.3) also show the negative fluxes in the center of breaking region in both the mean and turbulent motions. The nondimensional depth of penetration and magnitude of the nondimensional fluxes are in rough agreement with the large scale results.

The quality of the measurements of these turbulence shear stresses presented is seen to be inferior to those of the normal stresses presented in Section 5.4. It appears that more averages are required to obtain good smooth estimates of these cross correlations. The results do, however, qualitatively show that both the mean motion advection and turbulence is responsible for distributing the horizontal momentum induced by breaking to depths of 2 - 3 wave amplitudes. It also shows that the magnitude of the normal stresses and shear stress are comparable.

5.6 The Balance of Total Momentum and Energy

The conservation of horizontal momentum and conservation of energy is applied to the control volume enclosing the breaking region to attempt a balance between the measured fluxes crossing the vertical boundaries x_1 and x_2 (figure 2.3.1), and the time increase in the corresponding densities (momentum and energy). These conservation equations were derived in section 2.3.

5.6.1 Momentum

From equation (2. 33), the conservation of total momentum is given by:

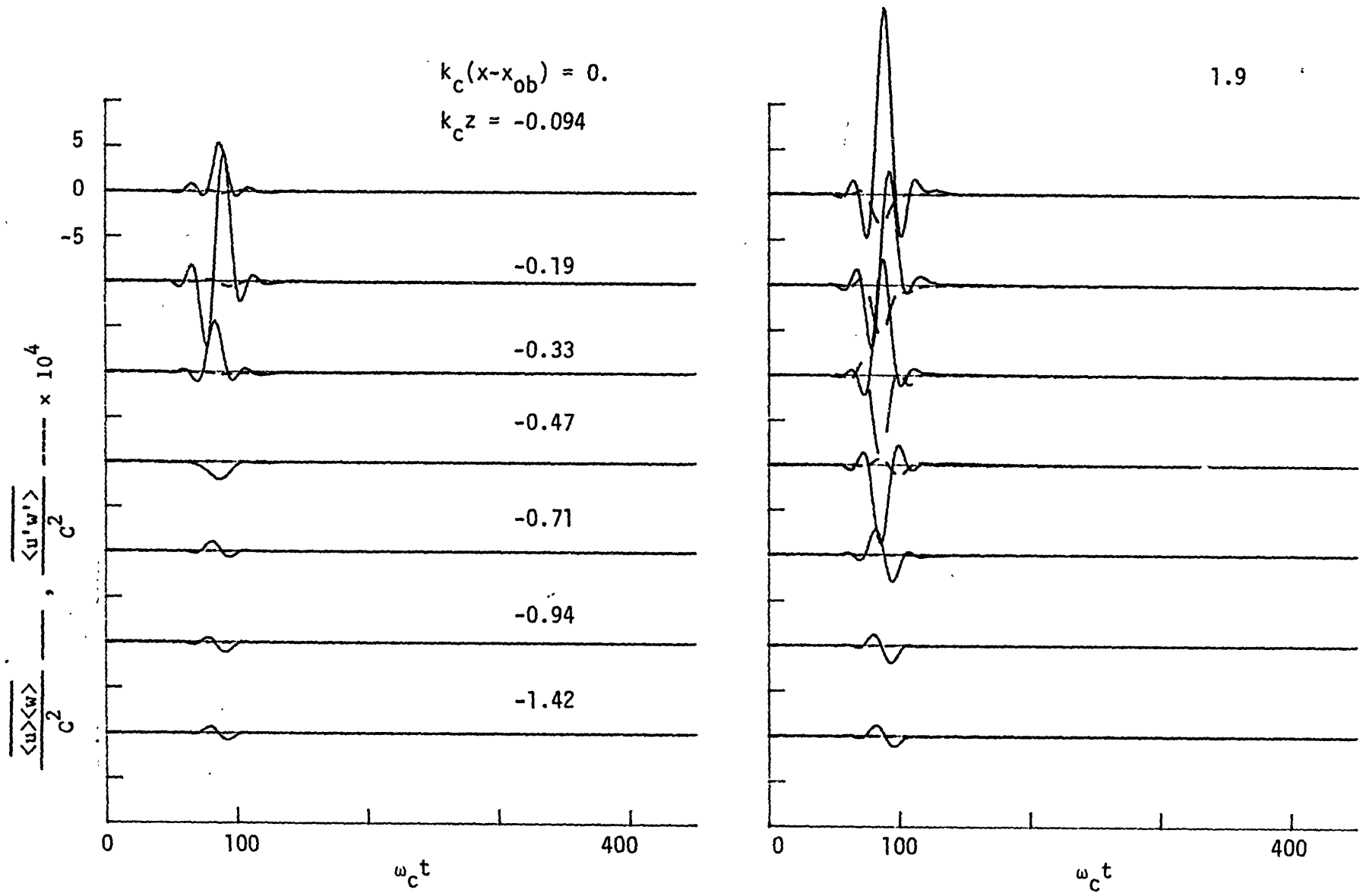

Figure 5.5.3a Time history of shear stress in the breaking region. $\overline{\langle u\rangle\langle w\rangle}$ ——— , $\overline{\langle u'w'\rangle}$ ---- . For f_c = 1.28 Hz ak_c = 0.420 (plunging).

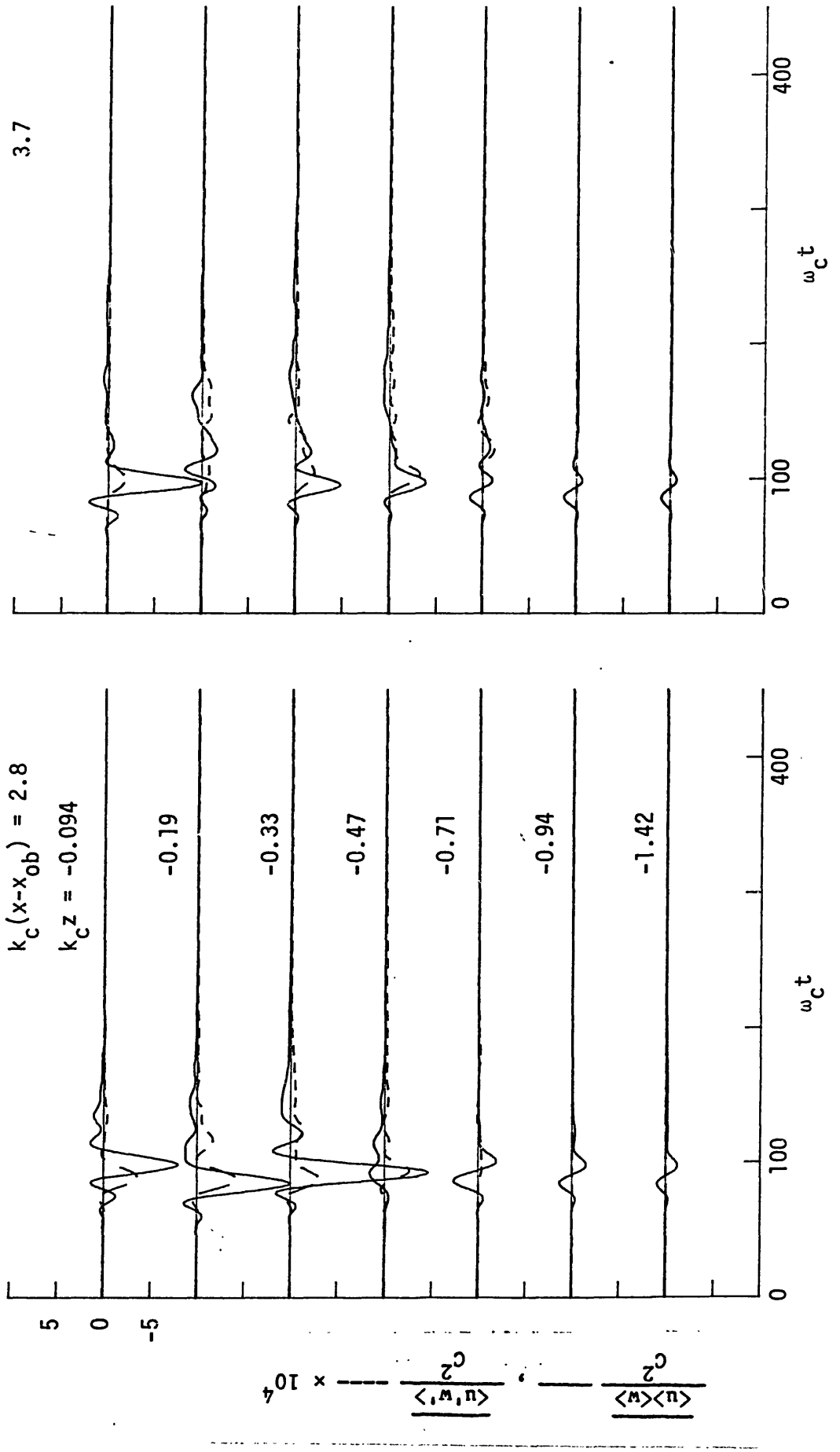

Figure 5.5.3b Shear stress. Continued from figure 5.5.3a.

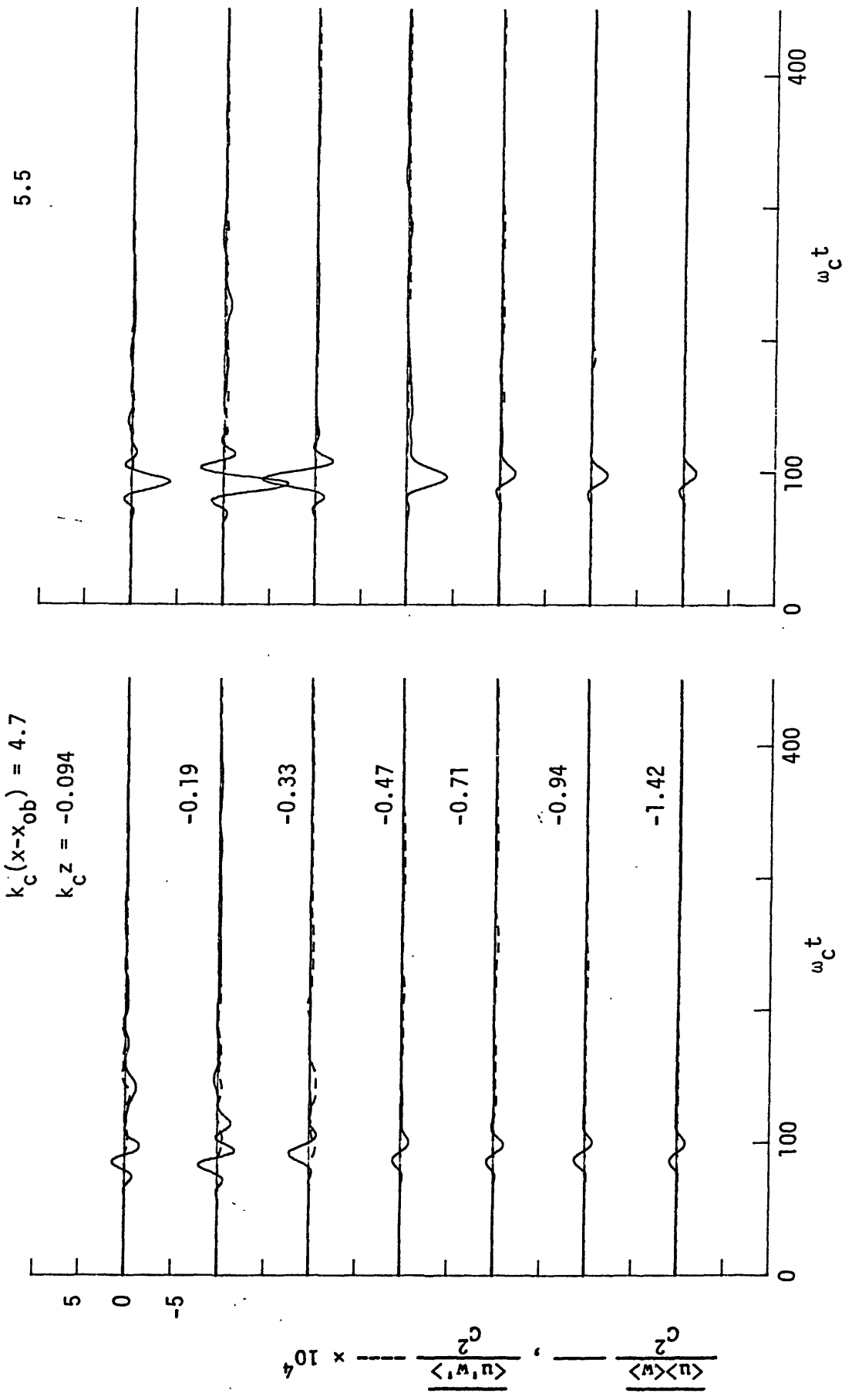

Figure 5.5.3c Shear stress. Continued from figure 5.5.3b

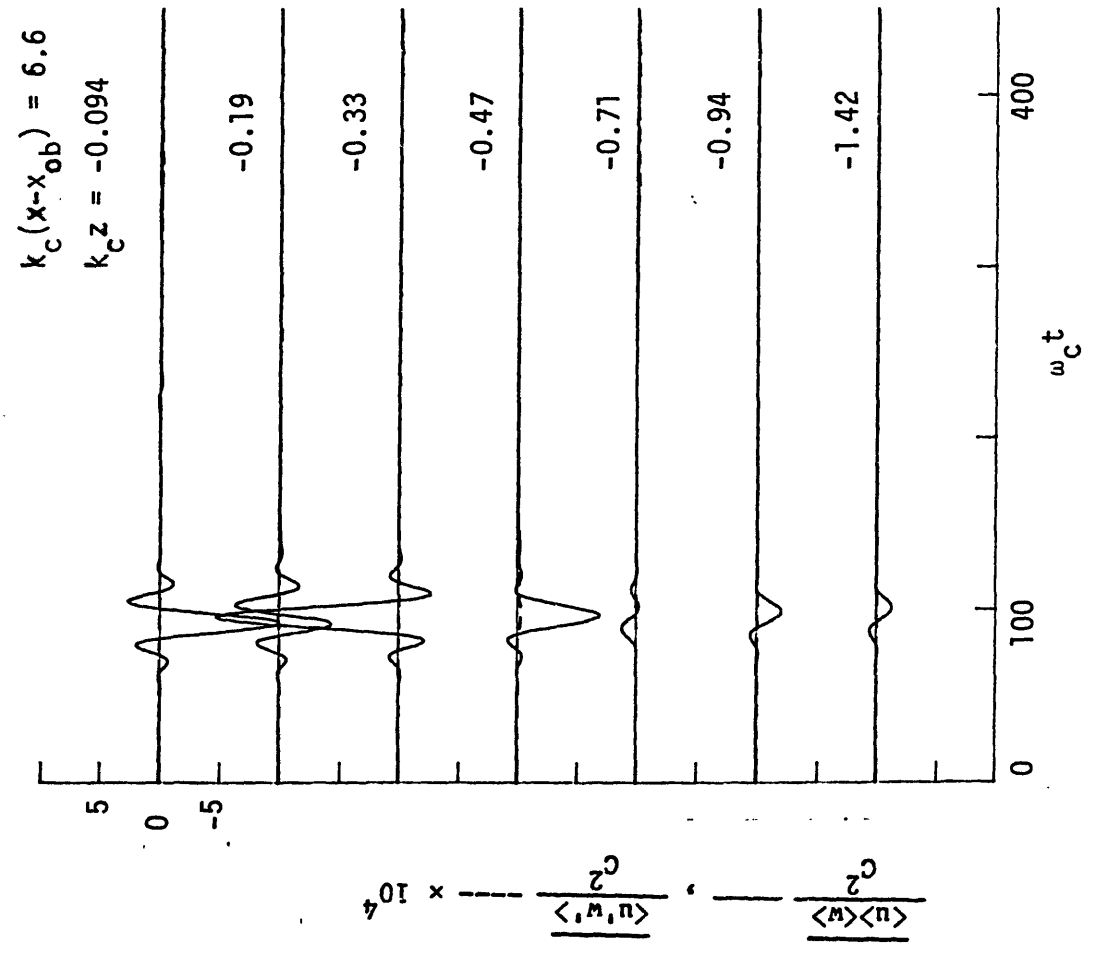

Figure 5.5.3d Shear stress. Continued from figure 5.5.3d

$$\underline{\Delta M} = -\Delta \underline{\overline{\overline{S}}} + \underline{\overline{\overline{\tau}}}_x \tag{5.13}$$

Again, the underbar is a space integration from x_1 to x_2 and the double overbar is a time integration over long time, typically 40 - 80 sec or 40 - 80 carrier wave periods. The change in the momentum flux is

$$\Delta \overline{\overline{S}} = \Delta \overline{\overline{S}}_{c.w.} + \rho g d \, \Delta \overline{\overline{\eta}} . \tag{5.14}$$

The momentum flux lost from the carrier waves $\Delta \overline{\overline{S}}_{c.w.}$ has been measured from the surface displacement variance and is plotted as $\Delta \overline{\overline{\eta^2}} / \overline{\overline{\eta_o^2}}$ as a function of ak_c in figure 3.3.1. The dimensional value of $\Delta \overline{\overline{S}}_{c.s.}$ is computed for each of the three wave cases where the detailed velocity measurements were made. It can be shown (see section 2.2) that

$$\overline{\overline{\eta_o^2}} = \frac{1}{2} \frac{a^2}{\Delta f} \tag{5.15}$$

where a is the input wave amplitude $a = a_n N$ and Δf is the bandwidth of the packet. The number of input frequency components is N = 32. For the case of $f_c = 0.88$ Hz, $ak_c = 0.352$. $\Delta f / f_c = 0.73$ we have $\Delta f = 0.643$ Hz and $k_c = 3.25$ 1/m. Then

$$\overline{\overline{\eta_o^2}} = 90.7 \text{ cm}^2 - \text{s} .$$

This compares with the measured value at the reference station of 90.1 cm^2 -s showing that the theoretical value of $\overline{\overline{\eta_o^2}}$ can be used to compute the dimensional form of the results in figure 3.3.1.

Then

$$\overline{\overline{\Delta S}}_{c.w.} = \rho g \frac{\overline{\overline{\Delta \eta^2}}}{\eta_o^2} \overline{\overline{\eta_o^2}} \left[\frac{2C_g}{C} - \frac{1}{2} \right] \tag{5.16}$$

For this breaking case

$$\frac{\overline{\overline{\Delta \eta^2}}}{\overline{\overline{\eta_o^2}}} = 0.24$$

from figure 3.1.1,

and

$$\overline{\overline{\Delta S}}_{c.w.} = 1.4 \times 10^4 \frac{cm^3}{s}$$

This is normalized by multiplying by k_c^3/ω_c and the results for the three breaking wave cases is shown in table 5.6.1.

The second term on the right in equation (5.14) is the change in the time integrated setdown under the packet and represents the loss of momentum flux from the forced wave. When integrated over the packet, excluding the setup of the transient waves propagating away at $C_g = \sqrt{gd}$, this is comparable to the loss in $\Delta S_{c.w.}$.

The change in total momentum ΔM, in the control volume is given by:

$$\underline{\Delta M} = \int_{x_1}^{2} \int_{-d} u \, \rho \, dz \, dx \tag{5.17}$$

since the fluid in the control volume is initially quiescent. As the volume integral of the turbulent fluctuations is zero, the total horizontal momentum was computed using $\langle \overline{u} \rangle$, the mean velocity. Elemental areas were computed around each measurement point and multiplied by the corresponding measured mean velocity. These were then summed over the 49 elemental areas (see Program MOMSUM in Appendix 3). This measured total momentum is

Table 5.6.1

Momentum Balance in Carrier Waves

		$\frac{\overline{\Delta\eta^2}}{\overline{\eta_0^2}}$	$\overline{\Delta S_{c.w.}}$	ΔM	Percent in current
Plunging					
f_c = 0.88 Hz	ak_c = 0.352	0.24	ρ 0.086	ρ 0.050	58%
f_c = 1.28 Hz	ak_c = 0.420	0.19	ρ 0.076	ρ 0.065	86%
Spilling					
f_c = 0.88 Hz	ak_c = 0.278	0.10	0.024	0.02	83%

ΔM represents the positive momentum left in the breaking region after four wave periods from breaking.

ΔS, ΔM are normalized by multiplying by $\frac{k_c^3}{\omega_c}$

plotted in figure 5.6.1. These time histories show, first, the positive going momentum due to the long transient wave propagating ahead of and away from the packet at $c_g = \sqrt{gd}$. This wave is discussed by McIntyre (1981) and Benjamin (1970). The forced wave negative return flow is seen as the packet crosses the integration region. Note that the Stokes drift should come close to balancing this; however, measurements were not taken above the still water line, where much of this flux is located; therefore the plot shows a net negative momentum here.

The total momentum is then seen to become very close to zero which it should in deep water. The momentum in the positive flowing surface drift is roughly balanced by the lower return flow. Apparently the carrier waves lose momentum which goes into a surface current, but since the packet envelope decreases in amplitude due to breaking, so does the forced wave and thus it loses momentum which is also left behind. This is sufficient to balance the positive flow above. Thus the eddy is generated, as was shown in figure 5.3.2.

Thinking of this in another way, the momentum in the finite length wave packet upstream of breaking is zero (McIntyre (1981 and section 2.3). Similarly, downstream of breaking it is also zero, so there can be no net momentum left behind. In shallow water, it was shown that the momentum is slightly negative according to equation (2.49). If a percentage of this negative flow is lost from the packet it will show up as a negative momentum in the breaking region. This seems to be the case in these results. Also evident is a slow oscillation of period ~28 sec which is likely due to the fundamental mode of oscillation in the channel. The long wave velocity is $C = \sqrt{gh} = 2.4$ m/sec. The length of

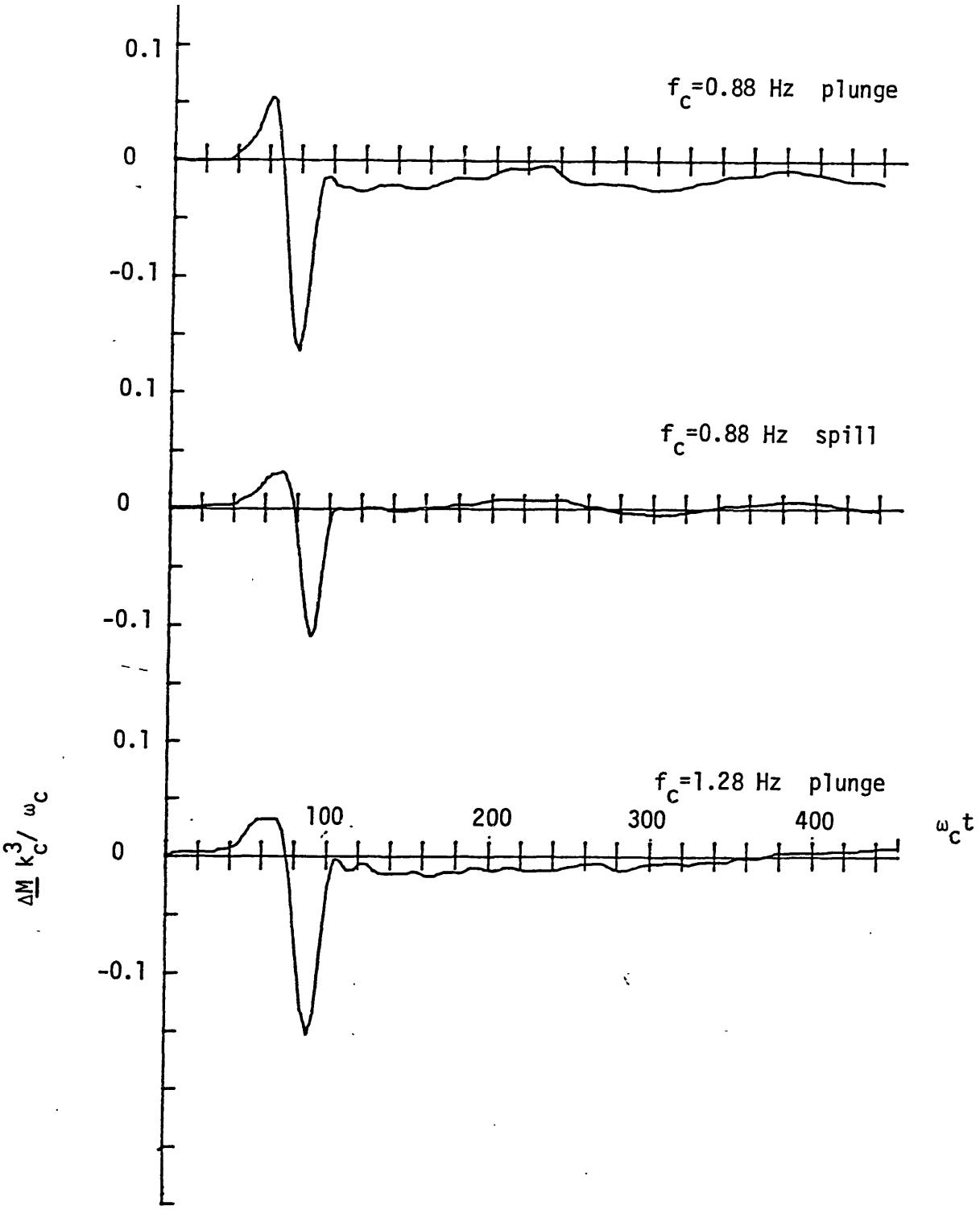

Figure 5.6.1 Total momentum in the breaking region as a function of time.

the channel is ~30 m giving the first mode oscillation of period T = 2L/C = 25 seconds which is close to that measured.

The results showing the zero net horizontal momentum in the breaking is consistent with the physics, however, we are interested in predicting the magnitude of the momentum transferred to surface currents from the carrier waves. This we can estimate by assuming that the negative going flow, set up by the forced wave, U_2, is uniform in depth (figure 5.6.2). (This seems reasonable, since the forced wave is long). Also we assume that the flow induced by momentum lost from the carrier waves U_1, decays to zero at some depth above the bottom. Then the velocity near the bottom is completely due to U_2 and this can be substracted throughout the depth to obtain U_1. This we have done for each time step from breaking. The volume integrated momentum was then computed to obtain the plots in figure 5.6.3. From these plots, the total momentum left in the breaking region after four wave periods has been estimated and listed in table 5.6.1. Comparing the momentum flux loss from the carrier waves $\overline{\overline{\Delta S}}_{c.w.}$ with that in the breaking region, it can be seen that 83 or 86% is accounted for in the mean flow for the spilling wave and the small scale plunging waves. Thus agreement is considered good given the estimation methods, and assumptions made. The discrepancy for the large scale plunging wave is difficult to explain; however, it may be noticed that $\overline{\overline{\Delta\eta^2}}/\overline{\overline{\eta_0^2}}$ from figure 3.3.1 is higher than in the other scales of plunging waves which leads to this discrepancy. We attributed this to additional spray and thus larger losses; however, these momentum balance results tend to cast some doubt on the high losses. Possibly finite depth effects are responsible. On the other hand, the error may be in the estimate of ΔM and the assumption that the breaking effects of the carrier

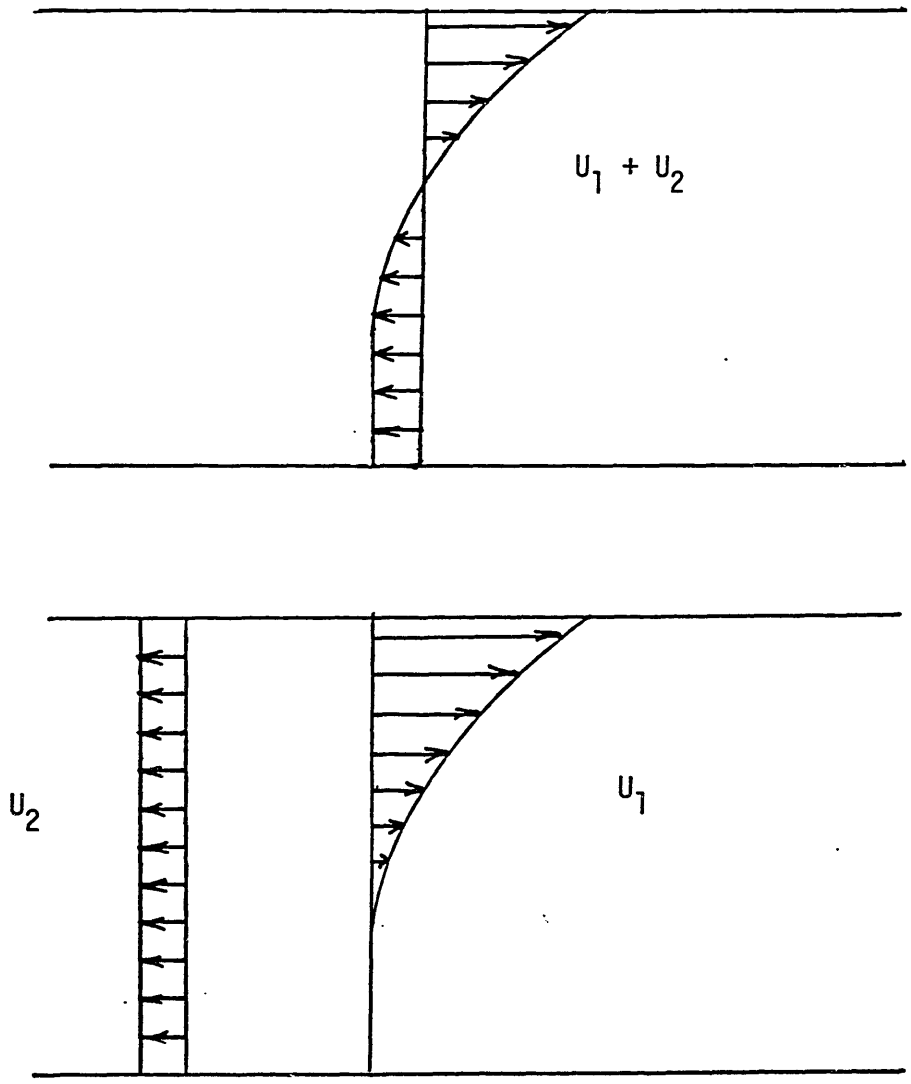

Figure 5.6.2 Model of mean velocity distribution in the breaking region. U_1 induced by carrier wave breaking, U_2 set up by forced wave.

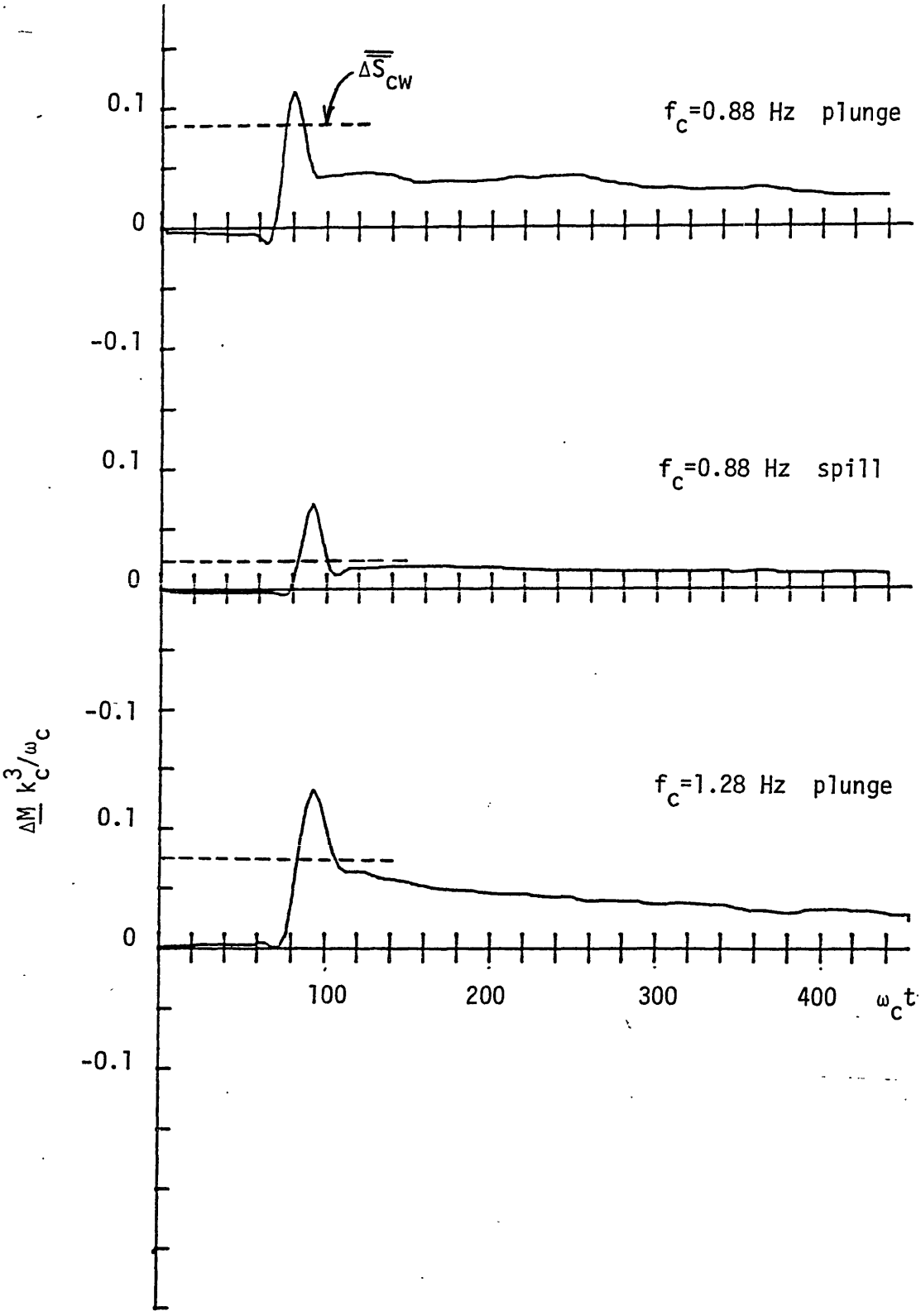

Figure 5.6.3 Total momentum estimated to be induced by breaking carrier waves. Also shown is $\overline{\overline{\Delta S}}_{c.w.}$, the time integrated change in momentum flux.

waves are not felt near the bottom. Possibly, there is cancellation between U_1 and U_2 (figure 5.6.2) at the lower depth and we underestimate U_2 which would give this error between $\Delta S_{c.w.}$ and ΔM.

Overall, however, these momentum balance results are encouraging, showing that indeed breaking can directly transfer horizontal momentum from waves to currents.

Energy

A similar balance is performed on the energy. From Eq. (2.35) the conservation of total energy is given by:

$$\Delta \underline{E} + \Delta \overline{\overline{F}} = -\rho \underline{\overline{\overline{\int_{-d}^{\eta} \varepsilon \, dz}}} \tag{5.18}$$

The difference in the energy flux crossing x_1 and x_2 is

$$\Delta \overline{\overline{F}} = C_g [\overline{\overline{E}}_{x_2} - \overline{\overline{E}}_{x_1}] \tag{5.19}$$

where C_g is assumed equal at these stations. Then

$$\Delta \overline{\overline{F}} = \rho g \, C_g \, \Delta \, \overline{\overline{\eta^2}} \tag{5.20}$$

The measured values of $\Delta\overline{\overline{\eta^2}}/\overline{\overline{\eta_o^2}}$ can be used to compute the change in the energy flux as was done for the momentum balance.

Here

$$\Delta \overline{\overline{F}} = \rho g \, C_g \, \frac{\Delta \overline{\overline{\eta^2}}}{\overline{\overline{\eta_o^2}}} \, \frac{1}{2} \, \frac{a^2}{\Delta f} \tag{5.21}$$

and is normalized by k_c^2/C^2 in table 5.6.2.

The increase in the total energy in the breaking region (integration region) is due to the kinetic energy of the mean motions together with the

Table 5.6.2

Energy Balance over the Breaking Region

		$\frac{\overline{\Delta\eta^2}}{\overline{\eta_0^2}}$	$\overline{\overline{\Delta F}}$	ΔE	$\frac{\Delta E}{\Delta F} \times 100$
Plunging					
$f_c = 0.88$ Hz	$ak_c = 0.352$	0.24	ρ 0.076	ρ 2.5×10^{-3}	3.3%
$f_c = 1.28$ Hz	$ak_c = 0.420$	0.19	ρ 0.072	ρ 2.5×10^{-3}	3.5%
Spilling					
$f_c = 0.88$ Hz	$ak_c = 0.278$	0.10	ρ 0.020	ρ 5.0×10^{-4}	2.5%

ΔE represents the total energy in the breaking region after four wave periods from breaking.

ΔF, ΔE are normalized by multiplying by $\frac{k_c^2}{c^2}$.

fluctuating turbulent motion. The still water level returns to its initial level after the waves have passed so the change in potential energy is assumed to be zero. The total energy is given as:

$$\Delta \underline{E} = \frac{1}{2} \rho \int_{x_1}^{x_2} \int_{-d}^{\eta} \langle \underline{V}^2 \rangle \, dx \, dz \tag{5.22}$$

where $\underline{V}^2 = u^2 + w^2 + v^2$

The contribution to the kinetic energy is computed by

$$\langle \underline{V}^2 \rangle = \langle u \rangle^2 + \langle w \rangle^2 + \langle u'^2 \rangle + \langle w'^2 \rangle + \langle v'^2 \rangle \, . \tag{5.23}$$

Since the transverse velocity, v, was not measured, the assumption was made that the mean motion was 2-D giving

$$\langle v \rangle^2 = 0 \, . \tag{5.24}$$

The turbulence, being 3-D, must include energy from the transverse direction so we set

$$\langle v'^2 \rangle = \langle w'^2 \rangle \, . \tag{5.25}$$

The squared velocities were multiplied by the elemental areas surrounding each measurement location and then summed.

The results are plotted in figure 5.6.4 for the three breaking cases. The kinetic energy is normalized by k_c^2/C^2 to make the comparison between the large scale plunging and small scale plunging. At times four wave periods after breaking, the decay of the total kinetic energy with time is seen to be proportional to

$$\omega_c (t - t_{ob})^{-1} \qquad t_{ob} = \text{time of observed breaking} \tag{5.25}$$

for both scales of plunging and also for the large scale spilling.

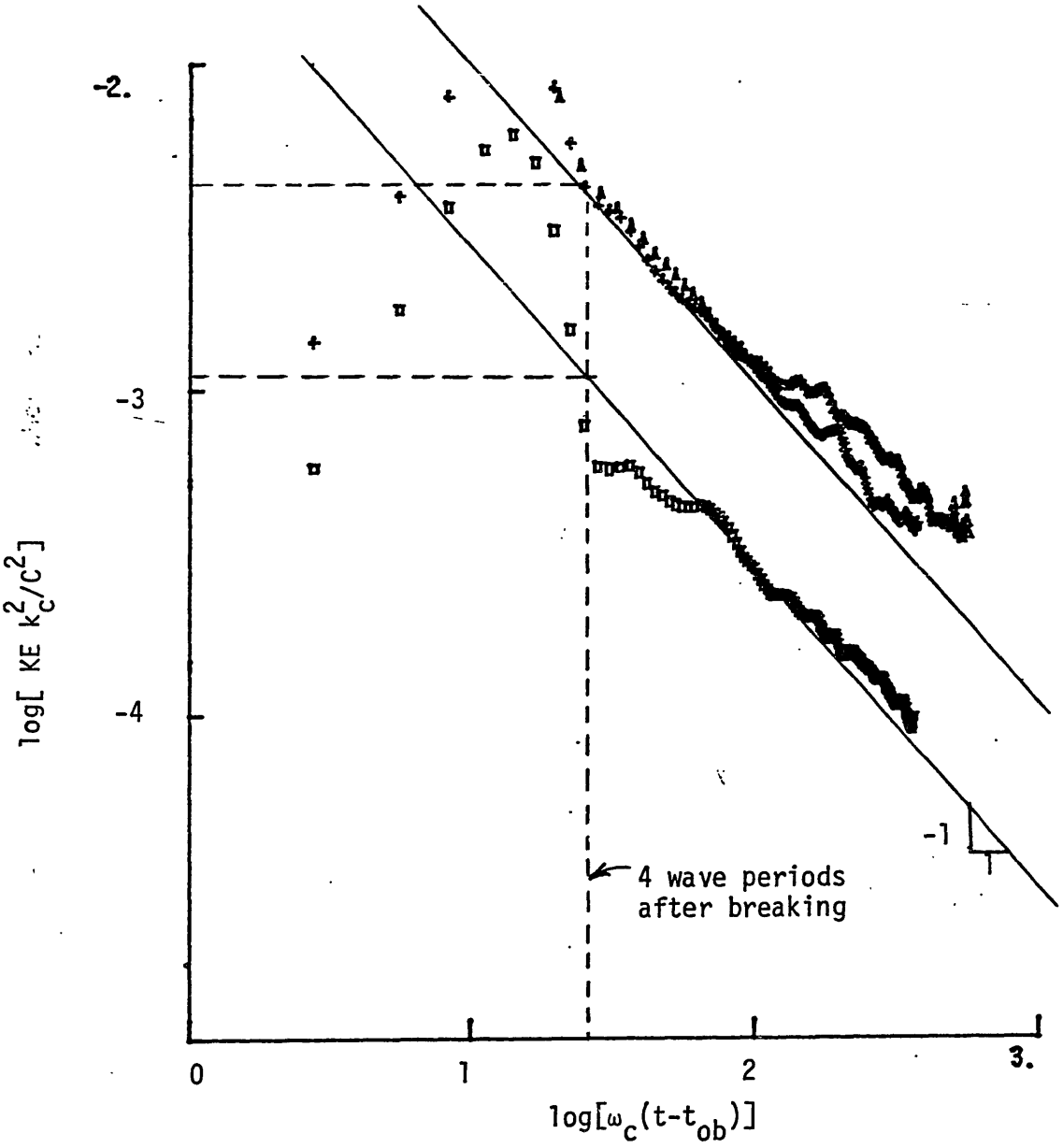

Figure 5.6.4 Total kinetic energy in the breaking region as a function of time. For f_c = 0.88 Hz, ak_c = 0.352 plunge (+), ak_c = 0.278 spill (□), f_c = 1.28 Hz, ak_c= 0.420 plunge (Δ).

The agreement between scales in the nondimensional kinetic energy left behind by the breaking wave packets is quite good.

The normalized kinetic energy measured in the breaking region after four wave periods is estimated from figure 5.6.4 and equation (5.22). These results are summarized in table 5.6.2. From this energy balance, it is shown that only a small percentage (2 - 4%) of the energy lost by the waves in breaking remains in the breaking region after four wave periods. From this time on, the kinetic energy decays as t^{-1}. Apparently 96 - 98% of the energy goes into turbulence and is dissipated within four wave periods.

5.6.3 Decay of turbulence and dissipation estimates

The decay rate of the total turbulent kinetic energy is of interest in estimating dissipation and diffusion rates in the turbulent flow generated by breaking. Plotted in figure 5.6.5 is the volume integrated turbulent kinetic energy contribution from the horizontal and vertical velocities u'^2, w'^2. The decay of each of these contributions also follows a t^{-1} power law, where the time origin is the time of observed breaking. The deviation from isotropy can be seen in the lower energy level in the vertical velocity. Estimates of dissipation based on isotropic flows must be interpreted with this knowledge in mind. However, the isotropic assumption does allow simple estimates of dissipation. Assuming an isotropic flow the turbulent kinetic energy is given by

$$\nabla KE_t \approx u_t^2 \nabla \approx t^{-1} \tag{5.26}$$

where ∇ is the volume of the turbulent region. From the dye mixing results presented in Chapter 4 we showed that

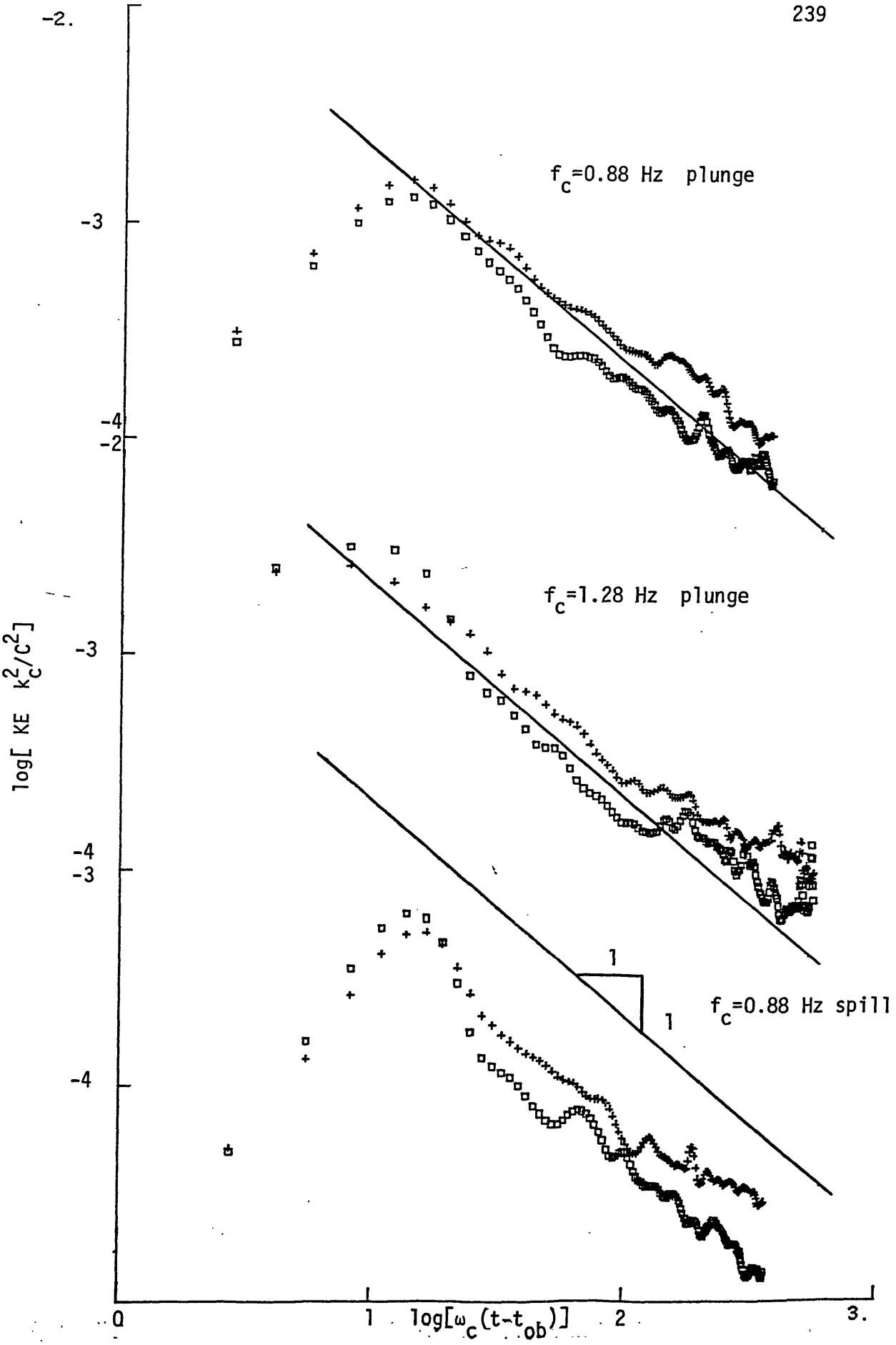

Figure 5.6.5 Turbulent contribution to volume integrated kinetic energy u'^2 (+), w^2 (□). Line of slope 1 is drawn at same location in each plot.

$$\forall \approx \text{Area} \approx \ell^2 \approx t^{1/2} \tag{5.27}$$

where ℓ is assumed to be proportional to the integral length scale of the turbulence.

Then

$$u_t^2 \approx \frac{t^{-1}}{t^{1/2}} \approx t^{-3/2} \tag{5.28}$$

and

$$u_t \approx t^{-3/4} \ . \tag{5.29}$$

The dissipation rate of turbulent kinetic energy is

$$\varepsilon \forall = \frac{\partial (u^2 \forall)}{\partial t} \approx t^{-2} \ . \tag{5.30}$$

Then

$$\varepsilon \approx \frac{t^{-2}}{\ell^{1/2}} \approx t^{-5/2} \tag{5.31}$$

where ε is the dissipation rate per unit mass.

The estimate of the dissipation, ε, based on isotropic turbulence given by Taylor (1935) assumes a large Reynold number flow and that the large eddies supply energy to the small eddies at a rate equal to the dissipation rate. The energy is dissipated at high wavenumbers (small eddies). In this flow field the Reynolds number Re $\approx$ 5000 which is large compared to 1.

The rate of energy transfer by the large eddies is estimated as:

$$\varepsilon \approx \frac{u_t^3}{\ell} \ . \tag{5.32}$$

Using the power laws for u_t and ℓ as measured above

$$\varepsilon \approx \frac{t^{-9/4}}{t^{1/4}} = t^{-5/2} \quad . \tag{5.33}$$

This independent estimate of the time dependence of ε is in agreement with the estimate given above from equation (5.31). This agreement supports the accuracy of these estimated power laws based solely on the measurements.

Our estimates of u,ℓ also show that an eddy diffusivity would vary as

$$K \approx u_t \ell \approx t^{-1/2} \tag{5.34}$$

This is also the time dependence for the Reynolds number of the flow which is in contrast to a wake flow where K ≈ constant.

Dissipation just after breaking

The dramatic loss of wave energy in the first four wave periods after breaking (96 - 99% of the energy lost from the waves) can be justified, at least to an order of magnitude. The total dissipation is estimated by

$$\text{DISS.} \approx \rho \int_0^{4T} \varepsilon \ (\text{area}) \ dt \tag{5.35}$$

where

$$\varepsilon \approx \frac{u_t^3}{\ell}$$ as above.

An estimate of the changing area can be made using equation 4.5 found from the dye mixing experiments in Chapter 4.

$$k_c^2 \text{ Area} = C_2(\omega_c t^*)^{1/2} \tag{5.36}$$

where $t^* = t - t_{ob}$.

Also letting $\ell \approx D$, the maximum depth

$$k_c D = C_1(\omega_c t^*)^{1/4} \tag{5.37}$$

An estimate of the characteristic velocity u is found from the rate of change of the maximum dye depth

$$U = \frac{dD}{dt} = \frac{\omega_c}{4k_c} C_1(\omega_c t^*)^{-3/4} \tag{5.38}$$

and

$$C = \frac{\omega_c}{k_c}$$

Note that this velocity becomes infinite at $t^* = 0$ which is not physically possible. The power laws pertain to the decay at some later times.

From the dye mixing results it seems reasonable to assume this relationship for U_t after one wave period.

The total dissipation from one to four wave periods can be found from equation (5.35) using the above relations. Then

$$\text{DISS} = \int_T^{4T} \rho C^3 \frac{C_1^2 C_2}{k_c} (\omega_c t^*)^{-2} \tag{5.39}$$

using $C_1 = C_2 \approx 0.5$

$$\text{DISS} \approx \rho\, 0.004 \frac{C^2}{k_c^2} \tag{5.40}$$

Over the first wave period we use U = 0.18 C from figure 4.3.2, showing the vertical velocity of the dye during this period. In this case

$$\text{DISS} \simeq \int_0^T (0.18\ C)^3 \frac{1}{k_c} (\omega_c t^*)^{1/4} \tag{5.41}$$

$$\text{DISS} \simeq \rho\ 0.012 \frac{C^2}{k_c^2} \tag{5.42}$$

Total dissipation over 0 -4T is then

$$\text{DISS} \simeq \rho\ 0.018 \frac{C^2}{k_c^2} \tag{5.43}$$

which is of the same order as the energy lost from the wave field table 5.6.2 of

$$\rho\ 0.076 \frac{C^2}{k_c^2}\ .$$

This rough estimate tends to support the large loss rate during the first four wave periods after breaking.

CHAPTER 6

Summary and Conclusions

The process of surface wave breaking has been studied by generating a single breaking wave group in the laboratory. In this way it is isolated from other physical influences, such as wind, and other breaking waves present in the field so that the full long-lived motions induced by breaking alone were successfully measured.

The breaking group was generated by a superposition of linear wave components with phases adjusted so that according to linear theory all components become in phase at a predetermined time and location in the tank. The highly dispersive resultant packet was modulated in frequency and amplitude; its energy density increased to a maximum near the theoretical (by linear theory) energy focal point and the packet dispersed downstream. The wave packet generation equation (equation 2.3) allowed straightforward specification of the parameters that describe the packet; these being the nondimensional wave packet amplitude ak_c, the bandwidth, $\Delta f/f_c$, and a phase specification $x_b k_c$, which was determined by the breaking location. Specification of the center frequency f_c allowed changes in the scale of the wave packet. Three scales of wave packets were generated: f_c = 0.88 Hz, 1.08 Hz, 1.28 Hz corresponding to center wavelengths of 0.9 m, 1.3 m, 1.9 m, respectively. Measurements were made on packets with the nondimensional variables over the following ranges: ak_c (0.1 → 0.5), $\Delta f/f_c$ (0.4 → 1.4), $x_b k_c$ (27 → 66).

As the input wave amplitude was increased, the packet went from non-breaking to incipient breaking at a location within 1/4 of a wavelength from the theoretical focal point. As ak_c was increased further, the breaking became more violent and the break point moved upstream at one wavelength intervals. A more vigorous plunging breaker was produced one wavelength upstream. Timestep photographs of the breaking wave showed the very high degree of repeatability between runs, to within 2 cm horizontal error at the same time step. These photographs also show the unsteadiness of the breaking process and the continual change in the local slope of the wave front through breaking.

Measurements of the local wave amplitude at breaking normalized by the center wave number showed that incipient breaking occurred over a wide range of this steepness parameter ranging from $0.2 \rightarrow 0.35$. The crest to trough height divided by the measured wavelength between zero up crossings, H/λ, did not result in a consistent predictor of breaking, either. The breaking criteria of Michell (1893), $H/\lambda = 1/7$, is roughly twice that found in these measurements.

Another wave steepness defined by the maximum wave amplitude divided by the horizontal distance from crest to forward zero crossing (figure 3.4.2) was a better predictor of incipient breaking, but did not give a constant value for the more vigorous plunging and spilling waves. These local measurements emphasize that the wave geometry <u>at</u> breaking is not a good indicator of the intensity of breaking. On the other hand, the value of ak_c, where a is the summation of the input amplitudes turned out to be a very good predictor of incipient breaking $ak_c \approx 0.25$ and also of the spilling breaking $ak_c \approx 0.3$ over the range of packet bandwidths and center frequencies measured.

The surface displacement variance integrated over the packet period, $\overline{\overline{\eta^2}}$, provided a good estimate of the momentum flux and energy flux in the carrier waves where the packet envelope was slowly varying. This was the case three wavelengths upstream and downstream of breaking. At locations closer to breaking, the surface displacement variance gave greater errors in predicting these fluxes. In fact, oscillations were observed in $\overline{\overline{\eta^2}}$ at intervals of one wavelength, which grew largest at the energy focal point. These were present even for nonbreaking wave groups. It is thought that this is the result of an exchange of energy between kinetic and potential energy; we only measure the potential energy flux. These oscillations could also result from oscillations in the group velocity. At the reference stations away from breaking, $\overline{\overline{\eta^2}}$ was constant in x. This allowed us to treat the breaking as a black box and determine the losses due to breaking by differencing the measured variance $\overline{\overline{\eta^2}}$ between these stations. Viscous losses in the channel side walls and bottom boundary layers (8%, over six wavelengths) were also subtracted so that the losses due to breaking were found.

The momentum flux lost from the wave group was found to depend strongly on the wave packet amplitude ak_c and less sensitive to changes in bandwidth $\Delta f/f_c$ and breaking location $x_b k_c$. Also the dependence on ak_c was found to be the same over the three scales measured.

Incipient breaking occurred at $ak_c = 0.25$ with essentially zero momentum flux loss. The losses increased rapidly to 15% as ak_c increased to 0.3. This corresponds to a moderately vigorous spilling breaker. Even for gentle breaking, losses of 5 - 10% result. With an increase in ak_c to ~ 0.38, a plunging breaker resulted in losses of

20 → 25%. From this we see that the transition from incipient breaking to spilling is very sharp and that losses increase rapidly up to this point. Larger increases in ak_c are required to reach the plunging breaker situation with only an additional 5 - 10% loss.

The scaling of this behavior is very good up to spilling; above this, the losses are 5% greater in the large scale, possibly due to the greater observed air entrainment due to a second sheet of fluid which is pushed ahead as the initial plunging jet hits the free surface. This effect was not as dramatic for the smaller scale waves.

The spectra of the surface displacement before and after breaking show that these losses from the wave field are from the high frequency end of the input band, also losses come from the second harmonic band. It is of interest to note that the spectra of η at the energy focal point, even without breaking, looks very different from its top hat shape upstream and downstream. This energy of the higher harmonics increases at the expense of energy in the primary band. This has implications for using surface displacement spectra to infer total wave energy spectra when the waves are very steep and nonlinear.

The breaking disturbance was observed to cause second free harmonic waves to be radiated both upstream and downstream from breaking. This was verified through spectral analysis. In this way breaking may be regarded as a source of high frequency wave energy to the spectrum.

The technique of using the boundaries of a dye cloud, generated when breaking occurred over dye initially floating on the surface, proved successful in defining a region directly influenced by breaking. This was justified by comparisons with the the spatial extent of measured turbulence. The maximum dye depth and dye area was found to follow power

laws in time; the same power for all three scales and intensities of breaking. The dye area is proportional to $(t - t_{ob})^{1/2}$ and the maximum depth of $(t-t_{ob})^{1/4}$. The reference time, t_{ob}, is the time of observed air entrainment and bubble generation. The coefficients multiplying these power laws give the magnitude of the quantities and were found to be related to the momentum flux loss from the wave field and thus to the input wave amplitude ak_c.

Dye was mixed down very quickly upon breaking to depths of 1-2 wave amplitudes within 1/2 wave period. The next passing wave trough carried thedye down further. From this time onward turbulent dispersion (from the turbulence generated by the breaking) caused the dye boundary to deepen to 3-4 wave amplitudes after 10 wave periods. The horizontal length of the dye cloud at the surface grew at the phase speed of the wave due to the advance of the breaking front. This length reached ~ 0.8 of a wavelength. Only for the case of the large scale plunging wave was there a discrepancy in this length. Again, the secondary sheet of fluid ejected by the plunging jet caused dye to be mixed at greater horizontal extent. The problem of scaling air entrainment seems to be persistent. This cascading effect resulted in two distinct patches of dye to be generated under the breaking region.

The boundaries of the dye cloud provided a guide for a detailed velocity survey in the breaking region to determine the mean motions and turbulence generated by breaking. Since the turbulence generated by breaking is not stationary and contains low frequencies, ensemble averaging rather than time averaging was required to determine the mean and turbulent averages. Of course, this required many repeats of the experiment. The data

acquisition and wave generation system was set to be triggered by computer every 8 - 10 minutes, thereby eliminating any user intervention. The ensemble averaging also had the desirable result of separating the deterministic wave motion from the turbulent velocities generated by breaking.

Currents of magnitude 0.02 C where C is the phase speed, were generated at the surface as the result of breaking. Scaling this to ocean waves of period T = 6 to 10 sec, this breaking induced current becomes 10-30 cm/s which is substantial. This positive flow penetrated to depths of 1-2 wave amplitudes. These motions were found to be very long lived, still above 0.005 C after 60 wave periods. It seems likely that in a moderately intense breaking wave field the next breaking wave will arrive well within this time to sustain this surface current. The unexpected feature of a deeper return flow left over after passage of the packet was found. This negative flow is of lower magnitude but goes to nearly the bottom of the channel. This mass flux balances that in the positive current above. Together these flows form a large circulation over approximately one wave length in horizontal extent. Apparently just as the carrier waves lose momentum so does the forced wave traveling with the Packet. The losses from the two are the same and go into generating this circulation. This eddy is very long lived; still evident after 60 wave periods. These motions may affect bottom processes such as sediment transport in shelf regions where the depth is small compared to the group length. The circulation may assist in transporting bottom matter to the surface.

The measured turbulence shows rms velocities of 0.02 C, which is of the same magnitude as the mean current. The turbulence levels decreased

with depth. However, noticeable levels were measured at depths of 2-3 wave amplitudes.

The volume integrated total kinetic energy left in the breaking region after four wave periods from breaking was only 2 to 4% of the energy lost from the waves. Essentially all of the lost wave energy then goes into turbulence and is dissipated within four wave periods. On the other hand, between 60 - 90% of the horizontal momentum lost from the carrier waves is shown to go into surface currents.

After four wave periods, the decay in time of the total kinetic energy as well as the decay of the turbulent kinetic energy alone, followed a $(t - t_{ob})^{-1}$ power law, this dependence, used with the time dependence of the dyed area and depth of

$$\text{area} \approx t^{1/2}$$

$$\ell \approx t^{1/4}$$

gave estimates for the average decay of the turbulence velocity, of dissipation, and eddy diffusivity for the flow generated by the unsteady breaking wave:

$$u_t \approx t^{-3/4}$$

$$\varepsilon \approx t^{-5/2}$$

$$K \approx t^{-1/2}$$

These values are in contrast to those measured under a steady spilling breaking indicative of a wake flow (Battjes and Sakai, 1981).

These values are in contrast to those measured under a steady spilling breaking indicative of a wake flow (Battjes and Sakai, 1981).

$$u_t \approx t^{-1/2}$$

$$\ell \approx t^{1/2}$$

$$\varepsilon \approx t^{-2}$$

$$K \approx \text{constant.}$$

It is felt that the empirical results presented here, of the losses of momentum flux from the carrier wave field due to breaking, may be used in conjunction with breaking wave statistics to estimate global loss rates over the wave field. Some preliminary estimates of this have already been made (Melville and Rapp, 1985). The average measured loss of 10% per breaking wave group was used in conjunction with an estimate by Thorpe and Humphries (1980) of the horizontal distance between breaking waves to arrive at an estimate of $\partial S/\partial x$ for the gradient of the momentum flux lost from the wave field. The order of this term agrees well with the corresponding wind input. This states that essentially all the momentum flux from the wind is going through the wave field and being lost in breaking. This, then, explains the much slower growth of the wave field as measured by Mitsuyasu (1985), since the full wind input is not expected to go into wave growth.

In the future it is hoped that the momentum flux loss, amplitude dependence can be incorporated into a surface wave model to obtain more

accurate estimates of the global losses. Also, similar models may be developed to predict the rate and extent of vertical mixing due to wave breaking over the wave field based on the empirical relations of dye mixing.

The scaling of these results by the wave frequency and length showed good agreement between scales; however, some discrepancy was reported for the more vigorous plunging at the large scale. The loss of momentum flux and the horizontal extent of mixing were larger than in the smaller scales. We suggested that this was due to the air entrainment and spray which may not scale with the wave variables. Larger scale experiments in a large laboratory facility are warranted to investigate the scaling.

Over all, the measurements have reemphasized the fact that breaking is a very important process in wave modeling, influencing mixing and in transferring horizontal momentum from the wind to the water surface. In addition, quantitative measures of dissipation, mixing rates, and transfers of momentum from waves to currents have been provided. As far as we are aware, this is the first controlled experimental verification that breaking transfers horizontal momentum from waves to currents. The large scale circulation left behind by the breaking has, to our knowledge, not been previously observed. Although the experiments simulate large scale oceanic breaking due to wave superposition, some of the mixing results may apply to smaller scale wind induced breaking.

TABLE 6.1

Summary of Main Results

- Method of wave generation proved to be very repeatable allowing "identical" wave conditions to be measured repeatably.

- The wave group loses 10-25% of its excess momentum flux and energy flux as the result of breakup. Even gentle spilling causes losses of 5 - 10%.

- Packet amplitude, ak_c, most sensitive parameter determining loss of excess momentum flux. $\Delta f/f_c$, $x_b k_c$ less sensitive.

- Loses are from high frequency end of input band.

- Local measure of wave height at breaking is a poor indicator of breaking inception and intensity.

- Mixed Region:

  Length 0.8 - 1.0 wavelength in 1-2 wave periods.

  Depth increases as time$^{1/4}$

  $k_c D = (0.28 - 0.43)[\omega_c (t - t_{ob}]^{1/4}$ Spilling wave

  $k_c D = (0.38 - 0.57)[\omega_c (t - t_{ob})]^{1/4}$ Plunging wave

  2 - 3 local waveheights in 5 wave periods

  3 - 4 local waveheights in 10 wave periods

Coefficients scale with f_c, and are functions of ak_c.

- Currents induced by breaking are 0.03 - 0.02 C, initially, slowly decay to 0.005 C after 60 waveperiods. C is the linear wave phase speed. Currents of 0.02 C penetrate to depths 1 - 2 waveheights.

- Turbulence velocity of 0.02 C at surface decaying to 0.005 C at depths 3 - 4 follows dye boundary quite well.

- Deeper return flow is also induced, presumably by forced wave traveling with the group.

- Together a large eddy is set up, 1 wavelength in horizontal extent and 4 waveheights in depth.

- 58 - 86% of momentum lost from carrier waves is accounted for in surface currents.

- Only 3% of the energy remains after 4 wave periods from breaking; 96 - 98% is dissipated in this time.
  Decay of total kinetic energy $\sim t^{-1}$

$$u' \sim t^{3/4}$$

$$\varepsilon \sim t^{-5/2}$$

REFERENCES

Baba, E. 1969, "A new component of viscous resistance of ships," J. of the Soc. of Nav. Arch. of Japan, 125, 22-34.

Baba, E. 1976, "Wave breaking resistance of ships," Proc. Int. Seminar on Wave Resistance, Tokyo. Soc. of Nav. Arch. of Japan, 75-92.

Banner, M.L. 1985, "On the hydrodynamics of small-scale breaking and their microwave reflectivity properties," in The Ocean Surface: Wave Breaking, Turbulent Mixing and Radio Probing, Reidel, Dordrecht, Holland, 245-248.

Banner, M.L. and Phillips, O.M. 1974, "On the incipient breaking of small scale waves," J. Fluid Mech., 65, 647-656.

Battjes, J.A. and Sakai, T. 1981, "Velocity field in a steady breaker," J. Fluid Mech., 111, 421-437.

Benilov, A.Ju. 1978, "The error of the linear filtration method in the analysis of the fluctuations of random fields of the near water atmospheric layer and the upper ocean," Oceanology, 18, 28-34.

Benjamin, T.B. 1970, "Upstream Influence," J. Fluid Mech., 40, part 1, 49-79.

Byatt-Smith, J.G.B. and Longuet-Higgins, M.S. 1976, "On the speed and profile of steep solitary waves," Proc. Roy Soc. Lond. A, 350, 175-189.

Chan, E.S. 1985, "Deep water breaking wave forces on structures," ScD Thesis, Massachusetts Institute of Technology.

Clay, C.S. and Medwin, H. 1977, Acoustical Oceanography, Wiley, New York.

Cokelet, E.D. 1977, "Steep gravity waves in water of arbitrary uniform depth," Phil. Trans. Roy. Soc. Lond. A, 286, 183-230.

Compte-Bellot, G. and Corrsin, S. 1966, "The use of a contraction to improve the isotropy of grid generated turbulence," J. Fluid Mech., 25, 657-682.

Donelan, M.A. 1978, "Whitecaps and momentum transfer," Turbulent Fluxes Through the Sea Surface, Wave Dynamics and Prediction Favre, Hasselmann, NATO Conf. Series, Plenum Press, New York.

Donelan, M.A., Longuet-Higgins, M.S. and Turner, J.S. 1972, "Periodicity in whitecaps," Nature, 239, 449-451.

Duncan, J.H. 1981, "An experimental investigation of breaking waves produced by a towed hydrofoil," Proc. Roy. Soc. Lond. A, 377, 331-348.

Dysthe, K. B. 1979, "Note on a modification to the nonlinear Schrödinger equation for application to deep water waves," Proc. Roy. Soc. Lond. A, 369, 105-114.

Greenhow, M. 1983, "Free surface flows related to breaking waves," J. Fluid Mech., 134, 259-275.

Greenhow, M., Vinje, T., Brevig, P. and Taylor, J. 1982, "A theoretical and experimental study of the capsize of Salter's duck in extreme waves, J. Fluid Mech., 118, 221-239.

Hinze, J.O. 1959, Turbulence: An Introduction to its Mechanism and Theory, McGraw-Hill, New York.

Hunt, J.N. 1952, "Viscous damping of waves over an inclined bed in a channel of finite width," Houille Blanche, 6, 836.

Hasselman, K. 1974, "On the spectral dissipation of ocean waves due to whitecapping," Boundary-Layer Meteo., 6, 107-127.

Iusim, R. and Stiassnie, M. 1982, "The induced mean flow accompanying a water-wave packet," (Personal communication).

Kitaigorodski, S.A., Donelan, M.A., Lumley, J.L., and Terray, E.A. 1983, "Wave-turbulence interactions in the upper ocean. Part II: statistical characteristics of wave and turbulent components of the random velocity field in the marine surface layer," J. of Phys. Ocean., 13, 1988-1999.

Kjeldsen, S.P. 1981, "Design waves," Norwegian Hydrodynamic Laboratories, Report No. 1 81008.

Kjeldsen, S.P. and Myrhaug, D. 1979, "Breaking Waves in Deep Water and Resulting Wave Forces," Proc. 11th Offshore Technology Conference, Houston, Texas, Paper No. 3646.

Kjeldsen, S.P., and Olsen, G.B. 1972, "Breaking Waves," (16 mm film), Lyngby, Technical University of Denmark.

Kjeldsen, S.P., Vinge, T., Myrhaug, D., Brevig, D. 1980, "Kinematics of deep water breaking waves," Proc. 12th Offshore Tech. Conf., Houston, Paper No. 3714.

Lin, W.M., Newman, N.J., and Yue, D.K. 1984, "Nonlinear forced motions of floating bodies," Proc. 15th Symposium on Naval Hydrodynamics.

Longuet-Higgins, M.S. 1963, "The generation of capillary waves by steep gravity waves," J. Fluid Mech., 16, 138-159.

Longuet-Higgins, M.S. 1969, "On wave breaking and the equilibrium spectrum of wind generated waves," Proc. Roy. Soc. Lond. A, 310, 151-159.

Longuet-Higgins, M.S. 1973a, "On the form of the highest progressive and standing waves in deep water," Proc. Roy. Soc. Lond. A , 331, 445-456.

Longuet-Higgins, M.S. 1973b, "A model of flow separation at a free surface," Proc. Roy. Soc. Lond. A, 57, 129-148.

Longuet-Higgins, M.S. 1974, "Breaking waves in deep or shallow water," Proc. 10th Conf. on Naval Hydrodynamics, M.I.T., 597-605.

Longuet-Higgins, M.S. 1980, "On the forming of sharp corners at a free surface," Proc. Roy. Soc. Lond. A, 371, 453-478.

Longuet-Higgins, M.S. 1981a, "On the overturning of gravity waves," Proc. Roy. Soc. Lond. A, 376, 377-400.

Longuet-Higgins, M.S. 1981b, "A parametric flow for breaking waves," Proc. Int. Sym. Hydro. in Ocean Engr., Trondheim, 121-135.

Longuet-Higgins, M.S. 1984, "Statistical properties of wave groups in a random sea state," Phil. Trans. R. Soc. Lond. A, 312, 219-250.

Longuet-Higgins, M.S. and Cokelet, E.D. 1976, "The deformation of steep surface waves on water. I. A numerucal method of computation," Proc. Roy. Soc. Lond. A, 350, 1-25.

Longuet-Higgins, M.S. and Fox, M.J.H. 1977, "Theory of the almost highest wave: the inner solution," J. Fluid Mech., 80, 721-742.

Longuet-Higgins, M.S. and Fox, M.J.H. 1978, "Theory of the almost highest wave: Part II. Matching and analytic extension," J. Fluid Mech., 85, 769-786.

Longuet-Higgins M.S. and Stewart R.W. 1962, "Radiation stress and mass transport in gravity waves, with application to surf-beats," J. Fluid Mech., 13, 481-504.

Longuet-Higgins, M.S. and Stewart, R.W. 1964, "Radiation stress in water waves; a physical discussion with application," Deep Sea Res., 11, 529-562.

Longuet-Higgins, M.S. and Turner, J.S. 1974, "An entraining plume model of a spilling breaker," J. Fluid Mech., 63, 1-20.

Madsen, O.S. 1970, "Waves generated by a piston-type wavemaker," Proc. 12th Conf. Coastal Engrg., 589-607.

Mei, C.C. 1983, The Applied Dynamics of Ocean Surface Waves, Wiley,New York.

Mei, C.C. and Liu, L.F. 1973, "The damping of surface gravity waves in a bounded liquid," J. Fluid Mech., 59, 239-256.

Melville, W.K. 1981, "The instability and breaking of deep-water waves," J. Fluid Mech., 115, 165-185.

Melville, W.K. and Rapp, R.J. 1983, "Velocity measurements at a breaking air-water interface," ASCE Specialty Conference, Purdue University, June, 1983.

Melville, W.K. and Rapp, R.J. 1985, "Momentum flux in breaking waves," Nature, 317, 514-516.

Melville, W.K., Rapp, R.J. and Chan, E.S. 1985, "Wave breaking, turbulence and mixing," The Ocean Surface: Wave Breaking, Turbulent Mixing and Radio Probing, Reidel Dordrecht, Holland, 413-418.

Michell, J.H. 1893, "On the highest waves in water," Phil. Mag., 36, 430-435.

Milgram, J.H. 1985, Personal communication.

Milgram, J.H., Donnelly, R.G., Van Houten, R.J. and Camperman, J.M. 1978, "Effect of oil slick properties on the dispersion of floating oil into the sea," U.S. Dept. of Transportation, U.S. Coast Guard.

McIntyre, M.E. 1981, "On the wave momentum myth," J. Fluid Mech., 106, 331-347.

Naess, A. 1980, "The mixing of oil spills into the sea by breaking waves," J. Petrol. Tech., 32, 1113-1122.

Nath, J.H. and Ramsey, F.L. 1976, "Probability distribution of breaking wave heights emphasizing the utilization of the JONSWAP spectrum," J. Phys. Ocean., 6, 316-323.

Openheim, A.V. and Shafer R.W. 1975, Digital Signal Processing, Prentice-Hall, Englewood Cliffs, New Jersey.

Peregrine, D.C., 1979, "Mechanics of breaking waves--A review of Euromech 102," in Mechanics of Wave Induced Forces on Cylinders, ed. T.L. Shaw, Pitman, London, 204-214.

Peregrine, D.H. and Svendsen, I.A. 1978, "Spilling breakers, bores, and hydraulic jumps," Proc. 16th Conf. on Coastal Engr., Hamburg, 540-550.

Phillips, O.M. 1959, "The scattering of gravity waves by turbulence," J. Fluid Mech., 5, 177-192.

Phillips, O.M. 1977, The Dynamics of the Upper Ocean, Cambridge Univ. Press, Cambridge.

Plant, W.J. 1980, "On the steady state energy balance of short gravity systems," J. Phys. Ocean., 10, 1340-1352.

Schwartz, L.W. 1974, "Computer extension and analytic continuation of Stokes' expansion for gravity waves," J. Fluid Mech., 62, 533-578.

Stokes, G.G. 1847, "On the theory of oscillatory waves," Trans. Camb. Phil. Soc., 8, 441-445.

Taylor, G. I. 1935, "Statistical theory of turbulence," Proc. R. Soc. Lond. A, 151, 421.

Thornton, E.B. 1979 "Energetics of breaking waves within the surf zone," J. Geopys. Res., 84, 4931-4938.

Thorpe, S.A. and Humphries, P.N. 1980, "Bubbles and breaking waves," Nature, 283, 463-465.

VanDorn, W.G. and Pazan, S.E. 1975, "Laboratory investigation of wave breaking," Scripps Inst. of Ocean. Ref No. 75-21, AOEL Report No. 71.

Vinje T. and Brevig, P. 1981, "Numerical simulation of breaking waves," Adv. Water Resources, 4, 77-82.

Whitham, G.B. 1962, "Mass. momentum and energy flux in water waves," J. Fluid Mech., 12, 135-147.

Wu, H.Y., Hsu, E.Y. and Street, R.L. 1979, "Experimental study of nonlinear wave - wave interaction and whitecap dissipation of wind generated waves," Dyn. of Atmos. Oceans, 3, 55-78.

Compte-Bellot, G. and Corrsin, S. 1966, "The use of a contraction to improve the isotropy of grid generated turbulence," J. Fluid Mech., 25, 657-682.

Hinze, J.O. 1959, Turbulence: An Introduction to its Mechanism and Theory, McGraw-Hill, New York.

Hunt, J.N. 1952, "Viscous damping of waves over an inclined bed in a channel of finite width," Houille Blanche, 6, 836.

Kjeldsen, S.P., and Olsen, G.B. 1972, "Breaking Waves," (16 mm film), Lyngby, Technical University of Denmark.

Lin, W.M., Newman, N.J., and Yue, D.K. 1984, "Nonlinear forced motions of

Longuet-Higgins, M.S. 1984, "Statistical properties of wave groups in a random sea state," Phil. Trans. R. Soc. Lond. A, 312, 219-250.

Madsen, O.S. 1970, "Waves generated by a piston-type wavemaker," Proc. 12th Conf. Coastal Engrg., 589-607.

Mei, C.C. and Liu, L.F. 1973, "The damping of surface gravity waves in a bounded liquid," J. Fluid Mech., 59, 239-256.

Milgram, J.H. 1985, Personal communication.

Peregrine, D.C., 1979, "Mechanics of breaking waves--A review of Euromech 102," in Mechanics of Wave Induced Forces on Cylinders, ed. T. S. Shaw, Pitman, London, 204-214.

Taylor, G. I. 1935, "Statistical theory of turbulence," Proc. R. Soc. Lond., A, 151, 421.

APPENDIX 1

Derivation of the Integrated Equations of Conservation of Mass, Momentum, and Their Fluxes

Similar derivations may be found in Mei (1981), Chapter 10.

Conservation of Mass

The conservation of mass, from an Eulerian specification, where the density ρ is a constant, is expressed as

$$\frac{\partial u}{\partial x} + \frac{\partial w}{\partial z} = 0 \ . \tag{A1.1}$$

Here, u and w are the horizontal and vertical velocities and z is taken as vertically upward, x is in the direction of wave propagation (see figure 2.3.1). This equation is integrated over depth from -d to the instantaneous free surface elevation, η, giving

$$\int_{-d}^{\eta} \frac{\partial u}{\partial x}\, dz + w_{z=\eta} - w_{z=-d} = 0 \tag{A1.2}$$

By invoking the exact free surface and bottom boundary conditions,

$$w = u\,\frac{\partial \eta}{\partial x} + \frac{\partial \eta}{\partial t} \qquad \text{at } z = \eta$$

$$w = 0 \qquad \text{at } z = -d \tag{A1.3a,b}$$

and Liebnitz's rule

$$\frac{\partial}{\partial x}\int_{-d}^{\eta} u\,dz = u\,\frac{\partial \eta}{\partial x}_{z=\eta} - \int_{-d}^{\eta} \frac{\partial u}{\partial x}\, dz \tag{A1.4}$$

The following is obtained

$$\frac{\partial}{\partial x}\int_{-d}^{\eta} u\,dz + \frac{\partial \eta}{\partial t} = 0 \ . \qquad \text{(A1.5)}$$

This equation is then averaged over one carrier wave period, T giving

$$\frac{\partial M}{\partial x} + \frac{\partial(\rho\bar{\eta})}{\partial t} = 0 \qquad \text{(A1.6)}$$

where

$$M = \overline{\int_{-d}^{\eta} \rho u\,dz} \ . \qquad \text{(A1.7)}$$

M is the mean mass flux averaged over one carrier wave period and

$$\bar{\eta} = \frac{1}{T}\int_{0}^{T} \eta\,dt \qquad \text{(A1.8)}$$

gives the local setdown or setup. M can also be interpreted as the time averaged momentum density.

Conservation of Momentum

The conservation of horizontal and vertical momentum is stated as:

$$\frac{\partial u}{\partial t} + \frac{\partial u^2}{\partial x} + \frac{\partial uw}{\partial z} = \frac{1}{\rho}\frac{\partial}{\partial x}(-P + \tau_{xx}) + \frac{1}{\rho}\frac{\partial \tau_{xz}}{\partial z} \qquad \text{(A1.9)}$$

$$\frac{\partial w}{\partial t} + \frac{\partial uw}{\partial x} + \frac{\partial w^2}{\partial z} = \frac{-1}{\rho}\frac{\partial}{\partial z}(P + \rho g z) + \frac{1}{\rho}\frac{\tau_{xz}}{\partial x} + \frac{1}{\rho}\frac{\tau_{zz}}{\partial z} \qquad \text{(A1.10)}$$

where P is the total pressure, τ is the shear stress tensor due to viscosity, g is gravity.

Again integrating over depth, the individual terms of the horizontal momentum equation become

$$\int_{-d}^{\eta} \frac{\partial u}{\partial t} = \frac{\partial}{\partial t} \int_{-d}^{\eta} u dz - \left[u \frac{\partial \eta}{\partial t}\right]_{z=\eta}$$

$$\int_{-d}^{\eta} \frac{\partial u^2}{\partial x} dz = \frac{\partial}{\partial x} \int_{-d}^{\eta} u^2 - \left[u^2 \frac{\partial \eta}{\partial t}\right]_{z=\eta}$$

$$\int_{-d}^{\eta} \frac{\partial (uw)}{\partial z} = [uw]_{z=\eta} - [uw]_{z=-d}$$

$$\int_{-d}^{\eta} \frac{1}{\rho} \frac{\partial}{\partial x}(-P)dz = \frac{1}{\rho} \frac{\partial}{\partial x} \int_{-d}^{\eta} (-P)\, dz + \left[-P \frac{\partial \eta}{\partial t}\right]_{z=\eta} . \qquad \text{(A1.11a, b,c,d)}$$

Once again making use of the boundary conditions at $z=\eta$ and $z=-d$ (equation A1.3), and $P_{z=\eta} = 0$, and for the present analysis neglecting viscosity, the momentum balance becomes

$$\frac{\partial}{\partial t} \int_{-d}^{\eta} \rho u dz + \frac{\partial}{\partial x} \int_{-d}^{\eta} (P + \rho u^2) dz = 0 \qquad \text{(A1.12)}$$

This states that the horizontal gradient of the momentum flux is equal to the local time rate of change of momentum. Filtering out the carrier wave oscillation by time averaging as before, the following form of the time averaged equation for the conservation of horizontal momentum is obtained:

$$\frac{\partial M}{\partial t} + \frac{\partial S}{\partial x} = 0 \qquad \text{(A1.13)}$$

where

$$S = \overline{\int_{-d}^{\eta} (P + \rho u^2) dz} \tag{A1.14}$$

is the total averaged horizontal momentum flux.

Weakly Nonlinear Wave Theory

Weakly nonlinear wave theory is used to specify the velocity field in terms of the surface displacement, which will allow estimates of the flux terms to be derived. Borrowing from Longuet-Higgins and Stewart (1962) and Dysthe (1979), the surface displacement η is represented as

$$\eta(x,t) = \bar{\eta}(x_1 t) + \eta^{(1)} + \eta^{(2)} \tag{A1.15}$$

where $\bar{\eta}$ is the mean setdown over a wave period T. $\bar{\eta}$ may represent a forced wave varying slowly in time and space as compared to the carrier waves, and is due to the modulation in the carrier waves. $\eta^{(1)}$ is the linear summation of frequency components as input to the wavemaker.

$$\eta^{(1)} = \sum_{n=1}^{N} a_n \cos(k_n x - \omega_n t + \psi_n) \tag{A1.16}$$

which can be represented as

$$\eta^{(1)} = A\, e^{i(k_c x - \omega_c t)} + c.c. \tag{A1.17}$$

where

$$A = \sum_{n=1}^{N} a_n e^{i[(k_n - k_c)x - (\omega_n - \omega_c)t + \psi_n]} \tag{A1.18}$$

The highest frequency contributing to the envelope is $\Delta\omega$, representing the bandwidth of the spectrum; thus if $\mu = \frac{\Delta\omega}{\omega_c}$ is small we can assume a large separation of scales between the envelope modulation and the carrier wave . This assumption serves two purposes; first it insures that $\eta^{(1)}$ and $\overline{\eta}$ are sufficiently separated in frequency so that they are uncorrelated $\left(\text{i.e., } \frac{1}{T}\int_0^T \overline{u}\, u^{(1)}\, dt = 0 \text{ since } \overline{u^{(1)}} = 0\right)$. Second, it allows a multiple scales analysis. A slow time and space scale is then introduced, $t_1 = \mu t$, $x_1 = \mu x$, so that

$$\eta^{(1)} = A(x_1,t_1)e^{i\theta} + c.c. \tag{A1.19}$$

$$\theta = k_c x - \omega_c t \tag{A1.20}$$

The parameter $\mu = \frac{\Delta\omega}{\omega}$ gives the envelope steepness as $= \mu ak = \mu\varepsilon$.

In these experiments the bandwidth is not always small, however; far from breaking, the envelope, $|A|$, is slowly varying. This is the important assumption in our analysis, as will become clear.

The second harmonic surface displacement $\eta^{(2)}$ is similarly given by

$$\eta^{(2)} = A_2(x_1,t_1)e^{2i\theta} + c.c. \tag{A1.21}$$

The velocity potential can also be decomposed as

$$\phi = \overline{\phi} + \phi^{(1)} + \phi^{(2)} \tag{A1.22}$$

$$\phi = \overline{\phi} + B\, F(z)e^{i\theta} + B_2\, F_2(z)e^{2i\theta} \tag{A1.23}$$

where B_1, B_2 are slowly varying functions of x_1, t_1 and $\overline{\phi}$ is a function of x_1, t_1, z_1 $(z_1 = \mu z)$.

The depth dependence is:

$$F(z) = \frac{\cosh k_c(z+d)}{\sinh k_c d} ; \qquad F_2(z) = \frac{\cosh 2k_c(z+d)}{\sinh^4 k_c d} \qquad \text{A1.24 a,b)}$$

(The use of k_c in the vertical eigenfunction F(z) is only good for a very narrow spectrum. This assumption can be relaxed when we consider interpretation over depth and time even with the relatively wide spectrum used in these experiments. The point is considered on page (283). Using a multiple scale analysis the derivatives in x and z become

$$\frac{\partial}{\partial x} \to \frac{\partial}{\partial x} + \mu \frac{\partial}{\partial x_1} ; \qquad \frac{\partial}{\partial z} \to \frac{\partial}{\partial z} + \mu \frac{\partial}{\partial z_1} , \qquad \text{(A1.25a.b)}$$

giving the horizontal and vertical fluid velocity as:

$$u = \frac{\partial \phi}{\partial x} = \mu \frac{\partial \bar{\phi}}{\partial x_1} + A\omega_c F(z) e^{i\theta} + \mu i \frac{\partial A}{\partial x_1} \frac{\omega_c}{k_c} F(z) e^{i\theta} - B_2 \omega_c F_2(z) e^{2i\theta}$$

$$+ \mu \frac{\partial B_2}{\partial x_1} F_2(z) e^{2i\theta} + o(\varepsilon)^3 \qquad \text{(A1.26)}$$

$$w = \frac{\partial \phi}{\partial z} = \frac{\partial \bar{\phi}}{\partial z_1} + \frac{iA\omega_c}{k_c} \frac{\partial F(z)}{\partial z} e^{i\theta} + B_2 \frac{\partial F_2(z)}{\partial z} e^{2i\theta} + O(\varepsilon)^3 \qquad \text{(A1.27)}$$

where $B = \frac{iA\omega_c}{k_c}$. (A1.28)

The velocities will be represented as

$$u = \bar{u} + u^{(1)} + u^{(2)} \tag{A1.29}$$

$$w = \bar{w} + w^{(1)} + w^{(2)} \tag{A1.30}$$

where

$$\bar{u} = \mu \frac{\partial \bar{\phi}}{\partial x_1} \tag{A1.31}$$

$$u^{(1)} = \left[A\omega_c + i\mu \frac{\partial A}{\partial x_1} \frac{\omega_c}{k_c} \right] F(z) e^{i\theta} \tag{A1.32}$$

$$u^{(2)} = \left[-B_2 \omega_c + \mu \frac{\partial B_2}{\partial x_1} \right] F_2(z) e^{i\theta} \tag{A1.33}$$

$$\bar{w} = \mu \frac{\partial \bar{\phi}}{\partial z_1} \tag{A1.34}$$

$$w^{(1)} = iA \frac{\omega_c}{k_c} \frac{\partial F(z)}{\partial z} e^{i\theta} \tag{A1.35}$$

$$w^{(2)} = B_2 \frac{\partial F_2(z)}{\partial z} e^{2i\theta} \tag{A1.36}$$

Note the appearance of the term in $u^{(1)}$ and $u^{(2)}$ due to the slow variation of the envelope.

The forced long wave variables $\bar{\phi}$, $\bar{\eta}$, $\bar{u}$, $\bar{w}$ can be determined for $kd = 0(ka)^{-1}$ as shown by Dysthe (1979) with the following set of equations:

$$\nabla^2\bar{\phi} = 0 \qquad 0 < z < -d$$

$$\frac{\partial\bar{\phi}}{\partial t} + g\bar{\eta} = 0 \qquad z = 0 \qquad \text{(A1.37a,b,c,d)}$$

$$\bar{w} - \frac{\partial\bar{\eta}}{\partial t} = \frac{\omega}{2}\frac{\partial}{\partial x}\left|A\right|^2 \qquad z = 0$$

$$\bar{w} = \frac{\partial\bar{\phi}}{\partial z} = 0 \qquad z = -d$$

The order of $\bar{\phi}$ can be estimated with a simple example. Assume a periodic envelope where

$$\left|A\right|^2 = A_o^2\left\{1 + b\cos\mu k(x - C_g t)\right\} \qquad \text{(A1.38)}$$

and where $\nu = \mu k$ is the long wave number, and $C_g = \frac{\Omega}{\nu}$ is the group velocity Assuming a packet of permanent form, then $\frac{\partial}{\partial x} \to \frac{-1}{C_g}\frac{\partial}{\partial t}$, and the solution can be found simply for deep water to be

$$\bar{\phi} = -b\frac{\omega}{2}A_o^2 e^{\nu z}\sin(\nu x - \Omega t) + Ex + Ft \qquad \text{(A1.39)}$$

$$\bar{\eta} = -\frac{1}{g}b\frac{\omega}{2}A_o^2\,\Omega\,\cos(\nu x - \Omega t) + F \qquad \text{(A1.40)}$$

$$\bar{u} = -b\,A_o^2\frac{\omega}{2}\nu\,e^{\nu z}\cos(\nu x - \Omega t) + E \qquad \text{(A1.41)}$$

$$\bar{w} = -b\,A_o^2\frac{\omega}{2}\nu\,e^{\nu z}\sin(\nu x - \Omega t) \qquad \text{(A1.42)}$$

The constants E, F are determined by the value of $\bar{u},\bar{\eta}$ at the nodes of the packet where $|A|^2$ is a minimum. This result is also shown by Longuet-Higgins & Stewart (1964) using a momentum flux balance approach.

If $\mu = ak = \epsilon$, that is, if the scale of the slow time and space variation is of the same order as the carrier wave slope, then

$$\bar{\phi} = O(\epsilon)^2, \quad \bar{\eta} = O(\epsilon)^3, \quad \bar{u} = O(\epsilon)^3, \quad \bar{w} = O(\epsilon)^3$$

(A1.43a,b,c,d)

in deep water.

The situation is different in shallower water where the group is long compared with depth. In this case, there is a mean set down $\bar{\eta}$ and return flow which is of order $O(\epsilon^2)$ and is derived from first order wave variables. Longuet-Higgins and Stewart (1962) derive this for $\nu d \ll 1$ to be

$$\bar{\eta} = \frac{-g}{2(gd - C_g^2)} \frac{|A|^2}{2} \tag{A1.44}$$

$$\bar{u} = \frac{-g}{d}\left[\frac{C_g}{2(gd - C_g^2)} + \frac{1}{C}\right] \frac{|A|^2}{2} \tag{A1.45}$$

This magnified setdown is a result of the zero-mean vertical velocity, due to the bottom constraint, and thus the fluid level cannot adjust itself,as in the case of deep water. The flux terms in the conservation equations can now be estimated.

Mass Flux

With the horizontal velocity given by equation A1.29,

$$u = \bar{u} + u^{(1)} + u^{(2)}$$

$$M = \overline{\rho \int_{-d}^{\eta} (\bar{u} + u^{(1)} + u^{(2)}) dz} \qquad \text{(A1.46)}$$

The mass flux due to the first harmonic is

$$M^{(1)} = \overline{\rho \int_{-d}^{\eta} u^{(1)} \, dz}$$

$$= \overline{\rho \int_{-d}^{0} u^{(1)} \, dz} + \overline{\rho \int_{0}^{\eta} u^{(1)} \, dz} \qquad \text{(A1.47a,b)}$$

In irrotational flow the first term is zero; thus

$$M^{(1)} = \overline{\rho \int_{0}^{\eta} \left(u^{(1)} + \frac{\partial u^{(1)}}{\partial z} \eta + \frac{1}{2} \frac{\partial^2 u}{\partial z} \eta^2 \ldots\right)_{z=0}} \qquad \text{(A1.48)}$$

$$M^{(1)} = \overline{\rho \, u_o^{(1)} \, \eta^{(1)}} + O(\varepsilon^3) \qquad \text{(A1.49)}$$

$$M^{(1)} = \overline{\rho \, \eta^{(1)^2}} \, \omega_c \coth k_c d + O(\varepsilon^3) \qquad \text{(A1.50)}$$

This flux is the stokes drift which, in this Eulerian description of the flow is concentrated in the trough to crest region of the wave.

The second harmonic only adds terms of $0(\varepsilon)^3$ and will not be considered here. The mass flux due to the mean current of the long wave is

$$M_{\bar{u}} = \rho \overline{\int_{-d}^{\eta} \bar{u}\, dz} \tag{A1.51}$$

where $\bar{u}$ from equation A1.41 or equation A1.45 for shallow and deep water may be substituted.

In the case of a uniform wave train of infinite extent in x, the total mass flux or momentum density is usually considered to be equal to to $M^{(1)}$ or the Stokes drift velocity, since $\bar{u} = 0$. However, where a finite length wave group in deep water is considered, the total momentum is zero(McIntyre, 1981, Longuet-Higgins & Stewart 1964). This can be seen as follows. The conservation of mass equation averaged over the entire group becomes

$$\rho\, \bar{\eta}_{t_2} - \rho\, \bar{\eta}_{t_1} = \frac{1}{t_2 - t_1} \int_{t_1}^{t_2} \frac{\partial M}{\partial x}\, . \tag{A1.52}$$

If the mean water level returns to its original level (which it does in deep water), after the entire group has passed, then

$$M = \text{constant} = 0\, . \tag{A1.53}$$

This is so because the fluid is assumed to be still far upstream and downstream of the group. This indicates that the forced long wave return flow $M_{\bar{u}}$ just balances the flux due to the Stokes drift. In a water depth, where the group is long compared to the depth, the water level does not return to its original level after the group has passed and the net momentum density or mass flux is

$$M = M^{(1)} + M_{\overline{u}} = \frac{-C_g}{gd-C_g^2} \frac{\rho g |A|^2}{2} \qquad \text{(A1.54)}$$

which is slightly negative (Longuet-Higgins & Stewart, 1962).

In generating the finite length wave groups in these experiments, it is known that a mean momentum is transferred to the fluid from the paddle; however, this momentum travels at the long wave velocity $C_g = \sqrt{gh}$ as a transient, distributing the momentum throughout the channel. The mean momentum density around the packet, after the transients have moved away from the packet, is theoretically zero in deep water and slightly negative in shallower water, according to equation (A1.54) (Whitham, 1977; Benjamin, 1970).

Momentum Flux

The total time averaged horizontal momentum flux

$$S = \overline{\int_{-d}^{\eta} (P + \rho u^2)\, dz} \qquad \text{(A1.55)}$$

can be derived in terms of u, w, η by substituting for the pressure. The pressure P(z) is derived by integrating the vertical momentum conservation equation over depth as follows.

$$\int_z^{\eta} \frac{dw}{dt}\, dz + \int_z^{\eta} \frac{\partial (uw)}{\partial x}\, dz + \int_z^{\eta} \frac{\partial w^2}{\partial z} = \frac{-1}{\rho} \int_z^{\eta} \frac{\partial}{\partial z} (P + \rho g z)\, dz$$

where the shear stress at the boundaries is neglected. The individual terms become

$$\int_z^\eta \frac{\partial w}{\partial t}\, dz = \frac{\partial}{\partial t}\int_z^\eta w dz - w\,\frac{\partial \eta}{\partial t}\Big|_{z=\eta}$$

$$\int_z^\eta \frac{\partial (uw)}{\partial z}\, dz = \frac{\partial}{\partial x}\int_z^\eta uw\, dz - uw\,\frac{\partial \eta}{\partial x}\Big|_{z=\eta}$$

$$\int_z^\eta \frac{\partial w^2}{\partial z}\, dz = w^2_{z=\eta} - w^2_z$$

$$-\frac{1}{\rho}\int_z^\eta \frac{\partial}{\partial z} P dz = \frac{-1}{\rho} P_{z=\eta} + \frac{1}{\rho} P_z$$

$$-\frac{1}{\rho}\int_z^\eta \frac{\partial}{\partial z}(gz)\, dz = -g\eta + gz \qquad \text{(A1.57a,b,c,d,e)}$$

Collecting terms and using the kinematic free surface boundary condition (equation A1.3) the pressure becomes

$$P(z) = \rho g(\eta - z) + \rho \frac{\partial}{\partial t}\int_z^\eta w dz + \rho \frac{\partial}{\partial x}\int_z^\eta uw dz - \rho w_z^2 \qquad \text{(A1.58)}$$

where $P_{z=\eta} = 0$.

Upon substitution of P into equation A1.55 for the total mean horizontal momentum flux, the following form is obtained.

$$S = \overline{\frac{\rho g(\eta+d)^2}{2}} + \overline{\rho \int_{-d}^{\eta} (u^2 - w^2) dz} +$$

(I) (II)

$$\overline{\rho \int_{-d}^{\eta} \frac{\partial}{\partial t} \int_{z}^{\eta} w \, dz \, dz'} \qquad \overline{+ \rho \int_{-d}^{\eta} \frac{\partial}{\partial x} \int_{z}^{\eta} uw \, dz \, dz'} \tag{A1.59}$$

(III) (IV)

This equation is exact for a general flow field. The velocities and surface displacement may contain carrier wave components u', long waves, $\bar{u}$, and turbulence, u_t. In general one may expect interactions between these motions which makes separating S into components impossible. However, if the time scales of the various motions are sufficiently separated, then the interaction terms will be small when a time averaging is performed. At stations far from breaking, turbulent velocities are zero and the wave packet is indeed slowly varying making $\bar{u}$ slowly varying, which allows a separation of scales analysis.

TERM I

The first term of S is already in terms of η and can be put in the following form

$$\frac{\rho g(\eta+d)^2}{2} = \frac{\rho g}{2} \overline{\eta'^2} + \frac{\rho g \bar{\eta}^2}{2} + \rho g \bar{\eta} d + \frac{\rho g}{2} d^2 \tag{A1.60}$$

shallow →	$O(\varepsilon^2)$	$O(\varepsilon^4)$	$O(\varepsilon^2)$	$O(1)$
deep →	$O(\varepsilon^2)$	$9(\varepsilon^6)$	∞	∞

where

$$\eta' = \eta^{(1)} + \eta^{(2)} \tag{A1.61}$$

The order of each term is shown for the case of a long group compared to depth and for deep water.

The first term on the right is due to the fluctuating motion. The second and third terms are due to the mean motion and the last term is due to the hydrostatic pressure, which is usually ignored since its x gradient is zero. In deep water the third term is seen to blow up; however, it will be seen that this will be balanced by the mean vertical acceleration in the equation for the total momentum flux.

TERM II

The second term in S may be expressed as

$$\rho \overline{\int_{-d}^{\eta} u^2 dz} = \rho \overline{\int_{-d}^{0} u^2 dz} + \overline{\int_{0}^{\eta} u^2 \, dz} \qquad \text{(A1.62)}$$

$$0(\varepsilon^2) \qquad 0(\varepsilon)^3$$

and then the second term expanded in a Taylor series,

$$= \rho \overline{\int_{-d}^{0} u^2 \, dz} + \overline{\rho u^2 \eta}\Big|_{z=0} + \overline{2u \frac{\partial u}{\partial z}\Big|_{z=0} \eta^2} + 0(\varepsilon^5) \, . \qquad \text{(A1.63)}$$

Using the derived equation (A1.29, A1.15) for u and η the following is obtained

$$\rho \overline{\int_{-d}^{\eta} u^2 dz} = \frac{\rho g}{2}\left|A\right|^2 G(kd) + 2\rho g \frac{\mu^2}{k_c^2} \frac{\partial A^*}{\partial x_1} \frac{\partial A}{\partial x} G(kd) +$$

$$0(\varepsilon^2) \qquad 0(\varepsilon^4)$$

$$\rho \overline{\int_{-d}^{o} \bar{u}^2 dz} + \frac{\rho g}{2}\left|B_2\right|^2 \int_{-d}^{0} F_2(z) \, dz + \rho g \bar{\eta} \left|A\right|^2 k_c G(kd) + 2\rho g \left|A\right|^4 k_c^2$$

$0(\varepsilon^5)$ in deep water $\qquad 0(\varepsilon^4)$ $\qquad$ (A1.64)

where $G(kd) = \left[1 + \frac{2kd}{\sinh 2kd} \right]$.

Using a similar expansion and after considerable algebra, the squared vertical velocity contributes as follows:

$$-\overline{\int_{-d}^{\eta} w^2 dz} = -\rho \int_{-d}^{0} \bar{w}^2 \, dz - \rho \int_{-d}^{0} \overline{w^{(1)^2}} \, dz - \rho \int_{-d}^{0} \overline{w^{(2)^2}} \, dz$$

$$- \overline{w^{(1)^2} \bar{\eta}} \Big|_{z=0} \qquad - \overline{2w^{(1)} \frac{\partial w^{(1)}}{\partial z} \eta'^2} \Big|_{z=0} + O(\varepsilon^5) \qquad \text{(A1.65)}$$

Upon substitution of expressions for w and η the following is obtained.

$$-\overline{\int_{-d}^{\eta} w^2 dz} = \frac{\rho g}{2} |A|^2 \left(\frac{2kd}{\sinh 2kd} - 1 \right) +$$

$$O(\varepsilon^2)$$

$$\frac{\rho g}{2} |B_2|^2 \left(F_2(z) \, dz \right) \Big|_{-d}^{o} - \bar{\eta} \, \rho g |A|^2 k_c \tanh k_c d - 2\rho g |A|^4 k_c^2 +$$

$$O(\varepsilon^4)$$

$$\rho \int_{-d}^{0} \bar{w}^2 \, dz \qquad \text{(A1.66)}$$

0 in shallow water

$O(\varepsilon^5)$ in deep water

TERM III

The third term of S due to the vertical acceleration is expanded as

$$\overline{\rho \int_{-d}^{\eta} \frac{\partial}{\partial t} \int_{z}^{\eta} w dz dz'} = \rho \int_{-d}^{0} \overline{\left[\frac{\partial}{\partial t} \int_{z}^{\eta} w dz \right]} dz' + \rho \int_{0}^{\eta} \overline{\frac{\partial}{\partial t} \int_{z}^{\eta} w \, dz dz'} \qquad \text{(A1.67)}$$

The second integral on the right adds terms one order higher than the first integral. Working on the first integral, the braketed term is expanded as

$$\overline{\frac{\partial}{\partial t} \int_{z}^{\eta} w dz} = \int_{z}^{0} \frac{\partial \bar{w}}{\partial t} dz + \frac{\partial}{\partial t} \left[\overline{w\eta} \Big|_{z=0} + \overline{\frac{\partial w}{\partial z} \eta^2} \Big|_{z=0} + \frac{1}{2} \frac{\partial^2 w}{\partial z^2} \eta^3 \Big|_{z=0} \right.$$

$$\left. + O(\varepsilon)^5 \right] \qquad \text{(A1.68)}$$

Retaining terms to fourth order, the contribution to S from the first integral become:

$$\overline{\rho \int_{-d}^{\eta} \frac{\partial}{\partial t} \int_{z}^{\eta} w dz dz'} = \rho \int_{-d}^{0} \int_{z}^{0} \mu \frac{\partial \bar{w}}{\partial t_1} dz dz' \qquad \text{(A1.69)}$$

$$O(\varepsilon^2)$$

In shallow water, $\bar{w} = 0$, and this term contributes nothing to the total. In deep water $\mu \frac{\partial \bar{w}}{\partial t_1}$ is order $O(\varepsilon^4)$; however, the two vertical integrations are over the long depth scale $z_1 = \mu z$ which make the contribution of order (ε^2). The existence of the term is discussed by Longuet-Higgins and Stewart (1964). This term can be manipulated using $\frac{\partial \bar{\phi}}{\partial z} = \bar{w}$.

Then

$$\rho \int_{-d}^{0} \int_{z}^{0} \mu \frac{\partial \bar{w}}{\partial t_1} \, dz dz' = \rho \int_{-d}^{0} dz' \mu \left[\frac{\partial \bar{\phi}}{\partial t_1}\right]_{z}^{0} \tag{A1.70}$$

$$= -\rho \int_{-d}^{0} \mu \frac{\partial \bar{\phi}}{\partial t_1} dz' - \rho g \bar{\eta} d \tag{A1.71}$$

since $\quad g\bar{\eta} = -\frac{\partial \bar{\phi}}{\partial t}\Big|_{z=0}$.

The hydrostatic term $-\rho g \bar{\eta} d$ is exactly cancelled by its positive counterpart in equation A1.60, thus rectifying the condition when $d \to \infty$.

The remaining contribution due to the second integral from $0 \to \eta$ is

$$\overline{\rho \int_0^{\eta} \frac{\partial}{\partial t} \int_z^{\eta} w\,dz\,dz'} = \overline{\eta\, \eta' \frac{\partial w'}{\partial t}}\Big|_{z=0} + \overline{2\eta'^3 \frac{\partial^2 w'}{\partial z \partial t}}\Big|_{z=0} + \overline{3\eta'^2 \frac{\partial w'}{\partial z} \frac{\partial \eta'}{\partial t}}\Big|_{z=0} \tag{A1.72}$$

After substituting for η' and w', the total contribution from the vertical acceleration is then

$$\rho \int_{-d}^{\eta} \frac{\partial}{\partial t} \int_z^{\eta} w\,dz\,dz' = -\rho \int_{-d}^{0} \mu \frac{\partial \bar{\phi}}{\partial t_1} dz - \rho g \bar{\eta} d +$$

$$O(\varepsilon^2)$$

$$+ \rho d \bar{\eta} \left|A\right|^2 k_c \tanh k_c d + 2\rho g \left|A\right|^4 k_c^2 + 3\rho g \left|A\right|^4 k_c^2 \tan k_c d$$

$$O(\varepsilon)^4$$

(A1.73)

Note that in shallow water the dynamic pressure $\frac{\partial \bar{\phi}}{\partial t}$ is constant over depth and equal to its surface value $\frac{\partial \bar{\phi}}{\partial t} = -g\eta$.

Then

$$-\rho \int_{-d}^{0} \frac{\partial \bar{\phi}}{\partial t} dz = +\rho g \bar{\eta} d \tag{A1.74}$$

and we recover the momentum flux of the shallow water long wave.

TERM IV

The last term contributing to the momentum flux is expanded as

$$\overline{\rho \int_{-d}^{\eta} dz' \frac{\partial}{\partial x} \int_{z}^{\eta} uwdz} = \rho \int_{-d}^{0} dz' \overline{\left[\frac{\partial}{\partial x} \int_{z}^{\eta} uwdz\right]} + \overline{\rho \int_{0}^{\eta} dz' \frac{\partial}{\partial x} \int_{z}^{\eta} uwdz}. \quad \text{(A1.75)}$$

The bracketed term is further expanded giving

$$\overline{\frac{\partial}{\partial x} \int_{z}^{\eta} (uw)\, dz} = \overline{\int_{z}^{\eta} \frac{\partial}{\partial x} (uw)\, dz} + \frac{\partial}{\partial x}\left[\overline{uw\eta} + \overline{\frac{\partial (uw)}{\partial z} \eta^2} \right]_{z=0} + O(\varepsilon)^4 \quad \text{(A1.76)}$$

The leading order contribution is $O(\varepsilon^4)$ in shallow depth, and $O(\varepsilon^2)$ in deep water and is due to

$$\rho \int_{-d}^{0} dz' \int_{z}^{0} \frac{\partial}{\partial x} \overline{u^{(1)} w^{(1)}}\, dz \,. \quad \text{(A1.77)}$$

Substituting for $u^{(1)}, w^{(1)}$ from equation (A1.32, A1.35) this becomes,

$$\frac{\rho g}{4}(-\mu^2) \frac{\partial}{\partial x_1} \left(A \frac{\partial A^*}{\partial x_1} \right) \frac{1}{2k^2} \left[2kd \coth 2kd - 1 \right] = \quad \text{(A1.78)}$$

$$\frac{\rho g}{4}(-\mu^2) \frac{\partial}{\partial x_1} \left(\frac{1}{2} \frac{\partial |A|^2}{\partial x_1} \right) \frac{1}{2k^2} \left[2kd \coth 2kd - 1 \right] . \quad \text{(A1.79)}$$

Collecting all terms:

$$S = \frac{\rho g}{4}|A|^2 + \frac{\rho g \bar{\eta}^2}{2} + \rho g \bar{\eta} d \qquad \text{I}$$

$$O(\varepsilon^2) \quad O(\varepsilon^4) \quad O(\varepsilon^2)$$

$$+ \frac{\rho g}{2}|A|^2 \left[1 + \frac{2kd}{\sinh 2kd}\right] + \frac{2\rho g \mu^2}{k_c^2} \frac{\partial A}{\partial x_1} \frac{\partial A^*}{\partial x_1} \left[1 + \frac{2kd}{\sinh 2kd}\right] + \bar{\rho u}^2 d \text{ (in shallow water)}$$

$$O(\varepsilon^2) \qquad 9(\varepsilon^4)$$

$$+ \frac{\rho g}{2}|B_2|^2 \left(\int_{-d}^{0} F_2(z)\, dz\right) + \rho g \bar{\eta} |A|^2 k_c \left[1 + \frac{2kd}{\sinh 2kd}\right] + 2\rho g |A|^4 k_c^2 \qquad \text{II}$$

$$O(\varepsilon^4)$$

$$+ \frac{\rho g}{2}|A|^2 \left[\frac{2kd}{\sinh 2kd} - 1\right] +$$

$$O(\varepsilon^2)$$

$$\frac{\rho g}{2}|B_2|^2 \left[F_2(z)\right]_{-d}^{0} - \rho g \bar{\eta} |A|^2 k_c \tanh k_c d - 2\rho g |A|^4 k_c^2$$

$$O(\varepsilon^4)$$

$$-\rho \int_{-d}^{0} \mu \frac{\partial \bar{\phi}}{\partial t}\, dz - \rho g \bar{\eta} d + \qquad \text{III}$$

$$O(\varepsilon^2)$$

$$\rho g \bar{\eta} |A|^2 k_c \tanh k_c d + 2\rho g |A|^4 k_c^2 + 3\rho g |A|^4 k_c^2 \tanh k_c d +$$

$$O(\varepsilon^4)$$

$$\rho g \frac{(-\mu^2)}{4} \frac{\partial^2 |A|^2}{\partial x_1^2} \frac{1}{k_c^2} \left[2kd \coth 2kd - 1\right] \qquad \text{IV}$$

(A1.80)

Second Order Estimates of S

For the case of a uniform plane progressive wave in deep water the following estimate of the momentum flux results. (c.w = carrier waves.)

$$S = S_{c.w.} = \frac{\rho g}{4}\left|A\right|^2 + o(\varepsilon^3) \tag{A1.81}$$

where $\left|\frac{A}{2}\right|^2 = \overline{\eta'^2}$ (A1.82)

For finite depth,

$$S = S_{c.w.} = \frac{\rho g}{2}\left|A\right|^2 \left[\frac{2kd}{\sinh 2kd} + \frac{1}{2} \right] + O(\varepsilon^3) \tag{A1.83}$$

The braketed term appears as for shallow water since $u^2 \neq w^2$. This can also be expressed as

$$S = S_{c.w.} = \frac{\rho g}{2}\left|A\right|^2 \left[\frac{2C_g}{C} - \frac{1}{2} \right] + O(\varepsilon^3) \tag{A1.84}$$

For a modulated wave train and one where the amplitude varies, a contribution must be added due to the local change in the mean sea level. In the case where the group is long compared to depth (but the carrier waves are deep water waves), the setdown $\bar{\eta}$ is second order, giving

$$S = \frac{\rho g}{2}\left|A\right|^2 \left[\frac{2kd}{\sinh 2kd} + \frac{1}{2} \right] + \rho g \bar{\eta} d + O(\varepsilon^3) \tag{A1.85}$$

As the depth increases the vertical mean acceleration becomes important and the long wave pressure is no longer hydrostatic (otherwise $\rho g \eta d$ would go to ∞ !) The resulting momentum flux becomes

$$S = \frac{\rho g}{2}\left|A\right|^2\left[\ \frac{2kd}{\sinh 2kd} + \frac{1}{2}\ \right] + \rho \int_{-d}^{0} \mu \frac{\partial \bar{\phi}}{\partial t_1}\, d\sigma + O(\varepsilon^3) \qquad \text{(A1.86)}$$

where the second term is the pressure term due to forced waves. When the momentum is integrated over long time, the only contribution comes from the carrier waves since

$$\int_{t_1}^{t_2} \bar{\eta} = 0 \qquad \text{(A1.87)}$$

$$\int_{t_1}^{t_2} \frac{\partial \bar{\phi}}{\partial t} = 0 \qquad \text{(A1.88)}$$

In this case the forced long wave may be treated as any other wave in computing its momentum flux except that it is not freely dispersing, and $C = C_g$. Its contribution to the total flux is small.

The higher order corrections to the momentum flux are a result of three effects: The steepness of the envelope $\frac{\partial |A|^2}{\partial x}$, $\frac{\partial A}{\partial x}\frac{\partial A}{\partial x}$, the forced long wave velocities $\bar{u}^2$, $\bar{w}^2$ and the steepness of the carrier waves, $|A|^4$, $|A_2|^2$. If the packet envelope is symmetric about its peak, terms like $\frac{\partial}{\partial x}|A|^2$ will average to zero over long time; the only corrections to fourth order are then due to terms like $|A|^4$, $|B_2|^2$, $\frac{\partial A}{\partial x}\frac{\partial A^2}{\partial x}$ and $\bar{u}^2 d$ in shallow water.

The preceding analysis holds for a narrow band spectrum as a single frequency wave where the velocity and pressure decays as $e^{k_c z}$. In a broad spectrum each velocity component will decay at different rates so, to second order, the fluxes of the individual components may be computed

and then summed. Then if the momentum flux of an individual component is

$$S_n = \frac{\rho g a_n^2}{2} G_n \tag{A1.89}$$

where

$$G_n = \left[\frac{2C_{gn}}{C_n} - \frac{1}{2} \right] = \left[\frac{k_n d}{\sinh 2k_n d} + \frac{1}{2} \right] \tag{A1.90}$$

Then

$$S = \sum_{n=1}^{N} S_n = \sum_{n=1}^{N} \frac{\rho g\, a_n^2}{2} G_n \tag{A1.91}$$

in deep water $G_n = \frac{1}{2}$ for all n.

Then

$$S = \sum_{n=1}^{N} \frac{\rho g}{4} a_n^2 = \frac{1}{2} \int_{t_1}^{t_2} g\, \rho\, \eta^2\, dt \tag{A1.92}$$

By Parseval's theorem, showing that to second order the surface displacement variance is a measure of the horizontal momentum flux.

APPENDIX 2

Wave Amplitude Attenuation due to Channel Walls

Following Mei and Liu (1973), Hunt (1952), for a time periodic wave train of small amplitude.

d = depth = 0.6 m

b = tank width = 0.76m

a = wave amplitude

ν = viscosity = 1.0×10^{-6} m^2/s

k = wave number

ω = radian wave frequency

The decay of the wave amplitude is given by:

$$-\frac{1}{a}\frac{\partial a}{\partial x} = B \qquad \text{(A2.1)}$$

where $B = \frac{2k}{b}\sqrt{\frac{\nu}{2\omega}}\left(\frac{kb + \sinh 2kd}{2kd + \sinh 2kd}\right)$

Integrating equation (A2.1) with respect to x

$$-B\,x + \alpha = -\ell n a + \beta$$

$$\alpha' e^{-Bx} = \beta' a$$

$$a = \alpha'' e^{-Bx}$$

$$\frac{a^2}{a_0^2} = e^{-2Bx} \qquad \text{(A2.2)}$$

$B = 4.89 \times 10^{-3}$ 1/m for f_c = 0.88 Hz

6.67×10^{-3} 1/m 1.08 Hz

8.66×10^{-3} 1/m 1.28 Hz

APPENDIX 3

Computer Software

The follwing FORTRAN AND MACRO programs have been referred to in various sections of the thesis which describes their application. The files are listed alphabetically.

The Batch run data aquisition command and control program is

ADDAT3.BAT.

This program runs the following programs:

ADDAT2	samples 2 digital channels and up to 4 analog channels continously using double buffering and a completion routine.
DIPRO3	converts raw digital data(velocity signal) to a velocity using the laser Doppler anemometer calibrations.
ANPRO5	converts analog voltage to a wave height using the wave gouge calibration file(see WGCAL3).

STAT7	computes a mean and variance of a signal.
DROP	sets dropout in velocity signal to zero, where dropout is set as N continuous identical values of the signal.
STAT12	computes a running ensemble average over the signals at constant time.

Other programs may be added to the Batch stream.

All data acquisition is performed by calls to Data Translation subroutines which access their boards. Refer to DTLIB/RT V2.2 Real-Time Peripheral Support Manual, 1979, Malborough, MA.

The File SSPFIL contains regressions routines. These were obtained from the Scientiffic Subprogram library at the Joint Computer Facility at The Massachusetts Institute of Technology.

FASTAL and CCSESX are adaptations of Fast Fourier Transform(FFT) routines obtained in Programs for Digital Signal Processing by IEEE press.

```
C-----------------------------------------------------------------------
C       ADDAT2.FOR  1-12-84
C
C       THIS IS IS AN ANALOG AND DIGITAL CHANNEL SAMPLING ROUTINE
C       WHICH UTILIZES A COMPLETION ROUTINE
C       TO ALLOW CONTINUOUS SAMPLING OF DATA.
C-----------------------------------------------------------------------
C
        EXTERNAL SAVE
        COMMON/SAVE/IBEFA,NBUFA,NCNT,NSUBSA,NOUT,NLINE,NREADA,
     #   IBEFD1,IBEFD2,NBUFD,NSUBSD,NREADD,NCCH,NDCCH,
     #   IBUFD1(2048),IBUFD2(2048),IBUFA(8192)
        LOGICAL*1 ANAL(15),DIG(15)
        LOGICAL*1 ERRFLG
        LOGICAL*1 HEADD(70),HEADA(70)
        DIMENSION GLOCX(6),GLOCZ(6),PVX(2),PVZ(2)
C
C
C INPUT BUFFERING PARAMETERS
C
        NLINE=512
        WRITE(5,30)
   30   FORMAT(1H,'ENTER TOTAL NUMBER OF SCANS PER MDC BUFFER- NREAD')
        READ(5,*)NREAD
        WRITE(5,32)
   32   FORMAT(1H,'ENTER THE NUMBER OF MEMORY DUMP CYCLES PER RUN- MDC'/
     #            ' MDC*NREAD= TOTAL NUMBER OF POINTS')
        READ(5,*)MDC
        WRITE(5,110)
  110   FORMAT(' NUMBER OF ANALOG INPUT CHANNELS- NCCH')
        READ(5,*)NCCH
        WRITE(5,111)
  111   FORMAT(' NUMBER OF DIGITAL INPUT CHANNELS- NDCCH')
        READ(5,*)NDCCH
C
C
C INPUT CLOCK PARAMTERS AND STOP CLOCK
C
        WRITE(5,69)
   69   FORMAT(' SET CLOCK PARAMETERS')
        WRITE(5,71)
   71   FORMAT(1H,'ENTER- IRATE,PRESET,MODEC')
        READ(5,*)IRATE,PRESET,MODEC
        IUNITC=0
        ICMFC=0
        CALL SETR(-1,IUNITC,MODEC,PRESET,ICMFC) !STOP THE CLOCK
C
C
C OPEN DIGITAL DATA OUTPUT FILES
C
        IF(NDCCH .EQ. 0)GO TO 841
        WRITE(5,35)
   35   FORMAT(' NAME OF DIGITAL OUTPUT FILE')
        CALL GETSTR(5,DIG,14,ERRFLG)
        OPEN(UNIT=1,NAME=DIG,TYPE='NEW',FORM='UNFORMATTED',
     #   RECORDSIZE=512)
        WRITE(5,36)
   36   FORMAT(' INPUT FILE HEADER')
        CALL GETSTR(5,HEADD,70,ERRFLG)
        WRITE(1)(HEADD(J),J=1,70)
```

```
C
C
C SET DIGITAL SAMPLING PARAMETERS DRS
C
      NREADD=NREAD*MDC
      ISIZD=NREAD
      NBUFD=2
      NSUBSD=ISIZD/NBUFD
      MODED=5
      MASK=-1
      ICMFD1=0
      ICMFD2=0
      WRITE(5,738)
  738 FORMAT(' INPUT PROBE VOLUME LOCATION- X, Z')
      READ(5,*)PVX(1),PVZ(1)
      PVX(2)=PVX(1)
      PVZ(2)=PVZ(1)
C
C
C OPEN ANALOG DATA OUTPUT FILE
C
  841 IF(NCCH .EQ. 0)GO TO 842
      WRITE(5,88)
   88 FORMAT(' ENTER NAME OF ANALOG OUTPUT FILE')
      CALL GETSTR(5,ANAL,14,ERRFLG)
      WRITE(5,120)
  120 FORMAT(' ENTER ANALOG FILE HEADER- A70')
      CALL GETSTR(5,HEADA,70,ERRFLG)
      OPEN(UNIT=2,NAME=ANAL,TYPE='NEW',
     # FORM='UNFORMATTED',RECORDSIZE=512)
      WRITE(2) (HEADA(J),J=1,70)
      WRITE(5,121)
  121 FORMAT(' INPUT GAUGE LOCATIONS, X')
      READ(5,*) (GLOCX(J),J=1,NCCH)
      DO 122 J=1,NCCH
      GLOCZ(J)=0.0
  122 CONTINUE
C
C
C SET ANALOG SAMPLING PARAMETERS RTS
C
      NREADA=NREAD*MDC
      ISIZA=NREAD*NCCH
      WRITE(5,248)
  248 FORMAT(' ANALOG INPUT IGAIN,1=1,2=2,3=4,4=8')
      READ(5,*)IGAIN
      MODEA=2
      NBUFA=2
      NSUBSA=ISIZA/NBUFA
      ISTCHN=0
      ICMFA=0
C
  842 IF(NDCCH .EQ. 0)GO TO 843
      WRITE(1)NREAD,ISIZD,MDC,NCCH,NDCCH,MODED,MODEA,IRATE,
     #  PRESET,MODEC,IGAIN,(PVX(J),PVZ(J),J=1,NDCCH)
  843 IF(NCCH .EQ. 0)GO TO 844
      WRITE(2)NREAD,ISIZD,MDC,NCCH,NDCCH,MODED,MODEA,IRATE,
     # PRESET,MODEC,IGAIN,(GLOCX(J),GLOCZ(J),J=1,NCCH)
  844 CONTINUE
C
```

```
C
C MAKE CALLS TO SAMPLING ROUTINES
C
      NCNT=0
      NOUT=0
C
      IF(NDCCH .EQ. 0)GO TO 51
      CALL DRS(IBUFD1,ISIZD,NBUFD,NREADD,0,0,
     #  MASK,MODED,ICMFD1,IBEFD1,,SAVE)
      IF(NDCCH .EQ. 1)GO TO 51
      CALL DRS(IBUFD2,ISIZD,NBUFD,NREADD,0,1,
     #  MASK,MODED,ICMFD2,IBEFD2)
 51   IF(NCCH .EQ. 0)GO TO 52
      CALL RTS(IBUFA,ISIZA,NBUFA,NREADA,ISTCHN,NCCH,
     # 0,IGAIN,MODEA,ICMFA,IBEFA)
C
 52   WRITE(5,50)
 50   FORMAT(1H,'INPUT AN INTEGER WHEN DATA AQUISITION IS TO START')
      READ(5,*)IQUE
C
      CALL SETR(IRATE,IUNITC,MODEC,PRESET,ICMFC)
      CALL LWAIT(ICMFD1,0)
      IF(ICMFD1 .EQ. -1)GO TO 61
      IF(ICMFD2 .EQ. -1)GO TO 62
      IF(ICMFA  .EQ. -1)GO TO 63
      WRITE(5,60)
 60   FORMAT(1H,'DATA AQUISITION COMPLETE'/)
      CLOSE(UNIT=1)
      CLOSE(UNIT=2)
      STOP 'SUCCESFUL COMPLETION'
C
C REPORT ERRORS
C
 61   WRITE(5,78)
 78   FORMAT(' ERROR IN DATA AQUISITION - DIG1')
      GO TO 80
 62   WRITE(5,72)
 72   FORMAT(' ERROR IN DATA AQUISITION - DIG2')
      GO TO 80
 63   WRITE(5,73)
 73   FORMAT(' ERROR IN DATA AQUISITION - ANALOG')
 80   CLOSE(UNIT=1)
      CLOSE(UNIT=2)
      STOP
      END

C
C
C
C-------------------------------------------------------------------------
C
C COMPLETION ROUTINE FOR ADDAT2, WRITE DIGITAL AND ANALOG DATA TO DISK
C
C-------------------------------------------------------------------------
C
      SUBROUTINE SAVE
      COMMON/SAVE/IBEFA,NBUFA,NCNT,NSUBSA,NOUT,NLINE,NREADA,
     #  IBEFD1,IBEFD2,NBUFD,NSUBSD,NREADD,NCCH,NDCCH,
     #  IBUFD1(2048),IBUFD2(2048),IBUFA(8192)
C
```

```
C WAIT FOR ANALOG BOARD TO CATCH UP
        IF(NCCH .EQ. 0)GO TO 10
        IDUM=IBEFD1+1
        CALL LWAIT(IBEFA,IDUM)
C
   10   CONTINUE
C
C SET BUFFER WRITE POINTER
C
        ISTD = NSUBSD*NCNT
        ISTA = NSUBSA*NCNT
        IFIND=ISTD + NSUBSD -1
        IFINA=ISTA + NSUBSA -1
C
C       IF(NDCCH .NE. 2)GO TO 20
        DO 100 I=ISTD,IFIND,NLINE/2
        WRITE(1,ERR=800,END=810)(IBUFD1(I+J),IBUFD2(I+J),J=1,NLINE/2)
  100   CONTINUE
        GO TO 30
C
   20   IF(NDCCH .NE. 1)GO TO 30
        DO 300 I=ISTD,IFIND,NLINE
        WRITE(1,ERR=800,END=810)(IBUFD1(I+J),J=1,NLINE)
  300   CONTINUE
C
   30   IF(NCCH .EQ. 0)GO TO 40
        DO 200 I=ISTA,IFINA,NLINE
        WRITE(2,ERR=800,END=810)(IBUFA(I+J),J=1,NLINE)
  200   CONTINUE
C
   40   NOUT=NOUT+1
        WRITE(5,1)NOUT
    1   FORMAT(' SUBBUFFER ',I5,' WRITTEN TO DISK')
        NCNT=NCNT+1
        IBEFD1=IBEFD1+1
        IBEFD2=IBEFD2+1
        IBEFA=IBEFA + 1
        IF(NCNT .LT. NBUFD)RETURN
        NCNT=0
        RETURN
C
C REPORT ERRORS
  800   CLOSE(UNIT=1)
        CLOSE(UNIT=2)
        STOP 'ERROR DURING WRITE TO DISK'
  810   CLOSE(UNIT=1)
        CLOSE(UNIT=2)
        STOP 'END OF FILE ENCOUNTERED DURING WRITE'
        END
```

```
$JOB/RT11
        TTYIO
        ! ADDAT3.BAT
        ! REVISED TO COMPUTE ENSEMBLE AVERAGES USING STAT12
        ! DATA AQUISITION UNDER BATCH CONTOL
        !
        ! THESE PROGRAMS CAN SAMPLE 2 DIGITAL CHANNELS AND 4 ANALOG
        ! CHANNELS
        !
        ! THIS BATCH JOB STREAMS THROUGH A SERIES OF PROGRAMS
        ! TO SAMPLE A ZERO RECORD,CALIBRATE,AND COMPUTE A ZERO
        ! A DATA RUN IS THEN SAMPLED, CALIBRATED, AND MEAN,VARIANCE
        ! IS COMPUTED. THE ZERO INITIALLY COMPUTED IS SUBTRACTED.
        !
        ! BE SURE TO UPDATE NAME OF CALIBRATION FILE IN THIS PROGRAM
        LET D="4
        LET A="4
LOOP1:
        LET N="0
LOOP2:
.'FF'
        !SAMPLE AND PROCESS ZERO RECORD
.RUN FW4:ADDAT2
*1024
*1
*1
*2
*5,4.,45
*FW7:D12'D''A''N'.DAZ
* ZERO RECORD-BWD39 AK=0.420, CH 1 HOR VEL, CH 2 VER VEL, FS=200K N=16
*3.502,-0.3      !PROBE VOL LOCATION
*FW7:A12'D''A''N'.DAZ
* ZERO RECORD-BWD39 AK=0.420   SURF DISP
*3.5020    !GAUGE LOCATION
*1
*'FF'
*1
        !PROCESS RAW DATA
.RUN FW4:DIPRO3
*FW7:D12'D''A''N'.DAZ
*200000.
*16
*FW7:D12'D''A''N'.ZEH
*200000.
*16
*FW7:D12'D''A''N'.ZEV
*N
.RUN ANPRO5
*FW7:A12'D''A''N'.DAZ
*FW7:C0124A.CAL
*3
*N
*FW7:A12'D''A''N'.ZE0
.'FF'
        !COMPUTE MEAN,VAR OF ZERO RECORD
.RUN FW4:STAT7
*FW7:D12'D''A''N'.ZER
*1024,2
*30000.
*FW7:D12'D''A''N'.ZEH
```

```
*FW7:D12'D''A''N'.ZEV
.'FF'
.RUN FW4:STAT7
*FW7:A12'D''A''N'.ZER
*1024,1
*2000.
*FW7:A12'D''A''N'.ZEO
.RUN PRINT
.'FF'
.TYPE FW7:D12'D''A''N'.ZER
.TYPE FW7:A12'D''A''N'.ZER
.'FF'
.RUN TERM
        !
        !SAMPLE AND PROCESS DATA RECORD
.RUN FW4:ADDAT2
*2048
*2
*1
*2
*5,2.,45
*FW7:D12'D''A''N'.DAT
* BWD39 AK=0.420 CH1 HOR VEL, CH2 VER VEL  FS=200K N=16
*3.502,-0.300    !PROBE VOL LOCATION
*FW7:A12'D''A''N'.DAT
* BWD39 AK=0.420- SURF DISP
*3.50200    !GAUGE LOCATION
*1
*'FF'
*1
        !PROCESS DATA RECORD
.RUN FW4:DIPRO3
*FW7:D12'D''A''N'.DAT
*200000.
*16
*FW7:D12'D''A''N'.VEH
*200000.
*16
*FW7:D12'D''A''N'.VEV
*N
        GOTO JUMP
.RUN FW4:DROP
*FW7:D12'D''A''N'.DAH
*FW7:D12'D''A''N'.VEH
*4096,1,10
.RUN FW4:DROP
*FW7:D12'D''A''N'.DAV
*FW7:D12'D''A''N'.VEV
*4096,1,10
JUMP:
.'FF'
.RUN ANPRO5
*FW7:A12'D''A''N'.DAT
*FW7:C0124A.CAL
*3
*Y
*FW7:A12'D''A''N'.ZER
*FW7:A12'D''A''N'.GAO
.'FF'
.RUN FW4:STAT7
```

```
*FW7:D12'D''A''N'.STA
*4096,2
*30000.
*FW7:D12'D''A''N'.VEH
*FW7:D12'D''A''N'.VEV
.'FF'
.RUN FW4:STAT7
*FW7:A12'D''A''N'.STA
*4096,1
*2000.
*FW7:A12'D''A''N'.GA0
.RUN PRINT
.'FF'
.TYPE FW7:D12'D''A''N'.STA
.TYPE FW7:A12'D''A''N'.STA
.'FF'
.RUN STAT12
*'N'
*FW7:D12'D''A''N'.VEH
*FW7:D12TEM.AVH
*FW7:D12'D''A''N'.AVH
*8
.COPY FW7:D12'D''A''N'.AVH FW7:D12TEM.AVH
.RUN STAT12
*'N'
*FW7:D12'D''A''N'.VEV
*FW7:D12TEM.AVV
*FW7:D12'D''A''N'.AVV
*8
.COPY FW7:D12'D''A''N'.AVV FW7:D12TEM.AVV
.RUN TERM
.'FF'
        !
        !PLOT RESULTS
        !.RUN RJPLT9
        !*50.,0.,81.92
        !*5.53
        !* A72'D''A''N'
        !*3
        !*N
        !*FW7:A72'D''A''N'.GA0
        !*0.0325,0.5
        !*FW7:D72'D''A''N'.VEH
        !*0.005877,0.5
        !*FW7:D72'D''A''N'.VEV
        !*0.005877,0.5
        !
        !COPY TO TAPE
.COPY FW7:D12'D''A''N'.* MT0:/POS:-1
.COPY FW7:A12'D''A''N'.* MT0:/POS:-1
.DEL/NOQUERY FW7:D12'D''A''N'.AV*
.DEL/NOQUERY FW7:D12'D''A''N'.DA*
.DEL/NOQUERY FW7:D12'D''A''N'.ZE*
.DEL/NOQUERY FW7:D12'D''A''N'.STA
.DEL/NOQUERY FW7:A12'D''A''N'.*
        %N
        IF(N-"1)-LOOP2,-LOOP2,END
CONT:
        %A
        IF(A-"0)-LOOP1,-LOOP1,END
```

!

```
END:
.RUN RJPL11
*50.,0.,81.92
*5.53
*D12'D''A''N'.AVH
*FW7:D12TEM.AVH
*2
*'FF''CTY'
*0.005577,0.3
*0.005577,0.3
*'FF''CTY'
.RUN RJPL11
*50.,0.,81.92
*5.53
*D12'D''A''N'.AVV
*FW7:D12TEM.AVV
*2
*'FF''CTY'
*0.005577,0.3
*0.005577,0.3
$EOJ
```

```
C       PROGRAM ANAOT2
C       PROGRAM TO OUTPUT ANALOG DATA
C       ALSO SEND 2 TRIGGER SIGNALS
C       15-11-84
        DIMENSION ISIG(4000)
        REAL SIG(6000)
        LOGICAL*1 INPSTR(15)
        WRITE(5,*)' DATA FILE NAME'
        CALL GETSTR(5,INPSTR,14,ERRFLG)
 5      CONTINUE
        WRITE(5,*)'  AMPLITUDE GAIN,WINDOW ST&ED(S)'
        READ(5,*)GAIN,TS,TE
        WRITE(5,*)'  TIME FOR 1st TRIGGER & SLOPE: 1:+5V ; 2:-5V'
        READ(5,*)TDLY1,ISLOP1
        WRITE(5,*)'  TIME FOR 2nd TRIGGER '
        READ(5,*)TDLY2
        ITS=TS/(0.0092)
        NPT=TE/(0.0092)
        NTDLY1=TDLY1/(0.0092)
        NTDLY2=TDLY2/(0.0092)
        DO 3 I=1,4000
 3      ISIG(I)=0
        OPEN(UNIT=3,NAME=INPSTR,TYPE='OLD',
     #  FORM='UNFORMATTED',RECORDSIZE=512)
        READ(3)SIG
        CLOSE(UNIT=3)
        DO 2 I=ITS,NPT
 2      ISIG(I)=SIG(I)*GAIN
        NPT=4000
C       ..SEND SIGNAL..
        IRATE=5
        PRESET=1.
        IUNIT=0
        MODE=0
        ICMF=0
        IITGL=INT(5.0*4096/20.)
        ITGL=0
        IF(ISLOP1.EQ.2)ITGL=IITGL
        CALL IDAC(0,IUNIT,ITGL)
        ITGL=IITGL
        IF(ISLOP1.EQ.2)ITGL=0
        ICHAN=1
 4      WRITE(5,*)' KEY 1 TO CONT ; 0 TO STOP; 3 TO CHANGE GAIN'
        READ(5,*)IGO
C*************************************************************************
C       REMOVE 'C' IN THE NEXT 2 STATEMENTS TO TRIGGER AT T=0
C*************************************************************************
C       ITGL=IITGL
C       CALL IDAC(0,IUNIT,ITGL)
        IF(IGO.EQ.0)GO TO 6
        IF(IGO.EQ.3) GO TO 5
C
        WRITE(5,*)' KEY 1 TO START'
        READ(5,*)IGO
C
        CALL SETR(-1,,,,)
        ICMF=0
        DO 1 I=1,NTDLY1
        ICMF=I
        CALL SETR(IRATE,,MODE,PRESET,ICMF)
```

```
      CALL LWAIT(ICMF,I)
      CALL IDAC(ICHAN,IUNIT,ISIG(I))
      CALL SETR(-1,,,,)
1     CONTINUE
      CALL IDAC(0,IUNIT,ITGL)
      DO 7 I=NTDLY1+1,NTDLY2
      ICMF=I
      CALL SETR(IRATE,,MODE,PRESET,ICMF)
      CALL LWAIT(ICMF,I)
      CALL IDAC(ICHAN,IUNIT,ISIG(I))
      CALL SETR(-1,,,,)
7     CONTINUE
      ITGL=0
      IF(ISLOP1.EQ.2)ITGL=IITGL
      CALL IDAC(0,IUNIT,ITGL)
      DO 8 I=NTDLY2+1,NPT
      ICMF=I
      CALL SETR(IRATE,,MODE,PRESET,ICMF)
      CALL LWAIT(ICMF,I)
      CALL IDAC(ICHAN,IUNIT,ISIG(I))
      CALL SETR(-1,,,,)
8     CONTINUE
      ITGL=0
      IF(ISLOP1.EQ.2)ITGL=IITGL
      CALL IDAC(0,IUNIT,ITGL)
      ITGL=IITGL
      IF(ISLOP1.EQ.2)ITGL=0
      GO TO 4
6     STOP
      END
```

```
C-----------------------------------------------------------------------
C       ANLDIG.FOR      4-29-85                                        !
C
C       PROGRAM TO ANALZE DIGITIZED FILM DATA. IT FINDS MAX AND MIN OF
C       X AND Y AXIS DYE BOUNDARIES, VOLUME OF DYE, VOLUME BELOW THE
C       STILL WATER LINE, AND MAX THICKNESS.
C-----------------------------------------------------------------------
C
        DIMENSION IXX(512),IYY(512),XX(512),YY(512),SCALE(10)
        DIMENSION ALBIN(300),AUBIN(300),NLO(300),NUP(300)
        LOGICAL*1 INFIL(15),OUTFIL(15),HEAD(70),ERRFLG
C
C OPEN IN FILE
        WRITE(5,*)' INPUT DATAFILE NAME'
        CALL GETSTR(5,INFIL,14,ERRFLG)
        OPEN(UNIT=1,NAME=INFIL,TYPE='OLD',FORM='UNFORMATTED',
     #  RECORDSIZE=512,ACCESS='DIRECT')
        READ(1'1) (HEAD(J),J=1,70)
        READ(1'2) (SCALE(J),J=1,10)
C
C OPEN OUT FILE
        WRITE(5,*)' OUTPUT DATA FILE NAME'
        CALL GETSTR(5,OUTFIL,14,ERRFLG)
        OPEN(UNIT=2,NAME=OUTFIL,TYPE='NEW')
C
        WRITE(5,*)' ENTER NO. OF FRAMES, START FRAME, INCREMENT'
        READ(5,*)NTFR,ISTRT,INCR
C
C LOOP ON EACH FRAME
C READ IN DATA
        DO 1000 NFR=1,NTFR
        IFRAME=ISTRT + (NFR-1)*INCR
        WRITE(5,3)IFRAME
    3   FORMAT(' ON FRAME ',I10)
        LINE=NFR*2+1
        READ(1'LINE)NPTS,(IXX(J),J=1,NPTS)
        READ(1'LINE+1)NPTS,(IYY(J),J=1,NPTS)
C
C CONVERT TO METERS
        DO 100 J=1,NPTS
        XX(J)=FLOAT(IXX(J))/1000.
        YY(J)=FLOAT(IYY(J))/1000.
  100   CONTINUE
C
C FIND ARRAY SUBSCRIPT OF XMAX,XMIN,YMAX,YMIN
        IXMAX=1
        IYMAX=1
        IYMIN=1
C FIND XMAX
        DO 200 J=1,NPTS
        IF(XX(J).GT.XX(IXMAX))IXMAX=J
  200   CONTINUE
C FIND XMIN
        IXMIN=IXMAX
        DO 201 J=IXMAX,NPTS
        IF(XX(J).LT.XX(IXMIN))IXMIN=J
  201   CONTINUE
C FIND YMAX, YMIN BETWEEN XMIN AND XMAX
        IYMAX=IXMIN
        IYMIN=IXMIN
```

```
      DO 202 J=1,NPTS
      IF(XX(J).LT.XX(IXMIN))GO TO 202
      IF(YY(J).GT.YY(IYMAX))IYMAX=J
      IF(YY(J).LT.YY(IYMIN))IYMIN=J
  202 CONTINUE
C
C OUTPUT RESULTS
      WRITE(2,1)XX(IXMAX),YY(IXMAX),XX(IXMIN),YY(IXMIN),
     #          XX(IYMAX),YY(IYMAX),XX(IYMIN),YY(IYMIN)
    1 FORMAT(1X,4(2F8.3,3X))
C
C COMPUTE ENCLOSED AREA OF DYE ABOVE SWL(AREA1), UNDER SWL (AREA2)
      AREA1=0
      AREA2=0
      DO 300 J=1,NPTS-1
      IF(XX(J).LT.XX(IXMIN))GO TO 300 !TEMPORARY
      AREA= ABS(YY(J+1) + YY(J)) * (XX(J+1)-XX(J))/2.
      IF(YY(J).GT.0.)AREA1=AREA1+AREA
      IF(YY(J).LE.0.)AREA2=AREA2-AREA
  300 CONTINUE
      AREAT=AREA1+AREA2
C
C COMPUTE THICKNESS OF DYE REGION
      A=XX(IXMIN)
      DX=0.01                    !1 CM BIN SIZE
C ZERO ARRAY
      DO 399 IBIN=1,300
      AUBIN(IBIN)=0.
      ALBIN(IBIN)=0.
      NLO(IBIN)=0
      NUP(IBIN)=0
  399 CONTINUE
C
      DO 400 I=1,NPTS-1
      J=(XX(I)-A)/DX
      IF(J.LE.0)GO TO 400
C  CHECK IF UPPER OR LOWER
      IF(XX(I+1).GT. XX(I))GO TO 401
      NLO(J)=NLO(J)+1
      ALBIN(J)=ALBIN(J) + YY(I)
      GO TO 400
  401 NUP(J)=NUP(J)+1
      AUBIN(J)=AUBIN(J) + YY(I)
  400 CONTINUE
      DO 600 J=1,300
      IF(NLO(J).EQ.0 .OR. NUP(J).EQ.0)GO TO 600
      ALBIN(J)=ALBIN(J)/FLOAT(NLO(J))
      AUBIN(J)=AUBIN(J)/FLOAT(NUP(J))
      AUBIN(J)=AUBIN(J)-ALBIN(J)
  600 CONTINUE
C
C FIND MAX THICKNESS AND X LOCATION
      ITHK=1
      DO 500 IBIN=1,300
      IF(ABS(AUBIN(IBIN)).GE.ABS(AUBIN(ITHK)))ITHK=IBIN
  500 CONTINUE
      XMAXTK=XX(IXMIN) + FLOAT(ITHK)*DX
C
      AUBIN(ITHK)=-AUBIN(ITHK)
C WRITE RESULTS
```

```
      ALEN=XX(IXMAX)-XX(IXMIN)
      WRITE(2,2)AREA1,AREA2,AREAT,AUBIN(ITHK),XMAXTK,ALEN,IFRAME
    2 FORMAT(1X,3F9.5,5X,2F9.5,5X,F8.3,I10)
C
 1000 CONTINUE
      CLOSE(UNIT=1)
      CLOSE(UNIT=2)
      STOP
      END
```

```
C       ANPRO5.FOR      7-23-85
C       REVISED ANPRO3 TO ALLOW DEGREE OF CALIB. TO BE INPUT
C
C
C       THIS PROGRAM PROCESSES ANALOG DATA TAKEN BY ADDATA
C       AND OUTS THE FILE INTO A SEPARATE FILE FOR EACH
C       CHANNEL. AMAX OF SIX CHANNELS
C
        DIMENSION NBUF(6,513),IBUF(3073),AMEAN(7),FF(6,5)
        DIMENSION GLOCX(6),GLOCZ(6)
        LOGICAL*1 INPSTD(15),IAOUT0(15),IAOUT1(15),IAOUT2(15)
        LOGICAL*1 IAOUT3(15),IAOUT4(15),IAOUT5(15)
        LOGICAL*1 ERRFLG,IDEC
        LOGICAL*1 HEAD(70),CALCOF(15),ZEROF(15)
        COMMON NREAD,ISIZD,MDC,NCCH,NDCCH,MODED,MODEA,IRATE,
     #   PRESET,MODEC,HEAD,IGAIN,GLOCX,GLOCZ
C
C
        WRITE(5,10)
   10   FORMAT(' INPUT ANALOG FILE NAME')
        CALL GETSTR(5,INPSTD,14,ERRFLG)
        OPEN(UNIT=3,NAME=INPSTD,TYPE='OLD',FORM='UNFORMATTED')
C  READ HEADERS
        READ(3) (HEAD(J),J=1,70)
        READ(3)NREAD,ISIZD,MDC,NCCH,NDCCH,MODED,MODEA,IRATE,
     #   PRESET,MODEC,IGAIN,(GLOCX(J),J=1,NCCH)
        DO 578 J=1,NCCH
        GLOCZ(J)=0.
  578   CONTINUE
C
        WRITE(5,11)
   11   FORMAT(' FILE NAME OF CALIBRATION COEFFICIENTS')
        CALL GETSTR(5,CALCOF,14,ERRFLG)
        OPEN(UNIT=1,NAME=CALCOF,TYPE='OLD')
        WRITE(5,*)' DEGREE OF CALIBRATION ,M?'
        READ(5,*)M
C
        DO 1 N=1,NCCH
        AMEAN(N)=0.0
    1   CONTINUE
C
        WRITE(5,12)
   12   FORMAT(' DO YOU HAVE ANOTHER FILE OF ZEROS? Y OR N')
        READ(5,13)IDEC
   13   FORMAT(1A1)
        IF(IDEC .EQ. 'N')GO TO 14
        WRITE(5,15)
   15   FORMAT(' INPUT NAME OF THIS ZERO FILE')
        CALL GETSTR(5,ZEROF,14,ERRFLG)
        OPEN(UNIT=2,NAME=ZEROF,TYPE='OLD')
        READ(2,16)
   16   FORMAT(/)
        DO 18 N=1,NCCH
        READ(2,19)NDUM,XLOC,ZLOC,AMEAN(N),VAR
   18   CONTINUE
   19   FORMAT(I10,2F15.2,2E20.8)
        CLOSE(UNIT=2)

   14   CONTINUE
C
```

```
      CALL OPNNEW(10,IAOUT0)
      READ(1,*) (FF(1,J),J=1,M+1)
      IF(NCCH.LT.2)GO TO 99
C
      CALL OPNNEW(11,IAOUT1)
      READ(1,*)FF10,FF11,FF12
      IF(NCCH.LT.3)GO TO 99
C
      CALL OPNNEW(12,IAOUT2)
      READ(1,*)FF20,FF21,FF22
      IF(NCCH.LT.4)GO TO 99
C
      CALL OPNNEW(13,IAOUT3)
      READ(1,*)FF30,FF31,FF32
      IF(NCCH.LT.5)GO TO 99
C
      CALL OPNNEW(14,IAOUT4)
      READ(1,*)FF40,FF41,FF42
      IF(NCCH.LT.6)GO TO 99
C
      CALL OPNNEW(15,IAOUT5)
      READ(1,*)FF50,FF51,FF52
C
   99 CONTINUE
      NBLKS=(NREAD/512)*MDC
      DO 50 NB = 1,NBLKS
C
C READ IN DATA IN BLOCKS OF 512*NCCH
      DO 100 K=1,NCCH
      IZ=(K-1)*512
      READ(3,END=128) (IBUF(J),J=1+IZ,512+IZ)
  100 CONTINUE
C
C SEPARATE OUT CHANNELS
      DO 101 N=1,NCCH
      DO 102 J=1,512
      K=NCCH*(J-1) + N
      NBUF(N,J)=IBUF(K)
  102 CONTINUE
  101 CONTINUE
      SCALE=20./4096.
C
C CALIBRATE CHANNELS
      DO 200 J=1,512
      AN0=FLOAT(NBUF(1,J))*SCALE
      ELEV0=FF(1,1)
      DO 510 II=1,M
      ELEV0=ELEV0 + FF(1,II+1)*(AN0**II)
  510 CONTINUE
      NBUF(1,J)=IFIX((ELEV0-AMEAN(1))*100)                    !UNITS *100
  200 CONTINUE
      WRITE(10) (NBUF(1,J),J=1,512)
      IF(NCCH .EQ. 1)GO TO 50

      DO 201 J=1,512
      AN1=FLOAT(NBUF(2,J))*SCALE
      AN1=FF10 + FF11*AN1 + FF12*(AN1**2) - AMEAN(2)
      NBUF(2,J)=IFIX(AN1*100)
  201 CONTINUE
      WRITE(11) (NBUF(2,J),J=1,512)
```

```
      IF(NCCH .EQ. 2)GO TO 50

      DO 202 J=1,512
      AN2=FLOAT(NBUF(3,J))*SCALE
      AN2=FF20 + FF21*AN2 + FF22*(AN2**2) - AMEAN(3)
      NBUF(3,J)=IFIX(AN2*100)
  202 CONTINUE
      WRITE(12) (NBUF(3,J),J=1,512)
      IF(NCCH .EQ. 3)GO TO 50
C
      DO 203 J=1,512
      AN3=FLOAT(NBUF(4,J))*SCALE
      AN3=FF30 + FF31*AN3 + FF32*(AN3**2) - AMEAN(4)
      NBUF(4,J)=IFIX(AN3*100)
  203 CONTINUE
      WRITE(13) (NBUF(4,J),J=1,512)
      IF(NCCH .EQ. 4)GO TO 50
C
      DO 204 J=1,512
      AN4=FLOAT(NBUF(5,J))*SCALE
      AN4=FF40 + FF41*AN4 + FF42*(AN4**2) - AMEAN(5)
      NBUF(5,J)=IFIX(AN4*100)
  204 CONTINUE
      WRITE(14) (NBUF(5,J),J=1,512)
      IF(NCCH .EQ. 5)GO TO 50
C
      DO 205 J=1,512
      AN5=FLOAT(NBUF(6,J))*SCALE
      AN5=FF50 + FF51*AN5 + FF52*(AN5**2) - AMEAN(6)
      NBUF(6,J)=IFIX(AN5*100)
  205 CONTINUE
      WRITE(15) (NBUF(6,J),J=1,512)
C
   50 CONTINUE
  128 CONTINUE          !END OF FILE
      CLOSE(UNIT=1)
      CLOSE(UNIT=3)
      CLOSE(UNIT=10)
      IF(NCCH .EQ. 2)CLOSE(UNIT=11)
      IF(NCCH .EQ. 3)CLOSE(UNIT=12)
      IF(NCCH .EQ. 4)CLOSE(UNIT=13)
      IF(NCCH .EQ. 5)CLOSE(UNIT=14)
      IF(NCCH .EQ. 6)CLOSE(UNIT=15)
      STOP
      END
```

```
C       CCSESX  5-3-84
C       SUBROUTINES TO BE LINKED WITH CCSEXM RUN ON XM MONITOR
C
C
C-----------------------------------------------------------------------
C SUBROUTINE:  HICMP
C THIS SUBROUTINE COMPUTES A NEW COMPOSITE NUMBER
C-----------------------------------------------------------------------
C
      SUBROUTINE HICMP(NNN, NEWNN)
C
C INPUT:  NNN = NUMBER OF DATA POINTS
C OUTPUT: NEWNN = A NEW COMPOSITE NUMBER ( A POWER OF 2 ) > OR = TO NNN
C
      DO 10 I=1,15
        M = I
        NT = 2**I
        IF (NNN.LE.NT) GO TO 20
  10  CONTINUE
C
  20  NEWNN = 2**M
C
      RETURN
      END
C
C-----------------------------------------------------------------------
C SUBROUTINE:  LREMV
C THIS SUBROUTINE CAN REMOVE THE DC COMPONENT AND SLOPE OF AN ARRAY OF
C DATA IF DESIRED
C-----------------------------------------------------------------------
C
      SUBROUTINE LREMV(XX, NNN, ISWCH, DC, SLOPE)
C
C INPUT:  XX = INPUT DATA ARRAY
C         NNN = NUMBER OF POINTS IN DATA ARRAY
C         ISWCH = 0 DO NOT REMOVE DC COMPONENT OR SLOPE
C               = 1 REMOVE THE DC COMPONENT
C               > 1 REMOVE THE DC COMPONENT AND SLOPE
C OUTPUT: DC = DC COMPONENT OF DATA
C         SLOPE = SLOPE OF DATA
C
      DIMENSION XX(1)
C
C ESTABLISH CONSTANTS
C
      FLN = FLOAT(NNN)
      DC = 0.0
      SLOPE = 0.0
C
      DO 10 I=1,NNN
        DC = DC + XX(I)
        SLOPE = SLOPE + XX(I)*FLOAT(I)
  10  CONTINUE
C
C COMPUTE STATISTICS
C
      DC = DC/FLN
      SLOPE = 12.0*SLOPE/(FLN*(FLN*FLN-1.0)) - 6.0*DC/(FLN-1.0)
C
C DETERMINE KIND OF TREND REMOVAL
```

```
C
      IF (ISWCH-1) 60, 40, 20
C
C REMOVE TREND (MEAN AND SLOPE)
C
  20  CONTINUE
      FLN = DC - 0.5*(FLN+1.0)*SLOPE
      DO 30 I=1,NNN
        XX(I) = XX(I) - FLOAT(I)*SLOPE - FLN
  30  CONTINUE
      GO TO 60
C
C REMOVE THE DC COMPONENT
C
  40  CONTINUE
      DO 50 I=1,NNN
        XX(I) = XX(I) - DC
  50  CONTINUE
C
  60  RETURN
      END
C
C-----------------------------------------------------------------------
C SUBROUTINE:  ZERO
C THIS SUBROUTINE STORES ZEROES IN A FLOATING POINT ARRAY
C-----------------------------------------------------------------------
C
      SUBROUTINE ZERO(ARRAY, NUMBR)
C
C INPUT:  ARRAY = AN ARRAY OF FLOATING POINT VALUES TO BE
C                 ZERO FILLED
C         NUMBR = NUMBER OF ARRAY VALUES
C
      DIMENSION ARRAY(1)
C
      DO 10 K=1,NUMBR
        ARRAY(K) = 0.0
  10  CONTINUE
C
      RETURN
      END
C
C-----------------------------------------------------------------------
C SUBROUTINE:  ZEROV
C TO ZERO A VIRTUAL ARRAY
C
C-----------------------------------------------------------------------
      SUBROUTINE ZEROV(ARRAY,NUMBR)
      VIRTUAL ARRAY(NUMBR)
C
      DO 10 K=1,NUMBR
        ARRAY(K)=0.0
  10  CONTINUE
      RETURN
      END
```

```
;  SUBROUTINE TO SEPARATE THE MANTISSA AND EXPONENT FROM THE
;  16 BIT DIGITAL SIGNAL FROM THE LASER ANNEMOMTER.
;  FILENAME:  DETSI.MAC
;
        .TITLE DETSI
        .PSECT  $CODE
        .GLOBL  DETSI

DETSI:  CMP     (R5)+,#2

        BEQ     OK
        TRAP    16.

OK:     MOV     @(R5)+,IIEXP
        MOV     @(R5)+,IMANT

        COM     IIEXP
        COM     IMANT           ; TAKE COMPLEMENT SINCE LOGIC OF
                                ; TSI AND DEC IS REVERSED

MASKM=-4096.                    ; 2'S COMPLEMENT OF DESIRED MASK
MASKE=-16.                      ; SINCE BIC DOES AN .AND. .NOT.

        BIC     #MASKM,IMANT    ; A LOGICAL .AND. .NOT. MASK

        MOV     IIEXP,R1        ; MOVE CONTENTS OF IIEXP TO R1
        ASH     #-12.,R1        ; SHIFTS 12 BITS TO RIGHT
        MOV     R1,IIEXP        ; MOVE CONTENTS OF R1 BACK
        BIC     #MASKE,IIEXP    ; A LOGICAL .AND. .NOT. MASK

        MOV     IIEXP,@-(R5)    ;LOAD RESULTS BACK TO R5
        MOV     IMANT,@-(R5)

RETURN: RTS     PC

IIEXP:  .WORD   0
IMANT:  .WORD   0

        .END
```

```
C-----------------------------------------------------------------------
C     DIPRO3.FOR  12-4-84
C
C     PROGRAM TO PROCESS DIGITAL DATA TAKEN WITH ADDAT2.FOR
C     THIS WILL SEPARATE AND CALIBRATE 2 DIGITAL CHANNELS OF
C     LDV MEASUREMENTS.
C-----------------------------------------------------------------------
        DIMENSION IBUFD1(512),IVEL1(512),IBUFD2(512),IVEL2(512)
        LOGICAL*1 INFILE(15),OUTF1(15),OUTF2(15),ZEROF(15)
        LOGICAL*1 ERRFLG,IDEC
        LOGICAL*1 HEADD(70)
        DIMENSION ICHAN(2),AMEAN(2),VAR(2)
        DIMENSION PVX(2),PVZ(2)
C
        WRITE(5,10)
   10   FORMAT(' INPUT DIGITAL FILE NAME')
        CALL GETSTR(5,INFILE,14,ERRFLG)
        OPEN(UNIT=1,NAME=INFILE,TYPE='OLD',FORM='UNFORMATTED')
        READ(1)  (HEADD(J),J=1,70)
        READ(1)NREADD,ISIZD,MDC,NCCH,NDCCH,MODED,MODEA,IRATE,
     #   PRESET,MODEC,IGAIN,(PVX(J),PVZ(J),J=1,NDCCH)
C
C
        WRITE(5,1)
    1   FORMAT(' BEWARE- CHECK LASER OPTICS AND FREQUENCY PARAMETERS')
        THETA=ATAN(50./250.4)          ! BEAM INTERSECTION ANGLE
        WRITE(5,69)(HEADD(J),J=1,70)
   69   FORMAT(70A1)
C
C
C CHANNEL 1 CALIBRATION PARAMETERS-BLUE BEAM, 2NS CLOCK,HORIZ VEL
C
        ALWL1=488.0E-09               ! BLUE LASER LIGHT WAVELENGTH
        FFAC1=ALWL1/(2.*SIN(THETA/2.))  !CONVERTS FREQ TO VELOCITY
        WRITE(5,65)
   65   FORMAT(' INPUT CHANNEL 1 FREQUENCY SHIFT')
        READ(5,*)FZ1                      ! FREQUENCY SHIFT IN BRAG- HZ
        WRITE(5,2)
    2   FORMAT(' INPUT CHANNEL 1 BURST COUNT')
        READ(5,*)IBC1
        WRITE(5,20)
   20   FORMAT(' CHANNEL 1 OUTPUT FILE NAME')
        CALL GETSTR(5,OUTF1,14,ERRFLG)
        OPEN(UNIT=2,NAME=OUTF1,TYPE='NEW',FORM='UNFORMATTED',
     #   RECORDSIZE=512)             !RECORDSIZE IN WORDS
        WRITE(2)(HEADD(J),J=1,70)
        WRITE(2)NREADD,ISIZD,MDC,NCCH,NDCCH,MODED,MODEA,IRATE,
     #   PRESET,MODEC,IGAIN,(PVX(J),PVZ(J),J=1,NDCCH)
C
C
C CHANNEL 2 CALIBRATION PARAMETERS- GREEN BEAM, 1NS CLOCK, VERT VEL
C
        ALWL2=514.5E-09                  !GREEN BEAM WAVELENGTH
        FFAC2=ALWL2/(2.*SIN(THETA/2.))
        WRITE(5,67)
   67   FORMAT(' INPUT CHANNEL 2 FREQUENCY SHIFT')
        READ(5,*)FZ2
        WRITE(5,68)
   68   FORMAT(' INPUT CHANNEL 2 BURST COUNT')
        READ(5,*)IBC2
```

```
      WRITE(5,70)
   70 FORMAT(' CHANNEL 2 OUTPUT FILE')
      CALL GETSTR(5,OUTF2,14,ERRFLG)
      OPEN(UNIT=3,NAME=OUTF2,TYPE='NEW',FORM='UNFORMATTED',
     #  RECORDSIZE=512)
      WRITE(3) (HEADD(J),J=1,70)
      WRITE(3)NREADD,ISIZD,MDC,NCCH,NDCCH,MODED,MODEA,IRATE,
     #  PRESET,MODEC,IGAIN,(PVX(J),PVZ(J),J=1,NDCCH)
C
C
C SUBTRACT A PREVIOUSLY MEASURED ZERO IF DESIRD
C
      WRITE(5,13)
   13 FORMAT(' DO YOU WANT TO REMOVE PREVIOUSLY MEASURED MEAN')
      READ(5,14)IDEC
   14 FORMAT(1A1)
      IF(IDEC .EQ. 'N')GO TO 15
      WRITE(5,16)
   16 FORMAT(' INPUT NAME OF THIS ZERO FILE')
      CALL GETSTR(5,ZEROF,14,ERRFLG)
      OPEN(UNIT=4,NAME=ZEROF,TYPE='OLD')
      READ(4,17)
   17 FORMAT(/)
      DO 19 N=1,2
      READ(4,21)ICHAN(N),XDUM,ZDUM,AMEAN(N),VAR(N)
   19 CONTINUE
   21 FORMAT(I10,2F15.2,2E20.8)
      CLOSE(UNIT=4)
   15 CONTINUE
C
C READ RAW DATA FILE AND SEPARATE COMPONENTS
C
      NDSJP=(NREADD/512)*MDC
      DO 100 N=1,NDSJP
      READ(1) (IBUFD1(J),IBUFD2(J),J=1,256)
      READ(1) (IBUFD1(J),IBUFD2(J),J=257,512)
C
C APPLY MASK TO INTERPRET BIT PATTERN
C
      DO 200 K=1,512
      IEXP1=IBUFD1(K)
      IEXP2=IBUFD2(K)
      MANT1=IEXP1
      MANT2=IEXP2
      CALL DETSI(MANT1,IEXP1)                          ! FILE DETSI.MAC
      CALL DETSI(MANT2,IEXP2)
      FREQ1=(FLOAT(IBC1)*10.0**9)/(MANT1*2.**(IEXP1-2)) !2 NS CLOCK
      FREQ2=(FLOAT(IBC2)*10.0**9)/(MANT2*2.**(IEXP2-3)) !1 NS CLOCK
      FREQ1=FREQ1-FZ1
      FREQ2=FREQ2-FZ2
      IVEL1(K)=MIN1((FREQ1*FFAC1*10000.),32767.)  !VELOCITY IN CM/SEC *100
      IVEL2(K)=MIN1((FREQ2*FFAC2*10000.),32767.)
  200 CONTINUE
C
C
C SUBTRACT MEAN IF DESIRD
C
      IF(IDEC .EQ. 'N')GO TO 799
      DO 788 K=1,512
      IVEL1(K)=IVEL1(K) - IFIX(AMEAN(1)*100.)
```

```
      IVEL2(K)=IVEL2(K)  - IFIX(AMEAN(2)*100.)
  788 CONTINUE
  799 CONTINUE
C
C .
C WRITE TO DISK
C
      WRITE(2,ERR=800,END=810) (IVEL1(J),J=1,512)
      WRITE(3,ERR=800,END=810) (IVEL2(J),J=1,512)
  100 CONTINUE
      CLOSE(UNIT=1)
      CLOSE(UNIT=2)
      CLOSE(UNIT=3)
      STOP
  800 STOP 'ERROR IN WRITE TO FILE'
  810 STOP 'END OF FILE WHILE WRITE'
      STOP
      END
```

```
C-----------------------------------------------------------------------
C       DROP.FOR        7-12-83
C
C       PROGRAM TO SET VELOCITY DROPOUT TO ZERO
C       INPUT DATA IN 512 INTEGER WORD (2 BYTES) RECORDS
C
C               NNN= # OF POINTS PER TIME HISTORY
C               NDSJP= # OF TIME HISTORY (SEGMENTS)
C
C       REV:    4-22-84 CHANGE NUMBER OF POINTS TO SEARCH FOR END
C                       OF DROP OUT TO 4096.
C               4-22-84 CHANGE NUMBER OF POINTS TO INITIATE SEARCH
C                       FROM 5 TO 15
C               12-4-84 READ AND WRITE MEASUREMENT LOCATION IN HEADER
C               5-29-85 INPUT WIDTH OF DROPOUT,NWID
C-----------------------------------------------------------------------
C
        DIMENSION IN(4096)
        LOGICAL*1 ERRFLG,INFIL(15),OUTFIL(15)
        LOGICAL*1 HEAD(70)
        DIMENSION PVX(2),PVZ(2)
C
        WRITE(5,1)
    1   FORMAT(' INPUT FILE NAME')
        CALL GETSTR(5,INFIL,14,ERRFLG)
        OPEN(UNIT=1,NAME=INFIL,TYPE='OLD',FORM='UNFORMATTED')
        READ(1) (HEAD(J),J=1,70)
        READ(1)NREAD,ISIZD,MDC,NCCH,NDCCH,MODED,MODEA,IRATE,
     #   PRESET,MODEC,IGAIN,(PVX(J),PVZ(J),J=1,NDCCH)

C
        WRITE(5,8)
    8   FORMAT(' OUTPUT FILE OF NEW SIGNAL')
        CALL GETSTR(5,OUTFIL,14,ERRFLG)
        OPEN(UNIT=2,NAME=OUTFIL,TYPE='NEW',FORM='UNFORMATTED',
     #   RECORDSIZE=512)
        WRITE(2) (HEAD(J),J=1,70)
        WRITE(2)NREADD,ISIZD,MDC,NCCH,NDCCH,MODED,MODEA,IRATE,
     #   PRESET,MODEC,IGAIN,(PVX(J),PVZ(J),J=1,NDCCH)
C
   21   WRITE(5,4)
    4   FORMAT(' INPUT- NNN,NDSJP,NWID')
        READ(5,*)NNN,NDSJP,NWID
        AJTOT=0
C
        LPTH=NNN/512    !LINES PER TIME HISTORY                    !
        DO 99 ND=1,NDSJP
C       INPUT DATA
        DO 100 N=1,LPTH
        K=(N-1)*512
        READ(1) (IN(J),J=1+K,512+K)
  100   CONTINUE
C
        NSTRT=1
  199   CONTINUE
        DO 200 N=NSTRT,4096
        DO 201 K=1,NWID
        IF(IN(N) .NE. IN(N+K))GO TO 200
  201   CONTINUE
C IF HERE THEN DROPOUT
```

```
C GO UNTIL END OF DROPOUT OR END OF ARRAY
      DO 202 J=NWID,4096
      IF(N+J .GT. 4096)GO TO 203
      IF(IN(N+K) .NE. IN(N+J))GO TO 203
  202 CONTINUE
      STOP ' NEVER FOUND END OF DROPOUT'
  203 CONTINUE
C N IS THE START OF DROPOUT, N+J IS THE END
C MAKE DROPOUT =0
      NN=N
      NJ=NN+J
      DO 204 I=NN,NJ
      IN(I)=0
  204 CONTINUE
      NSTRT=NJ+1
      AJTOT=AJTOT+FLOAT(J)
      GO TO 199
  200 CONTINUE
C
      DO 600 N=1,LPTH
      K=(N-1)*512
      WRITE(2)(IN(J),J=1+K,512+K)
  600 CONTINUE
   99 CONTINUE
C
      WRITE(5,9)AJTOT
    9 FORMAT(' TOTAL DROPOUT = ',F12.3)
      CLOSE(UNIT=1)
      CLOSE(UNIT=2)
      STOP
      END
```

```
C-----------------------------------------------------------------------
C       EGYSUM.FOR      9-11-85
C       PROGRAM TO INTEGRATE VELOCITY**2 (KINETIC ENERGY)OVER FLUID AREA
C       READS FORM OUTPUT OF VECLST
C-----------------------------------------------------------------------
C
        DIMENSION X(10),Z(10),UB(8,8),WB(8,8)
        DIMENSION AREA(8,8),TEU(2,161),TEW(2,161),WT(161),ENEGU(161)
     #           ,ENEGW(161)
        LOGICAL*1 ERRFLG,INFIL(15),HEAD(70)
C
        WRITE(5,*)' ENTER IDELAY FOR LOG PLOT ORIGIN'
        READ(5,*)IDELAY
        DO 578 IF=1,1
C OPEN DATA FILE
        WRITE(5,*)' ENTER INPUT FILE NAME'
        CALL GETSTR(5,INFIL,14,ERRFLG)
        OPEN(UNIT=1,NAME=INFIL,TYPE='OLD')
        CALL GETSTR(1,HEAD,69,ERRFLG)
        READ(1,*) (X(IX),IX=1,7)
C
        WRITE(5,*)'INPUT NUMBER OF TIME STEPS'
        READ(5,*)NTS
        WRITE(5,*)'INPUT NORMALIZING PARAMETERS-AK,WC,CP,XZERO'
        READ(5,*)AK,WC,CP,XZERO
        ANORM=(AK**2)/(CP**2)
C
C TIME STEP LOOP
        DO 100 IT=1,NTS
C
C READ IN DATA
        READ(1,1)TIME
    1   FORMAT(5X,F10.2)                                              !
        DO 301 IZ=1,7
        READ(1,*)Z(IZ),(UB(IX,IZ),IX=1,7)
        READ(1,*) (WB(IX,IZ),IX=1,7)
  301   CONTINUE
C
        IF(IT.NE.1)GO TO 59
C COMPUTE ELEMENTAL AREAS
        DO 200 IX=2,6
        DX=(X(IX+1)-X(IX-1))/2.
        DO 201 IZ=2,6
        DZ= -(Z(IZ+1)-Z(IZ-1))/2.
        AREA(IX,IZ)=DX*DZ
  201   CONTINUE
C
        DZ= -(Z(2)+Z(1))/2.
        AREA(IX,1)=DX*DZ
        DZ=0.6 + (Z(7)+Z(6))/2.
        AREA(IX,7)=DX*DZ
  200   CONTINUE
C
C IX=1
        DX= X(2)-X(1)
        DZ= -(Z(2)+Z(1))/2.
        AREA(1,1)=DX*DZ
        DO 300 IZ=2,6
        DZ= -(Z(IZ+1)-Z(IZ-1))/2.
        AREA(1,IZ)=DX*DZ
```

```
  300   CONTINUE
        DZ=0.6 + (Z(7)+Z(6))/2.
        AREA(1,7)=DX*DZ
C
C IX=7
        DX=X(7)-X(6)
        DZ= -(Z(2)+Z(1))/2.
        AREA(7,1)=DX*DZ
        DO 400 IZ=2,6
        DZ= -(Z(IZ+1)-Z(IZ-1))/2.
        AREA(7,IZ)=DZ*DX
  400   CONTINUE
        DZ=0.6 + (Z(7)+Z(6))/2.
        AREA(7,7)=DX*DZ
   59   CONTINUE
C
        TEU(IF,IT)=0.
        TEW(IF,IT)=0.
C INTEGRATE VELOCITY**2 OVER AREA
        DO 500 IX=1,7
        DO 501 IZ=1,7
        TEU(IF,IT)=TEU(IF,IT) + (UB(IX,IZ)**2)*AREA(IX,IZ)
        TEW(IF,IT)=TEW(IF,IT) + (WB(IX,IZ)**2)*AREA(IX,IZ)
  501   CONTINUE
  500   CONTINUE
C
C NORMALIZE
        TEU(IF,IT)=TEU(IF,IT)*ANORM
        TEW(IF,IT)=TEW(IF,IT)*ANORM
        WT(IT)=TIME*WC
  100   CONTINUE
        CLOSE(UNIT=1)
  578   CONTINUE
        ENEGU(1)=0.
        ENEGW(1)=0.
        NPTS=NTS-IDELAY
        DO 957 IT=1,NPTS
        NIT=IT+IDELAY
        WT(IT)=ALOG10(AMAX1(WT(IT),1.0E-30))
        ENEGU(IT)=TEU(1,NIT)
        ENEGW(IT)=TEW(1,NIT)
        ENEGU(IT)=ALOG10(ENEGU(IT))
        ENEGW(IT)=ALOG10(ENEGW(IT))
  957   CONTINUE
C
        PAUSE' CHANGE PAPER'
        CALL SETERM("176500)
        CALL ERASE
        CALL GRID('',3.,0.,0.,'',-2.,-5.,-5.,1)
        CALL RJTICK(-5.,0.,0.,3.,-5.,-2.,1.,1.)
        CALL SIZSYM(3.,0.,-2.,-5.,0.01,DX,DY)
        CALL PLUS(NPTS,WT,ENEGU,DX,DY)
        CALL BOX(NPTS,WT,ENEGW,DX,DY)
        CALL EXIT
C
        STOP
        END
```

```
C       PROGRAM NAME: EW6
C       ..GENERATES WAVE PACKET CONSISTING OF SINUSOIDAL COMPONENTS...
C       ..DATE 29-MAR-84
C
C       ********INPUT PARAMETERS*****************************************
C               BW--BANDWIDTH IN HZ
C               FR--HIGHEST FREQUENCY COMPONENT (IN HZ) IN PACKET
C               NFC--NO OF FREQUENCY COMPONENT
C               AA--AMPLITUDE OF EACH COMPONENT IN VOLTS
C               XB--BREAKING LOCATION AWAY FROM PADDLE IN METRES
C               PH--TIME FROM START OF PADDLE WHEN WAVE BREAKS
C               NPT--NO OF POINTS; PERIOD BETWEEN POINTS=0.01S
C
C       MODIFICATIONS: 4-5-84 NFC-NO OF FREQ COMP.
C                      6-JUN-84 ALLOW PHASE AND AMP CORRECTION
C                      7-JUN-84 ALLOW DEPTH DEPENDENCE
        REAL LSBVAL,ITE(6000)
        INTEGER IRATE
        DIMENSION F(32),A(32),PHA(32),RK(32)
        LOGICAL*1 INPSTR(15)
        X=0.0
        WRITE(5,10)
 10     FORMAT(' HIGHEST FR(HZ),BW(HZ),NO OF COMP,AMP(VOLTS)')
        READ(5,*)FR,BW,NFC,AA
        WRITE(5,11)
 11     FORMAT(' XB(M),TB(TIME),PERIOD')
        READ(5,*)XB,PH,PNPT
        SEC=0.01*0.92
        NPT=PNPT/SEC
        PI=4*ATAN(1.)
        LSBVAL=4096/20.6
C
C       COMPUTES FREQ. COMP.
        DBW=BW/NFC
        DO 5 I=1,NFC
        F(I)=(FR-((I-1)*DBW))
 5      CONTINUE
        TPI=2*PI
C
C       COMPUTES WAVENUMBER
        WRITE(5,*)'  WATER DEPTH (M)'
        READ(5,*)HO
        DO 12 I=1,NFC
        W2G=((TPI*F(I))**2)/9.81
        RKO=W2G
 14     RK(I)=W2G/TANH(RKO*HO)
        IF(ABS(RK(I)-RKO).LT.0.0001)GO TO 12
        RKO=RK(I)
        GO TO 14
 12     CONTINUE
C
C       COMPUTE PHASE WITH CORRECTION FOR TRANSFER FUNCTION
C       WRITE(5,*)'  PHASE CORRECTION -dphase/dfreq'
C       READ(5,*)DPHA
        DPHA=-0.556
        DO 4 I=1,NFC
 4      PHA(I)=(RK(I)*XB - TPI*F(I)*PH) + (FR-F(I))*DPHA
C       WRITE(5,*)' AMPLITUDE CORRECTION A=A0+A1F+A2F*F+A3F*F*F'
C       WRITE(5,*)' KEY IN A0,A1,A2,A3'
C       READ(5,*)A0,A1,A2,A3
```

```
      A0=-0.499284
      A1=4.152147
      A2=-1.64425
      DO 6 I=1,NFC
      A(I)=AA/(A0+A1*F(I)+A2*F(I)*F(I))
6     CONTINUE
      DO 1 I=1,NPT
      X=(I-1)*SEC
      ATE=0.
      DO 2 JJ=1,NFC
      ATE=ATE+A(JJ)*COS(-TPI*F(JJ)*X-PHA(JJ))
2     CONTINUE
      ATE= ATE*LSBVAL
      ITE(I+5)=ATE
1     CONTINUE
      NPTT=NPT-50
      DO 8 I=NPTT,NPT
      ITE(I)=ITE(NPTT)*EXP((NPTT-I)/20.)
8     CONTINUE
      WRITE(5,*)' DATA FILE NAME'
      CALL GETSTR(5,INPSTR,14,ERRFLG)
      OPEN(UNIT=3,NAME=INPSTR,TYPE='NEW',
     # FORM='UNFORMATTED',RECORDSIZE=512)
      WRITE(3)ITE
      CLOSE(UNIT=3)
      STOP
      END
```

Fastal.for

```
C-----------------------------------------------------------------------
C SUBROUTINE:  FAST
C REPLACES THE REAL VECTOR B(K), FOR K=1,2,...,N,
C WITH ITS FINITE DISCRETE FOURIER TRANSFORM
C-----------------------------------------------------------------------
C
      SUBROUTINE FAST(B, N)
C
C THE DC TERM IS RETURNED IN LOCATION B(1) WITH B(2) SET TO 0.
C THEREAFTER THE JTH HARMONIC IS RETURNED AS A COMPLEX
C NUMBER STORED AS  B(2*J+1) + I B(2*J+2).
C THE N/2 HARMONIC IS RETURNED IN B(N+1) WITH B(N+2) SET TO 0.
C HENCE, B MUST BE DIMENSIONED TO SIZE N+2.
C THE SUBROUTINE IS CALLED AS  FAST(B,N) WHERE N=2**M AND
C B IS THE REAL ARRAY DESCRIBED ABOVE.
C
      DIMENSION B(2)
      COMMON /CONS/ PII, P7, P7TWO, C22, S22, PI2
C
C IW IS A MACHINE DEPENDENT WRITE DEVICE NUMBER
C
      IW = 5
C
      PII = 4.*ATAN(1.)
      PI8 = PII/8.
      P7 = 1./SQRT(2.)
      P7TWO = 2.*P7
      C22 = COS(PI8)
      S22 = SIN(PI8)
      PI2 = 2.*PII
      DO 10 I=1,15
        M = I
        NT = 2**I
        IF (N.EQ.NT) GO TO 20
   10 CONTINUE
      WRITE (IW,9999)
 9999 FORMAT (33H N IS NOT A POWER OF TWO FOR FAST)
      STOP
   20 N4POW = M/2
C
C DO A RADIX 2 ITERATION FIRST IF ONE IS REQUIRED.
C
      IF (M-N4POW*2) 40, 40, 30
   30 NN = 2
      INT = N/NN
      CALL FR2TR(INT, B(1), B(INT+1))
      GO TO 50
   40 NN = 1
C
C PERFORM RADIX 4 ITERATIONS.
C
   50 IF (N4POW.EQ.0) GO TO 70
      DO 60 IT=1,N4POW
        NN = NN*4
        INT = N/NN
        CALL FR4TR(INT, NN, B(1), B(INT+1), B(2*INT+1), B(3*INT+1),
     *      B(1), B(INT+1), B(2*INT+1), B(3*INT+1))
   60 CONTINUE
C
C PERFORM IN-PLACE REORDERING.
```

```
C
  70  CALL FORD1(M, B)
      CALL FORD2(M, B)
      T = B(2)
      B(2) = 0.
      B(N+1) = T
      B(N+2) = 0.
      DO 80 IT=4,N,2
        B(IT) = -B(IT)
  80  CONTINUE
      RETURN
      END
C
C-----------------------------------------------------------------------
C SUBROUTINE:  FSST
C FOURIER SYNTHESIS SUBROUTINE
C-----------------------------------------------------------------------
C
      SUBROUTINE FSST(B, N)
C
C THIS SUBROUTINE SYNTHESIZES THE REAL VECTOR B(K), FOR
C K=1,2,...,N, FROM THE FOURIER COEFFICIENTS STORED IN THE
C B ARRAY OF SIZE N+2.  THE DC TERM IS IN B(1) WITH B(2) EQUAL
C TO  0.  THE JTH HARMONIC IS STORED AS B(2*J+1) + I B(2*J+2).
C THE N/2 HARMONIC IS IN B(N+1) WITH B(N+2) EQUAL TO 0.
C THE SUBROUTINE IS CALLED AS FSST(B,N) WHERE N=2**M AND
C B IS THE REAL ARRAY DISCUSSED ABOVE.
C
      DIMENSION B(2)
      COMMON /CONST/ PII, P7, P7TWO, C22, S22, PI2
C
C IW IS A MACHINE DEPENDENT WRITE DEVICE NUMBER
C
      IW = 5
C
      PII = 4.*ATAN(1.)
      PI8 = PII/8.
      P7 = 1./SQRT(2.)
      P7TWO = 2.*P7
      C22 = COS(PI8)
      S22 = SIN(PI8)
      PI2 = 2.*PII
      DO 10 I=1,15
        M = I
        NT = 2**I
        IF (N.EQ.NT) GO TO 20
  10  CONTINUE
      WRITE (IW,9999)
9999  FORMAT (33H N IS NOT A POWER OF TWO FOR FSST)
      STOP
  20  B(2) = B(N+1)
      DO 30 I=4,N,2
        B(I) = -B(I)
  30  CONTINUE
C
C SCALE THE INPUT BY N
C
      DO 40 I=1,N
        B(I) = B(I)/FLOAT(N)
  40  CONTINUE
```

```
      N4POW = M/2
C
C SCRAMBLE THE INPUTS
C
      CALL FORD2(M, B)
      CALL FORD1(M, B)
C
      IF (N4POW.EQ.0) GO TO 60
      NN = 4*N
      DO 50 IT=1,N4POW
        NN = NN/4
        INT = N/NN
        CALL FR4SYN(INT, NN, B(1), B(INT+1), B(2*INT+1), B(3*INT+1),
     *      B(1), B(INT+1), B(2*INT+1), B(3*INT+1))
  50  CONTINUE
C
C DO A RADIX 2 ITERATION IF ONE IS REQUIRED
C
  60  IF (M-N4POW*2) 80, 80, 70
  70  INT = N/2
      CALL FR2TR(INT, B(1), B(INT+1))
  80  RETURN
      END
C
C-----------------------------------------------------------------------
C SUBROUTINE:  FR2TR
C RADIX 2 ITERATION SUBROUTINE
C-----------------------------------------------------------------------
C
      SUBROUTINE FR2TR(INT, B0, B1)
      DIMENSION B0(2), B1(2)
      DO 10 K=1,INT
        T = B0(K) + B1(K)
        B1(K) = B0(K) - B1(K)
        B0(K) = T
  10  CONTINUE
      RETURN
      END
C
C-----------------------------------------------------------------------
C SUBROUTINE:  FR4TR
C RADIX 4 ITERATION SUBROUTINE
C-----------------------------------------------------------------------
C
      SUBROUTINE FR4TR(INT, NN, B0, B1, B2, B3, B4, B5, B6, B7)
      DIMENSION L(15), B0(2), B1(2), B2(2), B3(2), B4(2), B5(2), B6(2),
     *    B7(2)
      COMMON /CONS/ PII, P7, P7TWO, C22, S22, PI2
      EQUIVALENCE (L15,L(1)), (L14,L(2)), (L13,L(3)), (L12,L(4)),
     *    (L11,L(5)), (L10,L(6)), (L9,L(7)), (L8,L(8)), (L7,L(9)),
     *    (L6,L(10)), (L5,L(11)), (L4,L(12)), (L3,L(13)), (L2,L(14)),
     *    (L1,L(15))
C
C JTHET IS A REVERSED BINARY COUNTER, JR STEPS TWO AT A TIME TO
C LOCATE THE REAL PARTS OF INTERMEDIATE RESULTS, AND JI LOCATES
C THE IMAGINARY PART CORRESPONDING TO JR.
C
      L(1) = NN/4
      DO 40 K=2,15
        IF (L(K-1)-2) 10, 20, 30
```

```
   10     L(K-1) = 2
   20     L(K) = 2
          GO TO 40
   30     L(K) = L(K-1)/2
   40   CONTINUE
C
        PIOVN = PII/FLOAT(NN)
        JI = 3
        JL = 2
        JR = 2
C
        DO 120 J1=2,L1,2
        DO 120 J2=J1,L2,L1
        DO 120 J3=J2,L3,L2
        DO 120 J4=J3,L4,L3
        DO 120 J5=J4,L5,L4
        DO 120 J6=J5,L6,L5
        DO 120 J7=J6,L7,L6
        DO 120 J8=J7,L8,L7
        DO 120 J9=J8,L9,L8
        DO 120 J10=J9,L10,L9
        DO 120 J11=J10,L11,L10
        DO 120 J12=J11,L12,L11
        DO 120 J13=J12,L13,L12
        DO 120 J14=J13,L14,L13
        DO 120 JTHET=J14,L15,L14
          TH2 = JTHET - 2
          IF (TH2) 50, 50, 90
   50     DO 60 K=1,INT
            T0 = B0(K) + B2(K)
            T1 = B1(K) + B3(K)
            B2(K) = B0(K) - B2(K)
            B3(K) = B1(K) - B3(K)
            B0(K) = T0 + T1
            B1(K) = T0 - T1
   60     CONTINUE
C
          IF (NN-4) 120, 120, 70
   70     K0 = INT*4 + 1
          KL = K0 + INT - 1
          DO 80 K=K0,KL
            PR = P7*(B1(K)-B3(K))
            PI = P7*(B1(K)+B3(K))
            B3(K) = B2(K) + PI
            B1(K) = PI - B2(K)
            B2(K) = B0(K) - PR
            B0(K) = B0(K) + PR
   80     CONTINUE
          GO TO 120
C
   90     ARG = TH2*PIOVN
          C1 = COS(ARG)
          S1 = SIN(ARG)
          C2 = C1**2 - S1**2
          S2 = C1*S1 + C1*S1
          C3 = C1*C2 - S1*S2
          S3 = C2*S1 + S2*C1
C
          INT4 = INT*4
          J0 = JR*INT4 + 1
```

```
          K0 = J1*INT4 + 1
          JLAST = J0 + INT - 1
          DO 100 J=J0,JLAST
            K = K0 + J - J0
            R1 = B1(J)*C1 - B5(K)*S1
            R5 = B1(J)*S1 + B5(K)*C1
            T2 = B2(J)*C2 - B6(K)*S2
            T6 = B2(J)*S2 + B6(K)*C2
            T3 = B3(J)*C3 - B7(K)*S3
            T7 = B3(J)*S3 + B7(K)*C3
            T0 = B0(J) + T2
            T4 = B4(K) + T6
            T2 = B0(J) - T2
            T6 = B4(K) - T6
            T1 = R1 + T3
            T5 = R5 + T7
            T3 = R1 - T3
            T7 = R5 - T7
            B0(J) = T0 + T1
            B7(K) = T4 + T5
            B6(K) = T0 - T1
            B1(J) = T5 - T4
            B2(J) = T2 - T7
            B5(K) = T6 + T3
            B4(K) = T2 + T7
            B3(J) = T3 - T6
  100     CONTINUE
C
          JR = JR + 2
          JI = JI - 2
          IF (JI-JL) 110, 110, 120
  110     JI = 2*JR - 1
          JL = JR
  120   CONTINUE
        RETURN
        END
C
C-----------------------------------------------------------------------
C SUBROUTINE:  FR4SYN
C RADIX 4 SYNTHESIS
C-----------------------------------------------------------------------
C
C
        SUBROUTINE FR4SYN(INT, NN, B0, B1, B2, B3, B4, B5, B6, B7)
        DIMENSION L(15), B0(2), B1(2), B2(2), B3(2), B4(2), B5(2), B6(2),
       *    B7(2)
        COMMON /CONST/ PII, P7, P7TWO, C22, S22, PI2
        EQUIVALENCE (L15,L(1)), (L14,L(2)), (L13,L(3)), (L12,L(4)),
       *    (L11,L(5)), (L10,L(6)), (L9,L(7)), (L8,L(8)), (L7,L(9)),
       *    (L6,L(10)), (L5,L(11)), (L4,L(12)), (L3,L(13)), (L2,L(14)),
       *    (L1,L(15))
C
        L(1) = NN/4
        DO 40 K=2,15
          IF (L(K-1)-2) 10, 20, 30
  10      L(K-1) = 2
  20      L(K) = 2
          GO TO 40
  30      L(K) = L(K-1)/2
  40    CONTINUE
```

```
C
      PIOVN = PII/FLOAT(NN)
      JI = 3
      JL = 2
      JR = 2
C
      DO 120 J1=2,L1,2
      DO 120 J2=J1,L2,L1
      DO 120 J3=J2,L3,L2
      DO 120 J4=J3,L4,L3
      DO 120 J5=J4,L5,L4
      DO 120 J6=J5,L6,L5
      DO 120 J7=J6,L7,L6
      DO 120 J8=J7,L8,L7
      DO 120 J9=J8,L9,L8
      DO 120 J10=J9,L10,L9
      DO 120 J11=J10,L11,L10
      DO 120 J12=J11,L12,L11
      DO 120 J13=J12,L13,L12
      DO 120 J14=J13,L14,L13
      DO 120 JTHET=J14,L15,L14
        TH2 = JTHET - 2
        IF (TH2) 50, 50, 90
 50     DO 60 K=1,INT
          T0 = B0(K) + B1(K)
          T1 = B0(K) - B1(K)
          T2 = B2(K)*2.0
          T3 = B3(K)*2.0
          B0(K) = T0 + T2
          B2(K) = T0 - T2
          B1(K) = T1 + T3
          B3(K) = T1 - T3
 60     CONTINUE
C
        IF (NN-4) 120, 120, 70
 70     K0 = INT*4 + 1
        KL = K0 + INT - 1
        DO 80 K=K0,KL
          T2 = B0(K) - B2(K)
          T3 = B1(K) + B3(K)
          B0(K) = (B0(K)+B2(K))*2.0
          B2(K) = (B3(K)-B1(K))*2.0
          B1(K) = (T2+T3)*P7TWO
          B3(K) = (T3-T2)*P7TWO
 80     CONTINUE
        GO TO 120
 90     ARG = TH2*PIOVN
        C1 = COS(ARG)
        S1 = -SIN(ARG)
        C2 = C1**2 - S1**2
        S2 = C1*S1 + C1*S1
        C3 = C1*C2 - S1*S2
        S3 = C2*S1 + S2*C1
C
        INT4 = INT*4
        J0 = JR*INT4 + 1
        K0 = JI*INT4 + 1
        JLAST = J0 + INT - 1
        DO 100 J=J0,JLAST
          K = K0 + J - J0
```

```
            T0 = B0(J) + B6(K)
            T1 = B7(K) - B1(J)
            T2 = B0(J) - B6(K)
            T3 = B7(K) + B1(J)
            T4 = B2(J) + B4(K)
            T5 = B5(K) - B3(J)
            T6 = B5(K) + B3(J)
            T7 = B4(K) - B2(J)
            B0(J) = T0 + T4
            B4(K) = T1 + T5
            B1(J) = (T2+T6)*C1 - (T3+T7)*S1
            B5(K) = (T2+T6)*S1 + (T3+T7)*C1
            B2(J) = (T0-T4)*C2 - (T1-T5)*S2
            B6(K) = (T0-T4)*S2 + (T1-T5)*C2
            B3(J) = (T2-T6)*C3 - (T3-T7)*S3
            B7(K) = (T2-T6)*S3 + (T3-T7)*C3
  100     CONTINUE
          JR = JR + 2
          JI = JI - 2
          IF (JI-JL) 110, 110, 120
  110     JI = 2*JR - 1
          JL = JR
  120   CONTINUE
        RETURN
        END
C
C-------------------------------------------------------------------------
C SUBROUTINE:  FORD1
C IN-PLACE REORDERING SUBROUTINE
C-------------------------------------------------------------------------
C
        SUBROUTINE FORD1(M, B)
        DIMENSION B(2)
C
        K = 4
        KL = 2
        N = 2**M
        DO 40 J=4,N,2
          IF (K-J) 20, 20, 10
   10     T = B(J)
          B(J) = B(K)
          B(K) = T
   20     K = K - 2
          IF (K-KL) 30, 30, 40
   30     K = 2*J
          KL = J
   40   CONTINUE
        RETURN
        END
C
C-------------------------------------------------------------------------
C SUBROUTINE:  FORD2
C IN-PLACE REORDERING SUBROUTINE
C-------------------------------------------------------------------------
C
        SUBROUTINE FORD2(M, B)
        DIMENSION L(15), B(2)
        EQUIVALENCE (L15,L(1)), (L14,L(2)), (L13,L(3)), (L12,L(4)),
       *    (L11,L(5)), (L10,L(6)), (L9,L(7)), (L8,L(8)), (L7,L(9)),
       *    (L6,L(10)), (L5,L(11)), (L4,L(12)), (L3,L(13)), (L2,L(14)),
```

```
*     (L1,L(15))
      N = 2**M
      L(1) = N
      DO 10 K=2,M
        L(K) = L(K-1)/2
10    CONTINUE
      DO 20 K=M,14
        L(K+1) = 2
20    CONTINUE
      IJ = 2
      DO 40 J1=2,L1,2
      DO 40 J2=J1,L2,L1
      DO 40 J3=J2,L3,L2
      DO 40 J4=J3,L4,L3
      DO 40 J5=J4,L5,L4
      DO 40 J6=J5,L6,L5
      DO 40 J7=J6,L7,L6
      DO 40 J8=J7,L8,L7
      DO 40 J9=J8,L9,L8
      DO 40 J10=J9,L10,L9
      DO 40 J11=J10,L11,L10
      DO 40 J12=J11,L12,L11
      DO 40 J13=J12,L13,L12
      DO 40 J14=J13,L14,L13
      DO 40 JI=J14,L15,L14
        IF (IJ-JI) 30, 40, 40
30      T = B(IJ-1)
        B(IJ-1) = B(JI-1)
        B(JI-1) = T
        T = B(IJ)
        B(IJ) = B(JI)
        B(JI) = T
40      IJ = IJ + 2
      RETURN
      END
```

```
C-----------------------------------------------------------------------
C
C       FILDES.FOR      21-AUG-85
C
C       PROGRAM TO DESIGN A LOW PASS FILTER USING A HAMMING WINDOW
C-----------------------------------------------------------------------
C
        REAL*4 H(2050),W(513),HP(513),XX(257),YY(257)
        LOGICAL*1 ERRFLG,IRFIL(15),FR(15),HEAD(70)
C
        NNN=2048
        TPI=8.*ATAN(1.)
        WRITE(5,*)' ENTER SAMPLE FREQ, FILTER CUTOFF FREQ, WINDOW L'
        READ(5,*)FS,FC,IWLEN
        NCUT=IFIX((FC/FS)*NNN)
C
C ZERO THE ARRAYS
        DO 200 J=1,NNN+2
        H(J)=0.
  200   CONTINUE
        DO 300 J=1,IWLEN+2
        W(J)=0.
        HP(J)=0.
  300   CONTINUE
        DO 301 J=1,IWLEN/2 +2
        XX(J)=0.
        YY(J)=0.
  301   CONTINUE
C
C COMPUTE IDEAL FREQ RESPONSE WITH NNN/2 DELAY
        H(1)=1.
        H(2)=0.
        DO 100 K=2,NCUT
        THETA=TPI*(K-1)/2
        H(2*K-1) = COS(THETA)    !REAL PART
        H(2*K) = SIN(THETA)      !IMAG PART
  100   CONTINUE
C
C COMPUTE IMPULSE RESPONSE
        CALL FSST(H,NNN)
C
C MULTIPLY BY HAMMING WINDOW OVER THE CENTER IWLEN-1 POINTS
        IWM1D2=(IWLEN-1)/2
        DO 400 N=1,IWM1D2
        W(N)=0.54 - 0.46*COS(TPI*(N-1)/(IWLEN-1))
        HP(N)=H(NNN/2 -IWM1D2 +N-1)*W(N)
        HP(IWLEN-N+1)=HP(N)
  400   CONTINUE
        HP(IWM1D2+1)=(0.54+0.46)*H(NNN/2)                !WINDOW PEAK
        HP(IWLEN+1)=0.
C
C WRITE RESULTS
        WRITE(5,*)' FILENAME FOR IMPULSE RESPONSE'
        CALL GETSTR(5,IRFIL,14,ERRFLG)
        WRITE(5,*)' FILE HEADER'
        CALL GETSTR(5,HEAD,70,ERRFLG)
        OPEN(UNIT=1,NAME=IRFIL,TYPE='NEW',FORM='UNFORMATTED',
     #  RECORDSIZE=512)
        WRITE(1) (HEAD(J),J=1,70)
        WRITE(1) (HP(J),J=1,IWLEN+1)
```

```
      CLOSE(UNIT=1)
C
C PLOT RESULTS
      WRITE(5,*)'ENTER NNN MAX , FREQ MAX FOR PLOTS'
      READ(5,*)XMAX1,XMAX2
      DO 500 N=1,IWLEN
      XX(N)= FLOAT(N)
  500 CONTINUE
      PAUSE ' LOAD PAPER TO PLOT IMPULSE RESPONSE'
      CALL SETERM("176500)
      CALL ERASE
      CALL GRID('',XMAX1,0.,0.,'',0.05,-0.05,0.,0)
      CALL RJTICK(0.,0.,0.,XMAX1,-0.05,0.05,50.,0.01)
      CALL PLOT(IWLEN,XX,HP)
C
C COMPUTE FREQ RESPONSE AND PLOT
      CALL FAST(HP,IWLEN+1)
      DO 600 N=1,IWM1D2+2
      YY(N)=ALOG10(SQRT(HP(2*N-1)**2 + HP(2*N)**2))
      XX(N)=FLOAT(N)*(FS/FLOAT(IWLEN+1))
  600 CONTINUE
      PAUSE ' LOAD PAPER TO PLOT FREQ RESP'
      CALL ERASE
      CALL GRID('',XMAX2,0.,0.,'',0.,-8.,-8.,0)
      CALL RJTICK(-8.,0.,0.,XMAX2,-8.,0.,1.,1.)
      CALL PLOT(IWM1D2+2,XX,YY)
C
      STOP
      END
```

```
C-----------------------------------------------------------------------
C
C       LPFIL2.FOR      23-AUG-85
C
C       PERFORMS LINEAR CONVOLUTION BY OVERLAP ADD METHOD OF DATA
C       SEGMENTS. READS IN IMPULSE RESPONSE OF FILTER.
C-----------------------------------------------------------------------
C
        REAL*4 HP(1026),XX(1026),SAVE(514),YY(1026)
        INTEGER*2 IBUF1(513),IBUF2(513),IXX(513)
        LOGICAL*1 ERRFLG,IRFIL(15),INFIL(15),OUTFIL(15),IRHEAD(70)
        LOGICAL*1 HEAD(70)
        DIMENSION GLOCX(6),GLOCZ(6)
        COMMON NREADD,ISIZD,MDC,NCCH,NDCCH,MODED,MODEA,IRATE,
     #  PRESET,MODEC,HEAD,IGAIN,GLOCX,GLOCZ
C
        WRITE(5,*)' ENTER DATA SEGMENT LENGTH-LL, # OF SEGMENTS-NDSJP'
        READ(5,*)LL,NDSJP
        WRITE(5,*)' ENTER FILTER LENGTH IN SAMPLES-MM'
        READ(5,*)MM
        NNN=LL+MM-1
        WRITE(5,*)' ENTER NUMBER OF FILES-NFILES'
        READ(5,*)NFILES
C
C  MAKE 2**N FOR FFT
        CALL HICMP(NNN,NPFFT)
        WRITE(5,2)NPFFT
    2   FORMAT(' NPFFT=',I6)
C
C ZERO ARRAYS
        CALL ZERO(HP,NPFFT+2)
C
C READ IN FILTER FILE
        WRITE(5,*)' ENTER FILENAME OF IMPULSE RESP.'
        CALL GETSTR(5,IRFIL,14,ERRFLG)
        OPEN(UNIT=1,NAME=IRFIL,TYPE='OLD',FORM='UNFORMATTED')
        READ(1) (IRHEAD(J),J=1,70)
        WRITE(5,1) (IRHEAD(J),J=1,70)
    1   FORMAT(70A1)
        READ(1) (HP(N),N=1,512)
C COMPUTE FREQ RESPONSE
        CALL FAST(HP,NPFFT)
C
        CALL OPNNEW(3,OUTFIL)
C
C FILE LOOP
        DO 999 IF=1,NFILES
        CALL OPNOLD(2,INFIL)
        CALL ZERO(SAVE,MM+2)
C
C BEGIN FILTERING SEGMENT BY SEGMENT
        DO 100 IS=1,NDSJP
        CALL ZERO(XX,NPFFT+2)
C READ IN SEGMENT
        READ(2) (IXX(J),J=1,512)
        READ(2) (IDUM,J=1,512)
C
C CONVERT TO REAL AND SQUARE (FOR UW ONLY)
        DO 102 J=1,512
        XX(J)=FLOAT(IXX(J))**2
```

```
  102   CONTINUE
C
        CALL FAST(XX,NPFFT)
C MULT BY FREQ RESP OF FILTER
        DO 200 K=1,NPFFT/2 + 1
        KR=2*K-1
        KI=2*K
        YY(KR)=XX(KR)*HP(KR)  - XX(KI)*HP(KI)
        YY(KI)=XX(KI)*HP(KR)  + XX(KR)*HP(KI)
  200   CONTINUE
C
        CALL FSST(YY,NPFFT)
C
C ADD FIRST MM POINTS TO LAST MM POINTS OF PREVIOUS FFT
        DO 300 J=1,MM
        YY(J)=YY(J)+SAVE(J)
  300   CONTINUE
C
C WRITE TO DISK
C USE DOUBLE BUFFERING AND SKIP FIRST 256 POINTS(IE THE FILTER DELAY)
        IF(IS.EQ.1)GO TO 62
        IF(MOD(IS,2).EQ.0)GO TO 60      !IS IS EVEN
   62   DO 600 J=1,256
        IBUF1(J+256)=IFIX(YY(J))
        IBUF2(J)=IFIX(YY(J+256))
  600   CONTINUE
        IF(IS.EQ.1)GO TO 61
        WRITE(3)(IBUF1(J),J=1,512)
        GO TO 61
C
   60   DO 601 J=1,256
        IBUF1(J)=IFIX(YY(J+256))
        IBUF2(J+256)=IFIX(YY(J))
  601   CONTINUE
        WRITE(3)(IBUF2(J),J=1,512)
   61   CONTINUE
C
C SAVE LAST MM POINTS
        DO 400 J=1,MM
        SAVE(J)=YY(J+LL)
  400   CONTINUE
C
C GO BACK FOR NEXT SEGEMENT
  100   CONTINUE
C
C PICK UP LAST SEGMENT
        DO 700 J=1,256
        IBUF1(J+256)=IFIX(YY(J+512))
  700   CONTINUE
        WRITE(3)(IBUF1(J),J=1,512)
C
        CLOSE(UNIT=2)
  999   CONTINUE
C
        CLOSE(UNIT=1)
        CLOSE(UNIT=3)
        STOP
        END
```

```
C-----------------------------------------------------------------------
C       MOMSUM.FOR      9-4-85
C       PROGRAM TO INTEGRATE VELOCITY OVER FLUID AREA
C       READS FORM OUTPUT OF VECLST
C-----------------------------------------------------------------------
C
        DIMENSION X(10),Z(10),UB(8,8),WB(8,8)
        DIMENSION AREA(8,8),TAMU(200),TAMW(200),WT(200)
        LOGICAL*1 ERRFLG,INFIL(15),HEAD(70)
C
C OPEN DATA FILE
        WRITE(5,*)' ENTER INPUT FILE NAME'
        CALL GETSTR(5,INFIL,14,ERRFLG)
        OPEN(UNIT=1,NAME=INFIL,TYPE='OLD')
        CALL GETSTR(1,HEAD,69,ERRFLG)
        READ(1,*) (X(IX),IX=1,7)
C
        WRITE(5,*)'INPUT NUMBER OF TIME STEPS'
        READ(5,*)NTS
        WRITE(5,*)'INPUT NORMALIZING PARAMETERS-AK,WC,CP,XZERO,DEPTH'
        READ(5,*)AK,WC,CP,XZERO,DEPTH
        ANORM=(AK)**2/CP
C
C TIME STEP LOOP
        DO 100 IT=1,NTS
C
C READ IN DATA
        READ(1,1)TIME
    1   FORMAT(5X,F10.2)
        DO 301 IZ=1,7
        READ(1,*)Z(IZ),(UB(IX,IZ),IX=1,7)
        READ(1,*) (WB(IX,IZ),IX=1,7)
  301   CONTINUE
C
        IF(IT.NE.1)GO TO 59
C COMPUTE ELEMENTAL AREAS
        DO 200 IX=2,6
        DX=(X(IX+1)-X(IX-1))/2.
        DO 201 IZ=2,6
        DZ= -(Z(IZ+1)-Z(IZ-1))/2.
        AREA(IX,IZ)=DX*DZ
  201   CONTINUE
C
        DZ= -(Z(2)+Z(1))/2.
        AREA(IX,1)=DX*DZ
        DZ=DEPTH + (Z(7)+Z(6))/2.
        AREA(IX,7)=DX*DZ
  200   CONTINUE
C
C IX=1
        DX= X(2)-X(1)
        DZ= -(Z(2)+Z(1))/2.
        AREA(1,1)=DX*DZ
        DO 300 IZ=2,6
        DZ= -(Z(IZ+1)-Z(IZ-1))/2.
        AREA(1,IZ)=DX*DZ
  300   CONTINUE
        DZ=DEPTH + (Z(7)+Z(6))/2.
        AREA(1,7)=DX*DZ
C
```

```
C IX=7
        DX=X(7)-X(6)
        DZ= -(Z(2)+Z(1))/2.
        AREA(7,1)=DX*DZ
        DO 400 IZ=2,6
        DZ= -(Z(IZ+1)-Z(IZ-1))/2.
        AREA(7,IZ)=DZ*DX
  400   CONTINUE
        DZ=DEPTH + (Z(7)+Z(6))/2.
        AREA(7,7)=DX*DZ
C
C COMPUTE TOTAL AREA AS A CHECK
        ARTOT=0.0
        DO 900 IX=1,7
        DO 901 IZ=1,7
        ARTOT=ARTOT + AREA(IX,IZ)
  901   CONTINUE
  900   CONTINUE
        WRITE(5,*)ARTOT
   59   CONTINUE
C
C INTEGRATE VELOCITY OVER AREA
        TAMU(IT)=0.0
        TAMW(IT)=0.0
        DO 500 IX=1,7
        DO 501 IZ=1,7
        DUM=UB(IX,IZ)
        UB(IX,IZ)=AMAX1(0.,DUM)
        WB(IX,IZ)=AMIN1(0.,DUM)
        TAMU(IT)=TAMU(IT) + UB(IX,IZ)*AREA(IX,IZ)
        TAMW(IT)=TAMW(IT) + WB(IX,IZ)*AREA(IX,IZ)
  501   CONTINUE
  500   CONTINUE
C
C NORMALIZE
        TAMU(IT)=TAMU(IT)*ANORM
        TAMW(IT)=TAMW(IT)*ANORM
        WT(IT)=TIME*WC
  100   CONTINUE
        CLOSE(UNIT=1)
C
        PAUSE' CHANGE PAPER'
        CALL SETERM("176500)
        CALL ERASE
        CALL GRID('',453.,0.,0.,'',.3,-.3,0.,1)
        CALL RJTICK(0.,0.,0.,453.,-.3,.3,20.,0.01)
        CALL PLOT(NTS,WT,TAMU)
        CALL PLOT(-NTS,WT,TAMW)
        CALL EXIT
C
        STOP
        END
```

```
C-----------------------------------------------------------------------
C
C       OPNFI2.FOR      2-13-83
C
C       PROGRAMS TO OPEN FILES OF STANDARD DATA .  READS AND WRITES
C       HEADER AND PARAMETER LINE.
C               OPNOLD : OPENS OLD FILE
C               OPNNEW : OPENS NEW FILE
C
C-----------------------------------------------------------------------
C
        SUBROUTINE OPNOLD(IUNIT,INFILE)
        LOGICAL*1 INFILE(1),ERRFLG,HEAD(70)
        DIMENSION GLOCX(6),GLOCZ(6)
        COMMON NREADD,ISIZD,MDC,NCCH,NDCCH,MODED,MODEA,IRATE,
     #   PRESET,MODEC,HEAD,IGAIN,GLOCX,GLOCZ
        WRITE(5,1)
    1   FORMAT(' INPUT FILE NAME')
        CALL GETSTR(5,INFILE,14,ERRFLG)
        OPEN(UNIT=IUNIT,NAME=INFILE,TYPE='OLD',FORM='UNFORMATTED',
     #   RECORDSIZE=512)
        READ(IUNIT) (HEAD(J),J=1,70)
        READ(IUNIT)NREADD,ISIZD,MDC,NCCH,NDCCH,MODED,MODEA,IRATE,
     #   PRESET,MODEC,IGAIN,(GLOCX(J),GLOCZ(J),J=1,NCCH)
        RETURN
        END
C
C
        SUBROUTINE OPNNEW(IUNIT,OTFILE)
        LOGICAL*1 OTFILE(1),ERRFLG,HEAD(70)
        DIMENSION GLOCX(6),GLOCZ(6)
        COMMON NREADD,ISIZD,MDC,NCCH,NDCCH,MODED,MODEA,IRATE,
     #   PRESET,MODEC,HEAD,IGAIN,GLOCX,GLOCZ
        WRITE(5,1)
    1   FORMAT(' OUTPUT FILE NAME')
        CALL GETSTR(5,OTFILE,14,ERRFLG)
        OPEN(UNIT=IUNIT,NAME=OTFILE,TYPE='NEW',FORM='UNFORMATTED',
     #   RECORDSIZE=512)
        WRITE(IUNIT) (HEAD(J),J=1,70)
        WRITE(IUNIT)NREADD,ISIZD,MDC,NCCH,NDCCH,MODED,MODEA,IRATE,
     #   PRESET,MODEC,IGAIN,(GLOCX(J),GLOCZ(J),J=1,NCCH)
        RETURN
        END
```

```
C-------------------------------------------------------------------------
C       RDIGT2.FOR      20-APR-84
C
C       THIS IS A DIGITIZING PROGRAM TO BE USED WITH THE CALCOMP 9000
C       DIGITIZING BOARD.  IT IS SET UP FOR MOVIE FRAME DIGITIZATION.
C       THE PROGRAM READS A NUMBER OF DATA POINTS FOR EACH FRAME, SCALES
C       THEM, AND WRITES THEM INTO AN UNFORMATTED DATA FILE.  THE PROGRAM
C       THEN GOES ON TO THE NEXT FRAME.  THE INCREMENT MODE IS MOST USEFULL
C       AND MUST BE SET FROM THE CURSOR.(SEE MANUAL)  EACH DATA PAIR CONSISTS
C       OF A STRING OF 13 ASCII CHARACTERS(FORMAT 3 IN CALCOMP MANUAL).
C       THIS STRING IS RECEIVED OFF THE RS232 PORT BY SUBROUTINE RPICK.MAC
C       IN FILE RPICK.(LINK WITH THIS). IT IS CONVERTED TO
C       DIRECT ACCESS FILES ARE USED
C       GOOD LUCK R.J. RAPP
C-------------------------------------------------------------------------
C
        LOGICAL*1 COOR(13),BUF(13312),OUTFIL(15),ERRFLG,HEAD(70),IDEC
        LOGICAL*1 CALFIL(15)
        INTEGER*2  IXX(512),IYY(512)
        DIMENSION DX(4),DY(4),PX(4),PY(4)
  13    FORMAT(T3,2F5.0)
  21    FORMAT(1A1)
        NFR=0
C
C OPEN OUTPUT FILE FOR COORDINATES
        WRITE(5,*)' OUTPUT FILE NAME?'
        CALL GETSTR(5,OUTFIL,14,ERRFLG)
        WRITE(5,*)' IS THIS AN EXISTING FILE? Y OT N'
        READ(5,21)IDEC
        IF(IDEC.EQ.'N')GO TO 50
        WRITE(5,*)' ENTER LAST FRAME NUMBER IN FILE'
        READ(5,*)NFR
        OPEN(UNIT=1,NAME=OUTFIL,TYPE='OLD',FORM='UNFORMATTED',
     #  RECORDSIZE=512,ACCESS='DIRECT')
        GO TO 99
   50   OPEN(UNIT=1,NAME=OUTFIL,TYPE='NEW',FORM='UNFORMATTED',
     #  RECORDSIZE=512,ACCESS='DIRECT')
        WRITE(5,*)' ENTER FILE HEADER'
        CALL GETSTR(5,HEAD,69,ERRFLG)
        WRITE(1'1) (HEAD(J),J=1,70)
C
   99   CONTINUE
C
C ENTER CALIBRATION FILE FOR SCALING
        WRITE(5,*)' ENTER FILENAME OF SCALING COEFF'
        CALL GETSTR(5,CALFIL,14,ERRFLG)
        OPEN(UNIT=2,NAME=CALFIL,TYPE='OLD')
        READ(2,*) (PX(J),J=1,4)
        READ(2,*) (PY(J),J=1,4)
C
C ENTER A REFERENCE POINT TO BE USED TO REFERENCE EACH FRAME
        WRITE(5,*)' ENTER FRAME REFERENCE POINT X,Y'
        READ(5,*)ZX,ZY
C ENTER NUMBER OF POINTS
        WRITE(5,*)' ENTER NO. OF POINTS PER FRAME'
        READ(5,*)NPTS
C
C FRAME LOOP
 1000   NFR=NFR+1
        WRITE(5,12)ZX,ZY
```

```
   12   FORMAT(' SEND REFERENCE POINT',2F6.3,' BY PRESSING 1 ON CURSOR')
        WRITE(5,*)' PRESS 3 TO END PROGRAM AND CLOSE FILE'
        CALL RPICK(13,COOR)
        IF(COOR(1).EQ.13.)CALL ROLL(COOR)
        IF(COOR(1).EQ.'3')GO TO 400
        DECODE(13,13,COOR)DXZ,DYZ
        WRITE(5,15)COOR
   15   FORMAT(1X,13A1)
        WRITE(5,16)DXZ,DYZ
   16   FORMAT(1X,2F10.3)
C
C CONVERT TO REAL COOR
        RX=PX(1)
        RY=PY(1)
        DO 302 II=1,3
        RX= RX + (DXZ**II)*PX(II+1)
        RY= RY + (DYZ**II)*PY(II+1)                              !
  302   CONTINUE
        WRITE(5,16)RX,RY
        WRITE(5,*)' BEGIN DIGITIZING CONTOUR LEFT TO RIGHT BY PRESSING 1'
        WRITE(5,*)' ON CURSOR AND HOLDING. PRESS 2 AT END OF CONTOUR'
C
C READ ALL POINTS
        NC=NPTS*13
        CALL RPICK(NC,BUF)
C
C ZERO OUTPUT ARRAY
        DO 700 N=1,NPTS
        IXX(N)=0.
        IYY(N)=0.
  700   CONTINUE
C
C CHECK TO INSURE THAT 1ST CHARACTER IS NOT A <CR>
        ISHIFT=0
        IF(BUF(1).EQ.13.)ISHIFT=1
C CONVERT DATA TO RELATIVE COORDINATES, CONVERTS TO MILLIMETERS
        DO 300 N=1,NPTS-1
        IZ=(N-1)*13 + ISHIFT
        DO 200 J=1,13
        COOR(J)=BUF(IZ+J)
  200   CONTINUE
        IF(COOR(1).EQ.'2')GO TO 600              !REST OF POINTS ARE ZERO
        DECODE(13,13,COOR)XX,YY
C
C CONVERT X,Y COOR
        DUMX=PX(1) - RX + ZX
        DUMY=PY(1) - RY + ZY
        DO 301 II=1,3
        DUMX=DUMX+ (XX**II)*PX(II+1)
        DUMY=DUMY+ (YY**II)*PY(II+1)
  301   CONTINUE
        IXX(N)=IFIX((DUMX)*1000.)
        IYY(N)=IFIX((DUMY)*1000.)
  300   CONTINUE
  600   CONTINUE
        WRITE(1'NFR*2+1)N-1,(IXX(J),J=1,N-1)
        WRITE(1'NFR*2+2)N-1,(IYY(J),J=1,N-1)
C
        DO 500 KK=1,10
        WRITE(5,14)IXX(KK),IYY(KK)
```

```
  500   CONTINUE
   14   FORMAT(2I10)
C
       GO TO 1000
C
  400   CONTINUE
       CLOSE(UNIT=1)
       STOP
       END
C
C
       SUBROUTINE ROLL(COOR)
C      SUBROUTINE TO ROLL CHARACTER ORDER IF A CARRIAGE RETURN IS IN THE
C      FIRST ELEMENT. A FIXIT ROUTINE
       LOGICAL*1 COOR(13),DUM(13)
       DO 10 N=1,13
       DUM(N)=COOR(N)
   10  CONTINUE
       DO 20 N=1,12
       COOR(N)=DUM(N+1)
   20  CONTINUE
       COOR(13)=DUM(1)
       RETURN
       END
```

```
C-----------------------------------------------------------------------
C       RJAOUT.FOR      7-22-85
C       REVISED VERSION OF ANAOUT TO ALLOW 6 MINUTE INTERVAL REPEATS.
C
C       PROGRAM ANAOUT1
C       PROGRAM TO OUTPUT ANALOG DATA
C       ALSO SEND TRIGGER SIGNAL
C       26-APR-84
C-----------------------------------------------------------------------
        DIMENSION ISIG(4000)
        REAL SIG(6000)
        LOGICAL*1 INPSTR(15)
C
        WRITE(5,*)' DATA FILE NAME'
        CALL GETSTR(5,INPSTR,14,ERRFLG)
 5      CONTINUE
        WRITE(5,*)'  AMPLITUDE GAIN,WINDOW ST&ED(S)'
        READ(5,*)GAIN,TS,TE
        WRITE(5,*)'  TIME DELAY'
        READ(5,*)TDLY
        ITS=TS/(0.0092)
        NPT=TE/(0.0092)
        NPTDLY=TDLY/(0.0092) + ITS
C
        DO 3 I=1,4000
 3      ISIG(I)=0
C
        OPEN(UNIT=3,NAME=INPSTR,TYPE='OLD',
     #  FORM='UNFORMATTED',RECORDSIZE=512)
        READ(3)SIG
        CLOSE(UNIT=3)
        DO 2 I=ITS,NPT
 2      ISIG(I)=SIG(I)*GAIN
C
C SET UP OUTPUT PARAMETERS
        IRATE=5
        PRESET=1.
        IUNIT=0
        MODE=0
        ICMF=0
        CALL IDAC(1,0,0)        !TO ZERO THE OUTPUT
        CALL IDAC(0,0,0)
C
C INITIATE THE SAMPLING SEQUENCE
        WRITE(5,*)' INITIATE SAMPLING SEQUENCE , TYPE 1'
        READ(5,*)IGO
C
 4      CONTINUE
C
C START THE TRIGGER TO SAMPLE A ZERO
        ITGL=(5*4096/20.)
        CALL IDAC(0,IUNIT,ITGL)
        ICHAN=1
        NPT=NPT+5
        WRITE(5,*)' ZERO SAMPLE TRIGGER SENT'
C
C WAIT 2 MINUTES
        ICMFW=0
        CALL SETR(5,0,0,12000.,ICMFW)
        CALL LWAIT(ICMFW,0)
```

```
C BRING TRIGGER DOWN AND WAIT 10 MORE SECONDS
        ITGL=0
        CALL IDAC(0,0,ITGL)
        ICMFW=0
        CALL SETR(5,0,0,1000.,ICMFW)
        CALL LWAIT(ICMFW,0)
C
C START WAVE SIGNAL AND TRIGGER
C SEND DELAY PART OF SIGNAL
        DO 1 I=ITS,NPTDLY
        ICMF=I
        CALL SETR(IRATE,,MODE,PRESET,ICMF)
        CALL LWAIT(ICMF,I)
        CALL IDAC(ICHAN,IUNIT,ISIG(I))
        CALL SETR(-1,,,,)
 1      CONTINUE
C
C SEND SIGNAL AND TRIGGER
        ITGL=(5*4096/20.)
        CALL IDAC(0,0,ITGL)
        IF(NPTDLY.GT.NPT) GO TO 4
        DO 7 I=NPTDLY+1,NPT
        ICMF=I
        CALL SETR(IRATE,,MODE,PRESET,ICMF)
        CALL LWAIT(ICMF,I)
        CALL IDAC(ICHAN,IUNIT,ISIG(I))
        CALL SETR(-1,,,,)
 7      CONTINUE
C BRING DOWN TRIGGER
        ITGL=0
        CALL IDAC(0,0,ITGL)
        WRITE(5,*)' WAVE SIGNAL AND TRIGGER SENT'
C
C WAIT 6 MINUTES
        ICMFW=0
        CALL SETR(5,0,0,36000.,ICMFW)
        CALL LWAIT(ICMFW,0)
        GO TO 4
 6      STOP
        END
```

```
C-----------------------------------------------------------------------
C       RJDSK.FOR       3-14-85
C
C       PROGRAM TO SAMPLE DT 3382 BOARD TO DISK(HIGH SPEED CONTINUOUS WRITE)
C
C-----------------------------------------------------------------------
C
        DIMENSION IBUFF(1024)
        INTEGER ICHANS(6)
        LOGICAL*1 OUTFIL(15),ERRFLG,IDEV(3)
C
        WRITE(5,*)' INPUT- NCHANS, NSCANS- 1 SCAN = 1024 WORDS'
        READ(5,*)NCHANS,NSCANS
        NBLKS=IFIX(FLOAT(NSCANS)*FLOAT(NCHANS)*4.)
C
C COMPUTE CHANNEL LIST AND SET UP SAMPLING MODE
        DO 100 I=1,NCHANS
        ICHANS(I)=I-1
  100   CONTINUE
        IGAINS=-1
        CALL DFCHZA(NCHANS,ICHANS,IGAINS,'ES')
C
C OPEN THE DISK OUTPUT FILE
        WRITE(5,*)' OUTPUT DEVICE?'
        CALL GETSTR(5,IDEV,3,ERRFLG)
        WRITE(5,*)' OUTPUT FILE NAME'
        CALL GETSTR(5,OUTFIL,14,ERRFLG)
        CALL DFOPEN(IDEV,OUTFIL,NBLKS,IFCHAN,NAVAIL)
        WRITE(5,2)IFCHAN,NAVAIL
    2   FORMAT(' IFCHAN=',I10,'   NAVAIL=',I10)
C
C SET THE CLOCK
        WRITE(5,*)' INPUT SAMPLING RATE - IDPWR,DIVSR'
        READ(5,*)IDPWR,DIVSR
        CALL STOPKA()    !STOP CLOCK IN CASE IT IS RUNNING
C
        CALL ARMKA(IDPWR,DIVSR) !ARM THE CLOCK
        WRITE(5,1)
    1   FORMAT(' CONVERTER IS ARMED, TRIGGER ON SCHMITT TRIGGER INPUT')
C
C SET UP SAMPLING TO DISK
        CALL RDSKZA(NBLKS,IFCHAN)
C
C READ DATA FILE
        CALL RMBLK(IFCHAN,1,4,IBUFF)
        CALL DFWAIT(IFCHAN)
        WRITE(5,3)IBUFF
    3   FORMAT(10I7)
C
C CLOSE UP SHOP
        CALL DFCLOS(IFCHAN,1)
        CALL CLOSZA()
        STOP
        END
```

SSPFIL.FOR

```
      SUBROUTINE GDATA (N,M,X,XBAR,STD,D,SUMSQ)                          GDAT 52
C     THE ABOVE CARD SHOULD BE PLACED IN PROPER SEQUENCE
C          BEFORE COMPILING THIS UNDER  IBM FORTRAN G.
C                                                                         GDAT  1
C     ..................................................................GDAT  2
C                                                                         GDAT  3
C        SUBROUTINE GDATA                                                 GDAT  4
C                                                                         GDAT  5
C        PURPOSE                                                          GDAT  6
C           GENERATE INDEPENDENT VARIABLES UP TO THE M-TH POWER (THE      GDAT  7
C           HIGHEST DEGREE POLYNOMIAL SPECIFIED), AND COMPUTE MEANS,      GDAT  8
C           STANDARD DEVIATIONS, AND CORRELATION COEFFICIENTS.  THIS      GDAT  9
C           SUBROUTINE IS NORMALLY CALLED BEFORE SUBROUTINES ORDER,       GDAT 10
C           MINV AND MULTR IN THE PERFORMANCE OF A POLYNOMIAL             GDAT 11
C           REGRESSION.                                                   GDAT 12
C                                                                         GDAT 13
C        USAGE                                                            GDAT 14
C           CALL GDATA (N,M,X,XBAR,STD,D,SUMSQ)                           GDAT 15
C                                                                         GDAT 16
C        DESCRIPTION OF PARAMETERS                                        GDAT 17
C           N      - NUMBER OF OBSERVATIONS.                              GDAT 18
C           M      - THE HIGHEST DEGREE POLYNOMIAL TO BE FITTED.          GDAT 19
C           X      - INPUT MATRIX (N BY M+1) .  WHEN THE SUBROUTINE IS    GDAT 20
C                    CALLED, DATA FOR THE INDEPENDENT VARIABLE ARE        GDAT 21
C                    STORED IN THE FIRST COLUMN OF MATRIX X, AND DATA FORGDAT 22
C                    THE DEPENDENT VARIABLE ARE STORED IN THE LAST        GDAT 23
C                    COLUMN OF THE MATRIX.  UPON RETURNING TO THE         GDAT 24
C                    CALLING ROUTINE, GENERATED POWERS OF THE INDEPENDENTGDAT 25
C                    VARIABLE ARE STORED IN COLUMNS 2 THROUGH M.          GDAT 26
C           XBAR   - OUTPUT VECTOR OF LENGTH M+1 CONTAINING MEANS OF      GDAT 27
C                    INDEPENDENT AND DEPENDENT VARIABLES.                 GDAT 28
C           STD    - OUTPUT VECTOR OF LENGTH M+1 CONTAINING STANDARD      GDAT 29
C                    DEVIATIONS OF INDEPENDENT AND DEPENDENT VARIABLES.   GDAT 30
C           D      - OUTPUT MATRIX (ONLY UPPER TRIANGULAR PORTION OF THE  GDAT 31
C                    SYMMETRIC MATRIX OF M+1 BY M+1) CONTAINING CORRELA-  GDAT 32
C                    TION COEFFICIENTS.  (STORAGE MODE OF 1)              GDAT 33
C           SUMSQ  - OUTPUT VECTOR OF LENGTH M+1 CONTAINING SUMS OF       GDAT 34
C                    PRODUCTS OF DEVIATIONS FROM MEANS  OF INDEPENDENT    GDAT 35
C                    AND DEPENDENT VARIABLES.                             GDAT 36
C                                                                         GDAT 37
C        REMARKS                                                          GDAT 38
C           N MUST BE GREATER THAN M+1.                                   GDAT 39
C           IF M IS EQUAL TO 5 OR GREATER, SINGLE PRECISION MAY NOT BE    GDAT 40
C           SUFFICIENT TO GIVE SATISFACTORY COMPUTATIONAL RESULTS.        GDAT 41
C                                                                         GDAT 42
C        SUBROUTINES AND FUNCTION SUBPROGRAMS REQUIRED                    GDAT 43
C           NONE                                                          GDAT 44
C                                                                         GDAT 45
C        METHOD                                                           GDAT 46
C           REFER TO B. OSTLE, 'STATISTICS IN RESEARCH', THE IOWA STATE   GDAT 47
C           COLLEGE PRESS, 1954, CHAPTER 6.                               GDAT 48
C                                                                         GDAT 49
C     ..................................................................GDAT 50
C                                                                         GDAT 51
      DIMENSION X(1),XBAR(1),STD(1),D(1),SUMSQ(1)                         GDAT 53
C                                                                         GDAT 54
C        ..............................................................GDAT 55
C                                                                         GDAT 56
C        IF A DOUBLE PRECISION VERSION OF THIS ROUTINE IS DESIRED, THE    GDAT 57
```

```
C        C IN COLUMN 1 SHOULD BE REMOVED FROM THE DOUBLE PRECISION      GDAT 58
C        STATEMENT WHICH FOLLOWS.                                       GDAT 59
C                                                                       GDAT 60
C     DOUBLE PRECISION X,XBAR,STD,D,SUMSQ,T1,T2                         GDAT 61
C                                                                       GDAT 62
C        THE C MUST ALSO BE REMOVED FROM DOUBLE PRECISION STATEMENTS    GDAT 63
C        APPEARING IN OTHER ROUTINES USED IN CONJUNCTION WITH THIS      GDAT 64
C        ROUTINE.                                                       GDAT 65
C                                                                       GDAT 66
C        THE DOUBLE PRECISION VERSION OF THIS SUBROUTINE MUST ALSO      GDAT 67
C        CONTAIN DOUBLE PRECISION FORTRAN FUNCTIONS.  SQRT AND ABS IN   GDAT 68
C        STATEMENT 180 MUST BE CHANGED TO DSQRT AND DABS.               GDAT 69
C                                                                       GDAT 70
C        .....GDAT 71
C                                                                       GDAT 72
C     GENERATE INDEPENDENT VARIABLES                                    GDAT 73
C                                                                       GDAT 74
      IF(M-1) 105, 105, 90                                              GDAT 75
   90 L1=0                                                              GDAT 76
      DO 100 I=2,M                                                      GDAT 77
      L1=L1+N                                                           GDAT 78
      DO 100 J=1,N                                                      GDAT 79
      L=L1+J                                                            GDAT 80
      K=L-N                                                             GDAT 81
  100 X(L)=X(K)*X(J)                                                    GDAT 82
C                                                                       GDAT 83
C     CALCULATE MEANS                                                   GDAT 84
C                                                                       GDAT 85
  105 MM=M+1                                                            GDAT 86
      DF=N                                                              GDAT 87
      L=0                                                               GDAT 88
      DO 115 I=1,MM                                                     GDAT 89
      XBAR(I)=0.0                                                       GDAT 90
      DO 110 J=1,N                                                      GDAT 91
      L=L+1                                                             GDAT 92
  110 XBAR(I)=XBAR(I)+X(L)                                              GDAT 93
  115 XBAR(I)=XBAR(I)/DF                                                GDAT 94
C                                                                       GDAT 95
      DO 130 I=1,MM                                                     GDAT 96
  130 STD(I)=0.0                                                        GDAT 97
C                                                                       GDAT 98
C     CALCULATE SUMS OF CROSS-PRODUCTS OF DEVIATIONS                    GDAT 99
C                                                                       GDAT100
      L=((MM+1)*MM)/2                                                   GDAT101
      DO 150 I=1,L                                                      GDAT102
  150 D(I)=0.0                                                          GDAT103
      DO 170 K=1,N                                                      GDAT104
      L=0                                                               GDAT105
      DO 170 J=1,MM                                                     GDAT106
      L2=N*(J-1)+K                                                      GDAT107
      T2=X(L2)-XBAR(J)                                                  GDAT108
      STD(J)=STD(J)+T2                                                  GDAT109
      DO 170 I=1,J                                                      GDAT110
      L1=N*(I-1)+K                                                      GDAT111
      T1=X(L1)-XBAR(I)                                                  GDAT112
      L=L+1                                                             GDAT113
  170 D(L)=D(L)+T1*T2                                                   GDAT114
      L=0                                                               GDAT115
      DO 175 J=1,MM                                                     GDAT116
      DO 175 I=1,J                                                      GDAT117
```

```
      L=L+1                                                          GDAT1180
  175 D(L)=D(L)-STD(I)*STD(J)/DF                                     GDAT1190
      L=0                                                            GDAT1200
      DO 180 I=1,MM                                                  GDAT1210
      L=L+I                                                          GDAT1220
      SUMSQ(I)=D(L)                                                  GDAT1230
  180 STD(I)= SQRT( ABS(D(L)))                                       GDAT1240
C                                                                    GDAT1250
C     CALCULATE CORRELATION COEFFICIENTS                             GDAT1260
C                                                                    GDAT1270
      L=0                                                            GDAT1280
      DO 190 J=1,MM                                                  GDAT1290
      DO 190 I=1,J                                                   GDAT1300
      L=L+1                                                          GDAT1310
  190 D(L)=D(L)/(STD(I)*STD(J))                                      GDAT1320
C                                                                    GDAT1330
C     CALCULATE STANDARD DEVIATIONS                                  GDAT1340
C                                                                    GDAT1350
      DF=SQRT(DF-1.0)                                                GDAT1360
      DO 200 I=1,MM                                                  GDAT1370
  200 STD(I)=STD(I)/DF                                               GDAT1380
      RETURN                                                         GDAT1390
      END                                                            GDAT1400
C
C
C
      SUBROUTINE ORDER (M,R,NDEP,K,ISAVE,RX,RY)                      ORDE  00
C                                                                    ORDE  10
C     .....ORDE  20
C                                                                    ORDE  30
C        SUBROUTINE ORDER                                            ORDE  40
C                                                                    ORDE  50
C        PURPOSE                                                     ORDE  60
C           CONSTRUCT FROM A LARGER MATRIX OF CORRELATION COEFFICIENTS ORDE  70
C           A SUBSET MATRIX OF INTERCORRELATIONS AMONG INDEPENDENT   ORDE  80
C           VARIABLES AND A VECTOR OF INTERCORRELATIONS OF INDEPENDENT ORDE  90
C           VARIABLES WITH DEPENDENT VARIABLE.  THIS SUBROUTINE IS   ORDE 100
C           NORMALLY USED IN THE PERFORMANCE OF MULTIPLE AND POLYNOMIAL ORDE 110
C           REGRESSION ANALYSES.                                     ORDE 120
C                                                                    ORDE 130
C        USAGE                                                       ORDE 140
C           CALL ORDER (M,R,NDEP,K,ISAVE,RX,RY)                      ORDE 150
C                                                                    ORDE 160
C        DESCRIPTION OF PARAMETERS                                   ORDE 170
C           M      - NUMBER OF VARIABLES AND ORDER OF MATRIX R.      ORDE 180
C           R      - INPUT MATRIX CONTAINING CORRELATION COEFFICIENTS. ORDE 190
C                    THIS SUBROUTINE EXPECTS ONLY UPPER TRIANGULAR   ORDE 200
C                    PORTION OF THE SYMMETRIC MATRIX TO BE STORED (BY ORDE 210
C                    COLUMN) IN R.  (STORAGE MODE OF 1)              ORDE 220
C           NDEP   - THE SUBSCRIPT NUMBER OF THE DEPENDENT VARIABLE. ORDE 230
C           K      - NUMBER OF INDEPENDENT VARIABLES TO BE INCLUDED  ORDE 240
C                    IN THE FORTHCOMING REGRESSION. K MUST BE GREATER ORDE 250
C                    THAN OR EQUAL TO 1.                             ORDE 251
C           ISAVE  - INPUT VECTOR OF LENGTH K+1 CONTAINING, IN ASCENDING ORDE 260
C                    ORDER, THE SUBSCRIPT NUMBERS OF K INDEPENDENT   ORDE 270
C                    VARIABLES TO BE INCLUDED IN THE FORTHCOMING REGRES- ORDE 280
C                    SION.                                           ORDE 290
C                    UPON RETURNING TO THE CALLING ROUTINE, THIS VECTOR ORDE 300
C                    CONTAINS, IN ADDITION, THE SUBSCRIPT NUMBER OF  ORDE 310
C                    THE DEPENDENT VARIABLE IN K+1 POSITION.         ORDE 320
```